

MICROFABRICATED PIEZORESISTIVE SHEAR STRESS
SENSORS FOR UNDERWATER APPLICATIONS

A DISSERTATION
SUBMITTED TO THE DEPARTMENT OF
MECHANICAL ENGINEERING
AND THE COMMITTEE ON GRADUATE STUDIES
OF STANFORD UNIVERSITY
IN PARTIAL FULFILLMENT OF THE REQUIREMENTS
FOR THE DEGREE OF
DOCTOR OF PHILOSOPHY

Arnoldus Alvin Barlian
January 2009

UMI Number: 3351486

Copyright 2009 by
Barlian, Arnoldus Alvin

All rights reserved.

INFORMATION TO USERS

The quality of this reproduction is dependent upon the quality of the copy submitted. Broken or indistinct print, colored or poor quality illustrations and photographs, print bleed-through, substandard margins, and improper alignment can adversely affect reproduction.

In the unlikely event that the author did not send a complete manuscript and there are missing pages, these will be noted. Also, if unauthorized copyright material had to be removed, a note will indicate the deletion.

UMI[®]

UMI Microform 3351486


Copyright 2009 by ProQuest LLC.

All rights reserved. This microform edition is protected against unauthorized copying under Title 17, United States Code.

ProQuest LLC
789 E. Eisenhower Parkway
PO Box 1346
Ann Arbor, MI 48106-1346

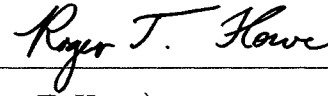
© Copyright by Arnoldus Alvin Barlian 2009
All Rights Reserved

I certify that I have read this dissertation and that, in my opinion, it is fully adequate in scope and quality as a dissertation for the degree of Doctor of Philosophy.




(Beth L. Pruitt) Principal Adviser

I certify that I have read this dissertation and that, in my opinion, it is fully adequate in scope and quality as a dissertation for the degree of Doctor of Philosophy.



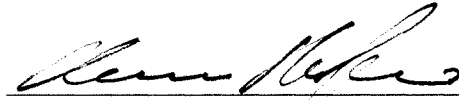
(Roger T. Howe)

I certify that I have read this dissertation and that, in my opinion, it is fully adequate in scope and quality as a dissertation for the degree of Doctor of Philosophy.



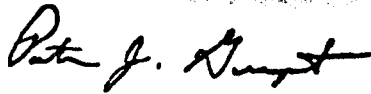
(Thomas W. Kenny)

I certify that I have read this dissertation and that, in my opinion, it is fully adequate in scope and quality as a dissertation for the degree of Doctor of Philosophy.



(Aaron Partridge)

Approved for the University Committee on Graduate Studies.



Abstract

Shear stress at the solid-fluid interface is a frequently studied parameter in fluid dynamics because of its relevance to many engineering applications, such as those in aerodynamic and hydrodynamic design. Shear stress measurements are also critical in biomedical and environmental science research. For example, shear stress data lead to improved understanding of fluid flow physics in cardiovascular systems and coral reef ecologies.

The core element of this work is the design, fabrication, characterization, and testing of piezoresistive floating-element shear stress sensors. Conventional and oblique-angle ion-implantation techniques were used to form piezoresistors on the top and sidewall surfaces of the tethers. Hydrogen anneal technology was used to smooth sidewall scallops commonly seen in the Deep Reactive Ion Etching process and to reduce the noise in sidewall piezoresistors by almost an order of magnitude. A micro-fabricated piezoresistive cantilever was used to characterize the in-plane sensitivity, while Laser Doppler Vibrometry was used to characterize its out-of-plane sensitivity.

The $\text{SiO}_2/\text{Si}_3\text{N}_4/\text{SiO}_2$ triplex layer and Parylene C were used as passivation schemes in two underwater experiments. The first experiment used a cylindrical water tank sitting on a rotating table to produce solid body rotation. The second experiment used a gravity-driven water flume to create a uniform, fully-developed flow over the sensor. Polymer flip-chip flexible interconnects were fabricated and used for the packaging of the sensor in the gravity-driven water flume experiment.

Finally, a novel sidewall epitaxial piezoresistor fabrication process using selective deposition and early findings on electromechanical characteristics of cantilevers fabricated using this technique were demonstrated for in-plane force sensing applications.

Acknowledgements

I would like to express my sincere gratitude to my advisor, Prof. Beth Pruitt, for her invaluable guidance, mentorship, and patience since supervising my “Independent Study” course in Winter 2003. She introduced me to the fascinating world of MEMS and was always available whenever I sought help and advice. I was fortunate to have the opportunity in assisting her set up the first micro and nanofabrication lab course at Stanford (ME342). Three years later, through her nomination, I was presented the Stanford Centennial Teaching Assistant Award from Stanford University. I am very thankful for her advice during my doctoral dissertation work and her mentorship while teaching the class.

I would also like to thank my reading and oral examination committee members, Prof. Roger Howe, Prof. Thomas Kenny, Dr. Aaron Partridge, Prof. Yoshio Nishi, and Prof. Jeffrey Koseff, for their time, encouraging support, and invaluable feedback.

I would like to acknowledge the Stanford Environmental Fluid Mechanics Laboratory, whose work motivated this project. In particular, I would like to thank Prof. Jeffrey Koseff and Prof. Stephen Monismith for their initial input during the design phase of the project and their insights on fluid mechanics. Also, thanks go to Ryan Lowe, Bob Brown, and Dr. Derek Fong for their assistance in setting up the underwater experiments in this project.

All fabrication described in this work was done at the Stanford Nanofabrication Facility (SNF). This project, therefore, would have not been possible without the help and support from SNF and its staff, particularly Mary Tang, Gladys Sarmiento, Maurice Stevens, Uli Thumser, Mahnaz Mansourpour, Nancy Latta, Paul Jerabek, and Ed Myers. SNF was an excellent place to exchange ideas, ask for process advice,

and learn from its senior members. I would like to especially thank Eric Perozziello. Many times I turned to him for his advice on fabrication issues and problems. I would also like to acknowledge my first mentor in the clean room, Mohammed Badi, who showed me all the tricks for working efficiently.

Financial support for this work was provided by the National Science Foundation (NSF) under grant CTS-0428889 and the Center of Integrated Nanomechanical Systems (COINS) under grant ECS-0425914. SNF (a member of the National Nanotechnology Infrastructure Network) is supported by the NSF under Grant ECS-9731293. I am also grateful for the scholarships I have received, most importantly “P.T. Caltex Pacific Indonesia (Chevron Corp.) Scholarship,” which fully sponsored my education in the U.S. for the first four and a half years.

I am thankful and proud of joining the Pruitt Group since its inception in 2003. This group has been a great source of inspiration, assistance, and humor. I have significantly benefited from daily interactions with its members and shared many fun memories in and out of school with many (if not all) of them, past and present: Edwin Adhiprakasha, Sung-Jin Park, Vikram Mukundan, Andrew Davenport, Matt Beasley, Sara Zhao, Eerik Hantsoo, Vanessa Chial, Frederic Declercq, Amy Lee, Ratul Narain, Caitlin Quance, Jeff Li, Ambert Ho, Sarah Coulthard, Gretchen Chua, Josh Stark, Mariana Meyer, Anthony Pettes, Tracy Fung, Joe Mallon, Ali Rastegar, Joey Doll, Rebecca Taylor, Pierre Ponce, Nahid Harjee, Dr. Tina Lamers, Dr. James Norman, Maria Suggs, Chelsey Simmons, Niveditha Arumugam, Holly Butterfield, and Bryan Petzold. Special thanks go to Pierre Ponce and Dr. Tina Lamers for proofreading this dissertation and to Nahid Harjee for introducing me to \LaTeX . Another special thanks goes to Doreen Wood for her administrative help and support. I would also like to thank all Kenny and Howe group members for their help, friendship, and laughter in and out of the clean room.

I am thankful to Prof. Michael Plesniak, who introduced me to engineering research during my senior year at Purdue University. His guidance and encouragement led me to pursue a Ph.D. degree. Many thanks to my friends who have supported me during my seemingly endless pursuit of a Ph.D. degree, especially my long-time friends from Purdue: Felix Rantow, Indra Tjahjono, Maxime Mbabele, and Murtaza,

and friends whom I met early in my years at Stanford: Paul “Wira” Lim, Nawee Butsunorn, Edwin Adhiprakasha, and Arief Suriadi. Very special thanks go to Rena Jardine, Mary Taylor, and Mike Jakoby for the all wonderful years living in “the hood.” I am greatly indebted to Stephanie Gunawan for her care and support during the most difficult times of my life.

Finally and most importantly, I owe an enormous debt of gratitude to my parents, Johannes and Huriaty Barlian, as well as my brother, Andre Barlian, without whom, I would not have been able to reach this critical achievement in my life. The completion of my Ph.D. would not have been possible without their full support, love, and patience.

*To my parents,
who have made innumerable sacrifices for my education.*

*I shall be telling this with a sigh
Somewhere ages and ages hence:
Two roads diverged in a wood, and I –
I took the one less traveled by,
And that has made all the difference.*

The Road Not Taken by Robert Frost (1916)

Contents

Abstract	iv
Acknowledgements	v
1 Introduction	1
1.1 Motivation	1
1.1.1 Biomechanics	2
1.1.2 Environmental Engineering and Science	6
1.1.3 Reliable Shear Stress Measurements	7
1.2 Background	11
1.2.1 Fluid Mechanics	11
1.2.2 Micro Electromechanical Systems (MEMS)	19
1.3 Overview of Dissertation	24
2 Prior Art	26
2.1 Macro-scale Measurement Techniques	26
2.1.1 Indirect Method: Hot-wire and Hot-film Anemometry	27
2.1.2 Direct Method: Surface Fence and Floating-Element Sensors	29
2.2 MEMS Shear Stress Sensors	32
2.2.1 Indirect Method: Hot-wire and Hot-film Anemometry	32
2.2.2 Direct Method: Surface Fence and Floating-Element Sensors	34
2.2.3 Indirect and Direct MEMS Sensors: Comparison	45
2.3 Shear Stress Sensors for Underwater Applications	52

3	Piezoresistors: History and Fundamentals	55
3.1	History of Piezoresistance	55
3.2	Fundamentals of Piezoresistance	59
3.2.1	Silicon Crystal Structure	61
3.2.2	Piezoresistance Theory	62
3.2.3	Piezoresistor Fabrication	69
3.2.4	Design and Process Parameters for Piezoresistor Performance	73
3.2.5	Noise in Piezoresistors	81
3.3	Note and Acknowledgement	84
4	Sensor Design and Fabrication	87
4.1	Design	87
4.1.1	Plate Element and Tethers	88
4.1.2	Gap Size	91
4.1.3	Piezoresistors: TSUPREM-IV Simulations	93
4.2	Fabrication	96
4.3	Note and Acknowledgement	100
5	Sensor Characterization	102
5.1	Sensitivities	102
5.1.1	In-plane Sensitivity	103
5.1.2	Out-of-plane Sensitivity	116
5.2	Temperature Coefficient of Sensitivity	117
5.3	Noise	118
5.4	Note and Acknowledgement	119
6	Sensor Passivation and Underwater Testing	121
6.1	Passivation Schemes	121
6.1.1	Review	121
6.1.2	Reliability Testing	124
6.2	Rotating Table	125
6.2.1	Theory and Setup	125

6.2.2	Results	127
6.3	Gravity Driven Water Flume	131
6.3.1	Packaging: Flip-Chip Flexible Interconnects	131
6.3.2	Experiment and Results	135
6.4	Micro Particle Image Velocimetry (μ PIV)	141
6.5	Note and Acknowledgement	147
7	Sidewall Epitaxial Piezoresistors	148
7.1	Motivation	148
7.2	Fabrication Method	150
7.2.1	Process Flow	150
7.2.2	Challenges and Problems	152
7.3	Characterization	153
7.3.1	Deposition Rate	156
7.3.2	I-V Curve and Noise Characteristics	156
7.3.3	Sensitivity	157
7.4	Improved Fabrication Method	162
7.5	Note and Acknowledgement	163
8	Conclusion and Future Work	165
8.1	Conclusion	165
8.2	Future Work	166
A	Process Run Sheets	169
B	Selective Epitaxial Deposition Recipe	180
C	TSUPREM-4 Codes	184
D	Chemical Symbols	196
	Bibliography	199

List of Tables

1.1	Approximate dynamic viscosities, μ , and densities, ρ , of common fluids (and those that are relevant in this dissertation) at Standard Atmospheric Pressure.	12
2.1	The summary of capacitive, piezoresistive, and optical transduction scheme characteristics.	49
3.1	Comparisons of doping methods.	74
4.1	The ion implantation process parameters for TSUPREM-4 simulations.	95
5.1	Range of peak concentration, $P(p)$, and sensitivity with respect to the input variations.	114
5.2	Change in $\frac{\Delta\rho}{\rho}$ due to dimensional variations of the tethers.	115
7.1	Voltage noise spectral densities of several ion-implanted and epitaxial layer piezoresistors at 10 Hz.	158
A.1	Shear stress sensor fabrication process run sheet.	170
A.2	Polymer flip-chip flexible interconnects fabrication process run sheet.	175
A.3	Selective sidewall epitaxial piezoresistor process run sheet.	177
B.1	Selective doped epitaxial deposition recipe.	181
D.1	Chemical symbols and names used in this work.	197

List of Figures

1.1	Typical blood flow, velocity profile, and range of wall shear stress magnitude in blood vessels.	3
1.2	Endothelial cell physiology and hemodynamic shear stress.	4
1.3	Computational model of mean shear stress distribution in the anterior wall and posterior wall.	5
1.4	Coral reef ecosystems from sites on the Great Barrier Reef and in the Caribbean.	8
1.5	PLIF image of dye transfer from the coral canopy under unidirectional flow and wave dominated flow.	9
1.6	A force acting on a surface and its components.	13
1.7	Stress at a point.	14
1.8	A fluid flow over a flat plate and the velocity boundary layer.	15
1.9	An internal flow: A fluid flow inside a duct.	17
1.10	Solid-body rotation.	18
2.1	Schematic diagram of the hot-wire/film anemometry principle.	28
2.2	Schematic diagram of the floating-element shear stress sensor principle.	30
2.3	Sources of error in shear stress measurements using floating-element shear stress sensors.	31
2.4	A macro-scale floating-element shear stress-sensor design.	31
2.5	Microfabricated thermal-based shear stress sensor using a polysilicon heater.	33
2.6	Four different polysilicon structure types of thermal-based shear stress sensors.	35

2.7	Underwater thermal-based shear stress sensor.	36
2.8	Additional force components acting on the floating element of a micro-fabricated shear stress sensor in a pressure-driven internal flow. . . .	38
2.9	Floating-element based shear stress sensors using capacitive transduction scheme and polyimide sacrificial layer.	40
2.10	A capacitive floating-element shear stress sensor with interdigitated fingers.	41
2.11	A piezoresistive floating-element shear stress sensor.	43
2.12	Piezoresistive microfabricated surface-fence shear stress sensor.	44
2.13	Optical floating-element shear stress sensor.	46
2.14	Optical fiber-based micromachined shear stress sensor using Fabry-Perot technique and floating-element concept.	47
2.15	Optical-based floating-element shear stress sensor based on the geometric Moiré technique.	48
3.1	The alteration of specific resistance produced in different metals by hammering-induced strain.	56
3.2	Technological advances in IC fabrication and micromachining.	60
3.3	Covalently bonded diamond cubic structure of silicon.	62
3.4	Commonly employed crystal planes of silicon, i.e. (100), (110), and (111) planes.	63
3.5	Notation for Smiths test configurations in 1954.	65
3.6	Test configuration and resulting schematic diagrams of probable constant energy surfaces in momentum space for n-type Si.	67
3.7	Microfabricated piezoresistive cantilever and TSUPREM4 simulation plots of doping profiles using ion implantation and epitaxial deposition techniques.	69
3.8	Room temperature piezoresistive coefficients in the (100) plane.	76
3.9	Piezoresistive coefficients as a function of doping.	77
3.10	The adjusted piezoresistance factor $P(N, T)$ as a function of impurity concentration and temperature.	78

3.11	Trends of key piezoresistive properties.	80
3.12	Carriers' number fluctuation based on McWhorter and Hooge models.	82
3.13	Plot of Hooge noise parameter, α , as a function of anneal diffusion length, \sqrt{Dt}	85
3.14	Typical noise curve of a full-bridged piezoresistor.	86
4.1	Piezoresistive floating element shear stress sensor.	88
4.2	Mechanical forces model of the shear stress sensor.	90
4.3	Cross section of a tether.	91
4.4	Illustration of angles used in TSUPREM-4 simulations.	95
4.5	Typical TSUPREM-4 simulation output plot.	97
4.6	Shear stress sensor fabrication process.	99
4.7	The sidewall roughness before and after hydrogen anneal.	100
4.8	SEM images of the finished microfabricated floating-element shear stress sensor.	101
5.1	The experimental setup for in-plane sensitivity characterization.	104
5.2	Microfabricated piezoresistive silicon cantilever force sensor used for the in-plane sensitivity calibration of the shear stress sensor.	105
5.3	Laser Doppler Velocimetry and resonance excitation technique to calibrate the microfabricated piezoresistive cantilever force sensor.	105
5.4	Experimental setup for the in-plane sensitivity calibration of the shear stress sensor.	108
5.5	Inverted microscope view and lumped parameter model of the cantilever-sensor system.	109
5.6	In-plane and out-of-plane sensitivities results.	110
5.7	Hysteresis and non-linearity in in-plane sensitivity calibration.	110
5.8	Repeatability of five sequential measurements.	111
5.9	TSUPREM-4 simulation results on the effect of implant parameters to the output of the piezoresistors.	113
5.10	First out-of-plane resonant frequency of the sensor predicted by COM-SOL finite element simulation.	117

5.11	Temperature Coefficient of Sensitivity (TCS).	118
5.12	Schematic diagram of the noise measurement setup.	119
5.13	Noise characteristics of the piezoresistors with and without hydrogen anneal.	120
6.1	Several examples of passivation layer's failure mechanisms.	122
6.2	Parylene C molecule.	124
6.3	Parylene Deposition System 2010 (PDS2010), manufactured by Spe- cialty Coating Systems.	125
6.4	Passivation schemes underwater test.	126
6.5	Cylindrical tank affixed onto a rotating table.	127
6.6	Acoustic Doppler Velocimetry (ADV) apparatus with three receivers for the reflected acoustic waves and aluminum arm.	128
6.7	Fluid flow and the velocity boundary layer over a flat plate in the rotating table experiment.	129
6.8	Velocity of fluid particles at several locations in the rotating table. . .	130
6.9	Fabrication process steps of the flip-chip flexible interconnects.	132
6.10	Polymer flip-chip flexible interconnects.	133
6.11	Conductive polymer used in the fabrication of the polymer flip-chip flexible interconnects.	133
6.12	The nylon structure and a sensor chip.	134
6.13	Sensor packaging for gravity-driven water flume experiment.	134
6.14	The gravity-driven water flume.	136
6.15	Gravity-driven water flume: the acrylic extension.	137
6.16	Gravity-driven water flume: the weir and the sink.	137
6.17	Gravity-driven water flume: the gate.	138
6.18	A typical DMM output of the piezoresistors on a released and an un- released sensors.	139
6.19	A typical output from top- and sidewall-implanted piezoresistors. . .	139
6.20	Comparison of the normalized change in resistance from experiment and theoretical prediction.	141

6.21	Gravity-driven water flume: non-ideal flow and sources of error. . . .	142
6.22	The difference in the experimental results and theoretical predictions were likely due to unexpected flow behavior (unsteady, non-uniform, and wavy), which affected uncertainty in the air-water interface slope measurements.	143
6.23	PDMS mini channel.	145
6.24	A schematic of the experimental setup for the μ PIV experiment. . . .	145
6.25	COMSOL simulation and μ PIV experiment results.	146
7.1	Sidewall epitaxial piezoresistor concept.	150
7.2	Sidewall epitaxial piezoresistor fabrication process flow.	151
7.3	Illustrations of problems encountered during the patterning of oxide and aluminum because of poor step coverage and significant non-uniformity in the photoresist over the topography in the sidewall epitaxial layer piezoresistor fabrication process.	154
7.4	SEM image of the cantilever with sidewall epitaxial layers.	155
7.5	SEM image of the cantilever with sidewall epitaxial layers and FIB platinum deposited on the top of one of the piezoresistors.	155
7.6	SEM images of the tip of a cantilever which did not have the protective oxide completely removed before epitaxial layer deposition.	156
7.7	Deposition rate as a function of gap size.	157
7.8	The noise spectrum and I-V curve of a typical sidewall epitaxial piezoresistor with platinum.	158
7.9	Experimental setup for sidewall epitaxial piezoresistor sensitivity calibration.	159
7.10	The values of experimental $P(N)$ from this work and other researchers, compared against the theoretical prediction.	162
7.11	An alternative fabrication method to improve the reliability and repeatability of the sidewall epitaxial piezoresistors process.	164

Chapter 1

Introduction

This chapter introduces the motivation behind direct measurements of wall shear stress, particularly in liquid environments, and the importance of reliable shear stress sensors. Reviews of relevant basic fundamentals of fluid mechanics and Micro Electromechanical Systems (MEMS) are presented. Finally, this chapter concludes with an overview of this dissertation.

1.1 Motivation

Shear stress at the solid-fluid interface is a frequently studied parameter in fluid dynamics because of its relevance in many engineering applications. Specifically, measurements of shear stress are important in aerodynamic and hydrodynamic designs. For example, an aircraft experiences a force (drag) from the shear stress exerted by the air on its body, causing decreased fuel efficiency and increased cost of operation. However, the body of these vehicles (shape, dimensions, materials, etc.) can be designed to minimize drag force if physical forces acting on the vehicle's body, including shear stress, are well understood.

A complete understanding of shear stress is also critical in other engineering fields and the life sciences. For example, information on shear stress distributions with high spatial and temporal resolution is essential in the study of turbulent boundary layers and for active control of turbulent flow. Measurements of shear stress are

also important in controlling polymer extrusion processes, turbomachinery design, robotics, tactile imaging, and many other engineering applications. The following sections discuss some “unconventional” applications where direct measurements of shear stress at the micro scale are critical for formulating accurate models.

1.1.1 Biomechanics

Shear stress data lead to improved understanding of fluid flow physics in biomechanical and biomedical research.

Endothelial cells¹) experience hemodynamic forces, shear stress and pressure, exerted by a non-Newtonian fluid (blood) in viscoelastic vessels [1, 2]. Osteoblasts² experience shear stress from fluid flow in the lacunar-canalicular network [3–5]. Improved understanding of the forces on cells exposed to fluid loading leads to better understanding of disease formation and prevention techniques. In these examples, shear stress was inferred from assumed flow profiles and theoretical models. These indirect methods provide good qualitative comparisons, but not calibrated, quantitative data. Direct measurements of wall shear stress are required to validate indirect techniques and computational models.

Cardiovascular Mechanics

Studies have shown that hemodynamic forces play a major role in the determination of blood vessel diameter [6, 7], vascular remodeling³ [8–11], and vascular diseases, such as atherosclerosis [12, 13] and aneurysm [14]. Atherosclerosis, the leading cause of death in the developed world, is a geometrically focal disease that tends to form in blood vessel bifurcations⁴ [15]. According to Malek et al. [15], blood flows more slowly near bifurcations and changes direction with the cardiac cycle (recirculation and oscillatory), resulting in relatively weaker net hemodynamic shear stress, the

¹a thin layer of cells covering the inner wall of blood vessels in a cardiovascular system.

²bone cells

³Vascular remodeling alters the structure of blood vessels. The remodeling process is caused by cell growth, cell death, cell migration, and production or degradation of extracellular matrix [8].

⁴division of a blood vessel into two branches.

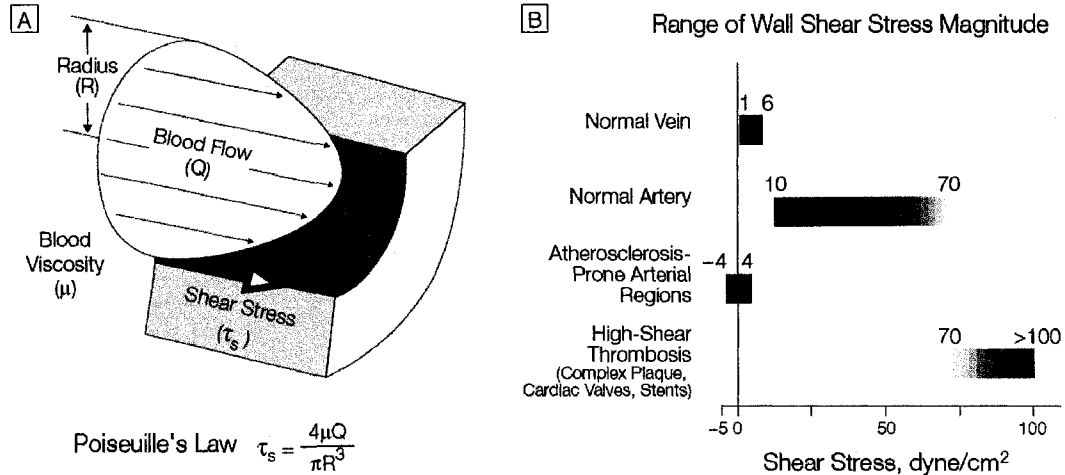


Figure 1.1: (a) Typical blood flow and velocity profile inside a blood vessel. (b) Range of wall shear stress magnitude for normal vein and arteries and plagued vessels. Source: Malek et al. [15]; ©1999 American Medical Association; reproduced with permission.

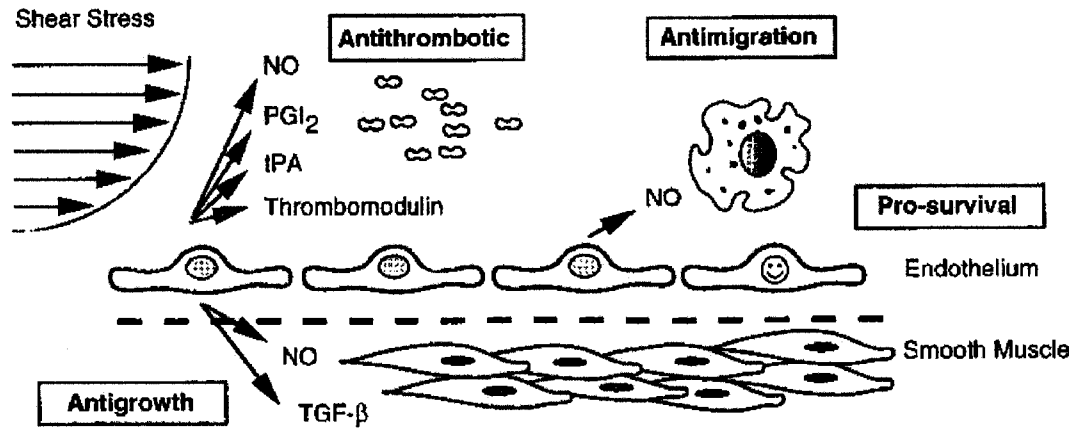
frictional force acting on the endothelial cell layer from blood flow inside the vessels (Figure 1.1). Lower shear stress levels (<4 dyne cm^{-2}) result in the production of endothelial cells with an atherogenic⁵ phenotype [15]. In contrast, the vessel regions that are exposed to steady laminar blood flow and higher shear stress levels (>15 dyne cm^{-2}) exhibit endothelial quiescence and atheroprotective⁶ gene expression profiles [15, 16]. These steady laminar flow regions remain relatively disease-free (Figure 1.2) [16].

Understanding the effect of hemodynamic forces, especially shear stress, on endothelial cell function and shear-stress regulated gene products⁷ under physiological flow conditions (oscillatory and pulsatile) can contribute toward earlier detection and prevention of cardiovascular diseases [17]. Advanced computational models can predict complex blood flow and the resulting shear stress in human cardiovascular

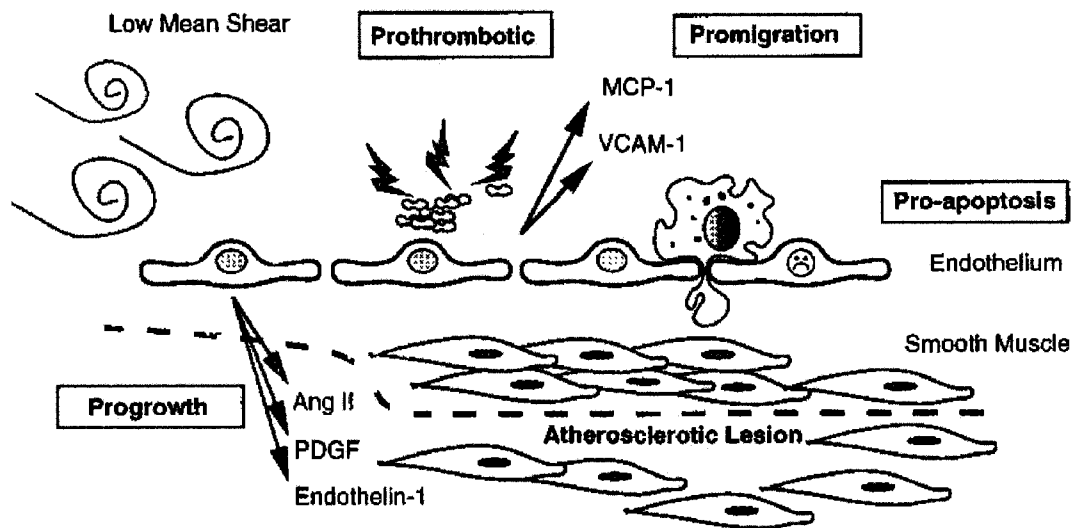
⁵tending to form fatty plaque underneath the endothelial cell layer in arteries.

⁶tending to prevent the formation of fatty plaque underneath the endothelial cell layer in arteries.

⁷proteins resulting from expression of a gene



(a) Steady laminar flow results in constant high-magnitude shear stress (typically $>15 \text{ dyne cm}^{-2}$ [15]). This level of shear stress promotes the release of factors that protect endothelial cells.



(b) Flow reversal and recirculation near blood vessel bifurcations result in time-varying low-magnitude shear stress (typically $<4 \text{ dyne cm}^{-2}$ [15]). This level of shear stress promotes the expression of surface molecules and the release of factors that favor the formation and development of atherosclerosis.

Figure 1.2: Endothelial cell physiology and hemodynamic shear stress. Source: Traub and Berk [16]; ©1998 American Heart Association; reproduced with permission.

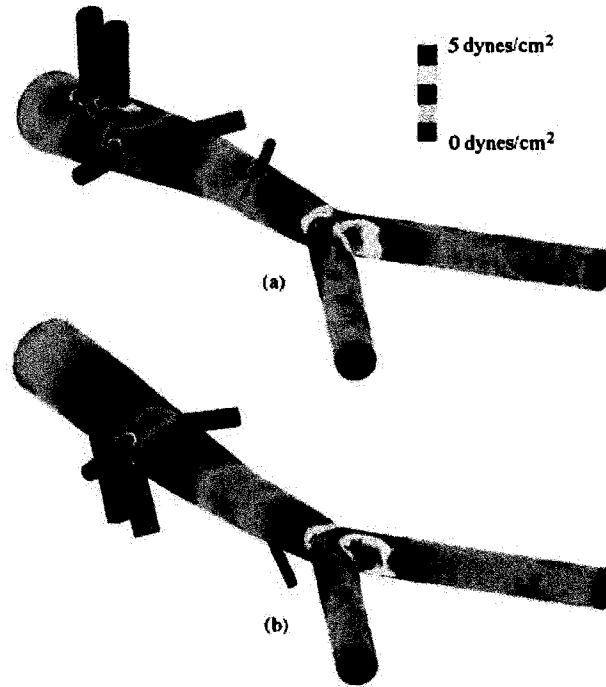


Figure 1.3: Computational model of mean shear stress distribution in (a) the anterior wall and (b) posterior wall. The regions of low mean shear stress, where atherosclerosis sites are commonly found, are predicted well in this model. Source: Taylor et al. [18]; ©1998 Springer Science and Business Media; reproduced with permission.

systems (Figure 1.3) [18,19]. Non-invasive techniques, such as Pulsed Doppler Sonography (PDS) and Magnetic Resonance Imaging (MRI), are used to estimate wall shear stress in arteries in vivo [17, 20–25]. However, these are indirect measurement techniques, i.e. shear stress is computed from flow velocity profiles inside arteries. Most indirect in vivo measurements of wall shear stress show qualitative agreement, but quantitative differences exist. Shaaban and Duerinckx [17] provide a review of wall shear stress measurement techniques in arteries.

Bone Mechanics

Experimental evidence has recently suggested that fluid flow induced forces in lacunar-canalicular networks are important biophysical signals (along with streaming potentials, piezoelectric signals, and matrix strain) in bone mechanotransduction [3–5]. In fact, osteoblasts are more responsive to fluid flow induced shear stress than mechanical strains [26, 27]. These fluid motions are dynamic and oscillatory. Jacobs et al. [28] reported on how various flow profiles affect the responsiveness of osteoblasts in vitro. Human fetal osteoblastic cells were cultured onto quartz microscope slides in a parallel plate flow chamber, exposed to oscillatory fluid flow, and assessed by using intracellular calcium concentration as the responsiveness parameter. Shear stress was then computed based on flow profile. You et al. [29] extended the work of Jacobs et al. and suggested that multiple mechanotransduction pathways exist in bone cells and that their activation depends on the stimulus type. Determining an appropriate cellular mechanical stimulus is important in understanding the role of mechanical loading in the regulation of bone growth. Donahue et al. [30] suggested that the mechanosensitivity of osteoblasts to oscillatory flow induced shear stress can also be modulated by chemotransport⁸ and the cells' biochemical surroundings.

1.1.2 Environmental Engineering and Science

Not only are the hydrodynamics in coral reef environments interesting and uncommonly studied in engineering applications, they play a major role in coral reef ecology (Figure 1.4). The hydrodynamics of coral reefs exist in a wide range of length scales, from eddies produced by island wakes (\sim km), down to scale comparable to single coral colonies (\sim mm) [31]. At scales \sim 1 m, for steady flows, the law of the wall gives a good description of the vertical variation in flow structure [31, 32]. However, at these scales, the hydrodynamics is typically modeled as a flow over a significantly rough surface [31]. The bottom drag coefficient, C_D , over coral pavements⁹ is four to

⁸mass transfer of chemicals

⁹extensive canopies made from corals [31]

ten times larger (or more) than over flat sandy or muddy bottoms [31, 33]. The turbulence caused by the roughness of the coral reef pavement affects mass transfer and transfer of nutrients between the coral reef and the surrounding ecosystem [33, 34].

Moreover, the hydrodynamics in shallow-water coral reef communities is dominated by surface gravity waves, significantly modifying the structure of the flow. First, wave stresses exist only in the wave boundary layer, although the law of the wall still holds outside of the boundary layer [36–38]. Second, the coral roughness is not completely submerged in the wave boundary layer, thus the “canopy theory” must be used [39, 40]. The “canopy theory” refers to the analysis of flows over and through large roughness elements, e.g. buildings in a city or trees in a forest, for understanding associated momentum, heat, and mass transfer processes [39]. However, adapting these ideas to flows over corals is not straightforward because of the presence of waves. Flow visualization experiments using Planar Laser-Induced Fluorescence (PLIF) to study mixing over corals, both with and without waves, show that there are dramatic differences in mass transfer (Figure 1.5) [41]. Furthermore, there are substantial variations in shear stress and mass transfer, even within a single coral head, that lead to flow-dependent changes in coral morphology [42–44].

While momentum transfer in wave-driven flows has been treated extensively, there is no comparable literature as to the effects of waves on mass transfer, since wave-driven flows do not occur in widely used engineering devices, e.g. heat exchangers, turbines, pipes, or chemical reactors. Shear stress sensors are needed to enable measurements at the scale of coral reef length characteristics, $\sim 100 \mu\text{m}$, and to study the effect of hydrodynamics on mass transfer in a wavy flow. A comprehensive review of the hydrodynamics in the coral reef environment is available elsewhere [31, 45].

1.1.3 Reliable Shear Stress Measurements

In the examples described in Sections 1.1.1 and 1.1.2, accurate shear stress measurements are needed to study the effect of complex fluid flow on biological cells (endothelial and osteoblast cells) and living organisms (coral reefs). For the aforementioned applications, a reliable shear stress sensor must have the following characteristics:

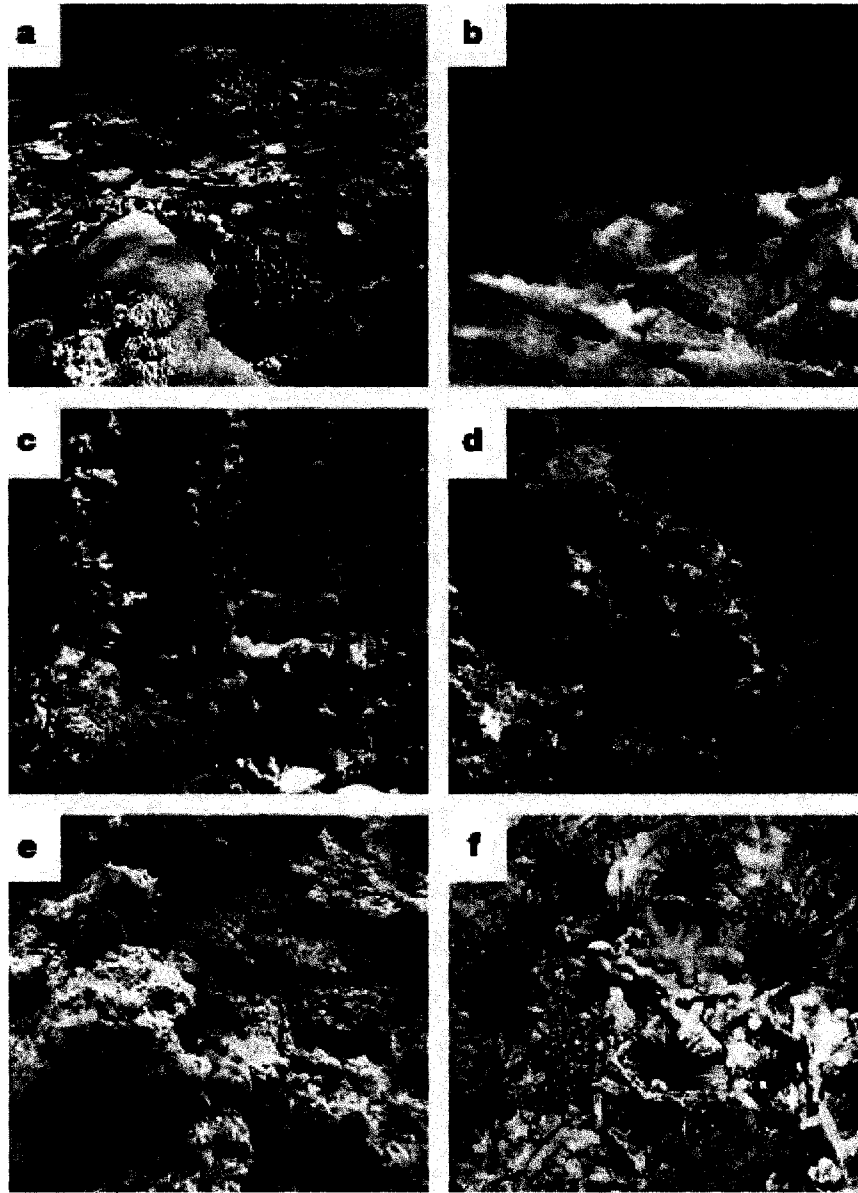


Figure 1.4: Coral reef ecosystems from sites on the Great Barrier Reef (a, c, d, e) and in the Caribbean (b, f) at various “health states”. (a) “healthy” (b) “stressed” (c) macro algae (d) turf (e) heterotrophic (f) sea urchin barren. Source: Bellwood et al. [35]; ©2004 Macmillan Publishers Ltd: Nature; reproduced with permission.

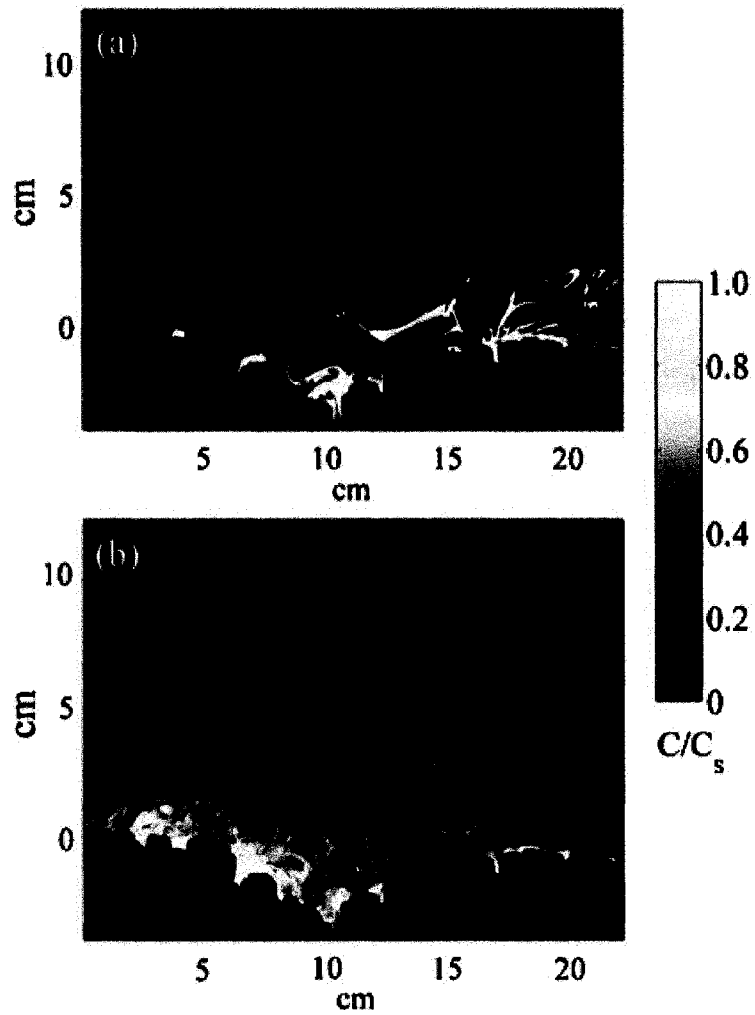


Figure 1.5: PLIF image of dye transfer from the coral canopy under (a) unidirectional flow and (b) wave dominated flow. Source: Reidenbach et al. [41]; ©2007 American Institute of Physics; reproduced with permission.

- Overall sensor dimension or footprint size of ~ 1 cm with a spatial resolution of ~ 1 mm.
- Bandwidth of ~ 1 kHz.
- Ability to detect flow reversals and recirculations.
- Ability to detect shear and normal forces at the same time.
- Ability to operate in ionic solution and reliable transduction scheme when operated underwater.
- Ability to sense shear stress directly.

Most macro-scale shear stress sensors have a spatial resolution of ~ 1 cm, overall sensor dimension of ~ 10 cm when electronics are included, and bandwidth of ~ 1 -100 Hz. MEMS and microfabrication techniques allow miniaturization of these devices with improved sensitivity and spatiotemporal resolution. However, most MEMS shear stress sensors are designed for aerial applications and based on indirect methods (Section 2.2.1), e.g. hot-wire/film anemometry. These indirect sensors are unable to detect flow reversals, recirculations, and normal forces and utilize empirical correlations. Therefore, their use is limited without a priori knowledge of the flow profile, which is difficult to obtain in unknown and complex flows.

This dissertation reports on a MEMS-based “floating-element” shear stress sensor with a piezoresistive transduction scheme for underwater applications. The sensors developed in this project have a spatial resolution of ~ 1 mm, overall device dimension of ~ 1 cm, and bandwidth of ~ 10 kHz. The “floating-element” feature of the sensor enables direct measurements of shear stress without a priori knowledge of the flow profile, and detection of flow reversal and recirculation. The sensors use a piezoresistive transduction scheme, which reduces the complexity of the circuitry, overall device dimension, and cost. An oblique-angle, ion-implantation method is used to form piezoresistors on the sidewalls of the tethers, allowing for in-plane force detection. Out-of-plane force detection is realized by forming piezoresistors on the top surfaces of the tethers through normal ion-implantation. A novel doped epitaxial

deposition method on the sidewall of the tether is also investigated as an alternative to ion-implantation.

1.2 Background

This section reviews some fundamentals of fluid mechanics and MEMS that are relevant to this dissertation. For more details on the subjects, interested readers are encouraged to see other texts referenced in this section.

1.2.1 Fluid Mechanics

Fluid mechanics is the study of the physics of fluids, including the areas of fluid statics and dynamics. Fluid statics examines fluids at rest, while fluid dynamics deals with their motion and the forces acting on them. Introduction and in-depth reviews on fluid mechanics are readily available [46–50].

Definition

A fluid is a type of matter that continuously deforms or flows under an applied shear stress. In contrast, an (elastic) solid, to a certain limit, can resist an applied shear stress and remain at rest. However, this distinction between fluids and solids is not always obvious, e.g. lead exhibits a gentle viscous creep at room temperature [49]. Some substances, such as polymers and gels, also exhibit the characteristics of both solids and fluids at room temperature. A fluid is classified either as a gas (e.g. air, oxygen, and steam) or a liquid (e.g. water, oil, and mercury) at Standard Temperature and Pressure (STP).

Density and Viscosity

Density, ρ (kg m^{-3}), represents a fluid's mass per unit volume. A fluid is called *incompressible* if its density remains constant with changes in pressure and *compressible* if its density changes as a function of pressure.

Table 1.1: Approximate dynamic viscosity, μ , and density, ρ , of some common fluids (and those that are relevant in this project) at Standard Atmospheric Pressure [47].

Fluids	Temperature (°C)	Density, ρ (kg m ⁻³)	Viscosity, μ (N sec m ⁻²)
Air (standard)	15	1.23	1.79×10^{-5}
Water	15.6	999	1.12×10^{-3}
Seawater	15.6	1030	1.20×10^{-3}
Mercury	20	1260	1.50×10^0
SAE 30 Oil	15.6	912	3.80×10^{-1}

Dynamic viscosity, μ (N sec m⁻² or kg m⁻¹ s⁻¹), is a measure of a fluid’s resistance to deformation under applied shear stress. Dynamic viscosity is commonly referred to as just “viscosity.” The higher the viscosity, the more resistant it is to flow under applied shear stress. A fluid is called *Newtonian* if its viscosity remains constant with applied strain rate and *non-Newtonian* if its viscosity changes as a function of applied strain rate. Kinematic viscosity, ν (m² s⁻¹), is a coefficient which describes the diffusion of a fluid’s momentum and is equal to dynamic viscosity, μ , divided by density, ρ . Table 1.1 shows some values of μ and ρ for common fluids.

Reynolds Number

In all viscous flows, the most important controlling parameter is the dimensionless parameter, *Reynolds number* (Re), defined by

$$Re_L = \frac{\rho U L}{\mu} \quad (1.1)$$

where U is a velocity scale and L is a characteristic length. The Reynolds number is the ratio of inertial to viscous forces and is commonly used as a determinant of flow regime. *Laminar* flow occurs at low Re where viscous forces dominate, while *turbulent* flow occurs at high Re where inertial forces dominate. In laminar flow, fluid particles flow in parallel layers smoothly, without any disruption. Turbulent flow is characterized by chaotic, stochastic changes of the fluid’s characteristics (velocity, pressure, and physical properties). For a given geometry, when Re reaches a

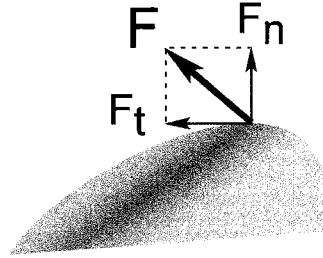


Figure 1.6: A force acting on a surface can be resolved into its normal, F_n , and tangential components F_t . The tangential component is commonly referred to as shear force, F_s .

critical value, Re_c , the flow pattern transitions from laminar to turbulent regime. In a boundary layer flow over a flat plate, Re_c is typically $\sim 1 \times 10^6$. In a pipe flow, Re_c is typically ~ 2300 .

Fluid Flow Characteristics

A fluid flow is considered *steady* when its characteristics do not vary with respect to time. In contrast, an *unsteady flow* is characterized by variations of one or more of its parameters (e.g. velocity, physical properties, etc.) with respect to time. In a closed channel, a fluid flow is called *uniform* when its velocity remains constant as a function of axial position along the channel. Otherwise, the flow is considered *nonuniform*.

Shear Stress

The forces acting on a fluid element can be categorized as body, surface, and line forces [48]. Body forces originate from gravitational, magnetic, electrostatic, or electromagnetic fields. Surface forces, which can be resolved into normal and shear forces (Figure 1.6), originate from direct contact between the fluid element with its surroundings. Line forces, accordingly, act along a line, e.g. surface tension forces in a liquid.

Shear force is translated into shear stress when divided by the area on which it is

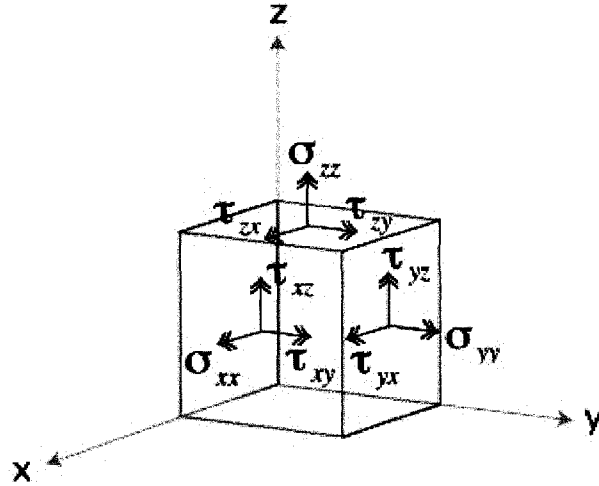


Figure 1.7: Stress at a point. The cube represents a differential element. The stress tensor is symmetric, therefore $\tau_{ij} = \tau_{ji}$.

acting. Nine components of the stress tensor, $\boldsymbol{\tau}$, as shown by

$$\boldsymbol{\tau} = \begin{pmatrix} \tau_{xx} & \tau_{xy} & \tau_{xz} \\ \tau_{yx} & \tau_{yy} & \tau_{yz} \\ \tau_{zx} & \tau_{zy} & \tau_{zz} \end{pmatrix} \quad (1.2)$$

can fully specify stress at a point [48]. Each component, τ_{ij} , can be specified using two indices. The first index, i , indicates the direction of the normal to the surface on which the stress is acting while the second index, j , indicates the direction in which the stress acts. These relationships are illustrated in Figure 1.7.

Shear stress that occurs at the fluid-solid interface in a fluid flow is caused by the relative motion and interaction between the fluid and the solid particles. Fluid particle velocity adjacent to the stationary solid object is zero. This is commonly known as the *no-slip* boundary condition. All fluids generally satisfy this condition, although a *slip* boundary condition has been demonstrated in hydrophobic channels [51]. The

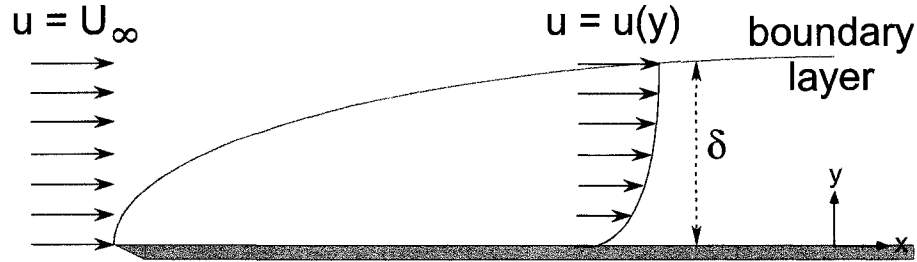


Figure 1.8: A fluid flow over a flat plate. At the leading edge, the fluid's velocity, u , is equal to the free-stream velocity, U_∞ , and the velocity profile is uniform. At some distance, x , along the flat plate, the velocity profile becomes parabolic due to viscous effects. The boundary layer thickness is defined to be the vertical distance from the flat plate where $U = 0.99U_\infty$.

magnitude of the shear stress at the wall, τ_{wall} , exerted by a Newtonian fluid in an incompressible flow is proportional to the velocity gradient and viscosity, as shown by

$$\tau_{wall} = \mu \left(\frac{du}{dy} \right)_{y=0} \quad (1.3)$$

where u is the velocity component in the x direction and y is the vertical distance from the wall (Figure 1.8).

Boundary Layer

The *boundary layer* is a thin region on the surface of a solid object in which the viscous effect is dominant (Figure 1.8). The majority of the drag experienced by a moving solid object immersed in a fluid is created inside the boundary layer [49]. Outside the boundary layer, viscous effects become negligible relative to inertial effects. The thickness of the boundary layer, δ , is commonly defined as the distance from the solid surface where the velocity of the fluid reaches 99% of the value of the freestream velocity, U_∞ .

Poiseuille Flow

Poiseuille flow is considered an internal flow due to the solid wall constraints (Figure 1.9). As fluid enters a duct, boundary layers start to form due to the viscous effect. The boundary layers coalesce at some distance commonly known as the *entrance length*, L_e . Downstream from this coalescing point, the lateral velocity components vanish, i.e. $v = w = 0$, and only the axial component, u , remains. The velocity profile varies only with the lateral coordinates, i.e. $u = u(y, z)$. The flow is said to be *fully developed*. The pressure gradient and the linearity of the shear stress distribution are constant for a fully developed channel flow even when it is turbulent [49]. Internal flows, such as duct flows, are common in engineering applications. The theory and solution to constant-area duct flow are well studied and formulated. Regardless of the duct shape, the entrance length can be correlated for laminar flow, as shown by

$$\frac{L_e}{D_h} \approx C_1 + C_2 Re_{D_h} \quad (1.4)$$

where $C_1 \approx 0.5$, $C_2 \approx 0.05$, and D_h is the characteristic diameter for the duct [49].

Solid-Body Rotation

Flows in circular paths are called *vortex flows* [48]. When the fluid velocity is proportional to the radius of the streamlines, the flow is called *solid-body rotation*. Here, fluid elements are spinning about their own centers while revolving around the origin (Figure 1.10). Therefore, the fluid elements do not deform, they behave as a rigid, rotating solid. Such a flow can be generated by steadily rotating a cylinder tank containing a viscous fluid until the fluid flow reaches equilibrium. The velocity field in such flow is described by

$$U_\theta = \omega_o r \quad (1.5a)$$

$$U_r = 0 \quad (1.5b)$$

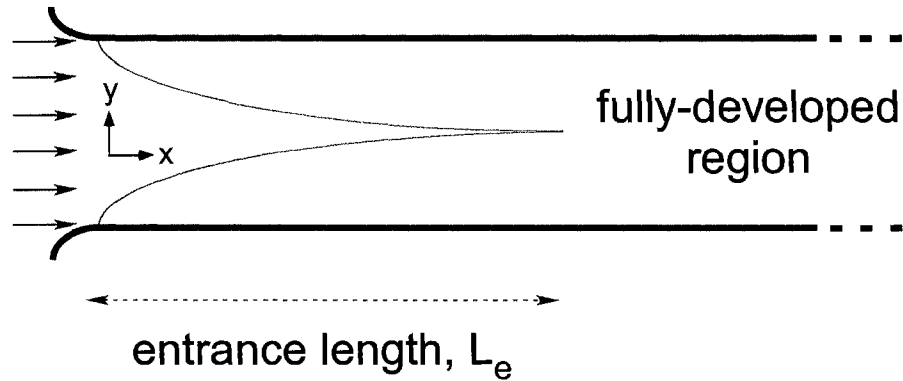


Figure 1.9: A fluid flow inside a duct. At the duct's entrance, the fluid's velocity profile is uniform. Along the length of the duct, the velocity profile becomes parabolic due to viscous effects, thus boundary layers on both side of the walls (in the 2-D case) are formed. The distance from the entrance to the point where these boundary layers meet at the center of the duct is called the entrance length and commonly noted as L_e . Beyond this point, the flow is fully developed. u , v , and w are velocity components in the x , y , and z directions, respectively.

where U_θ , U_r , and ω_ϕ are the tangential, radial, and angular velocity components of a fluid particle, respectively, and r is the radial distance measured from the origin.

Navier-Stokes Equation

A general differential equation of motion for a fluid element can be derived from Newton's second law (body and surface forces acting on a differential fluid element). Substituting stress-deformation relationships into this equation of motion produces the *Navier-Stokes equation* for incompressible flow:

$$\rho \frac{D\mathbf{u}}{Dt} = -\nabla p + \rho \mathbf{g} + \mu \nabla^2 \mathbf{u} \quad (1.6)$$

Together with the continuity equation for incompressible flow,

$$\nabla \cdot \mathbf{u} = 0 \quad (1.7)$$

the three components of the Navier-Stokes equation (x , y , and z) provide a complete

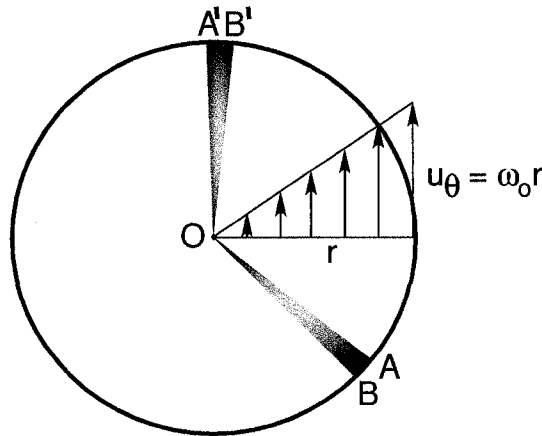


Figure 1.10: Solid-body rotation. Fluid elements do not deform in this type of flow. An example, fluid element OAB rotates around its own center and becomes $OA'B'$, while revolving around origin O .

mathematical description of incompressible, Newtonian flow. Navier-Stokes equation consists of four unknowns (three components of the velocity and a pressure component), therefore the problem is “well-posed” in mathematical terms. Readers are encouraged to refer to fluid mechanics handbooks [46–50] for a complete derivation of Navier-Stokes equation.

Coral Reef Hydrodynamics

A *free surface* flow occurs when the liquid fluid is exposed to atmosphere of either gas or vapor, instead of being completely bounded by solid walls. An example of this type of flow is ocean flow.

Surface gravity waves occur at the free surface of a body of water. When the water surface is disturbed by an inertial force, the gravitational and surface tension forces restore the displaced surface back to its undisturbed position [52]. The surface tension force is considered negligible compared to the gravitational force in ocean engineering. The balance between gravitational and inertial forces at the water surface creates a surface oscillation, which disturbs the neighboring water surface and propagates the disturbance away as a wave. Gravity waves that occur at the interface between two

fluids of different density are called *internal gravity waves* [48]. Treatments on the theory of surface gravity waves is available elsewhere [48, 52–54].

Open-channel flow is a type of fluid flow in which the free surface of the liquid is subjected to atmospheric pressure [55]. Some examples of this flow include river and canal flows. Treatments on the theory of open-channel flows is also available elsewhere [55, 56].

1.2.2 Micro Electromechanical Systems (MEMS)

MEMS, commonly referred to as Microsystems in Europe, are engineered devices with a microscale characteristic length (between 1 μm and 1 mm). These microscale devices, as the name implies, consist of two components, mechanical and electrical, to form a functional system. In terms of its system functionality, MEMS can loosely be categorized into sensors, actuators, or a combination of these.

The techniques used to create MEMS devices are commonly referred to as *micro-fabrication* or *micromachining*, a term first coined by Prof. James Angell of Stanford University [57]. Generally, MEMS devices are fabricated using silicon-based micromachining techniques, which originated from the integrated circuit (IC) industry. However, non-silicon materials, such as glass, quartz, silicon carbide, diamond, and polymers, have recently been used to fabricate MEMS devices. The use of these new materials are mainly driven by applications. For example, silicon carbide and diamond have been used to fabricate high-temperature and high-pressure MEMS sensors [58–65]. Biocompatible polymeric materials, such as SU-8 and parylene, have been used to fabricate “bio-MEMS” (MEMS for biological applications) [66–70]. SU-8 is a negative, epoxy-type, near-UV photoresist originally developed and patented by International Business Machines (IBM) Corporation [71, 72]. MEMS fabrication techniques have also advanced to accommodate new applications and new materials. Some examples of these techniques include plastic molding (LIGA - *Lithographie Galvanoformung Abformung*), electroplating of metals, sol-gel deposition, plasma spraying, gray-scale lithography, and SU-8 processing. Recently, researchers have also integrated nanostructures, such as carbon nanotubes (CNT) [73, 74] and nanowires [75–77], with

MEMS sensors to improve the sensors' performance (e.g. sensitivity, resolution). Interested readers are encouraged to read other MEMS texts [78–82].

MEMS devices are ubiquitous in our everyday lives. Some of the earliest MEMS devices consist of pressure sensors and accelerometers [83–86]. These sensors still make up a significant part of the MEMS devices share in the 1990's and early 2000's. The automotive, consumer product, and life sciences industries are still the biggest consumers of these devices. According to a technical market research report in 2006 [87], the global market for MEMS devices and production equipment is estimated to reach \$12.5 billion in 2010 with microfluidic MEMS occupying the largest segment of the market, followed by accelerometers. Several advantages of MEMS-based devices include

- A significant improvement in the spatial resolution (typically in the order of μm).
- A smaller mass, thus increasing the devices' bandwidth significantly. Resonant frequency (or bandwidth) of a device is governed by

$$f \propto \sqrt{\frac{k}{m}} \quad (1.8)$$

where f is the resonant frequency, k is the spring stiffness (constant), and m is the mass of the device.

- High temporal resolution.
- A significant improvement in sensitivity.
- Better resolution (minimum detectable signal) of the parameters of interest.
- Batch fabrication. Typically, tens to thousands of these devices can be made on a single 4"-wafer. Ideally, they all have the same characteristics, although in reality, some non-uniformity across a wafer still exist. Since they can be batch-fabricated, the cost per unit device decreases significantly.
- Lower power consumption.

- Ability to withstand extreme environments (high temperature, high pressure, corrosive, etc), depending on the material chosen.

As previously mentioned, microfabrication techniques offers the possibility to create miniaturized sensors, actuators, and systems with several orders of magnitude in device performance improvement when compared to their macro-scale counterparts. The next sections discuss the basic microfabrication techniques relevant to this dissertation, summarized from Plummer et al. [88].

Thermal Oxidation

A major advantage of silicon, compared to other semiconductor materials, is that its surface can be easily passivated by thermally growing a high-quality oxide layer. *Thermal oxidation* of silicon is done either within an oxygen (*dry oxidation*) or a steam (*wet oxidation*) gas environment inside a furnace. Typically, the oxidation temperature ranges from 600 to 1200°C. The oxidation process involves breaking silicon into silicon bonds on the surface of the substrate, inserting oxygen atoms between the broken bonds, and forming silicon to oxygen bonds. Oxidation requires volume expansion in the silicon substrate because of the space needed for the oxygen atoms. The resulting oxide layer is, therefore, amorphous and in compressive stress. In some MEMS structures, this compressive stress can be significant and can change the mechanical properties of the structures, hence must be taken into account in the design process. *Rapid Thermal Oxidation* (RTO) refers to an oxidation process in which the temperature ramps up from 200–400°C to the desired oxidation temperature (600–1200°C) in ~10 seconds. In the conventional oxidation process, the temperature ramp-up is typically 10-40 minutes.

Annealing

Annealing in this dissertation refers to the process of activating ion-implanted dopants in the silicon substrate and “fixing” damage within the crystal lattice because of the high-energy ion implantation process. Dopants introduced by ion implantation need to be annealed so that they can relocate themselves properly in the crystal lattice

and contribute to electrical conductance. Annealing is typically done in a nitrogen gas environment at a temperature of 600–1200°C inside an oven or a furnace. *Rapid Thermal Annealing* (RTA), as in thermal oxidation, refers to a process in which the temperature ramps up from 200–400°C to the desired annealing temperature (600–1200°C) in ~ 10 seconds. In conventional annealing, the temperature ramp-up is typically 10–40 minutes.

Thin-Film Deposition

Thin films of silicon oxide, as well as of silicon nitride and metals, can be deposited onto silicon surface. Thin film deposition is usually done in a deposition chamber or a furnace. The two primary methods of thin-film deposition are *Chemical Vapor Deposition* (CVD) and *Physical Vapor Deposition* (PVD). In CVD, reactant gases introduced into the deposition chamber chemically react at high temperatures (500 to 850°C), to form a film on the substrate surface. In contrast, PVD use physical processes, such as *sputtering* and *evaporation* to produce the desired thin-film atoms and deposit them onto the substrate surface in very low-pressure environments. In sputtering, a solid source is bombarded with energetic ions, while evaporation involves heating the source until it vaporizes. In this work, aluminum films are deposited using the PVD sputtering technique, while gold and copper films are deposited using the PVD evaporation technique.

Silicon nitride films mentioned in this dissertation are deposited using the *Plasma-Enhanced Chemical Vapor Deposition* (PECVD) process. This process uses plasma as an energy source in addition to the conventional thermal source. PECVD is preferred when there are temperature restrictions on the substrate during film deposition, e.g. when aluminum is already deposited on the substrate. PECVD is typically done at temperatures lower than 400°C. Silicon oxide films in this dissertation are deposited using PECVD, as well as *Low-Pressure Chemical Vapor Deposition* (LPCVD). LPCVD is often used for depositing thick oxide films ($\sim \mu\text{m}$) in a low pressure environment. When deposited at temperatures lower than 500°C, the resulting oxide is called *Low-Temperature Oxide* (LTO).

Photolithography

Pattern transfer in microfabrication always involves a photo process, commonly referred to as *photolithography*. First, a thin film of photo-sensitive hydrocarbon-based material, *photoresist*, is spun onto a substrate. In this dissertation, the thickness of the photoresist used varies from 1 to 10 μm , depending on the subsequent fabrication steps. The photoresist layer is then selectively exposed to an ultra-violet (UV) light for a few seconds by placing a chrome-patterned glass mask in between the photoresist and the UV light source. Some of the UV light is blocked by the chrome pattern, while some passes through the glass and hit the photoresist. In this dissertation, *positive photoresist* is used, which means that the chemical bonds in the UV-exposed region of the photoresist become weaker. Finally, the substrate is exposed to a developing solution and the regions of the photoresist with weak chemical bonds are washed away, leaving the pattern of the remaining photoresist. The patterned photoresist becomes a mask for the subsequent processing steps (etching, ion-implantation, etc.). There are several types of substrate exposure systems, i.e. contact printing, proximity printing, and projection printing. Contact printing, the method where a mask is placed chrome-side down in direct contact with the photoresist on the substrate, is used in this work.

Doping

Doping refers to a process where dopant atoms are added into a region within the substrate, changing the electrical properties of that region. The *dopant atoms* used in this dissertation are boron and phosphorous. Each boron atom creates an additional *hole*, while each phosphorous atom creates an additional *electron* in the crystal lattice. These extra holes and electrons contribute to changes in electrical conduction. The typical dopant concentration used in this work is 10^{15} cm^{-3} to 10^{19} cm^{-3} . For reference, the atomic density in the silicon lattice is $\sim 5 \times 10^{22} \text{ cm}^{-3}$. There are several methods of introducing dopants into a silicon substrate, i.e. diffusion, ion-implantation, and doped epitaxial deposition. Please refer to Section 3.2.3 for more discussion on these techniques.

Etching

Etching in microfabrication refers to the process of removing patterned material from the bulk. From the process point of view, etching can be loosely categorized into wet and dry (plasma) etching. In *wet etching*, the substrate is immersed into a liquid etchant and the process is mostly chemical in nature. In this work, wet etching is performed to remove parts of silicon oxide and metals (aluminum, chrome, and gold) thin films. In *dry* or *plasma etching*, the substrate is exposed to a gas-phase or plasma etchant. The etching process is both physical and chemical. In this work, plasma etching is used to etch silicon oxide (particularly LTO), silicon nitride, and the silicon substrate itself. From a directional point of view, etching can be loosely divided into isotropic and anisotropic etching. *Isotropic etching* removes materials at the same rate in all directions, while *anisotropic etching* removes materials faster in a particular direction. A perfect anisotropic etching removes material only in one direction. *Etch selectivity* is the ratio of the etch rates between two different materials simultaneously exposed to the same etchant. Typically, the more physical an etch process is, the less selective and the more directional it is. In contrast, the more chemical an etch process is, the less directional and the more selective it is.

1.3 Overview of Dissertation

This dissertation is organized as follows:

- **Chapter 1:** This chapter presents the motivation for direct measurements of wall shear stress, particularly in liquid environments, and the importance of reliable shear stress sensors. Reviews of relevant basic fundamentals of fluid mechanics and MEMS are presented.
- **Chapter 2:** This chapter reviews “traditional” and MEMS-based shear stress measurement techniques, including the use of micromachined shear stress sensors that have been demonstrated in the past two decades. Advantages and drawbacks of each technique are discussed. Finally, a review of micromachined shear stress sensors for underwater applications is presented.

- **Chapter 3:** This chapter reviews the history of piezoresistance in semiconductors, including some early experimental results. Piezoresistance fundamentals are then presented: commonly used notation, theory, fabrication techniques, noise analysis, design parameters, and examples of piezoresistive sensors.
- **Chapter 4:** This chapter presents the design and the fabrication process of floating-element piezoresistive shear stress sensors using the oblique-angle ion-implantation technique.
- **Chapter 5:** This chapter presents the experimental setups and characterization results of ion-implanted sensors. The characterization process includes measurements of in-plane and out-of-plane sensitivities, the temperature coefficient of resistivity, and noise. Uncertainty analyses addressing variations due to the fabrication process are also presented.
- **Chapter 6:** This chapter starts with a review of common passivation schemes used in MEMS devices and continues with results of reliability tests on different passivation layers. Next, the results from two underwater experiments using ion-implanted sensors are presented. These experiments highlight the response to solid-body rotation using a cylindrical tank and steady, laminar, uniform flow using gravity-driven flume. This chapter concludes with a micro-scale particle image velocimetry (μ PIV) experiment to test the effect of gap size on fluid flow.
- **Chapter 7:** This chapter presents an alternative method for forming sidewall piezoresistors by using selective epitaxial deposition. The fabrication process and the characterization results for microfabricated piezoresistive cantilevers using this selective epitaxial deposition technique are presented.
- **Chapter 8:** This chapter presents a summary of the microfabricated floating-element based piezoresistive shear stress sensors for underwater applications.

Chapter 2

Prior Art

This chapter reviews “traditional” and MEMS-based shear stress measurement techniques, including some of the micromachined shear stress sensors that have been demonstrated in the past two decades. Advantages and drawbacks of each technique are also discussed. Finally, a review of micromachined shear stress sensors for underwater applications is presented.

2.1 Macro-scale Measurement Techniques

This section reviews some of the most commonly used shear stress measurement techniques at macro scale, i.e. hot-wire/film anemometry, surface fence, and floating-element sensors. Other techniques include Preston tube [89], Clauser graphical method [90], Stanton tube [91], wall pulsed wire technique [92], oil-film interferometry [92], etc. Interested readers are encouraged to see other fluid mechanics measurement handbooks and journal articles [91–94]. A review of modern developments in shear stress measurement techniques is available elsewhere [95]. Shear stress measurement techniques can be loosely categorized into *direct* and *indirect* methods [93, 94]. The direct methods rely on measurements of integrated shear stress acting on a sensing area and do not require any assumptions regarding the flow field. These sensors have a free-to-move sensing element, typically a plate-like element, on which shear stress

is acting. Shear stress can be directly computed from the sensing element displacement. Floating-element and fence sensors are considered direct methods. The indirect methods rely on measurements of other physical parameters and empirical correlations to determine shear stress. These parameters include pressure, wall temperature, velocity profile, heat convection coefficients, etc. Preston tube, Stanton tube, Clauser graphical method, and hot-wire/film anemometry are considered indirect methods.

2.1.1 Indirect Method: Hot-wire and Hot-film Anemometry

Hot-wire and hot-film anemometry are based on thermal transfer principles, i.e. the rate of heat loss from a heated resistive element to fluid flow is dependent on the velocity profile in the flow boundary layer. The rate of heat loss can be calculated by monitoring the change in resistance of the heated element and shear stress can be inferred from the velocity profile.

A hot-wire/hot-film anemometry sensor consists of a heating element (a thin wire or thin film) located on the surface of interest (Figure 2.1). Current is passed through the heating element (heater), so that the temperature of the heater is higher than the the temperature of the fluid. The heater is typically made of metal, such as aluminum or platinum. As fluid flows over the heater, heat is convected away by the moving fluid, hence reducing the temperature of the heater. Variation in the heater temperature affects the resistance and the Joule heating rate.

The resistance of the heater, R , at any temperature T is governed by

$$R = R_o (1 + \alpha (T - T_o)) \quad (2.1)$$

where R_o is the resistance of the heater at a reference temperature, T_o , and α is the heater temperature coefficient of resistance (TCR). The relationship between the input power, wall shear stress, and temperature of the heated element is well studied and can be analytically expressed [96] by

$$i^2 R = \Delta T \left(0.807 A_e \left(\frac{C_p k_T \rho \tau}{L \mu} \right)^{1/3} + B \right) \quad (2.2)$$

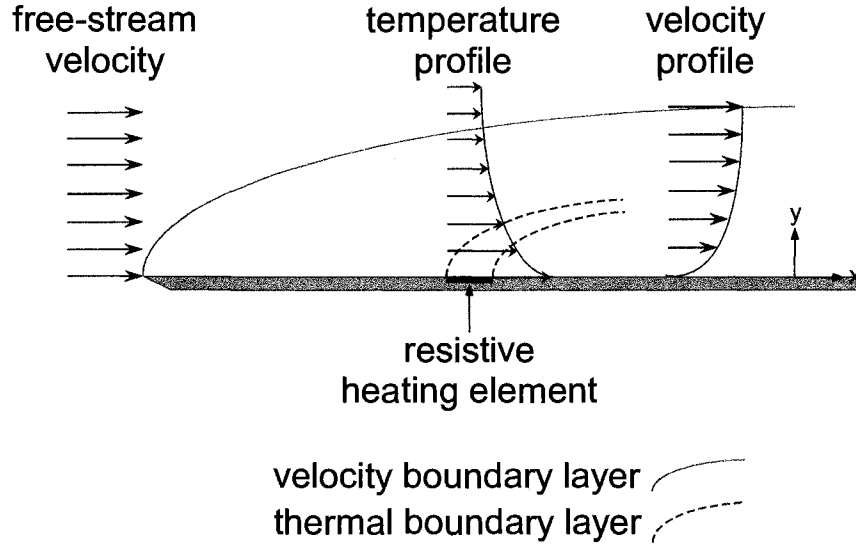


Figure 2.1: Hot-wire/film anemometry. As fluid flows on top of the heating element (heater), heat is convected away by the moving fluid. Shear stress is related to the rate of heat loss based on an empirical correlation.

where A_e is the effective area of the heater, C_p is the heat capacity of the flow, k_T is the thermal conductivity of the fluid, ρ is the fluid density, L is the stream-wise length of the resistor, μ is the viscosity of the fluid, and τ is the shear stress to be measured. The coefficient B in (2.2) corresponds to the conduction heat loss from the heater to the substrate. Ideally, B is zero. Shear stress sensitivity decreases as the ratio between B and $0.807A_e \left(\frac{C_p k_T \rho \tau}{L \mu} \right)^{1/3}$ increases. Note that (2.2) holds only when the following assumptions are true [96].

1. The thermal boundary layer of the heated element is within the velocity boundary layer.
2. The heat transfer perpendicular to the flow is negligible compared to the heat transfer parallel to the flow.
3. Natural convection is negligible compared to forced convection.

Since hot-wire and hot-film anemometry are based on empirical correlations (hence considered an indirect method), a sensor needs to be calibrated for different flow

conditions. An empirical correlation only holds for a specific type of flow. A set of assumptions must be fully met before the empirical correlation can be applied to measure shear stress correctly in a given flow. In an unknown flow, this technique does not produce accurate shear stress measurements. In addition, the dynamic response of the sensor is limited by its thermal inertia. Details on hot-wire and hot-film anemometry principles are available elsewhere [91–93, 95, 97–99].

2.1.2 Direct Method: Surface Fence and Floating-Element Sensors

Theoretically, direct methods are ideal for shear stress measurements since they do not depend on a priori knowledge of the flow nor the fluid properties. However, direct methods may present a disturbance to the flow. This section reviews the most common direct measurement techniques.

A surface fence sensor consists of a fence-like structure and a manometer to measure the pressure difference, δp , upstream and downstream of the fence. The pressure difference, δp is proportional to the magnitude of the wall shear stress, τ_{wall} , and independent of the height of the fence, H [92]. However, the fence must remain within the viscous sublayer of the boundary layer. Details on surface fence sensors are available elsewhere [92, 100].

A floating-element sensor consists of a flush-mounted free-to-move sensing element, on which shear stress is acting. The sensing element is suspended by beam-like structures or springs, which are anchored to a fixed ground (typically a non-moveable part of the sensor). In this configuration (Figure 2.2), the sensing element is suspended, free to displace when subjected to an external force. At the same time, the sensing element is also anchored to a fix ground by the springs to restore it back to its undisturbed position, hence the name “floating element”. In an ideal measurement, the only external force is the shear stress acting on the element, integrated over the

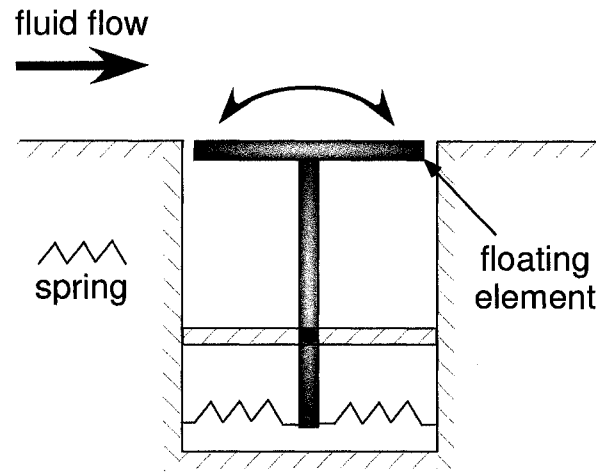


Figure 2.2: Schematic diagram of the floating-element shear stress sensor principle. Source: Allen [101].

area of the element as shown by

$$F_{shear} = \int_A \tau dA \quad (2.3)$$

where τ is the shear stress and dA is the differential area of the element.

Winter [91] reviewed floating-element shear stress (or skin-friction) balances and discussed the major sources of errors during measurements. Allen [101,102] performed a systematic study of potential sources of errors in shear stress balance measurements in supersonic flows and improved its sensing element design by using a parallel linkage instead of a single-pivot design. Winter [91] and Allen [101,102] discussed the importance of gap width between the sensing element and the wall, element protrusion or depression, and element lip thickness (Figure 2.3). Acharya et al. [103] built a floating-element instrument based upon a precision galvanometer as the balance mechanism. The dimensions of most floating-element sensors (or instruments) that were designed and built before the use of micromachining were $\sim 1 - 10$ cm (Figure 2.4).

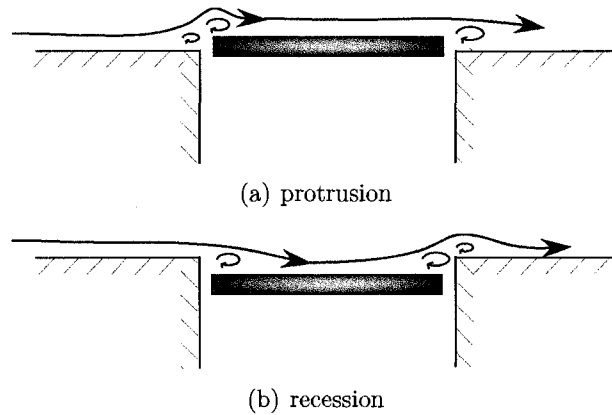


Figure 2.3: Sources of error in shear stress measurements using floating-element shear stress sensors. Shown are the modified flow patterns due to protrusion and recession of the element with respect to the wall. These modified flow patterns result in flow recirculations and additional force and pressure components, on top of the actual shear forces on the element. Source: Allen [101].

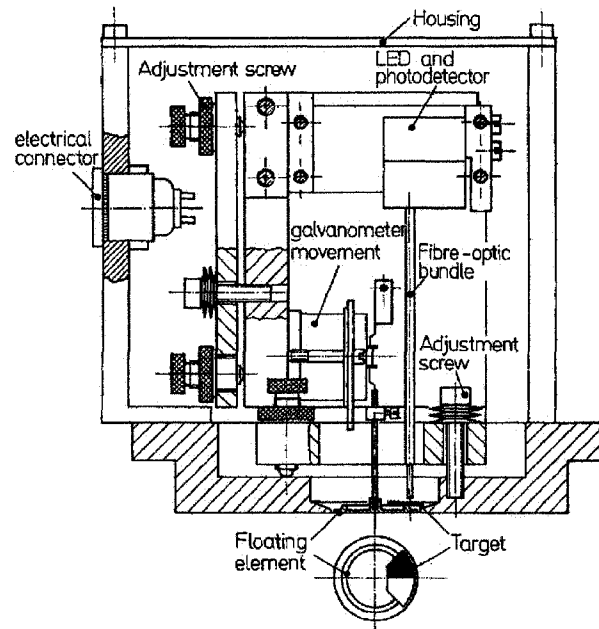


Figure 2.4: A macro-scale floating-element shear stress-sensor design. The diameter of the circular-shape floating element shown in the figure is ~ 2 cm. Source: Acharya et al. [104]; ©1986 Springer Science and Business Media; reproduced with permission.

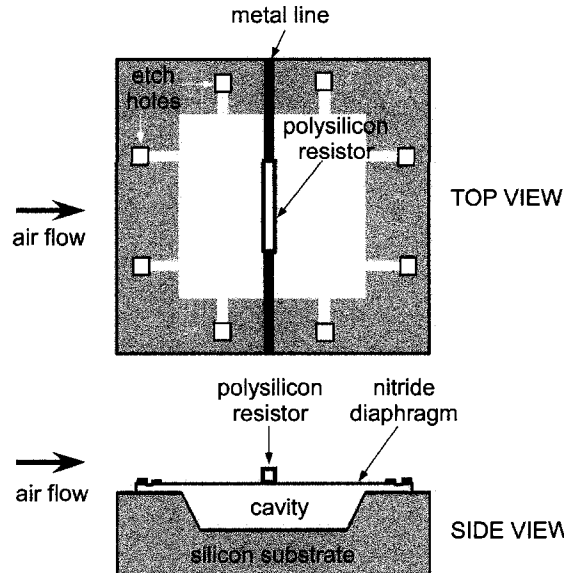
2.2 MEMS Shear Stress Sensors

Similar to their macro-size counterparts, MEMS-based shear stress measurement techniques can be loosely categorized into direct and indirect methods. A review of recent progress and promise on MEMS shear stress sensors is available elsewhere [105]. Regardless of the method, micromachining technology allows the possibility of batch production and increase in sensitivity and resolution of the sensors (Section 1.2.2).

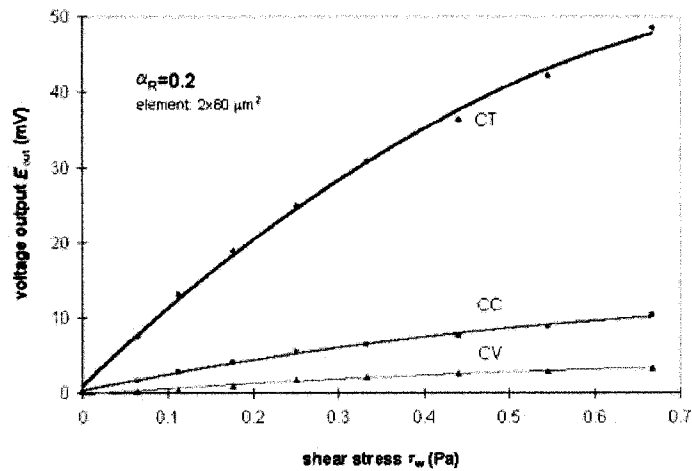
2.2.1 Indirect Method: Hot-wire and Hot-film Anemometry

Micromachining allows the use of semiconductor materials with higher resistance as the heater (sensing element), such as polysilicon and doped silicon. Higher resistance reduces the bias current needed to produce heat. Micromachining also permits the use of more efficient heat insulation material between the heating element and the substrate to reduce heat loss via conduction (the term B in (2.2)). Finally, micromachining enables batch production and miniaturization (vacuum cavity, heating element size, and the overall footprint size) of the sensors.

Oudheusden and Huijsing [106] developed one of the earliest micromachined thermal-based shear stress sensors. The device was not thermally isolated and still had a large footprint (~ 10 mm). Huang et al. [107–109] designed, fabricated, and tested a thermal-based micromachined shear stress sensor using *surface micromachining* technology. A polysilicon strip ($2\ \mu\text{m} \times 80\ \mu\text{m}$) was deposited on the top of the silicon nitride film as the heater. By using the sacrificial-layer technique, a vacuum cavity (~ 300 mTorr) with dimensions of $200\ \mu\text{m} \times 200\ \mu\text{m} \times 2\ \mu\text{m}$, was placed between the silicon nitride film and the silicon substrate. This cavity significantly improved the sensitivity of the sensor by reducing the amount of heat loss to the substrate (the term B in (2.2)). Wind tunnel calibration of the sensor with a cavity showed a sensitivity of $\sim 10\ \text{mV Pa}^{-1}$. However, the cavity was found to reduce the bandwidth of the sensor. When operated in constant temperature mode, the bandwidth of the sensor with and without cavity were 9 and 130 kHz, respectively. Liu et al. [96] reported on the wind-tunnel testing results under three operation modes, i.e. constant current, constant voltage, and constant temperature (Figure 2.5).



(a) A schematic diagram of the top and the side views of a microfabricated thermal-based shear stress sensor.



(b) The typical voltage output signal as a function of shear stress on three different operating modes, i.e. constant temperature (CT), constant current (CC), and constant voltage (CV).

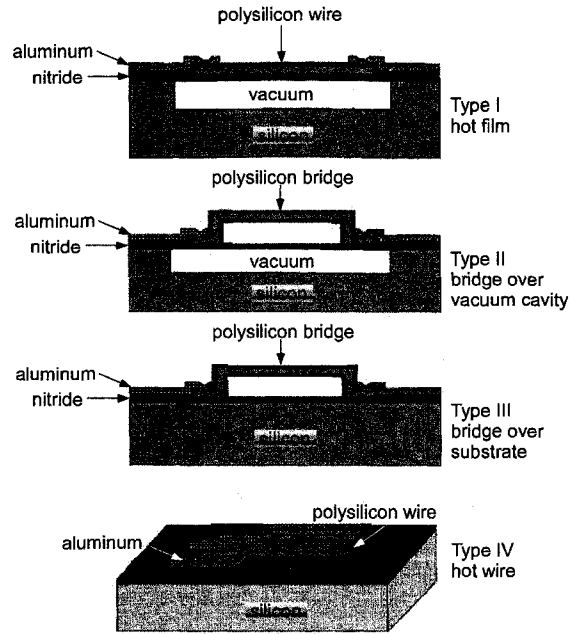
Figure 2.5: Microfabricated thermal-based shear stress sensor using a polysilicon heater. Source: Liu et al. [96]; ©1999 Institute of Electrical and Electronics Engineers; reproduced with permission.

Jiang et al. [110] designed, fabricated, and characterized micromachined shear stress sensors with four types of polysilicon structures for flow measurements and control (Figures 2.6). All four structures were shown to be reliable with some trade-off between the sensitivity and bandwidth. Arrays of these sensors were employed to image shear stress distribution in turbulent boundary layer studies [111]. Jiang et al. [112] also reported on a novel microfabrication technique, which integrated MEMS devices on a flexible polyimide skin. The skin consisted of 100 sensors in an area of $3 \text{ cm} \times 1 \text{ cm}$. These flexible shear stress sensor skin was successfully tested in a wind tunnel and used in delta wing leading edge real-time 2-D shear stress imaging and in an aerodynamic study of a MEMS-controlled super-maneuverable low-altitude unmanned aerial vehicle [113].

Xu et al. [114] developed a micromachined, vacuum-cavity insulated, thermal shear stress sensors (Figure 2.7) and addressed two major challenges in designing these sensors for underwater applications, i.e. waterproof coating and pressure sensitivity. *Parylene N* was used as a passivation layer against liquid medium and the crosstalk between pressure and shear stress sensitivities were dependent on the diaphragm width and polysilicon resistor length. Xu and Tai [115] improved the passivation scheme by selective deposition of *parylene C* to allow better interaction between the heater and the surrounding water, thus increasing sensitivity. These devices were further improved by integrating them with ICs on flexible skins [116, 117]. The ICs were formed from arrays of silicon islands sandwiched by two polyimide layers. The complete system included 16 shear stress sensors, arranged in 1-D array, with on-skin sensor bias, signal-conditioning, multiplexing circuitry, and ability to be installed on non-planar surfaces.

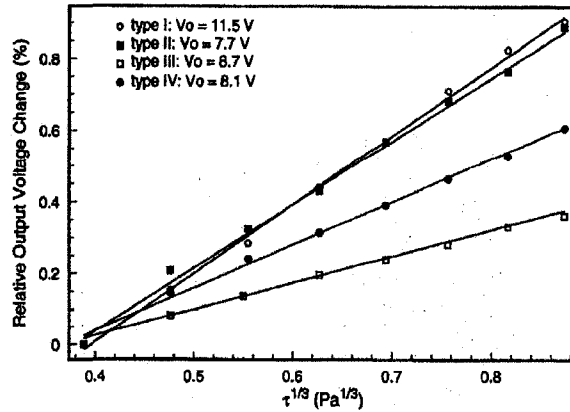
2.2.2 Direct Method: Surface Fence and Floating-Element Sensors

Floating-element sensors can be categorized as a direct method of measuring shear stress. Similar to its macro-scale counterpart, a MEMS-based floating-element sensor consists of a plate element suspended by four tethers anchored to the substrate.



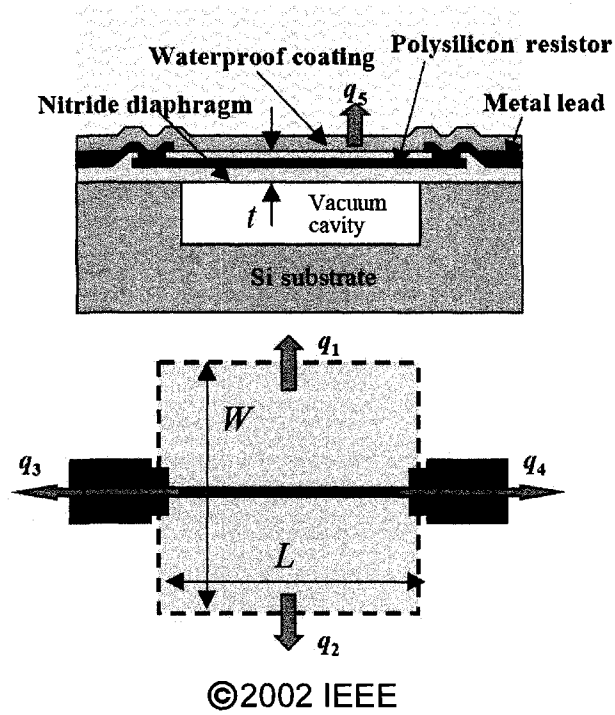
©1995 IEEE

(a) Four different polysilicon structure types of thermal-based shear stress sensors.

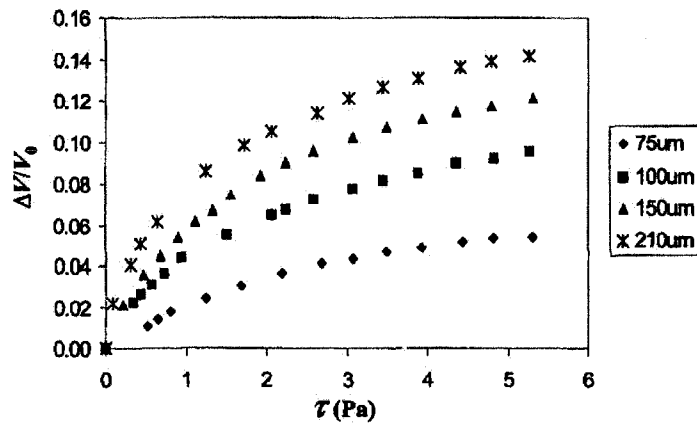


(b) Relative output voltage change (%) as a function of shear stress for all four polysilicon structures in constant temperature mode. Type I and II are the most sensitive.

Figure 2.6: Four different polysilicon structure types of thermal-based shear stress sensors. Source: Jiang et al. [110]; ©1995 Institute of Electrical and Electronics Engineers; reproduced with permission.



(a) The cross section and top view of the underwater thermal-based shear stress sensor.



(b) Normalized output voltages of four different sensors with various diaphragm widths (75-210 μm).

Figure 2.7: Underwater thermal-based shear stress sensor. Source: Xu et al. [114]; ©2002 Institute of Electrical and Electronics Engineers; reproduced with permission.

Due to the nature of its design, floating-element sensors can be flush-mounted with the surface of interest, thus minimizing disturbance to the flow. As fluid flows over the sensor, it exerts shear stress on the plate element, causing the plate element to displace in-plane. The plate in-plane displacement causes the four tethers, which act as springs, to bend. To first order, this problem can be modeled by

$$F_{shear} = kx_{plate} \quad (2.4)$$

where F_{shear} is the shear force acting on the element, k is the equivalent spring constant of all four tethers, and x_{plate} is the displacement of the plate element. The displacement of the plate element is equal to the deflection of the tip of each tether. The equivalent spring constant can be theoretically computed using beam mechanics equations or computer simulation. Shear stress, τ , can be calculated by dividing the shear force, F_{shear} , by the area of the plate element, A_{plate} . The spatial resolution of floating-element based sensors is determined by the floating element size and the bandwidth is limited by the first resonant frequency. Smaller dimensions translate into smaller mass, which in turn increase the first resonant frequency and the bandwidth of the device to \sim kHz (the order of temporal distribution needed to measure shear stress in turbulent boundary layer [118,119]).

Many of the problems associated with floating-element sensors, such as gaps size and pressure-gradient errors [91], can be reduced with miniaturization. The presence of the gaps allows flow beneath the plate, which results in a shear force acting on the bottom surface of the plate and pressure-gradient resultant force acting on the lip of the plate (Figure 2.8) [120]. The effective shear stress from for all these forces can be calculated using

$$\tau_{w,eff} = \tau_w \left(1 + \frac{t_{gap}}{h} + \frac{2t_p}{h} \right) \quad (2.5)$$

where $\tau_{w,eff}$ is the effective shear stress, τ_w is the actual shear stress, t_{gap} is the vertical gap between the floating element and the substrate underneath, t_p is the thickness of the element, and h is the height of the channel for an internal flow. Micromachined sensors also have negligible misalignment errors because the floating element, the

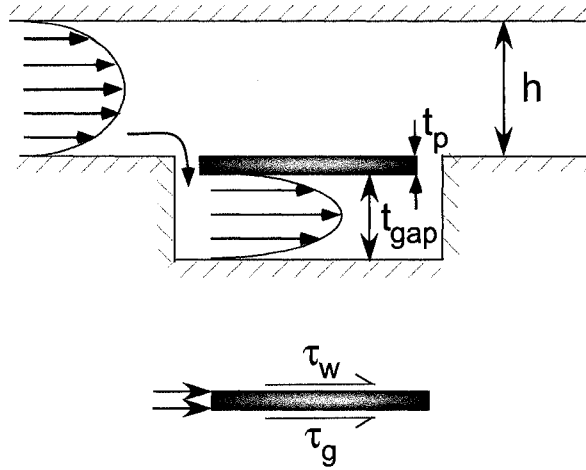


Figure 2.8: Additional force components acting on the element in a pressure-driven internal flow. τ_w is the actual shear stress acting on the top surface of the element, τ_g is the shear stress acting on the bottom surface of the element, t_{gap} is the vertical gap between the floating element and the substrate underneath, t_p is the thickness of the element, and h is the height of the channel. Source: Schmidt et al. [120]; ©1988 Massachusetts Institute of Technology; reproduced with permission.

tethers, and the substrate are all monolithically fabricated. However, these sensors are still prone to misalignment errors due to thin film stress, sensor packaging, and external factors during operation, such as buoyancy forces when used underwater, wind tunnel vibration, etc.

The next sections discuss the most common transduction mechanisms used in MEMS-based floating-element sensors (capacitive, piezoresistive, and optical) and some examples of each technique. Each of these transduction techniques has advantages and drawbacks.

Capacitive

Schmidt et al. [121] reported the first microfabricated floating-element shear stress sensor in the literature. The sensors were used for measurements of shear stress in turbulent boundary layer, which was ~ 1 Pa. The spatial and temporal resolutions for turbulent boundary layer measurements in air were roughly $100 \mu\text{m}$ and 20 kHz ,

respectively. Surface micromachining of polyimide and aluminum sacrificial layer were used to fabricate a sensor with a plate element dimension of $500\ \mu\text{m} \times 500\ \mu\text{m}$ (Figure 2.9(a)). A differential-capacitor readout scheme was chosen to detect displacement of the plate element. Three passivated electrodes were located on the surface of the wafer, just underneath the plate element, and a conductor was embedded in the polyimide (Figure 2.9(b)). The change in capacitance between the drive and the sense electrodes was measured to calculate the displacement of the plate element, and in turn the shear stress acting on it.

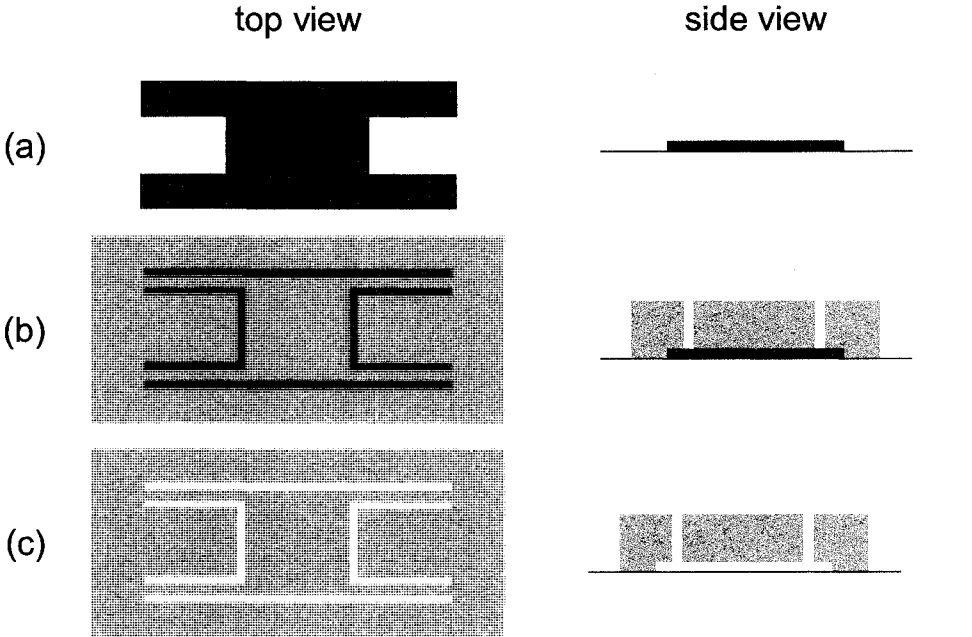
Pan et al. [122] and Hyman et al. [123] reported on floating-element shear stress sensors using polysilicon surface micromachining technology. The floating elements were attached to the substrate through folded-beam cantilever suspensions (Figure 2.10(a)) because this configuration relieved residual stress in the deposited polysilicon layer. The deflection of the floating element was measured using capacitive coupling to the interdigitated sense electrodes (Figure 2.10(b)).

Desai and Haque [124] reported on capacitive floating-element shear stress sensors. The sensors were designed to measure shear stresses in two directions, i.e. in-flow and cross-flow. The fluid flow contact area or plate element area ($100\ \mu\text{m} \times 20\ \mu\text{m}$) was significantly reduced to achieve high spatial resolution by fabricating the actual sensing area (plate element area) perpendicular to the wafer plane.

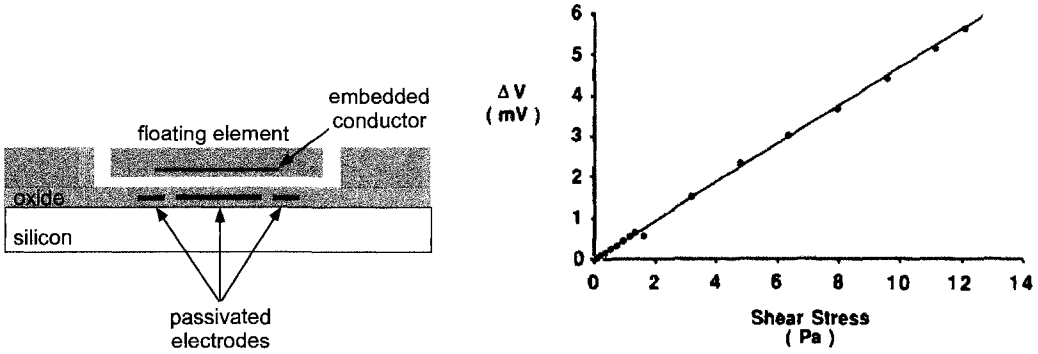
Zhe et al. [125] reported on capacitive floating-element shear stress sensors for low magnitude wall shear stress measurements. The detection of the floating-element motion was accomplished using either direct or differential capacitance measurements. Shear stress measurements as low as $0.04\ \text{Pa}$ with an 8% uncertainty on a $200\ \mu\text{m} \times 500\ \mu\text{m}$ floating-element plate were demonstrated.

Piezoresistive

Ng et al. [126] and Shajii et al. [127] reported the first microfabricated floating-element shear stress sensors using piezoresistive transduction mechanism. Their work was an extension of the work done by Schmidt et al. [121]. Wafer-bonding technology was used to form the plate element and the tethers, while ion implantation (arsenic, 80 keV and $7 \times 10^{15}\ \text{cm}^{-2}$ dose) was chosen to form the piezoresistors. The piezoresistors

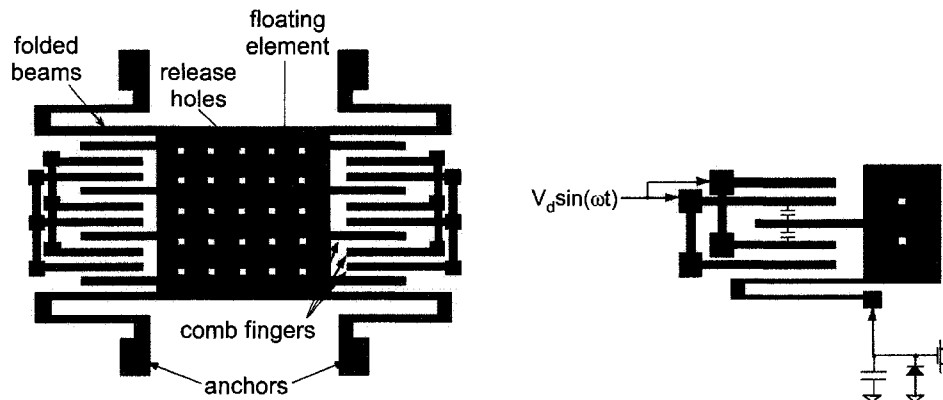


(a) Simplified process flow of a microfabricated floating-element shear stress sensor. Dark color indicates the aluminum sacrificial layer and the light color indicates the polyimide material. Cross section is taken through the center of the element.



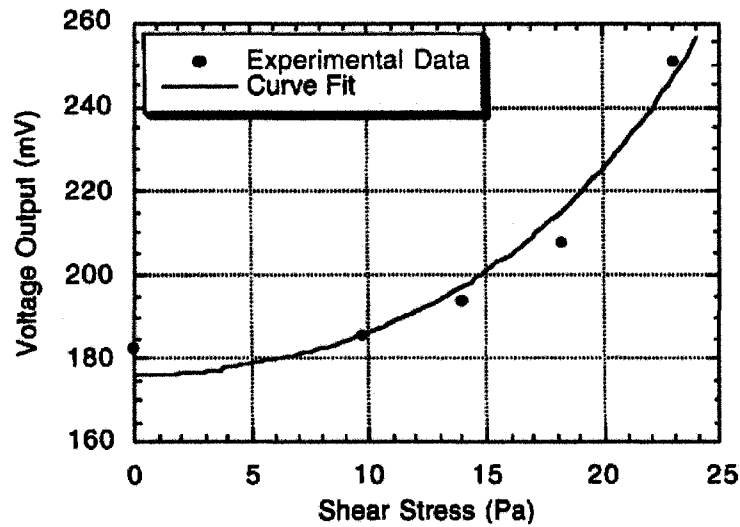
(b) Cross section of the floating element showing the conductors and electrodes for capacitive sensing. (c) Sensor output voltage as a function of shear stress when tested in dry air.

Figure 2.9: Floating-element based shear stress sensors using capacitive transduction scheme and polyimide sacrificial layer. Source: Schmidt et al. [121]; ©1988 Institute of Electrical and Electronics Engineers; reproduced with permission.



(a) Schematic diagram of the sensor from top view. Source: Pan et al. [122].

(b) Schematic of the interdigitated-finger sense capacitors. Source: Pan et al. [122].



(c) The typical output signal of a shear stress sensor with synchronous driving of sense electrodes. Source: Hyman et al. [123].

Figure 2.10: A capacitive floating-element shear stress sensor with interdigitated fingers. Source: Pan et al. [122] and Hyman et al. [123]; ©1999 American Institute of Aeronautics and Astronautics; reproduced with permission.

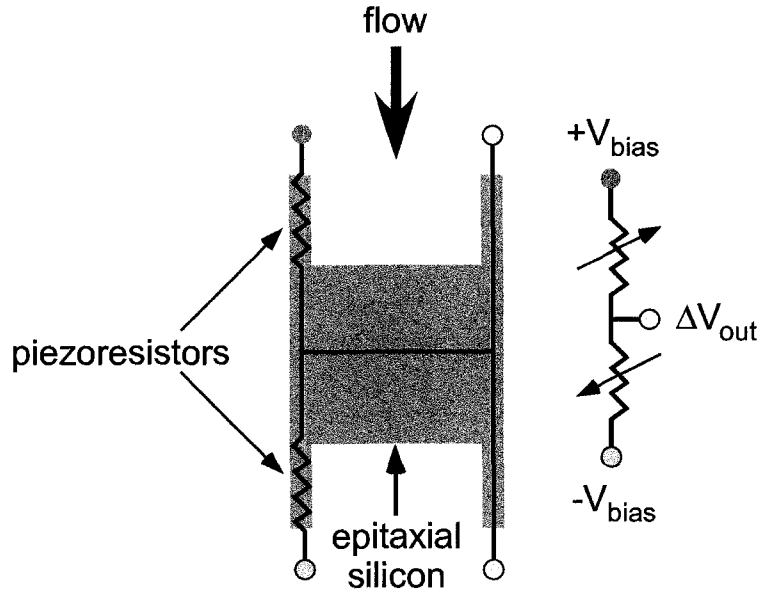
were placed at the root of the tethers in a $\frac{1}{2}$ -bridge configuration. The sensors were designed to detect large shear stress in fluid environments (1 – 100 kPa), therefore, the sensor was orientated such that the length of the tethers is parallel to the flow direction to increase the robustness of the sensors (Figure 2.11). All four tethers experienced axial stress (two in tension and two in compression) when fluid exerted shear stress on the plate element. As a result, one of the piezoresistors was in tension ($-\frac{\Delta R}{R}$), while the other one was in compression ($+\frac{\Delta R}{R}$), thus increasing the sensitivity of the sensor by a factor of two in a $\frac{1}{2}$ -bridge configuration. By detecting the change in resistance from both piezoresistors, axial stresses in the beams were calculated using a general piezoresistive equation:

$$\frac{\Delta R}{R} = \pi \sigma \quad (2.6)$$

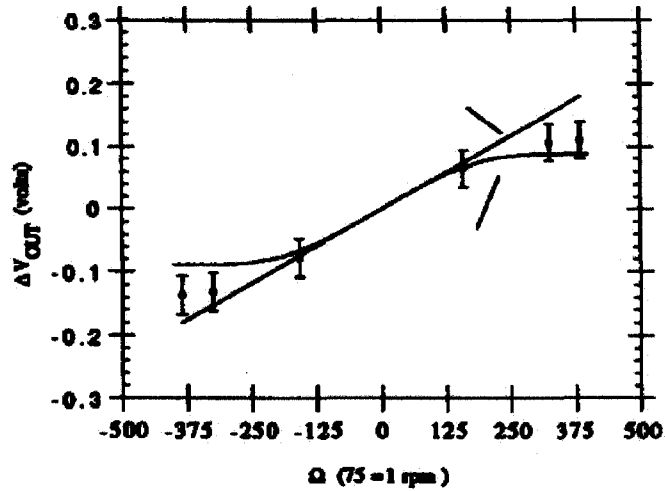
where $\frac{\Delta R}{R}$ is the relative change in resistance, π is the piezoresistive coefficient, and σ is the applied stress. More details of piezoresistance theory is discussed in Section 3.2.2). Once the axial stress was known, the shear force (and stress) on the plate element was computed from beam mechanics. The sensors were also designed to withstand temperature of up to 300°C for applications in reaction screw extruder processes. Goldberg et al. [128] continued on Ng et al. [126] and Shajii et al. [127] work by incorporating backside contacts.

Schober et al. [129] reported on piezoresistive surface fence sensors (Figure 2.12). The sensors were in the order of mm and designed for measurements of separated flow in air. Two pairs of piezoresistors were located at both ends of the micro fence and form a Wheatstone bridge configuration. The strain at the root of the fence was proportional to the pressure difference, $\varepsilon \propto \Delta p$. The sensitivity increased with increasing shear stress. This trend was the opposite of hot-wire anemometry, where sensitivity decreased with increasing shear stress. The sensor was calibrated from -0.7 – 0.7 N m⁻² with a resolution of 0.02 Pa.

All of the aforementioned piezoresistive sensors used normal ion-implantation technique to form the piezoresistors. In this dissertation, the floating-element design was chosen and an oblique-angle ion-implantation technique (Section 3.2.3) was



(a) Schematic diagram of the sensor from top view.



(b) The typical output signal of the sensor.

Figure 2.11: A piezoresistive floating-element shear stress sensor designed for detecting large shear stress in fluid environment. Two piezoresistors are formed on the top surface of the tethers and configured in a $\frac{1}{2}$ -bridge configuration. Source: Ng et al. [126]; ©1991 Institute of Electrical and Electronics Engineers; reproduced with permission.

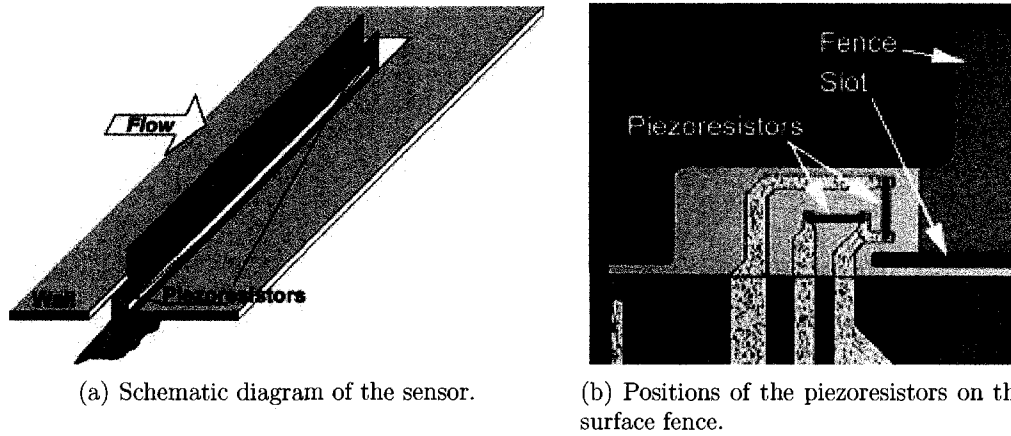


Figure 2.12: Piezoresistive microfabricated surface-fence shear stress sensor. Source: Schober et al. [129]; ©2004 Springer Science + Business Media; reproduced with permission.

used to form the piezoresistors on the sidewalls of the tethers. Independently, Li et al. [130–133] also developed sensors with a similar design using the oblique-angle ion-implantation technique.

Optical

Padmanabhan et al. [134,135] reported on floating-element shear stress sensors using an optical transduction scheme. The dimensions of the plate element were $120\ \mu\text{m} \times 120\ \mu\text{m}$ and $500\ \mu\text{m} \times 500\ \mu\text{m}$, both with thickness of $7\ \mu\text{m}$. The sensors were used for measurement of shear stress in laminar and turbulent boundary layers. The sensors had a measurement range of 0-10 Pa and a resolution of 0.1 Pa. The sensing principle consisted of a floating-element optical shutter and integrated photodiodes (Figure 2.13). Two symmetrical and identical photodiodes were positioned under the floating element and a laser source illuminated the sensor above the floating element such that some of the photons were blocked by the plate element, while some hit the photodiodes. In the absence of any fluid flow (equilibrium position), the exposed areas of the two photodiodes were the same, resulting in zero differential photocurrent (ΔI_{photo}). In the presence of a flow, the fluid exerted shear stress on the plate element,

thus displacing it laterally (in-plane). The plate element lateral displacement resulted in an increase in the exposed area of the leading-edge photodiode and a decrease in the exposed area of the trailing-edge photodiode. The resulting differential photocurrent was proportional to the magnitude and sign of the wall shear stress [135]. The sensors were able to measure shear stresses of 0.01 Pa and lower in a laminar boundary layer during wind tunnel tests.

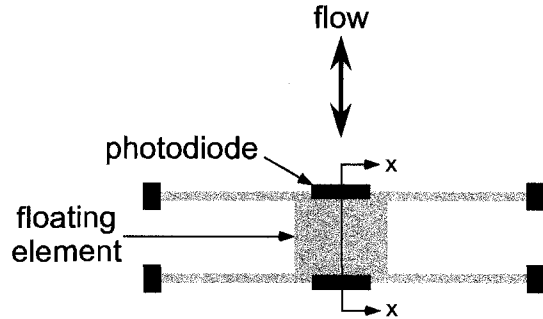
Tseng and Lin [136] reported on a novel optical fiber-based micromachined shear stress sensor employing polymer MEMS-based processes, including micromolding, lithography, and plasma surface treatment (Figure 2.14). The sensor structure consisted of a flexible silicon rubber membrane and double SU-8 resist layers. Shear stress measurements with a resolution of 0.065 Pa were demonstrated. Displacement of the floating element was detected by using a single-mode optical fiber as a micro Fabry-Perot interferometer. This sensor could be used in air or liquid environments with high sensitivity because of its waterproof design.

Horowitz et al. [137, 138] reported on a geometric Moiré optical-based floating-element shear stress sensor for wind tunnel turbulence measurements (Figure 2.15). The fabrication process included an aligned wafer-bonding and thin-back processes to produce optical gratings on the backside of a floating element and on the top surface of the support wafer. The size of the floating element was $1280 \mu\text{m} \times 400 \mu\text{m} \times 10 \mu\text{m}$. The displacement of the plate element was detected by measuring the displacement of the Moiré fringe, δ , using a CCD camera. Shear stress measurements in a laminar, incompressible, fully developed, 2-D pressure driven flow in a flow cell with dynamic range of 0.0062 – 1.3 Pa were demonstrated.

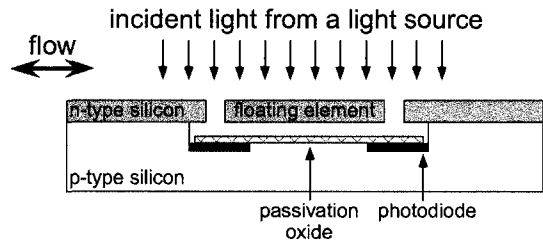
Table 2.1 shows a summary of the characteristics of the transduction mechanisms (capacitive, optical, and piezoresistive) described in previous sections.

2.2.3 Indirect and Direct MEMS Sensors: Comparison

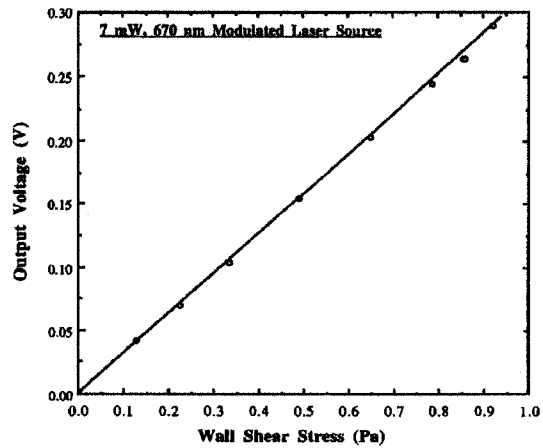
Each of the techniques above has advantages and drawbacks. In choosing a method that best suits a specific application, one should carefully investigate and consider all the parameters of interest, such as the minimum sensitivity and resolution required,



(a) Schematic diagram of the top view of the sensor.

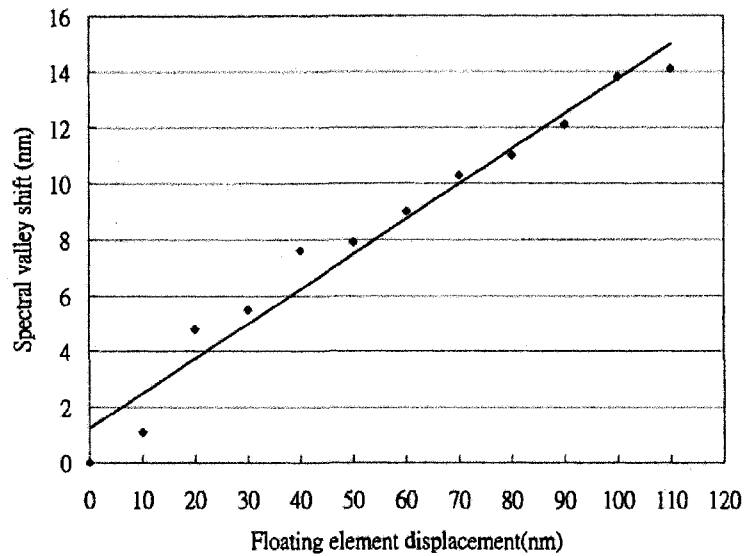
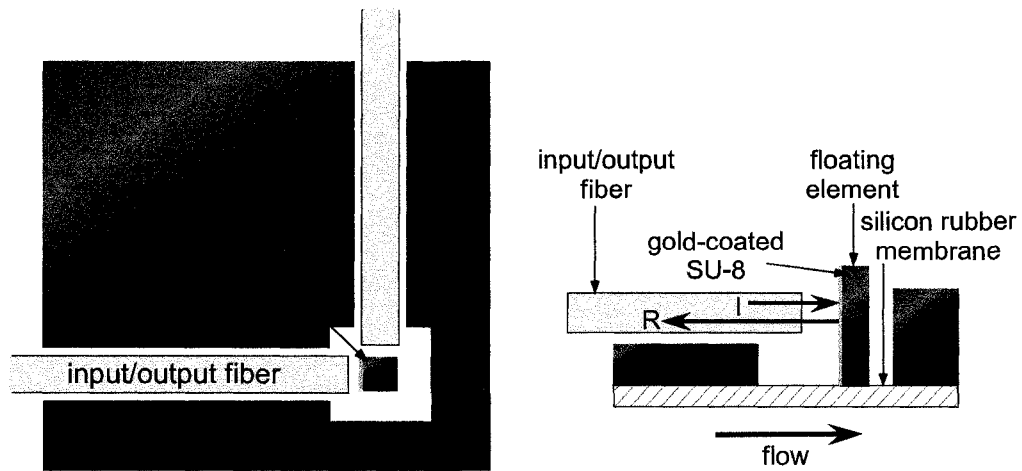


(b) Schematic diagram of the cross section view of the sensor (x-x), illustrating the sensing principle.



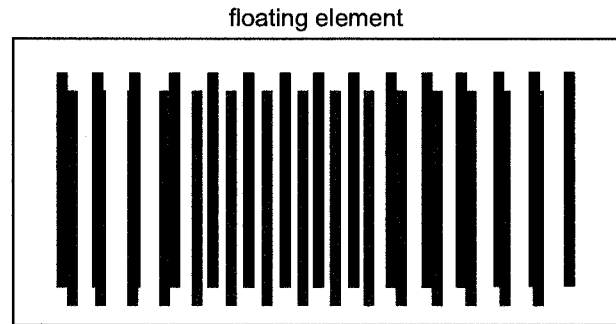
(c) The typical output signal of a sensor in a calibration flow cell using 7 mW, 670 nm modulated laser source.

Figure 2.13: Optical floating-element shear stress sensor. Source: Padmanabhan et al. [135]; ©1996 Institute of Electrical and Electronics Engineers; reproduced with permission.

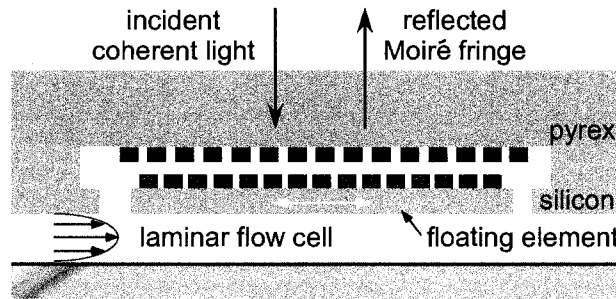


(c) The typical output signal (wavelength shift of spectral valley) of a sensor.

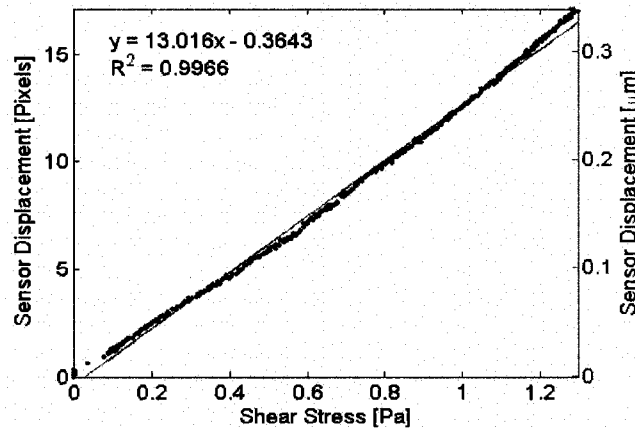
Figure 2.14: Optical fiber-based micromachined shear stress sensor using Fabry-Perot technique and floating-element concept. Source: Tseng and Lin [136]; ©2003 Institute of Electrical and Electronics Engineers; reproduced with permission.



(a) Schematic top view of the sensor. The gratings are made of aluminum.



(b) Schematic cross section view of the sensor tested in a flow cell.



(c) The typical static output signal of a sensor in terms of Moiré fringe pixel displacement and the corresponding floating element displacement as a function of mean shear stress.

Figure 2.15: Optical-based floating-element shear stress sensor based on the geometric Moiré technique. Source: Horowitz et al. [138]; ©2004 Transducer Research Foundation; reproduced with permission.

Table 2.1: The summary of capacitive, optical, and piezoresistive transduction scheme characteristics.

Transduction Schemes	Characteristics
Capacitive	- sensitive, easier to fabricate - nonlinear, difficult to use underwater
Optical	- very sensitive - high power consumption, complex and more expensive setup, more difficult to fabricate, difficult to use underwater, electromagnetic noise
Piezoresistive	- simpler circuitry, lower power consumption, linear to a certain limit, can be passivated, easier to use underwater - not as sensitive as optical and capacitive, very sensitive to temperature and light

fabrication cost and complexity, reliability, and measurement conditions (temperature, pressure, types of flow, environment, etc). The comparisons below are between MEMS indirect and direct shear stress sensors.

Advantages of hot-wire anemometry (indirect method) include:

1. High spatial resolution. Typically, a sensor consists of a heating element and a vacuum underneath the membrane. Without metal lines and bond pads, the typical footprint of these sensors is $\sim(100 \mu\text{m})$. Typical floating-element sensors have footprint $\sim(1000 \mu\text{m})$.
2. Minimal perturbation to the flow since it does not have any gap or moving part and is relatively flush to the surface. Heat transfer to the fluid is the only source of perturbation.
3. High bandwidth. Huang et al. [108] demonstrated bandwidth as high as 130 kHz using compensation techniques, such as constant current and constant temperature.
4. Improved reliability and robustness since no moving or “floating” part is involved.

Drawbacks of hot-wire anemometry (indirect sensor) include:

1. Tradeoff between sensitivity and bandwidth. The sensitivity can be improved by reducing the amount of heat loss due to the conduction to the substrate (Section 2.1.1). Huang et al. [109] showed an order of magnitude improvement in sensitivity by placing a vacuum cavity underneath the membrane where the heating element sit. However, this cavity also resulted in the loss of bandwidth. The bandwidths for sensors with and without vacuum cavity were 9 and 130 kHz, respectively.
2. Complications in the dynamic response due to the frequency-dependent conductive heat transfer into the substrate.
3. Requirement for a priori knowledge of the flow conditions (laminar, turbulent, oscillating, steady, unsteady, etc). Hot-wire anemometry technique is based on empirical correlations. A set of assumptions must be met before the correlations can be used. These sensor and correlations only apply to specific types of flow, therefore the sensors need to be calibrated for different types of flow. When the flow conditions are unknown, such as in the human cardiovascular system, coral reef environments, or turbulent flows in a complex geometry, calibrations of these sensors can be challenging.
4. Measurement errors because of mean temperature drift.
5. Significant pressure sensitivity crosstalk when used underwater [114].
6. Incapability in detecting flow reversal.

Advantages of floating-element sensors (direct sensors) include:

1. No a priori knowledge of the flow conditions and profile are needed since this technique is not based on empirical correlations.
2. Ability to detect flow reversal.

3. Relatively simpler and inexpensive circuitry and instrumentation compared to hot wire anemometry, when piezoresistive transduction scheme is used. When optical or capacitive transduction scheme is used, temperature compensation is not needed.

Winter [91] reviewed and summarized the sources of errors and limitations associated with floating-element sensors. Although the summary was for macro-scale sensors, it applies to MEMS-based floating-element sensors as well. Drawbacks of floating-element sensors (direct sensors) include:

1. The tradeoff between spatial resolution and minimum detectable shear stress. Floating-element shear stress sensors depend on the integration of shear stress acting on the element. Smaller element results in smaller resultant shear force, which in turn translates into smaller element's deflection. This deflection may not be detectable depending on transduction scheme used. If spring characteristics and circuitry are kept the same, then the area of the element needs to be increased to achieve the minimum detectable force (and element's deflection). However, increasing the element's size results in larger footprint and lower spatial resolution.
2. Measurement errors because of the sensor vertical misalignment (Figure 2.3) and the gap between the element and the substrate. For macro-scale sensors, the vertical misalignment is the result of imperfection in the "traditional" manufacturing assembly process. For MEMS sensors, the vertical misalignment is the result of thin film stress, such as passivation oxide on top of the sensor. Moreover, sensors operated underwater also experience a buoyancy force. This force pushes the plate element above the wall level, which in turn results in an additional force component on the element and a disturbance to the fluid flow. Allen [101, 102] reported that the presence of the gap also affect the measurements.
3. Measurement errors because of the pressure gradient in the flow. Any flow with a pressure gradient upstream and downstream of the sensor results in an additional force component on the element.

4. Measurement errors because of cross-axis sensitivity to acceleration and vibration. Acceleration and vibration on a mass (the floating element) results in a force. Like all the other additional force components mentioned earlier, this acceleration- and vibration-induced force is included in the signal, resulting in inaccurate shear force (stress) measurements.

2.3 Shear Stress Sensors for Underwater Applications

Most of the MEMS-based shear stress sensors mentioned in Section 2.2 are designed for aerial applications. The biggest challenge in designing MEMS-based shear stress sensors for underwater applications is to integrate a waterproof, reliable passivation and packaging scheme to protect the electrical components of the sensors from ionic media (water, saline solution, etc). These components include metal lines, bond pads, piezoresistors, and electrodes for capacitive sensing. The passivation scheme should be thick enough to minimize pinholes and ion diffusion from the ionic solution to the electrical elements to prevent corrosion and electrical shorting. At the same time, the passivation scheme should not change the sensors' characteristics (bandwidth, sensitivity, alignment, etc.) significantly. The next section reviews some micromachined shear stress sensors (Section 2.2) that have been developed and tested for underwater applications.

1. Micromachined hot-wire anemometry sensors (indirect method) developed by Xu et al. [114, 117] (Figure 2.7) faced two major challenges, i.e. passivation against water and pressure sensitivity. Parylene C was chosen as a reliable passivation scheme (2 μm of parylene N survived for at least one month when operated at 55°C underwater). However, pressure sensitivity remained a challenge. This crosstalk was minimized by reducing the diaphragm size and increasing its thickness, with an expense of reduced sensitivity because of more conductive heat loss to the substrate. The signal contribution from pressure could be compensated by having a pressure sensor nearby. The average sensor

sensitivities were between 0.31 V Pa^{-1} and 1.10 V Pa^{-1} . Hysteresis because of imperfect temperature compensation or imperfect flow rate monitoring of the water tunnel was observed during the tests [117].

2. Piezoresistive floating-element shear stress sensors developed by Ng et al. [126] and Shajii et al. [127] (Figure 2.11) were intended for high shear stress applications (1 – 100 kPa), specifically in reaction screw extruder processes. The sensors were tested in a viscometer using a special liquid (Cannon N2700000). The chip was mounted flush with the surface and epoxy was used to protect the bonded wires on the chip. The bond pads were placed $\sim 4 \text{ mm}$ away from the sensor to minimize flow disturbance around the sensor element. The measured sensitivity was $13.7 \mu\text{V V}^{-1} \text{ kPa}^{-1}$.
3. Optical fiber-based micromachined shear stress sensors developed by Tseng and Lin [136] employed polymer MEMS-based processes. The sensitivity of the fiber sensor to wall shear stress was 0.65 Pa nm^{-1} (shear stress/spectrum shift) with the minimum resolution of 0.065 Pa based on the resolution of the spectrometer of 0.1 nm . A major advantage of optical transduction scheme over the others was its superior sensitivity. A major drawback was the need of relatively complex and expensive equipment setup (high resolution camera, laser source, etc).

The hot-wire anemometry [114,117] is an indirect sensor. Therefore, it requires a priori knowledge of the flow profile and extensive calibration in the same flow condition. In a coral reef environment or a cardiovascular system, a priori knowledge of the flow conditions is difficult to obtain. Moreover, empirical correlations between mass and heat transfers in a wave-driven turbulent flow environment are not readily available since this type of flow does not always occur in most engineering devices, thus making calibration a challenging task.

Optical-based floating-element sensors developed by Tseng and Lin [136] requires a more complex setup. Moreover, SU-8 (the material used in the design) is prone to swelling when submerged underwater, thus modifying the mechanical characteristics of the floating element. Finally, the presence of micro particles in a coral reef environment may interfere with the light/laser path and result in accurate shear stress

measurements.

Piezoresistive floating-element sensors developed by Ng et al. [126] and Shajii et al. [127] offer several advantages when used underwater. This technique does not require a priori knowledge of the flow profile since it is a direct technique. It requires less complex and relatively cheaper calibration process and measurement setup, especially compared to optical setups. It also requires less power consumption compared to heat transfer and optics based devices. Finally, it is able to detect flow reversal. However, piezoresistors are sensitive to temperature changes, thus a reliable temperature compensation scheme is needed. Noise due to photoelectric effect may reduce the minimum detectable shear stress on piezoresistive sensors. Particles or blood cells may get trapped in the gaps between the floating element and the substrate, resulting in inaccurate shear stress measurements when used in a coral reef environment or a cardiovascular system.

Chapter 3

Piezoresistors: History and Fundamentals

This chapter reviews the history piezoresistance in semiconductors, which include some early experimental results. Next, piezoresistance fundamentals are presented, which include notation commonly used, theory, fabrication techniques, noise, design parameters, and some examples of piezoresistive sensors.

3.1 History of Piezoresistance

William Thomson (Lord Kelvin) [139] first reported on the change in resistance with elongation in iron and copper in 1856. Telegraph wire signal propagation changes and time-related conductivity changes, nuisances to telegraph companies, motivated further observations of conductivity under strain. In his classic Bakerian lecture to the Royal Society of London, Kelvin reported an elegant experiment where joined, parallel lengths of copper and iron wires were stretched with a weight and the difference in their resistance change was measured with a modified Wheatstone bridge. Kelvin determined that, since the elongation was the same for both wires, “the effect observed depends truly on variations in their conductivities.” Observation of these differences was remarkable, given the precision of available instrumentation.

Motivated by Lord Kelvins work, Tomlinson confirmed this strain-induced change

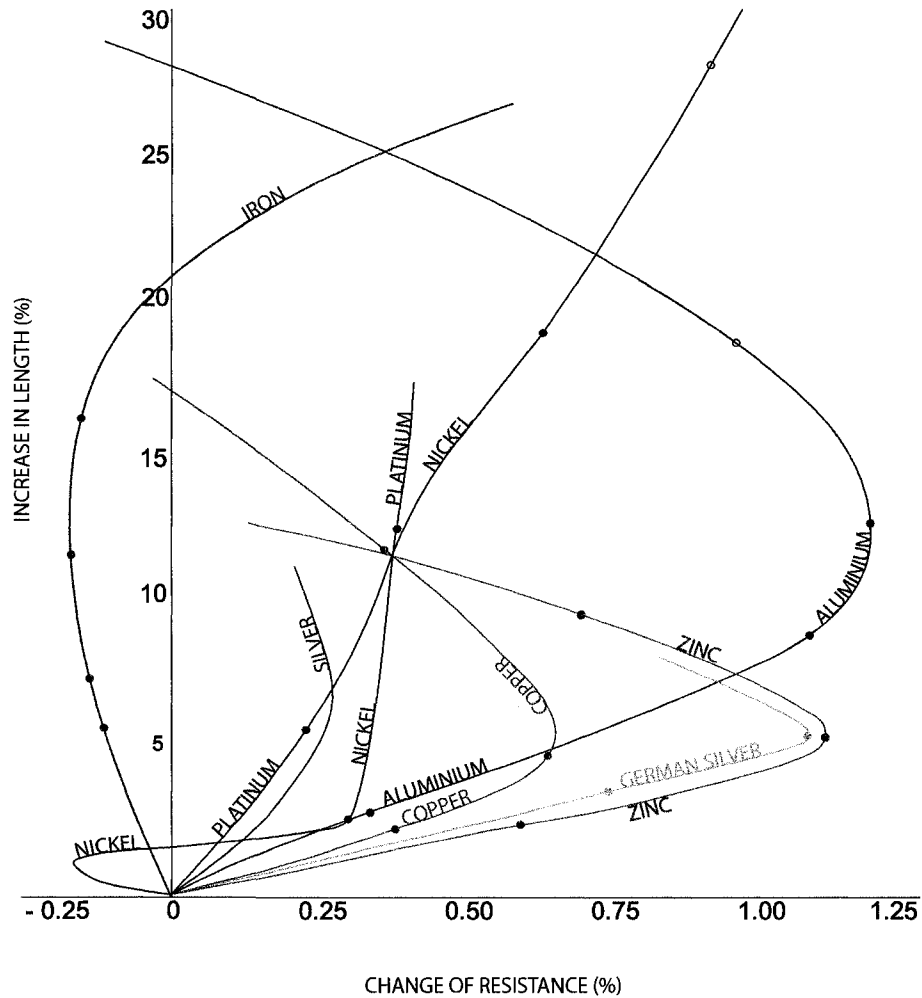


Figure 3.1: The alteration of specific resistance produced in different metals by hammering-induced strain. Source: Tomlinson [141]; ©1883 Royal Society Publishing; reproduced with permission.

in conductivity. He subsequently studied “The Influence of Stress and Strain on the Action of Physical Forces and reported a compiled set of measurements of temperature and direction dependent elasticity and conductivity of metals under varied orientations of mechanical loads and electrical currents (Figure 3.1) [140,141].

The steady state displacement measurement techniques of Thomson and Tomlinson were replicated, refined, and applied to other polycrystalline and amorphous conductors by several researchers [142–144]. In 1930, Rolnick [145] presented a dynamic technique to quantify the resistance change in vibrating wires of 15 different metals. These measurements also captured the thermal component of strain on resistance. In 1932, Allen [146–149] presented the first measurements of direction-dependent conductivity with strain in single crystals of bismuth, antimony, cadmium and zinc and tin. Based on her work, Bridgman [144, 146] developed a tensor formulation for the general case of homogeneous mechanical stress on the electrical resistance of single crystals.

In 1935, Cookson [150] first applied the term piezoresistance to the change in conductivity with stress, as distinct from the total fractional change of resistance. The term was most likely coined after piezoelectricity, the generation of charge with applied stress, a reversible ferroelectric-mediated effect that is quite different from piezoresistivity. Hanke coined the term piezoelectricity in 1881 after *piezen* from the Greek to press [151, 152]. The now standard notation for piezoresistivity was adapted from analogous work on piezoelectricity [153]. Voigt [154] formalized so called 'Voigt' or tensor notation for stress and strain in crystals and formulated tensor expressions for generalized Hookes Law and piezoelectricity. He adapted this notation from the works of Curie and Kelvin [153, 155–158].

More than 80 years after the discovery of piezoresistance, the bonded strain gauge was employed for the measurement of strain in stressed members. In 1938, Clark and Datwyler [159] used a bonded wire to monitor strain in a stressed member. In 1938, Arthur Ruge independently reinvented the bonded metallic strain gauge which had been first suggested by Edward Simmons Jr. in 1936 [160]. Ultimately, Simmons work was recognized as having priority by the U.S. patent office [161, 162] and Ruge was awarded an improvement invention [163]. Simmons and Ruge are generally credited with the invention of the modern strain gauge. In 1950, Bardeen and Shockley [164] predicted relatively large conductivity with deformation changes in single crystal semiconductors. In his seminal paper on semiconductor piezoresistance, C. S.

Smith [165] (a researcher visiting Bell Laboratories from Case Western Reserve University who was interested in anisotropic electrical properties of materials), reported the first measurements of the exceptionally large piezoresistive shear coefficient in silicon and germanium.

In 1957, Mason and Thurston [166] first reported silicon strain gauges for measuring displacement, force, and torque. Semiconductor strain gauges, with sensitivity more than fifty times higher than conventional strain gauges, were considered a leap forward in sensing technology. Early silicon strain gauges were fabricated by sawing orthogonal grooves in rectangular silicon or germanium wafers. The wafer was then back-lapped and polished to separate it into bars. Wires were attached to each end of the gage by alloying, soldering or welding. Finally, the strain gauges were chemically etched until sufficiently thin (on the order of 5 μm) to form a bar shaped strain gauge [167]. The gage was then attached to a material surface with cement. This method was successful and allowed the development of the first bonded semiconductor pressure sensors. However, the serial manufacturing and placement of the sensor elements were expensive, so many of the newer applications were eventually served by integrated pressure sensors that integrally combined piezoresistive elements with a silicon force-collecting diaphragm. The first commercial piezoresistive silicon strain gauges and pressure sensors started to appear in the late 1950s. Kulite Semiconductor, founded in 1958 to exploit piezoresistive technology, became the first licensee under the Bell piezoresistive patents [168]. By 1960 there were at least two commercial suppliers of bulk silicon strain gauges: Kulite-Bytrex and Microsystems [168].

Developments in the manufacture of semiconductors, especially Hoernis invention of the planar transistor in 1959, resulted in improved methods of manufacturing piezoresistive sensors [169]. Subsequently, silicon piezoresistive devices evolved from bonded single strain gauges to sensing devices with 'integrated' piezoresistive regions (in the sense that the piezoresistive region was co-fabricated with the force collector). The field benefited, to a degree that no other sensor technology has, from developments in silicon processing and modeling for the integrated circuits (IC) industry. Technological advances in the fabrication of ICs including doping, etching,

and thin film deposition methods, have allowed significant improvements in piezoresistive device sensitivity, resolution, bandwidth, and miniaturization (Figure 3.2). Reviews of advances in MEMS, microstructures, and microsystems are available elsewhere [170,171]. In their classic 1961 paper, Pfann and Thurston [172] proposed the integration of diffused piezoresistive elements with a silicon force collecting element. The first such 'integrated' device, a diffused piezoresistive pressure sensing diaphragm was realized by Tufte et al. [173] at Honeywell Research in 1962.

During the first decades of silicon processing, piezoresistive sensors were the most important commercial devices requiring three-dimensional micromachining of silicon; this technology was a singularly important precursor to the MEMS technology that emerged in the 1980s. In 1982, Petersens seminal paper on Silicon as a Mechanical Material [174] reviewed several micromachined silicon transducers, including piezoresistive devices, and the fabrication processes and techniques used to create them. Petersens paper helped drive the growth in innovation and design of micromachined silicon devices over the subsequent years.

3.2 Fundamentals of Piezoresistance

The electrical resistance (R) between two points of a homogeneous structure is a function of its dimensions and resistivity (ρ),

$$R = \frac{\rho l}{A} \quad (3.1)$$

where R is resistance, l is length, and a is average cross-sectional area. Similarly, the change in resistance due to applied stress is a function of geometry and resistivity changes. The cross-sectional area of a bulk material reduces in proportion to the longitudinal strain by its Poisson's ratio, ν . The isotropic lower and upper limit for ν are -1.0 and 0.5 [175]. Poisson's ratio for most metals ranges from 0.20 to 0.35. For silicon, the ratio of lateral strain to longitudinal strain is anisotropic, ranging from a low of 0.06 to a high of 0.36 [176,177].

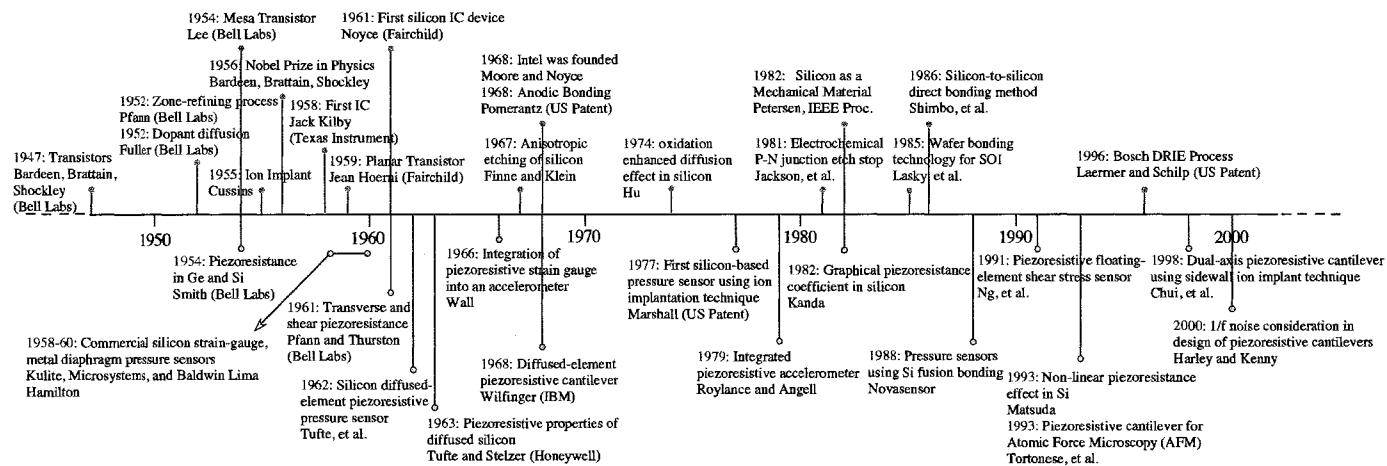


Figure 3.2: Technological advances in IC fabrication (above the horizontal line) and micromachining (below the horizontal line) [86, 126, 165, 168, 169, 172–174, 178–202]

The gauge factor (GF) of a strain gauge is defined as

$$GF = \frac{\frac{\Delta R}{R}}{\epsilon} \quad (3.2)$$

where ϵ is strain and $\frac{\Delta R}{R}$ is fractional resistance change with strain. Early papers isolate components of the fractional resistance change $\frac{\Delta R}{R}$ into geometric effects $(1 + 2\nu)\epsilon$ and fractional change in resistivity $\frac{\Delta\rho}{\rho}$ of the material with strain [145]:

$$\frac{\Delta R}{R} = (1 + 2\nu)\epsilon + \frac{\Delta\rho}{\rho} \quad (3.3)$$

Geometric effects alone provide a GF of approximately 1.4 to 2.0, and the change in resistivity, $\frac{\Delta\rho}{\rho}$, for a metal is small (on the order of 0.3). However, for silicon and germanium in certain directions, $\frac{\Delta\rho}{\rho}$ is 50 – 100 times larger than the geometric term. For a bar-type silicon strain gauge, the GF may be calculated or measured and 3.3 may be used as an approximation. Note that the concept of a gauge factor intrinsically assumes a bulk, linear elastic strain behavior and linear conductivity fluctuations with stress. Other factors can affect the fractional change in resistivity (e.g. temperature, doping, and bias voltage).

A more rigorous treatment, beyond the uniaxial tension 'wire' gauge configuration, is needed for an integrated sensor made from an anisotropic single crystal semiconductor. Such a device requires a multi-dimensional analysis of direction-dependent elasticity (stiffness coefficients) and conductivity (piezoresistive coefficients) under specified directions of loads (stress, strain) and fields (potentials, currents). To this end, this section first reviews notation, then discusses fundamentals of piezoresistivity in semiconductors.

3.2.1 Silicon Crystal Structure

Crystals have periodic arrangements of atoms arranged in one of 14 lattice types. Crystalline silicon forms a covalently bonded diamond-cubic structure with lattice constant $a = 5.43 \text{ \AA}$ (Figure 3.3). The diamond-cubic structure is equivalent to two interpenetrating face-centered-cubic (FCC) lattices with basis atoms offset by $\frac{1}{4}a$

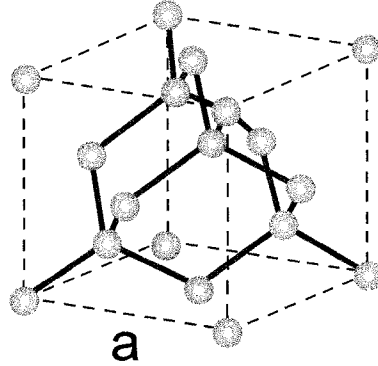


Figure 3.3: Covalently bonded diamond cubic structure of silicon.

in the three orthogonal directions [203]. Silicons diamond-cubic lattice is relatively sparse (34% packing density) compared to a regular face-centered-cubic (FCC) lattice (74% packing density).

In a cubic crystal lattice (with orthogonal symmetry), such as silicon and germanium, three Miller indices, hkl , enclosed in different types of brackets are sufficient to describe the planes and directions. The Miller indices specify crystal planes by n-tuples. One first identifies plane intercepts of a plane on the crystallographic axes of a representative (typically primitive) cell, then takes the reciprocals of those numbers, and finally normalizes them to integer form. The resulting indices identify that crystallographic plane. Commonly used wafer surface orientations in micromachining include (100), (111), and (110) (Figure 3.4). Etch techniques can create devices in various directions to access desirable material properties. Directionality of silicon piezoresistive coefficients is discussed in Section 3.2.4. Complete reviews on crystal structures and Miller indices are available elsewhere [203, 204].

3.2.2 Piezoresistance Theory

Both p-type and n-type silicon have large piezoresistive coefficients, and both have proven useful for sensors. The discovery of such large piezoresistive effects demanded a theory of the underlying physics. Smith reported the first measurements of large piezoresistive coefficients in these semiconductor crystals in 1954 and noted that work

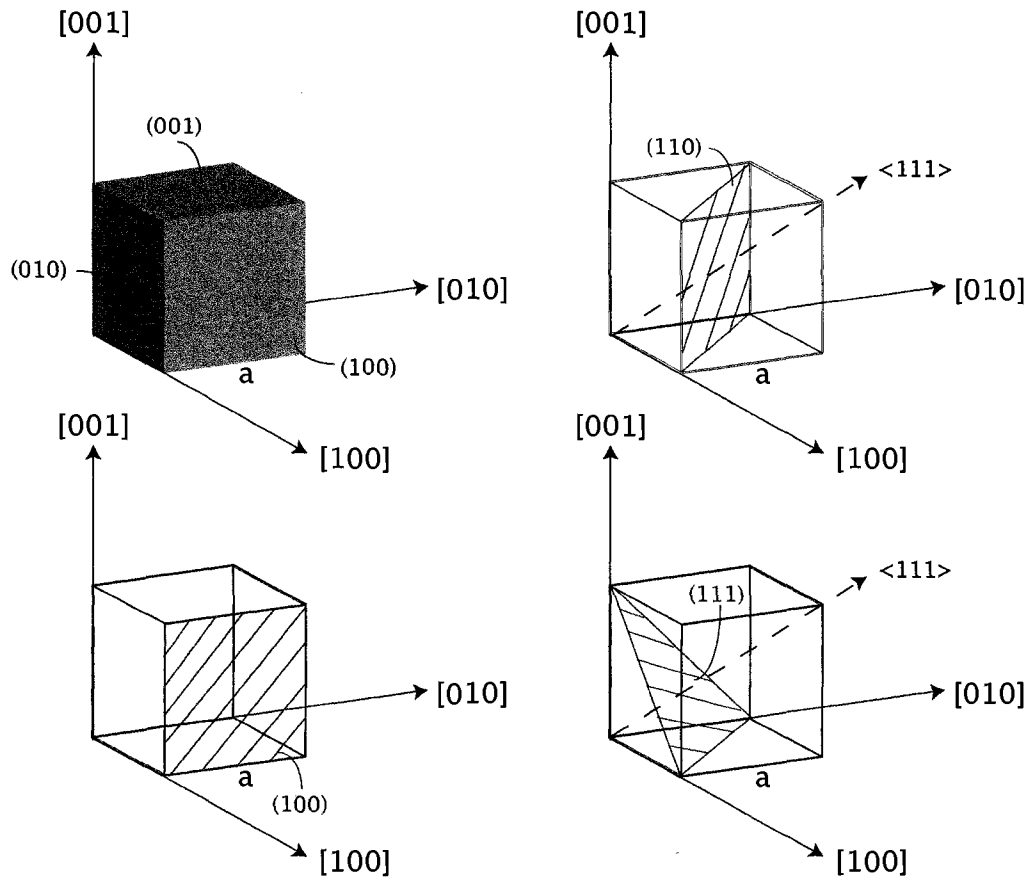


Figure 3.4: Commonly employed crystal planes of silicon, i.e. (100), (110), and (111) planes. Silicon has four covalent bonds and coordinates itself tetrahedrally. The {111} planes, oriented 54.74° from {100} planes, are most densely packed. Mechanical and electrical properties vary greatly with direction, especially between the most dense {111} and the least dense {100} planes.

by Bardeen and Shockley, and later Herring, could explain the phenomena [165]. Smith applied Bridgman's tensor notation [144] in defining the piezoresistive coefficients, π , and geometry of his test configurations (Figure 3.5). Kanda [178] later generalized these relations for a fixed voltage and current orientation (ω) as a function of stress (λ):

$$\frac{\Delta\rho_\omega}{\rho} = \sum_{\lambda=1}^6 \pi_{\omega\lambda}\sigma_\lambda. \quad (3.4)$$

This section discusses the prevailing theories at the time of Smith's measurements as well as more recent advances. The theories of semiconductor piezoresistance are grounded in one-dimensional descriptions of electron and hole transport in crystalline structures under strain (potentially extended to three dimensions and to include crystal defects, electric potentials, and temperature effects). The various models require some framework of bandgap energy models, wave mechanics, and quantum effects; the interested reader is referred to other references for more information [203, 205–207].

At the time of Smith's piezoresistance measurements, existing theories were based on shifts in bandgap energies. The band structure of diamond was first calculated by Kimball in 1935 [208] and that of silicon by Mullaney in 1944 [209]. In 1950, Bardeen and Shockley [164] presented a model for mobility changes in semiconductors subjected to deformation potentials and compared both predicted and measured conductivity changes in the bandgap with dilation. This work served as the basis for later analyses, such as that of Herring [210, 211] and Long [212].

The mobilities and effective masses of the carriers (holes and electrons) are significantly different from one another and fluctuate under strain. N-type and p-type piezoresistors exhibit opposite trends in resistance change and different direction-dependent magnitudes under stress. The magnitudes and signs of the piezoresistive coefficients depend on a number of factors including impurity concentration, temperature, crystallographic direction, as well as the relation of voltage, current and stress to one another and to the crystallographic axes. The relationship between carrier characteristics and strain has been investigated both experimentally [165, 166, 179] and analytically [164, 172, 178, 211, 213, 214]. Focusing on n-type silicon, these early

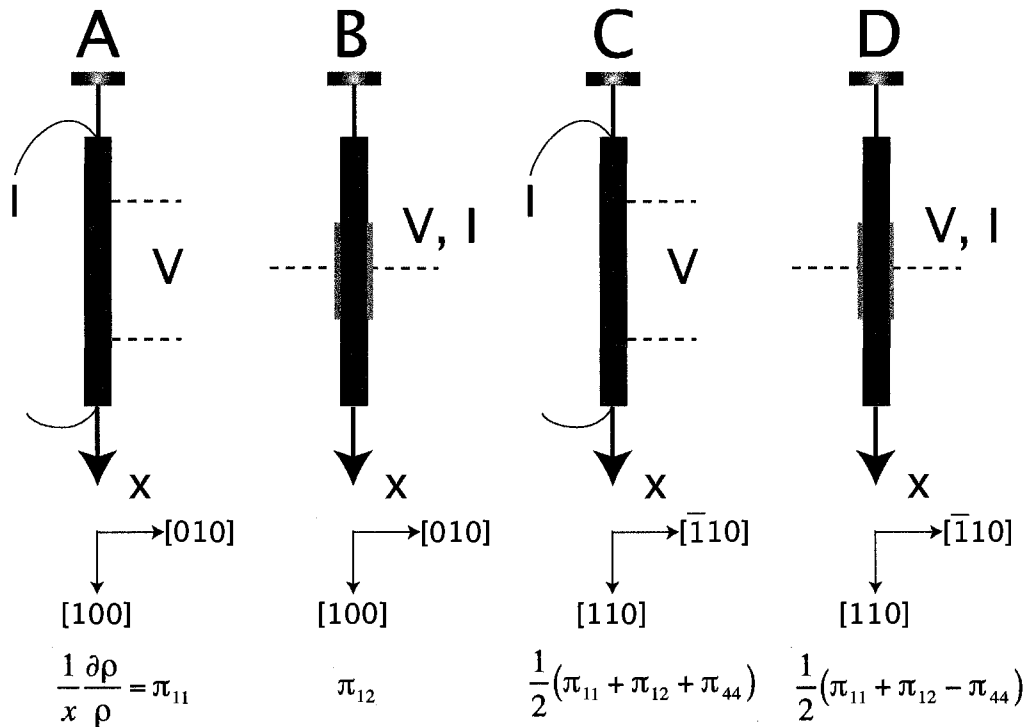


Figure 3.5: Notation for Smiths test configurations in 1954. Configurations A and C measured longitudinal piezoresistance, while configurations B and D provided transverse coefficients. Voltage drops between the electrodes (dotted lines) were measured while uniaxial tensile stress, X , was applied to the test sample by hanging a weight with on a string. The experiments were done in constant-current mode in a light-tight enclosure with controlled temperature ($25 \pm 1^\circ\text{C}$). Source: Smith [165]; © 1954 American Physical Society; reproduced with permission.

studies utilized either effective mass or energy band calculations with wave propagation in one direction at a time. The change in mobility (and conductivity) with lattice strain is attributed to band warping or bending and the non-uniform density of states.

The implications for the related large mobility and resistance changes were not realized prior to Smith's discovery [215,216]. Following Bardeen and Shockley's models for mobility changes with deformation potentials, more refined models of transport and energy band structure based on new experimental work became available. In 1955, Herring proposed his Many-Valley model, which adequately explained piezoresistance for n-type silicon and germanium [164,172,211,213,214,217–220].

Herring's Many-Valley model for n-type silicon [211] proposes three symmetrical valleys along the [100] direction. His model projects the band energy minima in three orthogonal directions (x, y, z) as locations of constant minimum energy (Figure 3.6). The minimum energy of each valley lies along the centerline of the constant energy ellipsoid of revolution. Electrons have a higher mobility along the direction perpendicular to the long axis of the ellipsoid. Since electrons occupy lower energy states first, they are found in these regions bounded by ellipsoids of constant low-energy. These ellipsoids, bounded by higher-energy regions, are referred to as valleys. With strain however, the symmetry is broken and the ellipsoids are asymmetrically dilated or constricted. This results in an anisotropic change in conductivity proportional to strain.

Most models represent the direction dependence of bandgap and electron energies by either directional waves (k has direction and magnitude) or momentum (p) and the effective masses of the carriers. The energy surfaces for electron mobility are accordingly represented in k -space or momentum space. The wave propagation is confined to quantum states by the periodicity of the lattice, and edges in the band diagrams correspond to the edges of the Brillouin zone (smallest primitive cell, or unit cell, of the reciprocal lattice) oriented in a direction of interest.

In the unstrained silicon crystal, the lowest conduction band energies (valleys) or highest mobility orientations are aligned with the $\langle 100 \rangle$ directions. The conduction electrons are thus imagined to be lying in six equal groups or valleys, aligned with

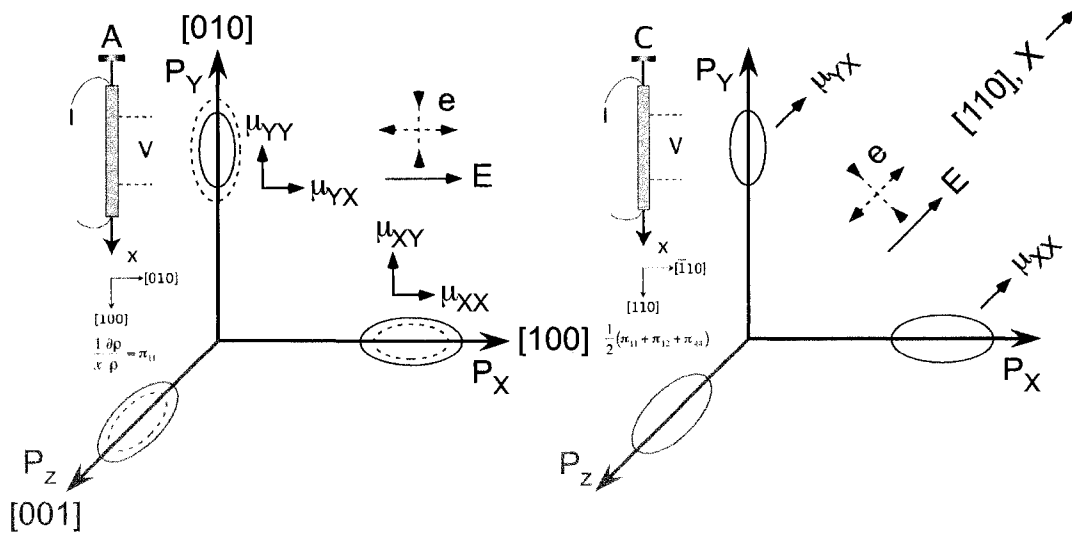


Figure 3.6: Test configuration and resulting schematic diagrams of probable constant energy surfaces in momentum space for n-type Si with potential, E , and strain, ϵ , as depicted. The electrons are located in six energy valleys at the centers of the constant energy ellipsoids, which are shown greatly enlarged. The effect of stress on the two valley energies shown is indicated by the dotted ellipsoids. The mobilities, μ , of the several groups of charge carriers in various directions are roughly indicated by the arrows. The test configurations correspond to Smith's experimental arrangements A and C (Figure 3.5). Source: Smith [165]; © 1954 American Physical Society; reproduced with permission.

three $\langle 100 \rangle$ directions. For any valley, the mobility is the lowest when parallel to the valley direction, and the highest when perpendicular to the valley, e.g. an electron in the z valley has higher mobility in the x and y directions. Net electron conductivity is the sum of the conductivity components along the three valley orientations and is independent of direction. Net mobility is the average mobility along the three valleys (two high and one low) [220]. Uniaxial elongation increases the band energy of the valley parallel to the strain and transfers electrons to perpendicular valleys, which also have high mobility along the direction of strain. Electrons favor transport in directions of higher mobility (higher conductivity and lower resistance) in the direction of strain, and tension removes electrons from the valley in that direction and transfers them to valleys normal to the tension. In n-type silicon, average mobility is increased in the direction of tension (longitudinal effect) and lowered transverse to that direction (transverse effect). Compression has the opposite effect. Lin provided an explanation of large mobility degradation at higher transverse electric fields and lower temperatures based on “the physics of electron population and scattering mechanisms of quantized subbands at (100) Si surfaces [221].”

In 1993, Ohmura [222] stated that “the [piezoresistance] effect for n-type Ge and Si has been successfully accounted for” while “the [piezoresistance] effect for p-type Si and Ge has not been fully understood. The piezoresistance theory for n-type semiconductors continued to be refined from 1954 onward, but until recently “piezoresistive effects in p-type silicon have not been fully clarified due to the complexity of the valence band structure” [223]. Recent computational advances have enabled improved understanding of p-type piezoresistance [207, 224–226]. Notably, most research and commercial piezoresistive devices are p-type and models of this successful technology have been largely based on empirical results. Theoretical studies (based on strain Hamiltonian [227–229]) on deformation potentials in strained silicon and cyclotron resonance experimental results showed several factors that affect the hole mobilities in semiconductors, e.g. band warping and splitting, mass change, etc. [230–234].

Historically, piezoresistive technology drew from mainstream IC research and continues to do so. Now, with the strong interest in “strain engineering” to increase transport speed in ICs, mainstream semiconductor technology is drawing on findings

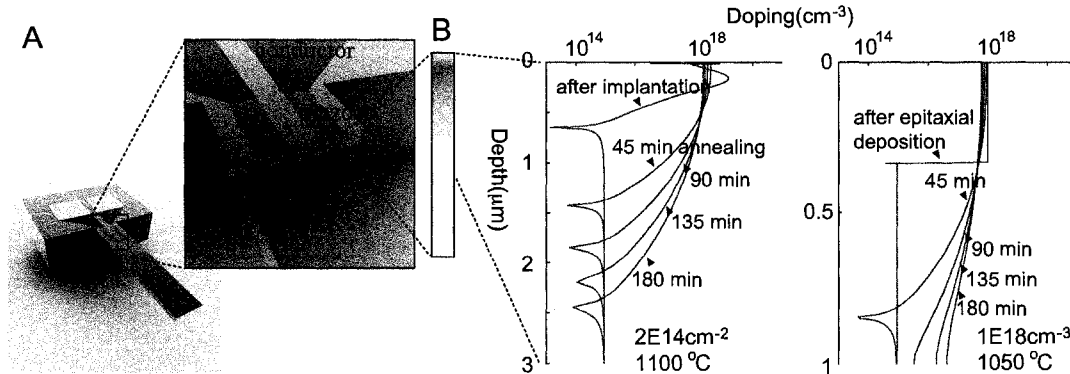


Figure 3.7: Microfabricated piezoresistive cantilever [238] and TSUPREM4 [239] simulation plots of doping profiles using ion implantation and epitaxial deposition techniques. Note the difference in the dopant profiles following ion-implantation and epitaxy and the progression of dopant diffusion with increasing time of thermal annealing. Figure is courtesy of Sung-Jin Park [238]; reproduced with permission.

of piezoresistive research. Strain engineered materials (e.g. inclusion of germanium into a silicon layer) can increase the mobility of a channel in an MOS (metal-oxide-semiconductor) devices [207, 235–237]. Suthram et al. applied large uniaxial stress on n-type MOS field-effect transistors (MOSFETs) and showed that piezoresistive coefficients were constant while the electron mobility enhancement increased linearly for stresses up to ~ 1.5 GPa [237].

3.2.3 Piezoresistor Fabrication

Several design and process parameters affect piezoresistor sensitivity and noise including doping parameters (energy, dose, method) and anneal (temperature, time, environment). These affect the dopant concentration profile and crystal quality. This section reviews several fabrication methods for forming piezoresistors on semiconductor substrates and discuss their advantages and drawbacks. Diffusion, ion implantation, and epitaxy are the most common impurity-doping techniques for introducing dopants into a silicon substrate. These techniques result in different doping profiles (Figure 3.7). A complete review of doping techniques is available elsewhere [88].

Diffusion

Diffusion is the migration of dopant atoms from a region of high concentration to a region of low concentration. The fabrication of piezoresistors using diffusion involves a pre-deposition and a drive-in step. During the pre-deposition step, wafers may be placed in a high-temperature furnace (900 – 1300°C) with a gas-phase or a solid-phase dopant source [88,240]. The gas-phase dopant source, e.g. diborane, phosphine, or arsine, is carried in an inert gas, e.g. nitrogen or argon. The solid-phase dopant source (a compound containing dopant atoms in a form of solid discs) is placed such that the active surface is facing the surface of the silicon wafer inside the furnace. Both the source and the wafer are heated, causing transport of dopants from the source to the wafer. Alternately, dopant pre-deposition may utilize doped glass layers on the wafer surface (spin-on-dopant technique) [241–243]. During pre-deposition, the boundary condition is a constant surface concentration and the doping profile is approximated by a complementary error function [88]. The source can be removed and dopants 'driven-in' deeper with high temperature annealing (900 – 1300°C). Gas-phase dopant sources provide inconsistent doses for surface concentrations below the solubility level.

Ion Implantation

Ion implantation was researched extensively in the 1950s and 1960s as an alternate pre-deposition method to provide better control of the pre-deposition dose [88, 180, 244–254]. Ion implantation gained wide use in the 1980s and remains the preferred method today. In ion implantation, dopant ions are accelerated with keV to MeV of energy into the substrate. The ions leave a cascade of damage in the crystal structure of the implanted substrate [88, 251]. Ion implantation is a stochastic process where ions scatter off the lattice, lose their energy, and come to rest at a probabilistic depth below the surface. Ion implantation provides excellent control in introducing a specific number of dopant atoms into the substrate. Ion implantation can be masked to modify the electrical conductivity of a specific region of a substrate. Any layer thick or dense enough to block the implanted ions, such as photoresist, silicon oxide,

silicon nitride, or metal, can be used for masking [88]. Typical silicon piezoresistor doses range from 1×10^{14} to 5×10^{16} cm^{-2} , with energy ranges from 30 to 150 keV [79]. Dopant distribution is approximated by a symmetric Gaussian distribution (Figure 3.7) [88]. Light ions, such as boron, tend to backscatter and fill in the front side of the distribution, while heavy ions, such as arsenic tend to fill in the back side of the distribution [88]. Most implants are done with a 7° tilt of (100) silicon wafers to avoid ion channeling, a phenomenon where ions deeply traverse gaps in the lattice without scattering. Larger implant angles (7° - 45°) are sometimes used to form piezoresistors on etched sidewalls of deep-reactive-ion-etched (DRIE) trenches as found in flexures or beams in dual-axis cantilevers, in-plane accelerometers, and shear stress sensors [255–257]. Sidewall techniques are impractical in high throughput implanters with fixed angles of less than 7° . However, 300-mm wafer implanters are typically high-current, single-wafer systems with adjustable implant angles of up to 60° and may be suitable for sidewall piezoresistor processing.

One major disadvantage of ion implantation is significant damage to the crystal, although lattice order is mostly restored by high-temperature dopant activation and annealing [88, 251]. Dopant ions are “activated” to occupy substitutional sites in the lattice where they donate holes or electrons. However, both diffusion length and lattice repair are proportional to temperature and time, therefore shallow junctions become difficult to obtain with high crystal quality. In addition, the excess interstitials created during implantation adds to the problem of minimizing dopant diffusion length. This damage transiently enhances the dopant diffusion where diffusion-lengths can be thousands of times higher than those without implantation damage [88]. In Transient-Enhanced Diffusion (TED), dopants may diffuse even further at low temperature with the same anneal time because the damage can persist. Other parameters that affect the junction depth include the acceleration energy, the ion mass, and the stopping power of the material [80, 88, 258].

Epitaxy

Epitaxy is the growth of atomic layers on single-crystal materials that conforms to the crystal-structure arrangement on the surface of the crystalline substrate [80, 88].

Chemical Vapor Deposition (CVD) technique can be used to deposit epitaxial silicon by decomposing silane or by reacting silicon chloride with hydrogen [88]. Conventional epitaxial growth is done at high temperatures (1000 – 1250°C) and reduced pressure (30–200 torr). The high temperature destabilizes and vaporizes any growth-inhibiting native oxide on the surface and enhances surface reactions for deposition. The reduced pressures are needed to obtain better control over on/off switching of dopant gas and to reduce autodoping, the incorporation of dopants originating from the substrate into the epitaxial layer. A clean surface is necessary to obtain a high quality epitaxial layer. Contaminants and native oxide will prevent single-crystal growth. Sometimes, wafers are subjected to an in situ hydrogen chloride clean to remove any contaminants and native oxide [88]. Halide source gases, such as silicon chloride, trichlorosilane, or dichlorosilane (DCS) are used to grow silicon with the advantage that chlorine is one of the net byproducts. The chlorine removes metal contaminants from the deposited silicon film, resulting in better quality single-crystal silicon. Selective deposition of epitaxial silicon, i.e. the silicon deposits only on exposed regions of silicon, but not on other dielectric films such as silicon oxide or silicon nitride, can be achieved by tailoring the deposition conditions [88, 259–262]. Halide source gases and hydrogen chloride have been found to increase the surface migration of silicon atoms and selectivity of deposition regions. Epitaxial silicon films may be doped during the deposition by introducing appropriate dopant source gases such as arsine, phosphine, or diborane into the chamber along with the silicon source gases [88]

Epitaxial piezoresistors require no annealing and have a uniform dopant profile (Figure 3.7). Epitaxy has enabled ultra thin piezoresistive layers and increased force sensitivity [182, 263, 264]. Harley and Kenny [263] and Liang et al. [264] demonstrated the use of epitaxially grown doped silicon to form piezoresistors in ultra-thin cantilevers (less than 100 nm). This is a practical method for such thin piezoresistive cantilevers, especially given the difficulties of implanting shallow junction depths (less than 50 nm), activating dopant atoms, and restoring lattice quality. Joyce and Baldrey [259] first demonstrated selective deposition of silicon epitaxial layers using oxide-masking techniques in 1962 and Zhang et al. [265] demonstrated a selective deposition technique without hydrogen chloride.

Tradeoffs in Process Selection

Ion implantation is the most common method of fabricating piezoresistors. Advantages of ion implantation include precise control of dopant concentration and depth. Disadvantages include lattice damage and annealing requirements for dopant activation. Diffusion has the advantage of batch processing, but suffers from poor dopant depth and concentration control. Epitaxy provides excellent depth control without annealing, which enables shallow junctions with abrupt dopant profiles cost, and availability. However, processing complexity and equipment costs and availability are drawbacks to epitaxy method. Table 3.1 compares ion-implantation, diffusion, and epitaxy techniques.

3.2.4 Design and Process Parameters for Piezoresistor Performance

Several other design and process parameters affecting piezoresistor sensitivity and noise are related to doping parameters and anneal. The sensitivity as a function of doping concentration and strain direction is a primary design parameter, however selection of doping, anneal, device geometry, and operating conditions must also consider the temperature coefficients of sensitivity and resistance, nonlinearity with strain (and temperature), and of course noise and resolution limits discussed in the next sections.

Piezoresistance with Doping and Direction

Initial experiments by Smith [165] used bars of silicon cut from wafers doped while growing the single-crystal ingot. Later, Pfann and Thurston [172] suggested diffusion techniques to integrate doped piezoresistors on the sensor surface. The piezoresistive properties of diffused layers were subsequently investigated by Tufte and Stelzer [179]. They also provided empirical data on piezoresistive coefficients for different surface concentrations and resistivities [179]. Kurtz and Gravel [266] replotted their data and noted that the piezoresistive coefficients decrease approximately with the log of surface concentration.

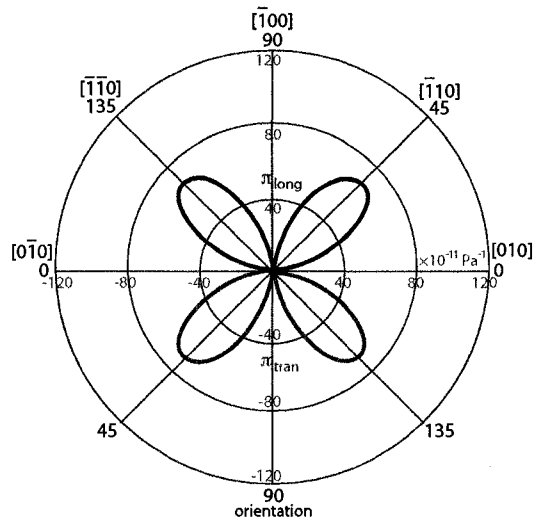
Table 3.1: Comparisons of doping methods (after Plummer et al. [88]).

	Ion Implantation	Diffusion	Epitaxy
Process Condition	room temperature vacuum batch process	high temperature batch process	high temperature low pressure single wafer
Damage	significant requires annealing enhances diffusion	none	none
Doping Concentration Control	excellent	acceptable	good
Dopant Depth Control	good	not good	very good
Typical Range of Doses or Concentration	1×10^{11} to $1 \times 10^{16} \text{ cm}^{-2}$	concentration is limited to solid solubility	1×10^{14} to $1 \times 10^{17} \text{ cm}^{-2}$
Masking	photoresist or hard mask (silicon oxide, silicon nitride, metal)	hard mask	oxide mask and selective deposition (more difficult) or etch back

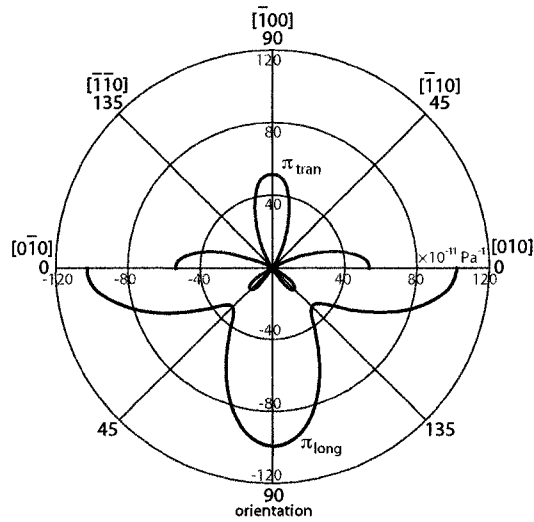
Early analyses by Smith, and Pfann and Thurston [165, 172], covered virtually all crystal orientations and piezoresistor designs for n-type and p-type piezoresistors in use today. Kanda extended these analyses with graphical representations of the piezoresistive coefficients in arbitrary directions by transforming the crystal axes. These graphs provide a useful picture of how piezoresistive coefficients vary with respect to crystal orientations, both for longitudinal and transverse directions. Kanda provided graphs for the (100), (110), and (211) silicon planes (Figure 3.8) [178].

Theoretical calculations of piezoresistive change versus dopant concentration were also presented by Kanda [178]. Kanda noted a discrepancy between his calculations and the experimental data (Figure 3.9) and suggested a simple power law dependence of the relaxation time with temperature [178]. Thus, the piezoresistive coefficient is calculated by multiplying the piezoresistive factor, $P(N, T)$ (Figure 3.10), by the room temperature piezoresistive coefficient. The calculated values of the $P(N, T)$, agree well with the experimental values obtained by Mason [267] for doping concentrations less than $1 \times 10^{17} \text{ cm}^{-3}$, over the temperature range of -50 to 150°C , but differ by 21% at a concentration of $3 \times 10^{19} \text{ cm}^{-3}$ at room temperature. The error was attributed to different scattering mechanisms at different concentrations, whereas the calculation only considered lattice scattering. Harley and Kenny [183] later evaluated data from several researchers and provided an empirical model of piezoresistance vs. concentration that better estimates the sensitivity of higher concentration devices.

Richter et al. [269–271] demonstrated a novel piezocoefficient-mapping device to measure 3D stresses in device packaging and also to extract directional piezoresistive coefficients. Using orthogonal [100] piezoresistors and 4-point bending strain along the [110] direction, Richter et al. [269] measured piezoresistance coefficients for silicon and strained silicon ($\text{Si}_{0.9}\text{Ge}_{0.1}$) molecular beam epitaxial (MBE) grown layers at boron doping levels of 1×10^{18} and $1 \times 10^{19} \text{ cm}^{-3}$. They extracted piezoresistive coefficients as a function of doping and direction; their results are higher than Smiths lower dose values and also showed that lattice strain raises the value of π_{44} for both doping levels. Four-point bending is commonly employed to measure piezoresistive effects in semiconductors [272, 273], though care must be taken in high-stress test conditions [237].



(a) p-type silicon



(b) n-type silicon

Figure 3.8: Room temperature piezoresistive coefficients in the (100) plane. Source: Kanda [178]; © 1982 Institute of Electrical and Electronics Engineers; reproduced with permission.

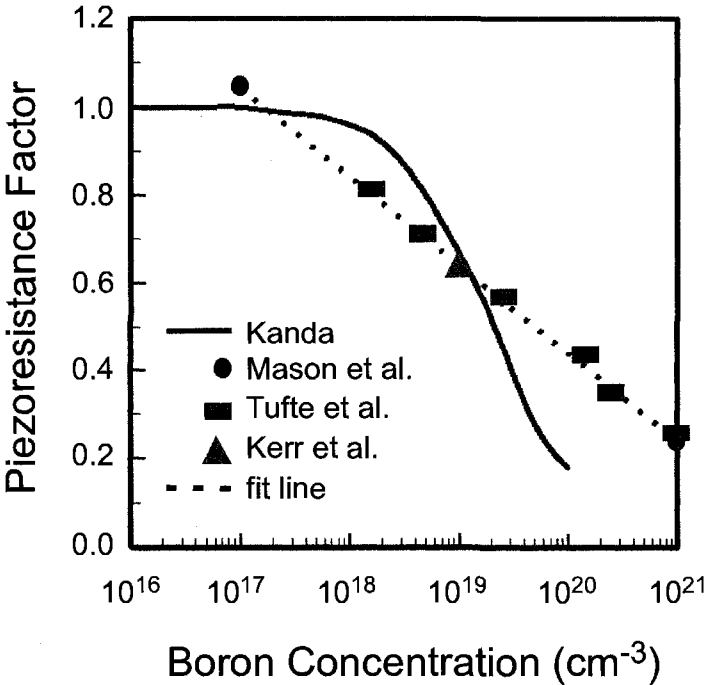
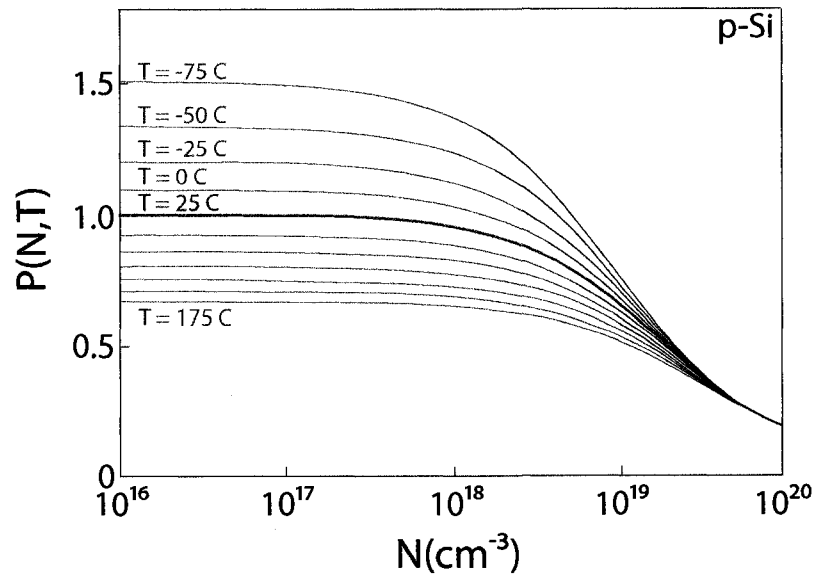
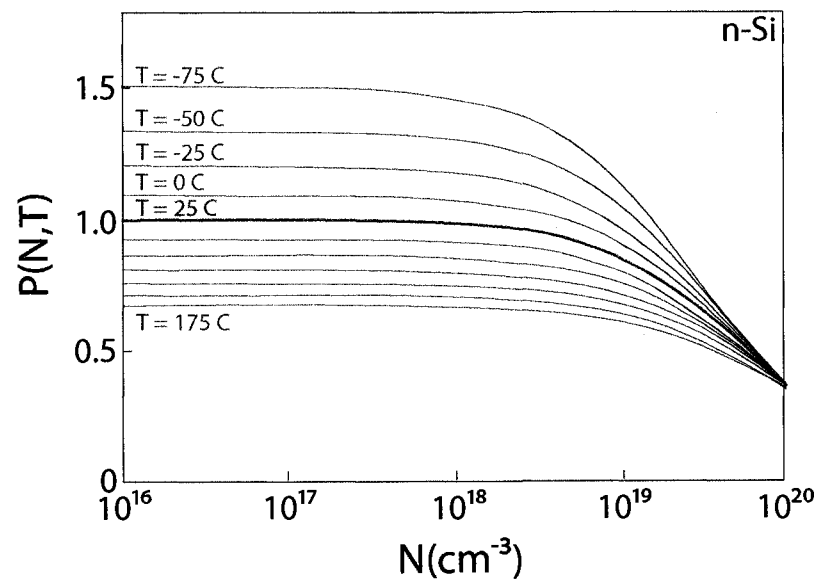


Figure 3.9: Piezoresistive coefficients as a function of doping. Experimental data obtained by Kerr, Tufté, and Mason are fitted by Harley and Kenny [179,183,267,268]. Theoretical prediction by Kanda overestimates the piezoresistive coefficients at higher concentrations [183]. Source: Harley and Kenny [183]; © 2000 Institute of Electrical and Electronics Engineers; reproduced with permission.



(a) p-type silicon



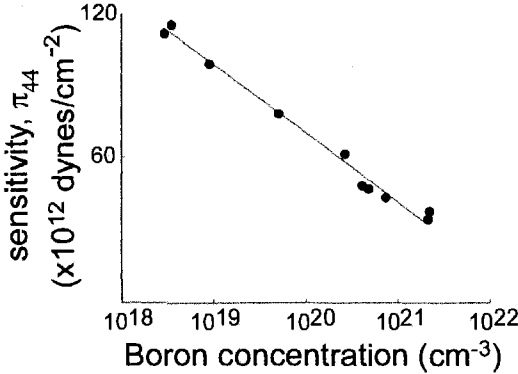
(b) n-type silicon

Figure 3.10: The adjusted piezoresistance factor $P(N, T)$ as a function of impurity concentration and temperature. Source: Kanda [178]; © 1982 Institute of Electrical and Electronics Engineers; reproduced with permission.

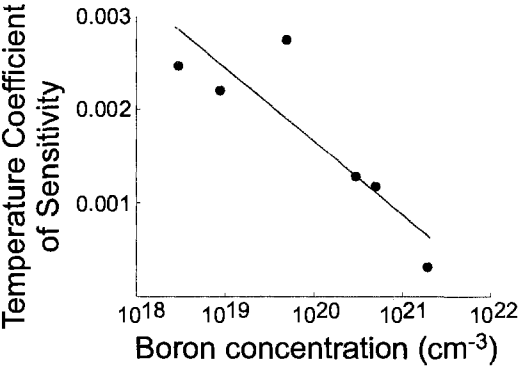
Temperature Coefficients of Sensitivity and Resistance

Piezoresistors are sensitive to temperature variation, which changes the mobility and number of carriers, resulting in a change in conductivity (or resistivity) and piezoresistive coefficients (sensitivity) [274]. Consequently, doped silicon can be used for accurate temperature sensing as in Resistance Temperature Detectors (RTD). Indeed, a typical commercial piezoresistive pressure sensor shows a thermal resistance change ten times the full-scale stressed resistance change over a temperature range of 100°C. Kurtz [275] presented data and discussed the trend of the piezoresistive coefficient (π), temperature coefficient of piezoresistive coefficient (TCS), resistivity (ρ), temperature coefficient of resistivity (TCR) and strain nonlinearity, as a function of dopant concentration (Figure 3.11). Temperature dependence decreases with higher surface concentration, but sensitivity also decreases. This trend is desirable except that increasing surface concentration sacrifices the sensitivity of the piezoresistors. However, while sensitivity is reduced at higher impurity doping levels, the temperature coefficients drops off faster for Kurtz's conditions. Also at higher doping levels, the strain and temperature nonlinearities in sensitivity, and change of sensitivity and resistance are very much reduced. Some piezoresistive pressure sensor manufacturers, such as Kulite Semiconductor Products, Merit Sensors, and GE NovaSensor manufacture high-dose piezoresistors, taking advantage of this reduced temperature sensitivity. Although temperature dependence for silicon strain sensors is inevitable, this dependence may be compensated by the use of a half or full-active Wheatstone bridge and conditioning circuitry.

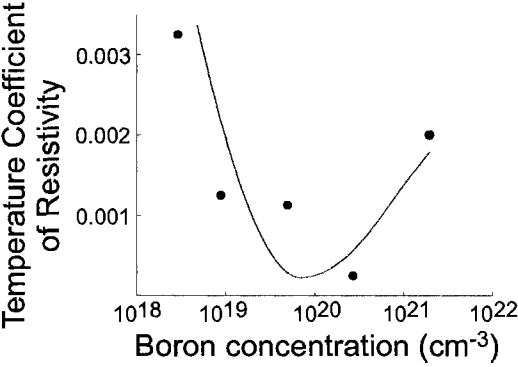
Tufte and Stelzer [179] presented detailed measurements of these parameters for diffused layers over a wide range of dopant concentrations ($10^{18} - 10^{21}$ atoms cm^{-3}) and temperatures (-90°C to 100°C). They also showed that the piezoresistive coefficient was relatively insensitive to the diffusion depth for a diffused layer. A more detailed analysis, presented by Kerr and Milnes [268], showed that the surface dopant concentration could be used as an adequate proxy for the average effective concentration in modeling the piezoresistivity of diffused layers. More recently, refined concentration-dependent temperature sensitivity measurements have been reported on integrated die using 4-point bending and finite element analysis of stress profiles [276].



(a) longitudinal piezoresistive coefficient (sensitivity), π_{44}



(b) Temperature Coefficient of Sensitivity (TCS)



(c) Temperature Coefficient of Resistivity (TCR) with dopant concentration.

Figure 3.11: Trends of key piezoresistive properties. Source: Kurtz [275]; © 1961 Instrument Society of America; reproduced with permission.

Nonlinearity

The response of piezoresistors to stress becomes nonlinear with large strain ($>0.1\%$). Understanding and compensating for the nonlinearity of piezoresistors is important for precision piezoresistive devices. Matsuda et al. [184,277] calculated and measured the piezoresistive coefficients and third-order effects for both p-type and n-type silicon. The measurements were for three major crystallographic orientations with strain up to 0.1% . Higher strain levels were difficult to measure since surface defects in the silicon lattice cause fracture at low strain levels. To overcome this problem, Chen and MacDonald [278] co-fabricated a microactuator and a $150\text{-}\mu\text{m}$ -long, 150-nm -diameter single-crystal silicon fiber from one single-crystal silicon substrate to reduce the possibility of defects. The reduced test sample (silicon fiber) and a MEMS electrostatic tensile tester allowed measurements of strains in the piezoresistor of more than 1% . With the increased range of strain, the second and third order fit for piezoresistive coefficients were quantified more accurately. Additional studies of the effects of strain on semiconductor properties have been undertaken recently as interest in strained substrates increases [207, 237, 269, 279].

3.2.5 Noise in Piezoresistors

The power spectral density of $1/f$ noise, as its name implies, is inversely proportional to frequency. The origins of $1/f$ noise are still not fully understood and remain an active topic of research [280–291]. In particular, $1/f$ noise in piezoresistors is dependent on fabrication process parameters, such as implant dose and energy, and anneal parameters. A larger than one value of $1/f^n$ noise exponent can be a measure of conductor reliability. Excessive $1/f$ noise can indicate poor fabrication process quality [292, 293]. Researchers have optimized piezoresistive device performance accounting for $1/f$ noise [183, 294–296].

Despite many decades of research, the source of $1/f$ noise is still being debated [289]. McWhorter and Hooge proposed two opposing theories of $1/f$ noise. These views are currently the leading explanations for the origin of $1/f$ noise. The McWhorter model [297, 298] attributes the $1/f$ noise to surface factors while the

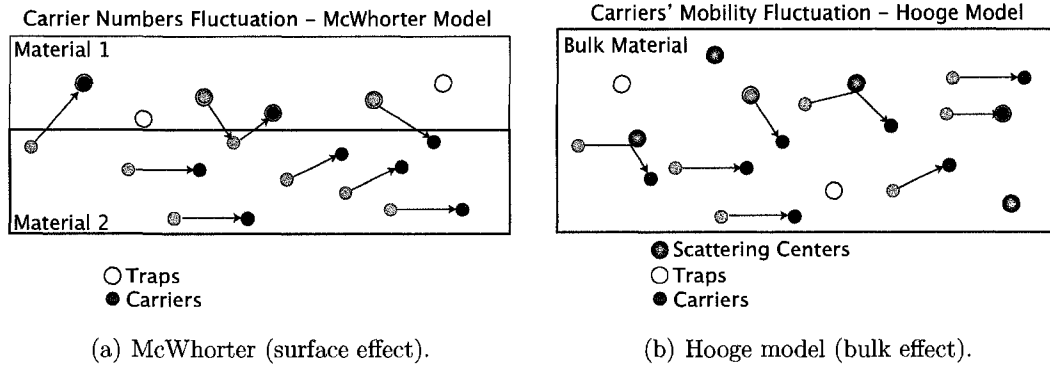


Figure 3.12: Carriers' number fluctuation based on McWhorter and Hooge models. Figure is courtesy of Paul Lim.

Hooge model [280, 290] implicates bulk defects (Figure 3.12).

Experiments show that $1/f$ noise is due to conductivity fluctuations in the resistor [290, 291]. Hooge showed that the $1/f$ low-frequency noise modulated the thermal noise even with no current flowing through the resistor [285]. This experiment demonstrates that $1/f$ noise is not current-generated. Current is only needed to transform the conductivity fluctuations into voltage fluctuations. Thermal and $1/f$ noise are fundamentally different. Thermal noise is a voltage noise; therefore it does not depend on the amount of current in the resistor. In contrast, $1/f$ noise is a conductivity noise; therefore the voltage noise is proportional to the current in the resistor.

Hooges empirical $1/f$ noise model, fit to observed data, predicts that the voltage noise density is given by:

$$V_{1/f} = V_b \sqrt{\frac{\alpha}{Nf}} \quad (3.5)$$

where f , N , and V_b , are frequency, total number of carriers in the resistor volume, and bias voltage across the resistor, respectively. A non-dimensional fitting parameter, α , is ascribed to the “quality of the lattice” and typically ranges from 10^{-3} down to 10^{-7} [183, 299].

Attempts to observe the lower limit of $1/f$, below which the spectrum flattens, have not been successful [290]. Measurements down to 3 μHz (or approximately 4

days per cycle) show a noise spectrum that is still $1/f$ [300]. Harley and Kenny [183] showed that resistors with different surface to volume ratios have the same $1/f$ noise characteristics, and $1/f$ noise scales with the resistor volume, consistent with Hooge's empirical equation [290].

Hooge [290] defines $1/f$ noise as only those spectra with a frequency exponent of 0.9–1.1. Noise with a different power spectral density and other frequency exponents, sometimes referred to as $1/f$ -like noise, is often confused with $1/f$ noise and is not predicted by the Hooge equation. According to Hooge [290], noise with a higher exponent, e.g. 1.5 or 2, indicates noise mechanisms other than mobility fluctuations that should not be considered $1/f$ noise. Abnormal $1/f$ noise characterization could give insights into piezoresistor reliability and failure analyses. For example, Neri found that the $1/f$ exponent is closer to 2 in metal traces that exhibit electromigration [301]. Vandamme [302] showed that excess $1/f$ noise in semiconductors can be attributed to small constrictions and current crowding. In some cases, devices with constriction resistance show third harmonics and nonlinearities in their output.

Current crowding theory also explains why polysilicon has higher $1/f$ noise than its crystalline counterpart [281]. At grain boundaries, small constrictions are present, thus reducing the total number of carriers (N) and effectively increasing the $1/f$ noise. Basically, $1/f$ voltage noise does increase linearly with the applied excitation. If the noise spectrum trends otherwise, then other mechanisms, such as current crowding, could be present. The noise floor of the experimental setup may be verified by reducing the applied excitation and observing only the thermal noise of the piezoresistor. Reducing the $1/f$ noise is important for low frequency applications. Chemical and bio-sensing applications based on displacement transduction require static and low frequency measurements and requires stability over time periods of tens of seconds to many hours. Lower $1/f$ -noise piezoresistors are required for these applications. The fabrication process parameters can be tailored to achieve low $1/f$ noise amplitude spectral densities. As suggested by Kandas model, low impurity doping is often used to achieve high sensitivity. However, this model underestimates sensitivity at high and low doping and leads to a device design that poorly trades-off sensitivity with noise for lower frequency applications. The empirical data of Tufte and Seltzer [179],

on the other hand, offer better guidance in these regimes. The advantages of high doping are lower noise and lower temperature coefficients for modest reduction of sensitivity. For example, if peak doping concentration, C_{peak} , decreases from 10^{19} cm^{-3} to 10^{17} cm^{-3} , the sensitivity increases by only 65% while the noise increases by a factor of ten. From (3.5), the $1/f$ noise can be reduced by increasing N and reducing α . The total number of carriers, N , depends on the piezoresistor volume and the impurity implant dose. Vandamme [292] showed that α depends on crystal lattice perfection, which increases with higher temperature anneals and longer anneal times. Annealing improves crystal lattice quality. Mallon et al. [299] extended the work of Harley and Kenny [183], showing that long high temperature anneals can produce very low noise piezoresistors with very low values of α (Figure 3.13).

Figure 3.14 shows the typical $1/f$ noise of a piezoresistor. The horizontal straight line is the thermal noise of the resistor. For reference, a 1 k Ω resistor has $4\text{nV}/\sqrt{Hz}$ of noise; all other resistor values are easily referenced to this value. The thermal noise of a resistor is also an excellent source to calibrate and verify the measurement system [305]. The straight, sloped line is the $1/f$ noise of the resistor, which depends on the applied bias voltage. If the resistor is unbiased the $1/f$ noise disappears, while the thermal noise remains. The $1/f$ noise is proportional to applied bias voltage with proportionality constant $\sqrt{\frac{\alpha}{Nf}}$. The total noise is the sum of thermal and $1/f$ noise. Since the noise sources are uncorrelated they are additive in the root mean squared fashion as,

$$V_{noise,total} = \sqrt{V_{thermal}^2 + V_{1/f}^2}. \quad (3.6)$$

3.3 Note and Acknowledgement

The content of this chapter is part of a paper, “Review: Semiconductor Piezoresistance for Microsystems,” which will be published in the *Proceedings of the IEEE* in 2009. I would like to thank my co-authors: Woo-Tae Park, Joseph Mallon, Jr., Ali Rastegar, and Beth Pruitt for their equal contributions in writing the paper.

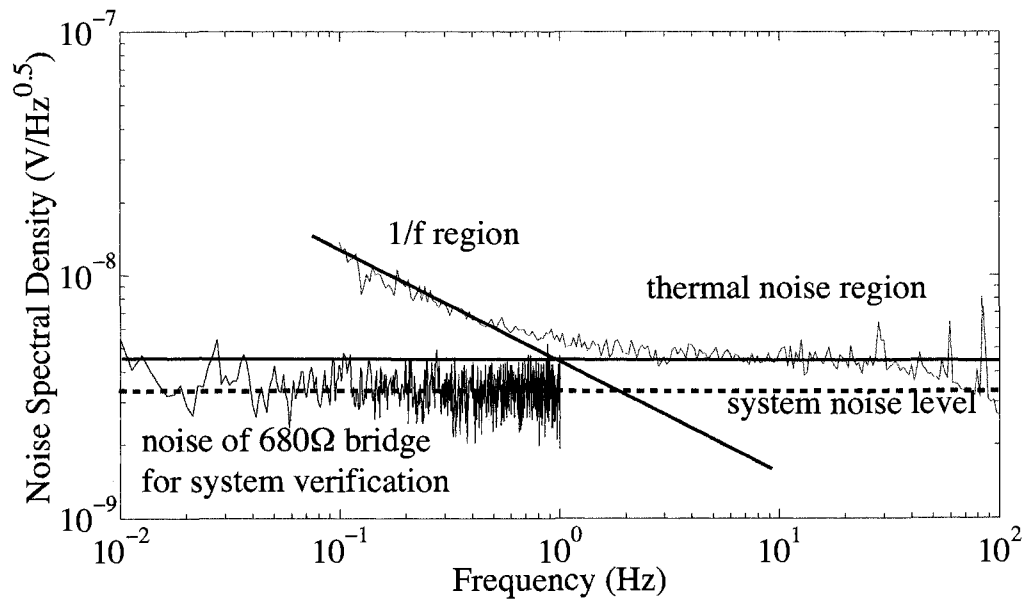


Figure 3.14: Typical noise curve of a full-bridged piezoresistor. The sloped solid line is the total noise dominated by $1/f$ -noise component, while the horizontal solid line is the total noise dominated by thermal-noise component. The $1/f$ noise corner frequency is the frequency at which the thermal noise is equal to the $1/f$ noise. In this noise spectrum, the corner frequency is ~ 1 Hz. The horizontal dashed line is the measurement system noise level, which is verified with a 680Ω resistor from 0.01 Hz. For clarity, system noise is not shown above 1 Hz. The noise is measured using modulation-demodulation technique [299]. The roll-off above 60 Hz is due to system bandwidth. Source: Mallon et al. [299]; © 2008 American Institute of Physics; reproduced with permission.

Chapter 4

Sensor Design and Fabrication

This chapter presents the design and the fabrication process of the floating-element piezoresistive shear stress sensors using oblique-angle ion-implantation technique.

4.1 Design

As discussed in Section 1.1.2, fluid flow in a coral reef environment is complex. Surface gravity waves superimposed on a turbulent flow significantly change the characteristics of the flow, therefore a priori knowledge of the flow is difficult to obtain. The direct technique is required to measure shear stress in the coral reef environment.

In this work, a floating element-based sensor was chosen over a fence sensor to minimize flow disturbance. Piezoresistive transduction scheme was chosen over the optical and capacitive techniques due to its relatively simple fabrication process, less complex circuitry, and less power requirement. The design consisted of a square floating element suspended by four tethers with square cross sections (Figure 4.1). Four piezoresistors were formed using the ion implantation technique. Each of these piezoresistors was placed on the surface of a tether to detect the tether's (and the plate element's) deflection. Two piezoresistors were formed using the normal ion implantation technique on the top surface of two tethers, while two other piezoresistors were formed using the oblique-angle ion implantation technique on the sidewall of the other two tethers. The two top piezoresistors were placed at the center of the

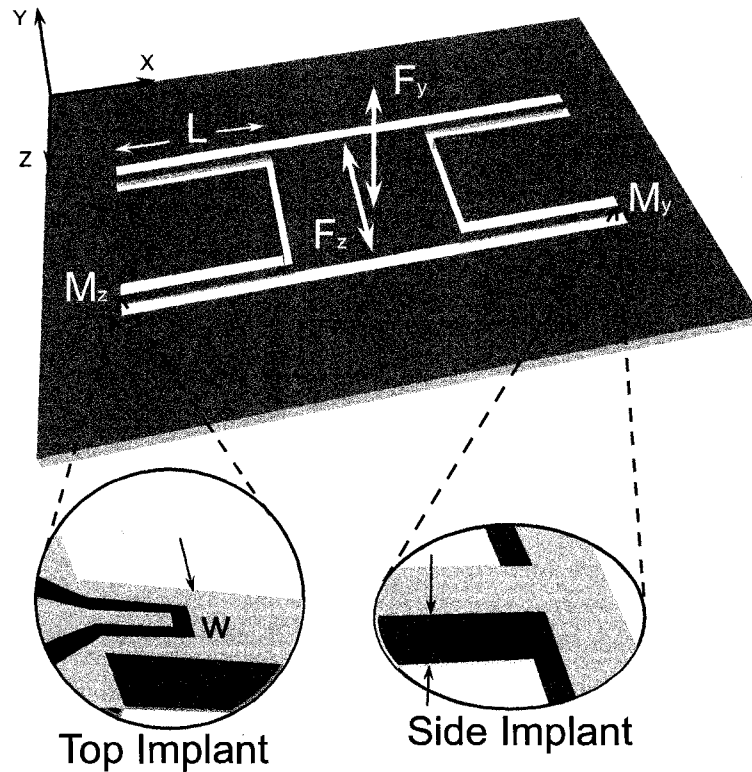


Figure 4.1: Piezoresistive floating element shear stress sensor. Two piezoresistors were formed on the top surface of two tethers using the normal ion-implantation technique and two piezoresistors were formed on the sidewall of the other two tethers using an oblique-angle ion-implantation technique.

top surface so that they were sensitive only to out-of-plane deflection of the tethers (and the plate element). The two sidewall piezoresistors were placed covering the whole width of the tethers so that they were sensitive only to in-plane deflection of the tethers (and the plate element).

4.1.1 Plate Element and Tethers

Each tether was modeled as a fixed-guided beam, i.e. fixed at one end to the substrate and guided at the other end by a quarter of the square plate element (Figure 4.2). From beam mechanics, the bending moments acting on both ends of each tether

(M_{guided} and M_{fixed}) was calculated using

$$M_{guided} = \frac{FL}{2} + \frac{fL^2}{6} \quad (4.1a)$$

$$M_{fixed} = \frac{FL}{2} + \frac{fL^2}{3} \quad (4.1b)$$

where F was the resultant fluid shear force acting on the top surface of $1/4$ of the plate element, f was the resultant fluid shear force acting on the top surface of a single tether, and L was the length of the tether.

The bending stress at both ends of the tether (σ_{guided} and σ_{fixed}) were calculated using

$$\sigma_{guided} = \frac{M_{guided}y}{I} \quad (4.2a)$$

$$\sigma_{fixed} = \frac{M_{fixed}y}{I} \quad (4.2b)$$

where y was the perpendicular distance from the tether neutral axis and I was the tether area moment of inertia about the neutral axis of the tether (Figure 4.3). Finally, the relative change in resistance ($\frac{\Delta R}{R}$) due to σ in (4.2) was derived from (3.4) and shown by

$$\frac{\Delta R}{R} = \pi_l \sigma \quad (4.3)$$

where π_l was the longitudinal piezoresistive coefficient.

Since the bending stress at the fixed end was larger than that at the guided end (from (4.1) and (4.2)), the piezoresistors were all formed at the fixed end to maximize for sensitivity. Moreover, the piezoresistors were oriented along the $\langle 110 \rangle$ direction of (100) p-type (boron-doped) silicon to achieve the maximum theoretical value for the longitudinal piezoresistive coefficient, π_l ($\sim 71 \times 10^{-11} \text{ Pa}^{-1}$) (Figure 3.8(a)) [178].

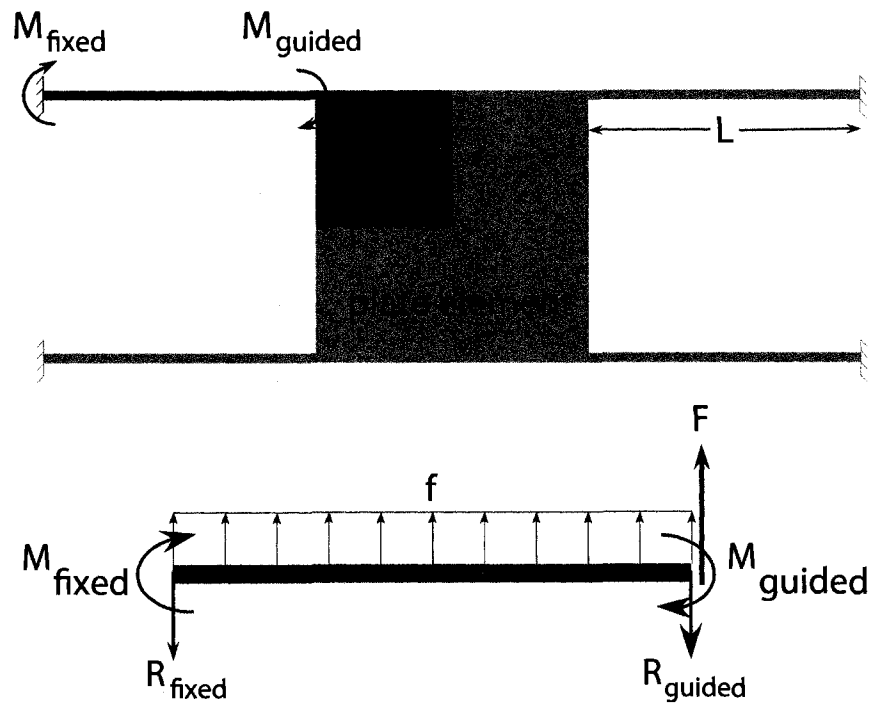


Figure 4.2: Each tether was modeled as a fixed-guided beam. The fixed end was anchored to the silicon substrate while the guided end was anchored to $1/4$ of the plate element. F was the resultant fluid shear force acting on the top surface of $1/4$ of the plate element, f was the resultant fluid shear force acting on the top surface of a single tether, and L was the length of the tether. M_{guided} and M_{fixed} were bending moments, while R_{fixed} and R_{guided} were reaction forces at both end of a tether.

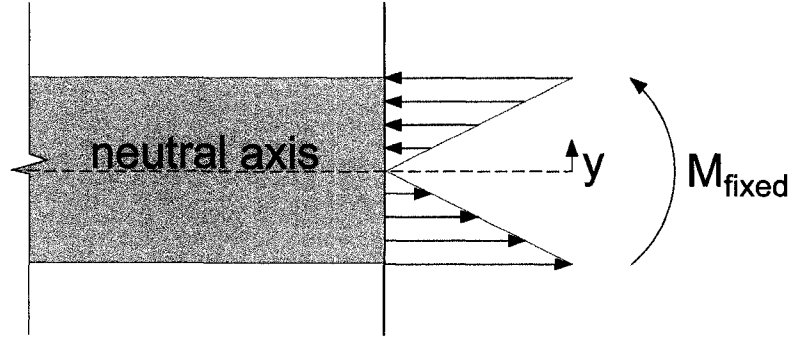


Figure 4.3: Cross section of a tether. The neutral axis and the bending stress are shown by the dashed line and horizontal arrows, respectively. Figure is courtesy of Stephanie Gunawan.

However, this value had to be adjusted to take into account the dependence of π_t on doping concentrations in the piezoresistors (Figure 3.10(a)) [178].

Each tether acted as a spring and the sensor was modeled as a mass suspended by four springs in parallel. An equivalent in-plane spring constant of the sensor, k_s , was derived from the Euler-Bernoulli beam theory and expressed by

$$k_s = \frac{96EI \left(\frac{A_p}{4} + A_t \right)}{L^3 \left(\frac{A_p}{2} + A_t \right)} \quad (4.4)$$

where E was the Young's modulus of the substrate, I was the area moment of inertia, A_p was the area of the top surface of the plate element, and A_t was the area of the top surface of the tether.

4.1.2 Gap Size

The presence of gaps between the floating element structure and the substrate was necessary to allow deflection of the tethers and displacement of the floating element. The gap size also limited the maximum displacement of the floating element, thus limiting the maximum measurable shear stress. Larger gaps were desirable to increase the upper limit of the measurement range. The drawback was that fluid flowed

through the gap and underneath the floating element, which resulted in additional force components acting on the plate element (Figure 2.8). Moreover, the difference in the velocity of fluid flowing above and underneath the floating element resulted in a pressure difference between the top and the bottom surfaces of the plate element. This pressure difference resulted in a net normal force, which in turn, created a misalignment between the floating element and the substrate surfaces. In underwater applications, especially when operated in seawater, larger gap sizes also increased the chance of particles getting into the gaps, thus blocking the movement of the floating element.

Allen performed an experimental study of error sources in skin-friction balance (floating element) measurements [102]. The test was done in a thick turbulent boundary layer (~ 7.6 cm) on a sidewall of a large supersonic wind tunnel at NASA Langley Research Center and at a free-stream Mach number of 2.19. The Reynolds number, calculated based on momentum thickness, was 1.62×10^4 and the diameter of the balance was 12.7 cm. The test parameters included were the element's vertical misalignment, gap size, and Reynolds number. The three forces analyzed in the experiment were friction force, lip force¹, and the normal pressure force. In reality, these forces were difficult to distinguish. Allen [101, 102] found that:

1. At zero protrusion, i.e. the device was flushed with the surrounding test section, the effect of gap was negligible.
2. Small protrusion errors were negligible in thick boundary layers, but important in thin boundary layer experiments. The experiment shows that the balance was much more sensitive to protrusion errors at the smaller gap sizes.
3. For the same gap size, small amount of positive and negative protrusions were equally damaging to the balance.

In underwater applications, zero protrusion is difficult to achieve due to the buoyancy force. The only way zero protrusion can be achieved in underwater applications

¹the force component acting on the thickness of the plate element due to pressure difference along the length of the channel

is by balancing the buoyancy force with the thin film stress on the tethers' surface, which is a difficult task given the uncertainties in the fabrication process.

Note that Allen's experiment was done in a supersonic airflow and using a macro-scale balance (~ 5 cm). The applicability of his empirical data to microfabricated sensors for underwater application, at low Reynolds numbers is not known, thus gap size effects is studied in this work by varying the gap size (5, 10, 15, and 20 μm).

4.1.3 Piezoresistors: TSUPREM-IV Simulations

As discussed in Chapter 3, early studies of piezoresistance, both experimental [179, 267, 268] and theoretical [178], have shown that the longitudinal piezoresistive coefficient, π_l , was also dependent on the doping concentration. At higher concentrations (above 10^{17} cm^{-3}), π_l decreased with increasing concentration (Figure 3.10(a)) [178]. Kanda [178] defined the piezoresistance factor, $P(N, T)$, as the ratio between the actual value of the piezoresistive coefficient at concentration N and its maximum value. Harley and Kenny compared a fit of available room-temperature experimental data for piezoresistive coefficients in the literature [179, 267, 268] to theoretical predictions from Kanda [178] at room temperature (Figure 3.9) [183]. Some discrepancy was observed, as Kanda's curve underpredicted experimentally observed π_l at higher concentrations. A straight line fit by Harley and Kenny [183] on a semilog plot of the experimental data was expressed by

$$P(p) = \log \left(\frac{b}{p} \right)^a \quad (4.5)$$

where $a = 0.2014$ and $b = 1.53 \times 10^{22}$ cm^{-3} . In this work, the longitudinal piezoresistive coefficient, π_l , was adjusted by multiplying the piezoresistance factor, $P(p)$, with its maximum value ($\sim 71 \times 10^{-11}$ Pa^{-1}) for p-type piezoresistor in (1 0 0) silicon along the $\langle 110 \rangle$ directions at room temperature).

TSUPREM-4 was used to simulate to find the dopant profile, and then adjust π_l accordingly. TSUPREM-4 [239] is a computer program that simulates the processing steps used in the manufacturing of silicon Integrated Circuits or MEMS devices,

e.g. ion implantation, oxidation/diffusion, and etching processes during the fabrication of the piezoresistors in this work. One dimensional simulation was done in the direction normal to the silicon surface. The depth of analysis used was 12 μm , which was the maximum plate thickness, with spacing interpolation from top to bottom. A denser grid was created near the wafer surface to yield more precise information in the area of steep dopant profiles. Simulated parameters of (1 0 0) wafer orientation, phosphorous background dopant, and initial resistivity of 18 $\Omega\text{-cm}$ represented the actual properties of the SOI device layer used in this work. The implant parameters for top and sidewall piezoresistors and conduction regions could be found in Table 4.1. The implant parameters were chosen to yield dopant concentration of $\sim 5 \times 10^{18} \text{ cm}^{-2}$ for the top and sidewall piezoresistors and $\sim 1 \times 10^{19} \text{ cm}^{-2}$ for the conducting regions. The tilt angle parameter in TSUPREM-4 was defined to be the angle of implant measured from the normal axis of the “implanted surface.” The sidewall implant was actually done at 20° from the normal axis of the wafer surface. However, since the wafer surface (the tether’s sidewall) was perpendicular to the implanted surface, therefore 70° was used as the tilt angle parameter in the TSUPREM-4 simulations (Figure 4.4). The top piezoresistor and conducting region implants were done at a 7° angle from the normal axis of the wafers’ surface to minimize ion-channeling. TSUPREM-4 Gaussian implant profiles and damage caused during ion implantation were incorporated in the simulation. The ion implantation process simulation also took into account amorphization, silicon atoms knocked out of lattice sites, interstitials produced when silicon atoms were displaced by implanted ions, and point defect recombination. The TSUPREM-4 “Full Method” of diffusion is chosen to simulate precisely damage due to ion implantation and oxidation enhanced diffusion. The resulting parameters of interests were material layers, metallurgical junction, electrical properties, such as sheet resistance, and plots of the dopant profiles/distributions. These parameters were solved at three different stages during the fabrication process, i.e. after ion implantation, after RTA anneal, and after oxidation of the final passivation layer (more discussion on this in Section 4.2).

Simulated dopant profile is shown in Figure 4.5. The peak doping concentration for the nominal dose of $4 \times 10^{15} \text{ cm}^{-2}$ was about $6.5 \times 10^{18} \text{ cm}^{-3}$. According to

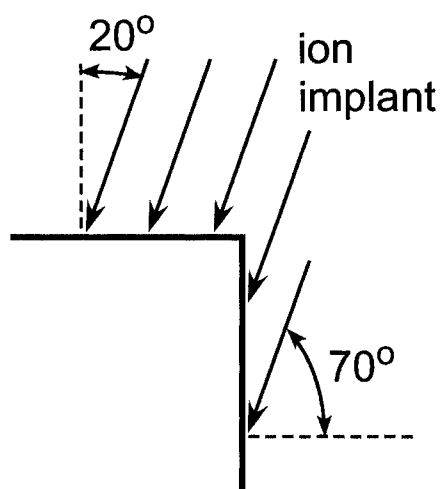


Figure 4.4: Illustration of angles used in TSUPREM-4 simulations. Although the sidewall implant was actually done at 20° from the normal axis of the wafer surface, 70° was used as the tilt angle parameter in the TSUPREM-4 simulations.

Table 4.1: The ion implantation process parameters for TSUPREM-4 simulations. The tilt angle was measured with respect to the implanted surface normal axis.

	Dopant Atom	Dose (cm^{-2})	Energy (keV)	Tilt Angle
Top Piezoresistors	boron	1×10^{15}	50	7°
Sidewall Piezoresistors	boron	4×10^{15}	40	70°
Conducting Regions	boron	1×10^{16}	50	7°

Harley's fit of the experimental data in the literature (4.5), this doping concentration corresponded to $P(p) = 0.68$ and an adjusted π_l of about $49 \times 10^{-11} \text{ Pa}^{-1}$. Using the adjusted π_l value and 4.1, 4.2, and 4.3, typical in-plane shear stress sensitivity of the side-wall piezoresistor was predicted to be 0.068 mV Pa^{-1} before amplification for a bridge bias voltage of 10 Volts in a Wheatstone-bridge configuration.

4.2 Fabrication

The fabrication process described in this section involves nine masks (lithography steps). Please refer to Section 1.2.2 for a brief review of the processes and terminology. In addition, please refer to Table A.1 in Appendix A for a summary of the process flow and Table D.1 in Appendix D for symbols of the chemical used in this process.

The fabrication process (Figure 4.6) started with 4" n-type (phosphorous-doped) double-polished (100) silicon-on-insulator (SOI) wafers. The typical resistivity of the device layer of the SOI wafers was $\sim 18\Omega\text{-cm}$. The device layer thickness ranged from 7-12 μm and determined the thickness of the tethers and the floating element. The nominal design had a device layer thickness of 10 μm . The handle layer and the buried oxide thicknesses were 300 and 0.5 μm , respectively. The wafers were first cleaned in a "piranha" solution (90% sulfuric acid and 10% hydrogen peroxide). Alignment marks, with a depth of about 2000 \AA were patterned on the wafers using an isotropic silicon etch. Next, about 250 \AA of thermal oxide was grown at 850°C in a wet environment (steam) for 13 minutes as a screening oxide for the subsequent ion implantation steps to minimize the damage on the silicon lattice. Next, two separate ion implantation steps formed the top piezoresistors and the conducting regions. The conducting regions were needed as intermediate conductors between the low-conducting regions (piezoresistors) and the very-conducting metals. As summarized in Table 4.1, both implants used boron atoms, accelerated at 50 keV of energy. The top piezoresistor dose was $1 \times 10^{15} \text{ cm}^{-2}$ and the conducting region dose was $1 \times 10^{16} \text{ cm}^{-2}$. After the implants, the screening oxide was etched away using a 6:1 Buffered Oxide Etch (BOE) solution, where BOE was composed of 34% ammonium fluoride, 7% hydrogen fluoride, and 59% water. Then, both implants were annealed using a Rapid Thermal

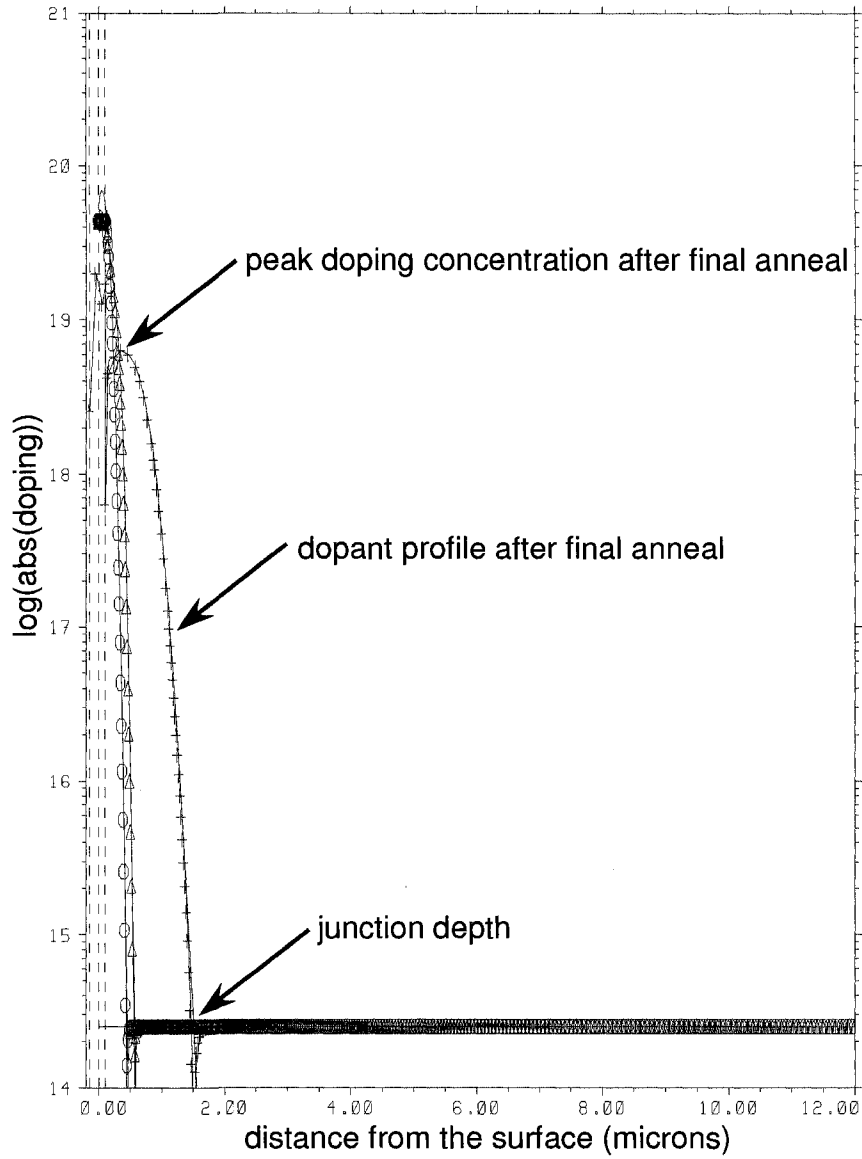


Figure 4.5: Typical TSUPREM-4 simulation output plot for Boron concentration vs. depth into the wafer. The simulation shown above was done for default values of 4×10^{15} , 40 keV, and 7° for dose, energy, and tilt angle, respectively.

Annealing (RTA) process at 1050°C for 75 seconds. This anneal step was needed to fix crystal-lattice damages due to the ion implantation processes. RTA was chosen over the conventional thermal annealing step to minimize the transient-enhanced diffusion (TED) process and further diffusion of the dopants (Section 3.2.3).

Next, about 1.1 μm of Low-Temperature Oxide (LTO) was deposited at 400°C for 1 hour using the LPCVD process in preparation of the side-wall implant. LTO and the silicon underneath were then etched to pattern the geometry of the sensor using anisotropic oxide plasma etch and Deep Reactive Ion Etch (DRIE), respectively. The buried oxide layer acted as an etch stop for the silicon etch. The etched trenches became the gap between the sensors and the silicon substrate. The wafers were hydrogen-annealed at 1000°C and 10 Torr for 5 minutes to smooth the sidewall from the resulting scallops due to DRIE process [306]. Figure 4.7 shows the sidewall roughness before and after the hydrogen anneal. The top surface was then covered with 10- μm thick photoresist (SPR220-7) and an opening near the root of each tether was patterned to allow for an angled ion implant at 20° from the normal axis of the wafer's surface. Boron, with a dose of $4 \times 10^{15} \text{ cm}^{-2}$, was implanted at 40 keV. Next, photoresist was stripped with the piranha solution and the LTO was etched using 6:1 BOE. The sidewall implant was then annealed using an RTA process at 1050°C for 75 seconds. A final passivation oxide of about 2100 Å was thermally grown at 1000°C for 30 minutes in a wet (steam) environment, followed by a post-oxidation inert anneal for 5 minutes to eliminate dangling bonds at the silicon-oxide interface. Next, the passivation oxide was patterned and etched using 6:1 BOE to open an electrical connection for aluminum to the conducting region. About 1 μm of 99%-aluminum/1%-silicon metal was sputtered, patterned, and etched using aluminum etch (72% phosphoric acid, 3% acetic acid, 3% nitric acid, and 12% water).

After the deposition and patterning of metal, on some of the wafers, a triplex layer of oxide-nitride-oxide was deposited as a passivation layer for the metal lines (more discussion on Section 6.1.2). The PECVD process was used to deposit 1300 Å of oxide layer, 7150 Å of nitride layer, and another 1300 Å of oxide layer. Next, these layers were patterned and etched using 6:1 BEO (oxide) and plasma etch (nitride) to open the bond pads and to remove these layers in the gaps between the

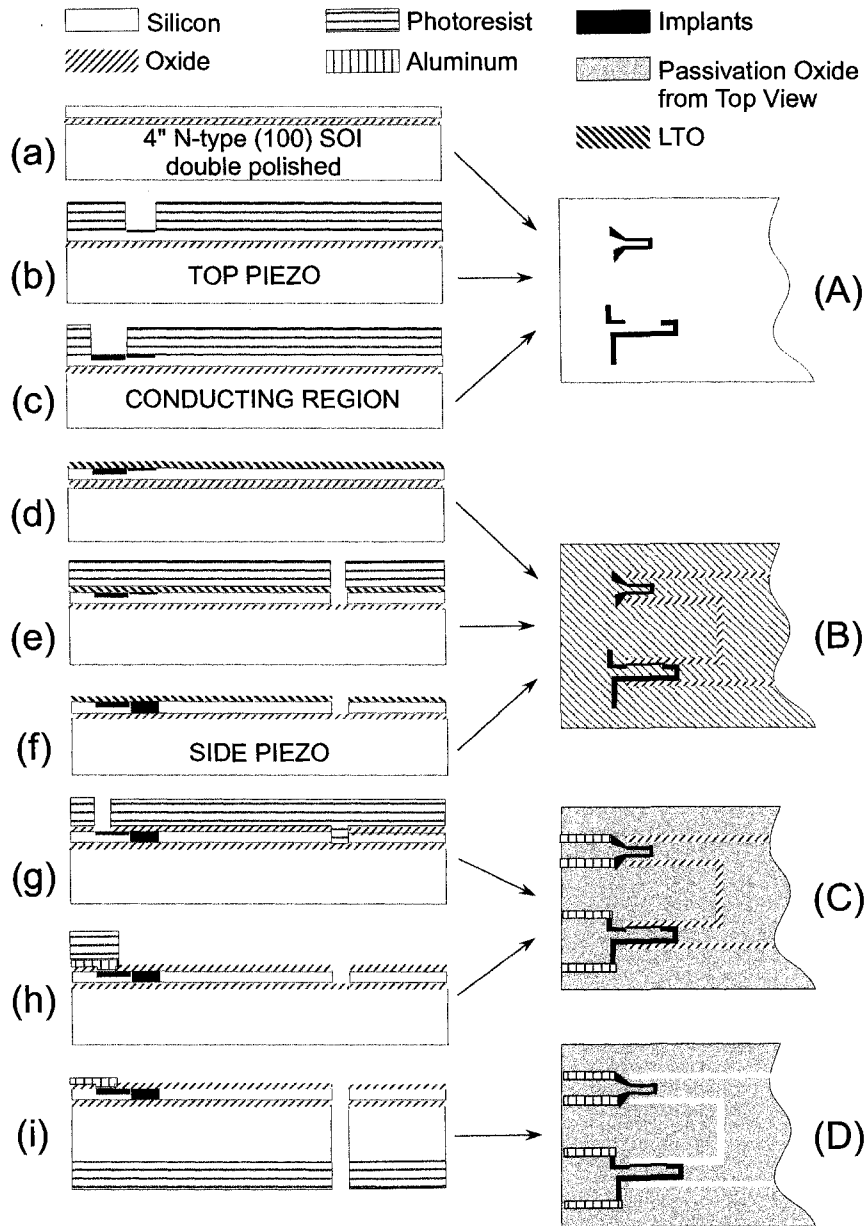


Figure 4.6: Shear stress sensor fabrication process. (a) Fabrication started with SOI wafer. (b, c, A) Top piezoresistors defined by boron implants. (d) Deposition of LTO. (e, f, B) Sensors defined by DRIE of trenches, silicon hydrogen anneal and sidewall implant came after trench etch. (g) LTO was stripped and passivation oxide was thermally grown, patterned, and etched. (h, C) Aluminum interconnects patterned. (i, D) Sensors released by backside DRIE.

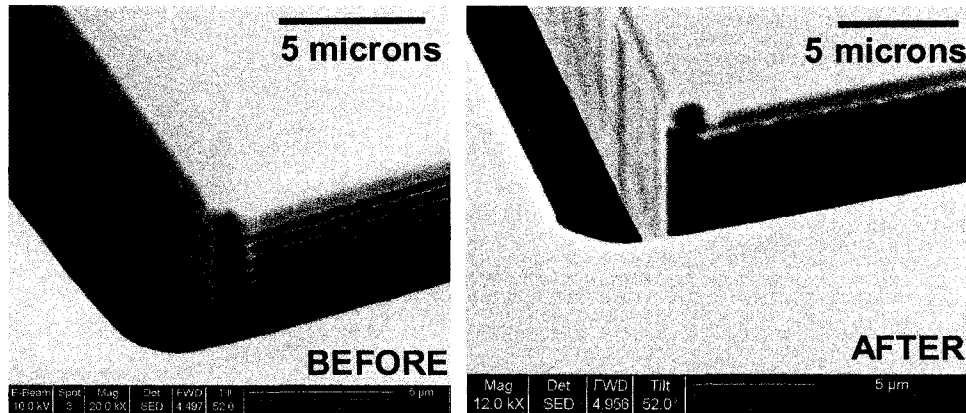


Figure 4.7: The sidewall roughness before and after hydrogen anneal.

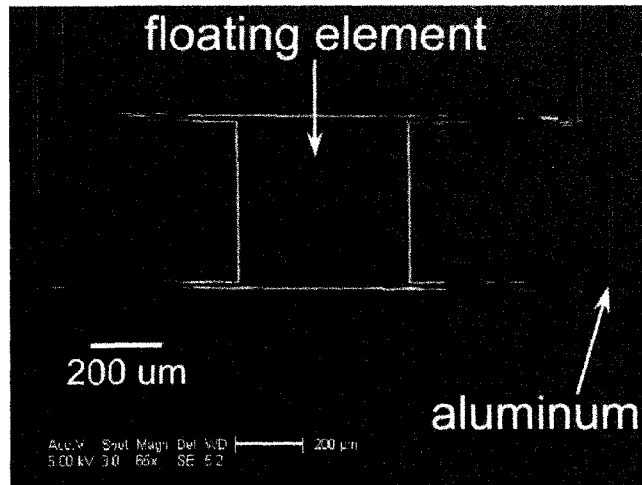
floating element and the substrate. The other wafers were passivated using parylene at the end of the fabrication steps (more discussion on Section 6.1.2).

For all the wafers, the sensors were then released from the backside using a DRIE process to etch the handle-layer silicon. Again, the buried oxide acted as an etch stop. Finally, the buried oxide was removed using 6:1 BOE and the wafers were treated to a forming gas (hydrogen) anneal at 400°C for 2 hours to reduce trapped charges due to incompletely oxidized silicon atom in the oxide, close to the silicon-oxide interface [88]. Figure 4.8 shows the Scanning Electron Microscopy (SEM) images of the released sensors.

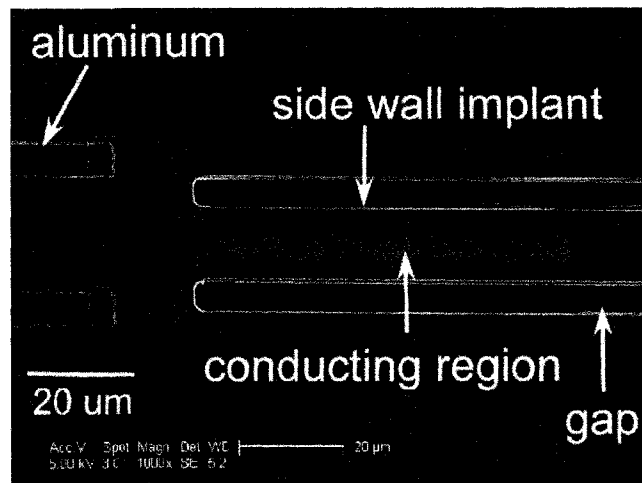
4.3 Note and Acknowledgement

The content of this chapter is part of

- “Design, Fabrication, and Characterization of Piezoresistive MEMS Shear Stress Sensors,” presented at the ASME International Mechanical Engineering Congress and Exposition in Orlando, FL in 2005 and included in the conference proceedings [307].
- “Design and characterization of microfabricated piezoresistive floating element-based shear stress sensors,” published in *Sensors and Actuators A* [308].



(a) SEM image of the whole sensor, 500- μm plate element.



(b) SEM image of the sidewall-implanted piezoresistor on a 15- μm wide tether.

Figure 4.8: SEM images of the finished microfabricated floating-element shear stress sensor.

Chapter 5

Sensor Characterization

This chapter presents the experimental setups and characterization results of the oblique-angle ion-implanted shear stress sensors. The characterization process includes in-plane and out-of-plane sensitivities of the sensor, temperature coefficient of resistivity, and noise. Uncertainty analysis because of the variation in the fabrication process is also presented.

5.1 Sensitivities

Sensitivity calibration is necessary to extract useful and correct information (magnitude and direction) of shear stress acting on a sensor. As described in section 4.1, each sensor is sensitive to both lateral and in-plane forces. Therefore, each sensor needs to be calibrated in both directions. A piezoresistive shear stress sensor sensitivity is the ratio of its piezoresistor output signal (typically, Volts) and the magnitude of shear stress acting on it (Pascal). The output signal can sometimes be expressed as the ratio of the change in resistance under strain and the value of the unstrained resistance, $\frac{\Delta R}{R}$.

5.1.1 In-plane Sensitivity

In-plane sensitivity is the most important parameter for a shear stress sensor. In this experiment, the tip of a microfabricated piezoresistive cantilever force sensor was used to push on the floating element of a shear stress sensor (Figure 5.1). The cantilever force sensor was calibrated using a benchmark technique. The voltage output of the cantilever, V_c is related to its tip deflection, x_c . Since the spring constant of the cantilever, k_c is also known from its calibration, the force felt by the cantilever, $F_{cantilever}$ can be computed using

$$F_c = k_c x_c. \quad (5.1)$$

From Newton's Third Law of Motion, the force felt by the cantilever, F_c is the same as the force felt by the floating element, F_s . This force is similar to the resultant shear force felt by the plate element due to shear stress, τ . In other words, shear force acting on the floating element can be computed using

$$F_s = \frac{\tau}{A_s} \quad (5.2)$$

where A_s is the area of the floating element.

By monitoring the output voltage from the piezoresistor on the cantilever, the shear force (or shear stress) acting on the element can be computed. Finally, by monitoring the output voltage from the piezoresistor on the shear stress sensor, we can determine the sensor sensitivity.

Experimental Setup

A microfabricated piezoresistive silicon cantilever force sensor (Figure 5.2) with a length, width, and thickness of 6000, 400, and 15 μm , respectively, was calibrated using the Laser Doppler Vibrometry (LDV) and resonance excitation technique (Figure 5.3). The cantilever and a surface mount board were glued onto a microscope slide using a five-minute epoxy. The microscope slide was mounted on a Jodon EV-30 piezoelectric shaker using a double-sided tape.

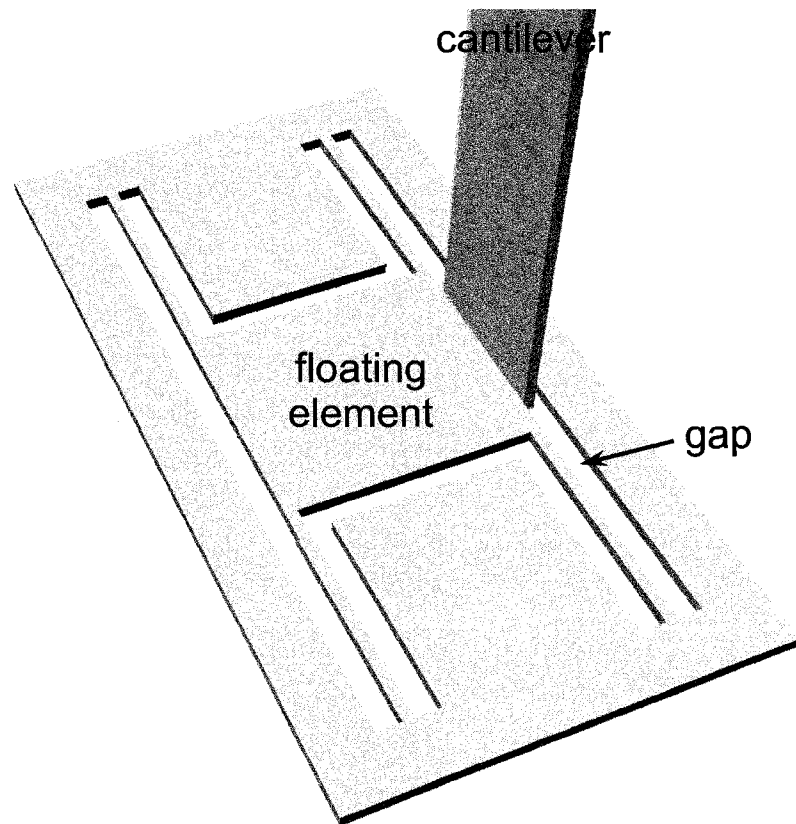


Figure 5.1: The experimental setup for in-plane sensitivity characterization. A tip of a microfabricated piezoresistive cantilever force sensor was used to push on the floating element. The thickness of the cantilever tip and the gap size were $15\ \mu\text{m}$ and $20\ \mu\text{m}$, respectively. Figure is courtesy of Stephanie Gunawan.

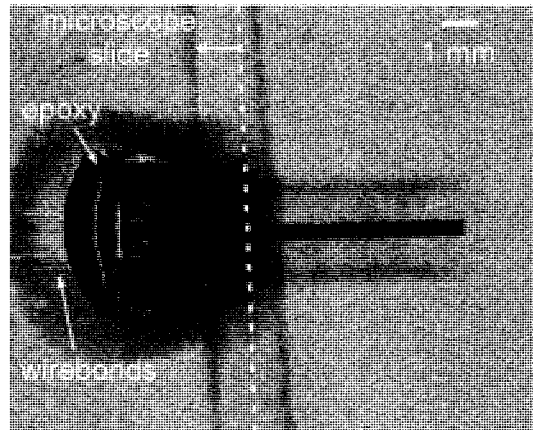


Figure 5.2: Microfabricated piezoresistive silicon cantilever force sensor. The length (l_c), width (w_c), and the thickness (t_c) of the cantilever were 6000, 400, 15 μm , respectively.

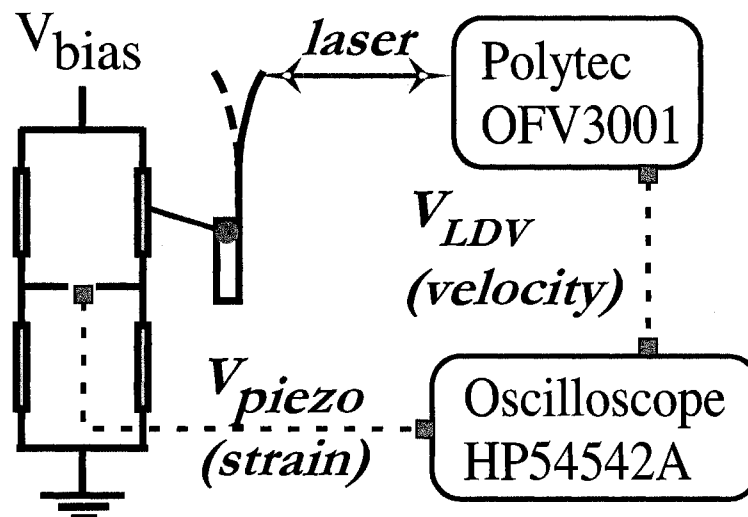


Figure 5.3: Laser Doppler Velocimetry and resonance excitation technique to calibrate the microfabricated piezoresistive cantilever force sensor. The cantilever was mounted on a Jodon EV-30 piezoelectric shaker and driven by a signal from HP89441A Vector Signal Analyzer (both are not shown here).

Initially, the shaker was driven with white noise signal with frequency ranging from 500 Hz to 50 kHz, amplified at fixed gain of $100\times$ by a Krohn-Hite 7500 Widebands Power Amplifier. The shaker was driven by a white noise input. A Polytec OFV3001 Laser Doppler Vibrometer was used to extract the average out-of-plane velocity of the cantilever tip. The LDV output was connected to an HP89441A Vector Signal Analyzer and its velocity filter was set to $5 \text{ mm sec}^{-1} \text{ V}^{-1}$. The frequency spectra on the analyzer showed peaks of the modes of vibration. The first resonant frequency was found to be 573 Hz. Next, the shaker was driven with a sinusoidal signal at the resonant frequency and the response from the vibrometer and the Wheatstone bridge (with $1000\times$ gain from AD622 amplifier) were captured with a HP54542A oscilloscope. The LDV measured the velocity of the tip of the cantilever, which was converted into displacement by integrating the signal. The theoretical spring constant, k_c , can be calculated from the beam theory:

$$k_c = \frac{Ew_c t_c^3}{4l_c^3} \quad (5.3)$$

where E , w_c , t_c , l_c are the Young's modulus of silicon, the width, the thickness, and the length of the cantilever, respectively. The tip displacement, x_c , was then converted into input force by multiplication with the theoretical spring constant (5.1), which was calculated to be 0.25 N m^{-1} . The Wheatstone bridge measured the strain at the root of the cantilever. The cantilever sensitivity was found to be 41.57 kV N^{-1} , with $200\times$ bridge output amplification. For details of the cantilever force sensor and its calibration technique (LDV), please refer to Pruitt et al. [309, 310].

A nominal-design shear stress sensor, with floating element size of $500 \mu\text{m} \times 500 \mu\text{m}$ and tether width (and thickness) of $10\text{-}\mu\text{m}$, was also mounted on a separate microscope slide using a five-minute epoxy. Theoretical spring constant of the shear stress sensor, k_s can be computed using beam theory by treating the four tethers as four springs in parallel and modeling each of the tether as a fixed-guided beam. The resultant spring constant of the shear stress sensor is calculated to be 52.5 N m^{-1} (4.4).

The cantilever was mounted on a piezoactuator stage vertically, with its tip pointing down, while the shear stress sensor is mounted on a glass on top of an inverted microscope horizontally and perpendicular to the cantilever (Figure 5.4). The tip of the cantilever was inserted from the top into the gap of one of the sensors with larger gap size, 20 μm (Figure 5.5(a)). The image in this figure was taken using a Leica DM IRB 20 \times inverted microscope.

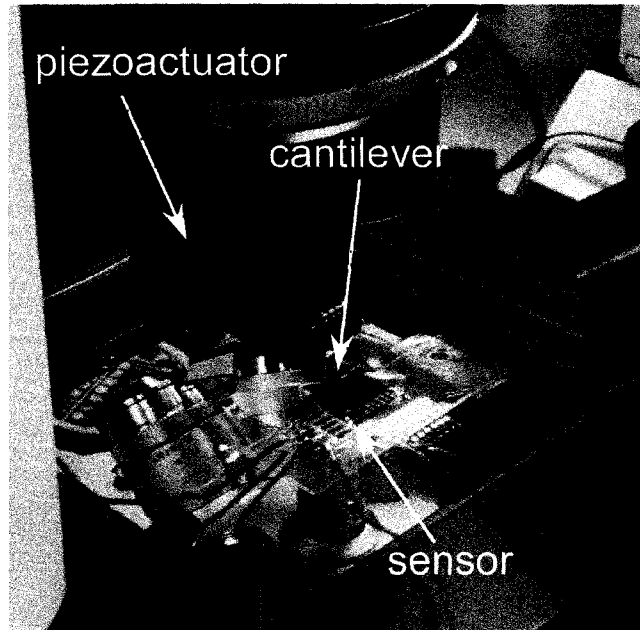
The cantilever was then moved to the left (Figure 5.5(a)) by a piezoactuator (PIHera P622.Z) with control electronics (E-505) in increments of 1 μm from 0 to 200 μm . The cantilever pushed against the shear sensor plate element. The shear sensor was $\sim 210\times$ stiffer than the cantilever ($k_s \gg k_c$). Conceptually, we modeled this as two springs in series (Figure 5.5(b)). Since the force applied by the cantilever, F_c , was the same as the force felt by the shear stress sensor, F_s , the relationship between the spring constants and the displacements can be expressed by

$$\frac{k_c}{k_s} = \frac{x_s}{x_c} \quad (5.4)$$

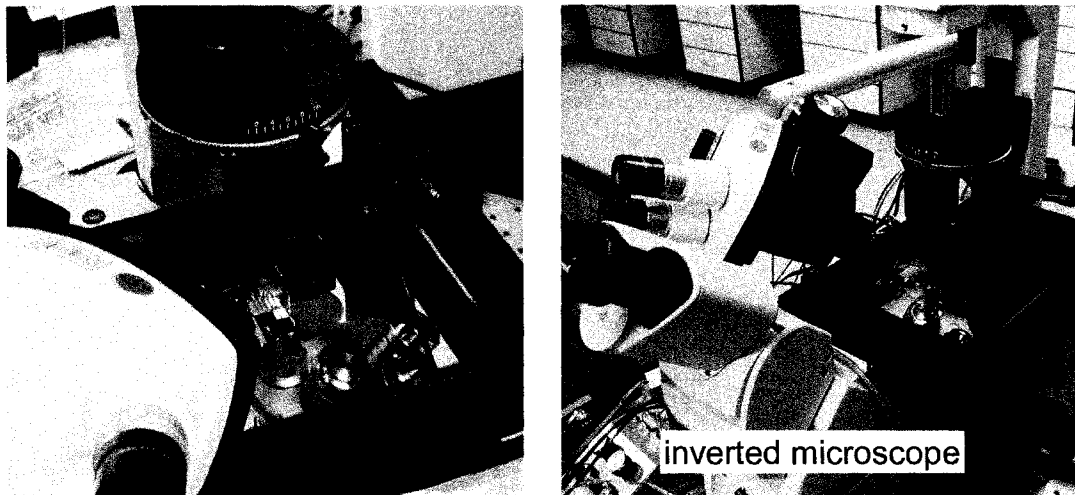
where x_c is the displacement of the tip of the cantilever and x_s is the displacement of the shear stress sensor. The piezoelectric-based actuator input displacement, x_{input} , is defined by

$$x_{input} = x_c + x_s. \quad (5.5)$$

Thus if we assume a 200- μm total displacement at the base of the cantilever, 99.53% of deflection was accommodated by the force sensing cantilever. Therefore, the applied displacement was assumed to be accommodated completely by deflection of the cantilever and moving the cantilever a known distance would then apply a well characterized force to the shear sensor in the in-plane direction. However, uncertainty in applied force due to uncertainty in k_c is 11.2%. Some error due to torsion of the cantilever was noted at the onset of loading as one corner always contacted first. Resistance change proportional to stress in the piezoresistors was conditioned with a Wheatstone bridge and the voltage outputs from the shear stress sensor piezoresistors and the cantilever force sensor were recorded using National Instruments LabVIEW.

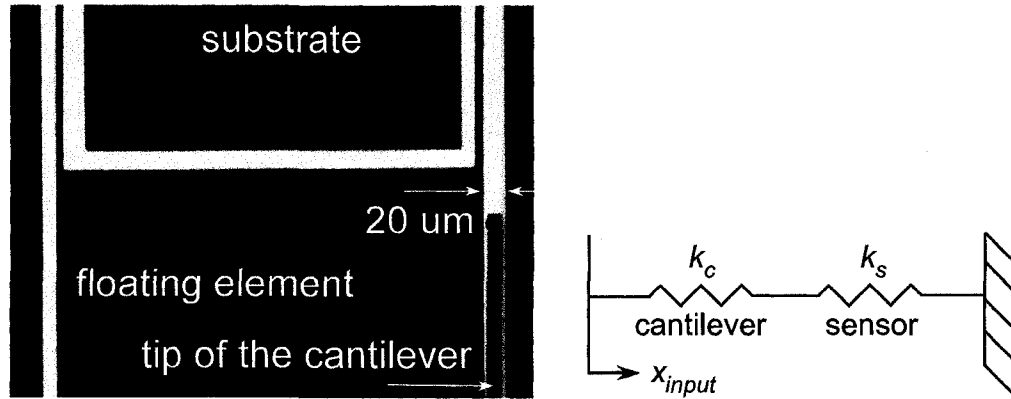


(a) The cantilever force sensor was mounted on a piezoactuator stage and the shear stress sensor was mounted on top of an inverted microscope. They were mounted perpendicular to each other



(b) Other views of the setup.

Figure 5.4: Experimental setup for the in-plane sensitivity calibration of the shear stress sensor.



(a) Inverted microscope view of the cantilever-sensor system. The image was taken using a Leica DM IRB 20 \times inverted microscope. The white regions are the gaps (20 μm) and the rectangular feature in the right gap is the cantilever (thickness of 15 μm). Only half of the sensor plate element and two tethers are visible in this figure.

(b) Lumped-parameter model of the cantilever-sensor system.

Figure 5.5: Inverted microscope view and lumped parameter model of the cantilever-sensor system.

Results and Uncertainty Analysis

Force was inferred from the cantilever voltage output. Sensitivity to shear stress was then inferred from data as shown in Figure 5.6. The elapsed time for each 1 μm piezoactuator step was 0.5 seconds; however, data were taken over the last 0.1 seconds to reduce the effects of ringing. Data taken at 2400 Hertz for 0.1 seconds were averaged to give a single data point for each piezoactuator step. In-plane force sensitivity was calculated to be $\sim 50 \text{ mV } \mu\text{N}^{-1}$. The crosstalk of the top-implant piezoresistor to in-plane force was quite low, $\sim 0.8 \text{ mV } \mu\text{N}^{-1}$, confirming low sensitivity to off-axis loads. The large noise component was likely due to low mechanical stiffness (ringing) in the experimental setup, slippage of the cantilever to plate contact during the test, uncontrolled light, and electromagnetic noise sources during the tests. These problems resulted in hysteresis and nonlinearity in the measurements (Figure 5.7).

Figure 5.8 shows the trendlines and repeatability of five sequential measurements of shear sensor output over the piezoelectric-based actuator displacement range. The

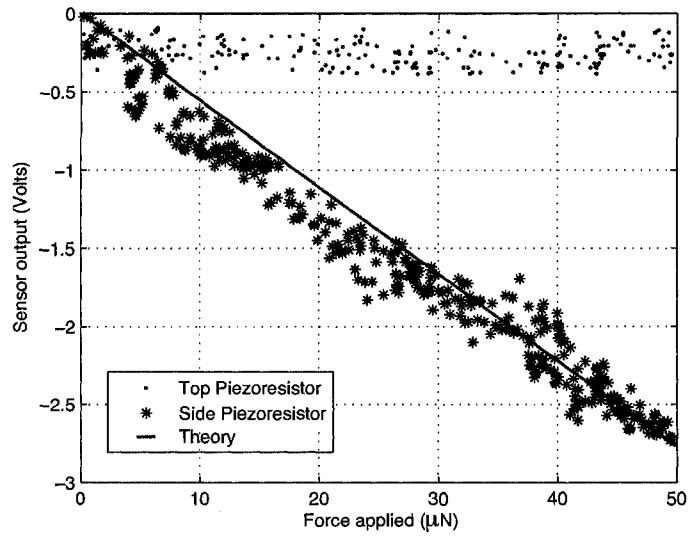


Figure 5.6: In-plane and out-of-plane sensitivities to in-plane motion (based on the slopes) are $50.3 \text{ mV } \mu\text{N}^{-1}$ (0.063 mV Pa^{-1}) and $0.8 \text{ mV } \mu\text{N}^{-1}$ (0.001 mV Pa^{-1}), respectively.

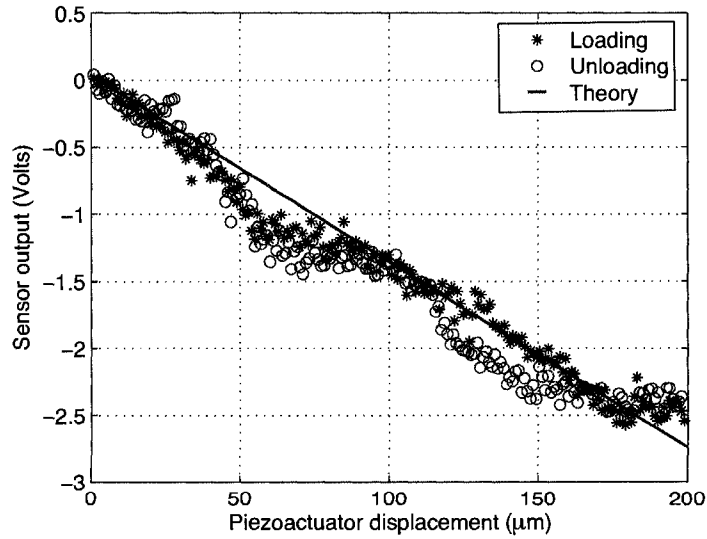


Figure 5.7: Some hysteresis and non-linearity in the measurements is apparent in this load/unload data.

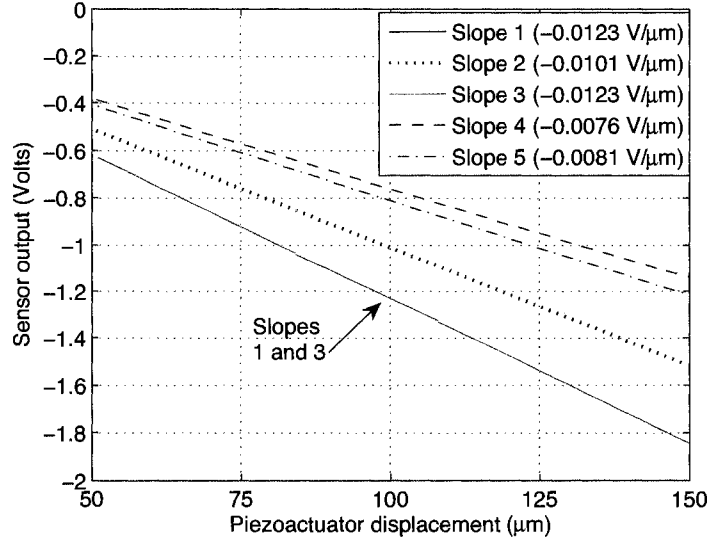


Figure 5.8: Repeatability of the five sequential measurements. The trendlines were normalized due to DC offsets caused by an unbalanced bridge at the beginning of the runs. The standard error of the slope was found to be $0.0022 \text{ V } \mu\text{m}^{-1}$.

trendlines were generated based on the data from 50 to 150 μm of piezoactuator displacement. This was done to minimize the effect of imperfect contact between the cantilever and the plate element in the first 50 μm and to satisfy small angle assumptions of the cantilever at large deflections. The average sensitivity of the shear sensor to input displacement was $0.0101 \text{ V } \mu\text{m}^{-1}$ with a standard error of slope of $0.0022 \text{ V } \mu\text{m}^{-1}$. Therefore, the sensitivity of the sidewall piezoresistor to shear stress translated to $0.052 \pm 0.011 \text{ mV Pa}^{-1}$ (before any amplification). The theoretical value was found from beam mechanics and piezoresistance equations with the adjusted π_t value (4.1, 4.2, 4.3, and 4.5) and predicted to be 0.068 mV Pa^{-1} .

We used TSUPREM-4 simulations as before to investigate the effect of fabrication process tolerance on the discrepancy between the theoretical and experimental values for the in-plane sensitivity. The ion-implantation simulations were done by varying the dose ($1 \times 10^{15} - 7 \times 10^{15} \text{ cm}^{-2}$), energy (40 – 60 keV), and the tilt angle (60 – 80°) from the normal axis of silicon surface. These were worst case variations of the default

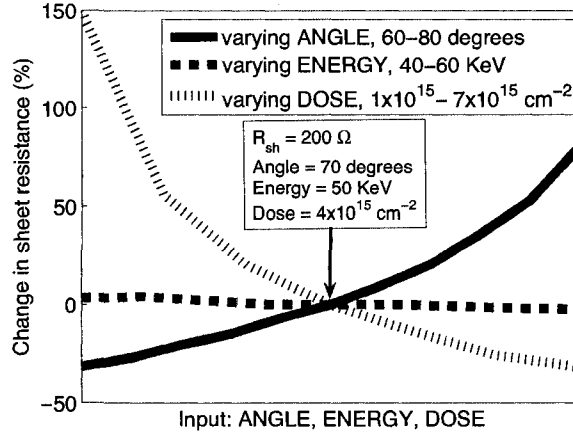
values of $1 \times 10^{15} \text{ cm}^{-2}$, 50 keV, and 70° for dose, energy, and tilt angle, respectively. The dopant profiles after ion implantation, after RTA anneal, and after oxidation of the passivation layer were plotted again. Figure 5.9 shows the summary of results of the simulations after oxidation of the passivation layer (final diffusion process). Variations in implant dose contributed the most offset in peak doping concentration, and thus the targeted sheet resistance, R_{sh} , (up to 150%) and sensitivity (up to 16%). Table 5.1 shows the range of $P(p)$ variations with respect to input parameters of tilt angle, energy, and dose.

The sensitivity of the sidewall implant could also be affected by dimensional variations due to other fabrication process errors, such as imperfection in lithography and etching ($\pm 1\mu\text{m}$), and wafers specifications tolerance. The device layer thickness, which defined the thickness of the plate element and the tethers, was quoted by the manufacturer to have $\pm 1\mu\text{m}$ tolerance. Table 5.2 shows the contribution of dimensional variations to the normalized change in resistance. Note that the normalized change in resistance was inversely proportional to the thickness and square of the width, while linearly proportional to the length of the tether for in-plane deflection of the tethers.

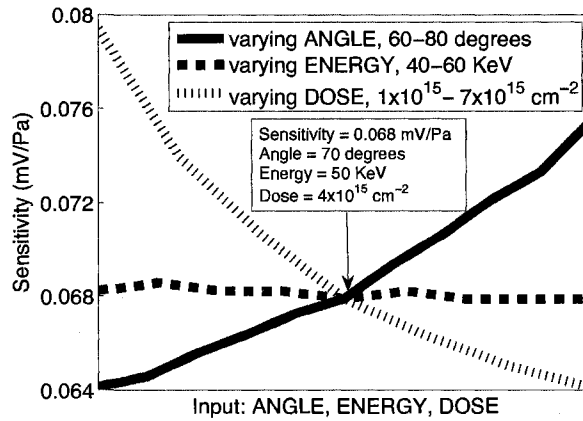
Theoretical calculations and experiments have been done in the past to determine the Youngs modulus (E) and other mechanical properties, e.g. Poisson's ratio, elasticity constants, and hardness of silicon [177, 311–313] for various crystal orientations. Youngs modulus of 160 GPa [311] for $[110]$ direction in a (100) silicon wafer, was used in the calculation of the predicted sensitivity. The uncertainty on k_s was calculated using

$$w_R = \left[\left(\frac{\partial R}{\partial x_1} w_1 \right)^2 + \left(\frac{\partial R}{\partial x_2} w_2 \right)^2 + \cdots + \left(\frac{\partial R}{\partial x_n} w_n \right)^2 \right]^{\frac{1}{2}} \quad (5.6)$$

where R was k_s , x was the independent variables on which k_s depend (Section 4.1.1), and w was uncertainties in the independent variables [314]. Given our process tolerances (Table 5.2) and discrepancies in reported values of E (measured and calculated varied by upwards of 10%), the uncertainty resulting uncertainty on k_s was 18.85%, which was in the order of other sources of variations in the experiment. For example,



(a) Change in sheet resistance with respect to varying angle, dose, and energy.



(b) Change in sensitivity with respect to varying angle, dose, and energy.

Figure 5.9: Results of the TSUPREM-4 simulations on the effect of implant parameters to the output of the piezoresistors.

Bhushan and Li [313] extracted estimates of moduli for bulk undoped silicon ranging from 179 to 202 GPa and as low as 62 GPa for heavily doped p⁺-type silicon.

Table 5.1: Range of peak concentration, $P(p)$, and sensitivity with respect to the input variations.

Input Range	Peak Concentration Range (cm^{-3})	$P(p)$	Sensitivity Range (mV Pa^{-1})
Tilt Angle ($40 - 60^\circ$)	$2.75 \times 10^{18} - 1 \times 10^{19}$	0.64 – 0.75	0.0640.075
Energy ($40 - 60 \text{ keV}$)	$6.0 \times 10^{18} - 6.5 \times 10^{18}$	~ 0.68	~ 0.068
Dose ($1 \times 10^{15} - 7 \times 10^{15} \text{ cm}^{-2}$)	$1.75 \times 10^{18} - 1.25 \times 10^{19}$	0.62 – 0.79	0.0620.079

Table 5.2: Change in $\frac{\Delta\rho}{\rho}$ due to dimensional variations of the tethers.

Dimension (nominal value)	Change in $\frac{\Delta\rho}{\rho}$	Sensitivity (mV Pa ⁻¹)
Length, 500 $\mu\text{m} \pm 1 \mu\text{m}$	$\pm 0.2\%$	~ 0.068
Width, 10 $\mu\text{m} \pm 1 \mu\text{m}$	-18% to +23%	0.0562 – 0.0840
Thickness, 10 $\mu\text{m} \pm 1 \mu\text{m}$	-10% to +11%	0.0618 – 0.0755

The in-plane force sensitivity of the side wall implant (S) was predicted by

$$V_{out} = \frac{\Delta R}{4R} V_b \quad (5.7a)$$

$$= \frac{V_b}{4} \pi_l \sigma$$

$$= \frac{V_b}{4} \pi_l \frac{FL\frac{W}{2}}{\frac{TW^3}{12}}$$

$$S = \frac{V_{out}}{F} = \frac{3}{2} V_b \pi_l \frac{L}{TW^2} \quad (5.7b)$$

where V_{out} and V_b were the output and bias voltage of the Wheatstone bridge, respectively, $\frac{\Delta R}{R}$ was the relative change in resistance, π_l was the longitudinal piezoresistive coefficient, σ was the bending stress at the root of the tether, F was the applied force, and L , W , and T were the length, width, and thickness of the tether, respectively. Uncertainty in S (w_S) was calculated using (5.6), shown by

$$w_S = \left[\left(\frac{\partial S}{\partial V_b} w_{V_b} \right)^2 + \left(\frac{\partial S}{\partial \pi_l} w_{\pi_l} \right)^2 + \left(\frac{\partial S}{\partial L} w_L \right)^2 + \left(\frac{\partial S}{\partial W} w_W \right)^2 + \left(\frac{\partial S}{\partial T} w_T \right)^2 \right]^{\frac{1}{2}}, \quad (5.8)$$

and multiplied by the plate element area to obtain uncertainty in shear stress sensitivity. Uncertainty in V_b (w_{V_b}) was negligible. Uncertainty in π_l (w_{π_l}) was dependent on the dopant concentration (Table 5.1 and Figure 3.10(a)). Uncertainties in the tether dimensions, w_L , w_T , and w_W were shown in Table 5.2. Therefore, the uncertainty in shear stress sensitivity was calculated to be ± 0.036 mV Pa⁻¹. Since the experimental

sensitivity ranged from 0.041 to 0.063 mV Pa⁻¹ (0.052 ± 0.011 mV Pa⁻¹), the experimental values fell within the theoretical sensitivity range (0.068 ± 0.036 mV Pa⁻¹) caused by one or more aforementioned sources of variations.

5.1.2 Out-of-plane Sensitivity

The sensitivity of the top-implanted piezoresistor to normal force was characterized using the previously reported benchtop calibration technique [309, 310], which was the same technique used to calibrate the cantilever force sensor described in Section 5.1.1. The sensor was mounted on a microscope slide and driven in out-of-plane motion by a Jodon EV-30 piezoelectric shaker. The shaker was driven by a white noise input with frequency ranging from 500 Hz to 50 kHz, amplified at fixed gain of 100× by a Krohn-Hite 7500 Widebands Power Amplifier. A Polytec OFV3001 Laser Doppler Vibrometer was used to extract the average out-of-plane velocity of the plate element. The LDV output was connected to an HP89441A vector signal analyzer and its velocity filter was set to 5 mm sec⁻¹ V⁻¹. The frequency spectra on the analyzer showed peaks of the modes of vibration. The first resonant frequency was experimentally found to be ~18.2 kHz, which is higher than that predicted by COMSOL finite element simulation, ~13.5 kHz (Figure 5.10). The higher experimental first resonant frequency was due to the presence of passivation layers on top of the sensor (Section 6.1), which increased the stiffness of the tethers in out-of-plane direction. Both signals from the LDV and the conditioned output of the Wheatstone bridge (which was amplified by 1000× using AD624) were captured using an HP54542A Oscilloscope. The sensor sensitivity in out-of-plane direction was found to be about 0.04 mV Pa⁻¹ without amplification. The signal from the sidewall piezoresistors were negligible (lower than the noise level of the electronics), confirming low sensitivity to out-of-plane forces.

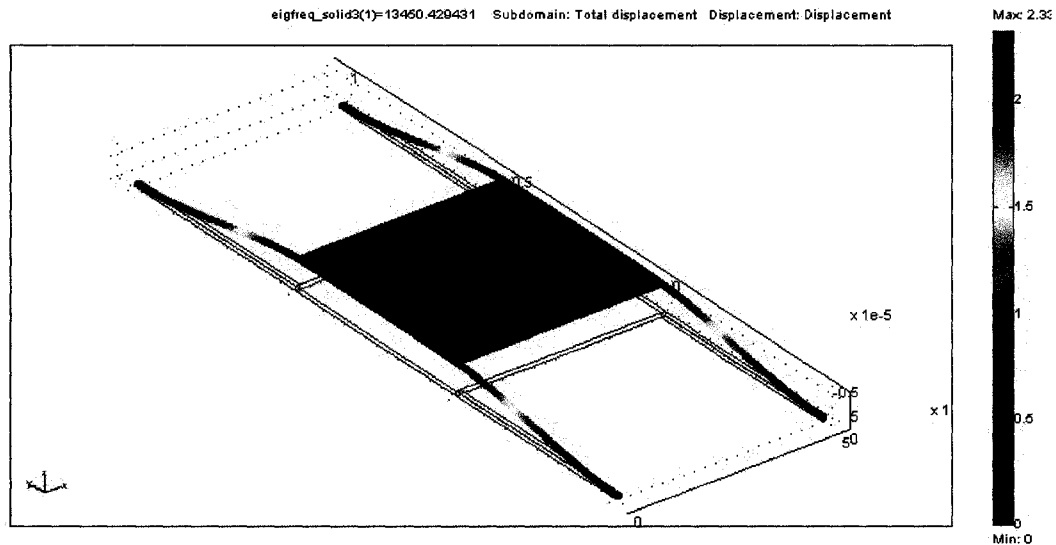


Figure 5.10: First out-of-plane resonant frequency of the sensor predicted by COMSOL finite element simulation. The colors show total displacement with respect to the undisturbed (equilibrium) position.

5.2 Temperature Coefficient of Sensitivity

Piezoresistors are sensitive to electromagnetic noise and temperature. A simple experiment was set up to characterize the sensitivity of the piezoresistor with respect to change in temperature. The sensor was submerged in a deionized water bath (a beaker) and enclosed by a foil-wrapped box to avoid contribution of electromagnetic interference to the change in resistance. The temperature of the water bath was monitored using a thermometer with a resolution of 0.5°C . The bath was slowly heated using a hotplate to 50°C and cooled down by adding ice to about 10°C . The change in resistance was monitored using a HP34401A Digital Multi Meter (DMM). Figure 5.11

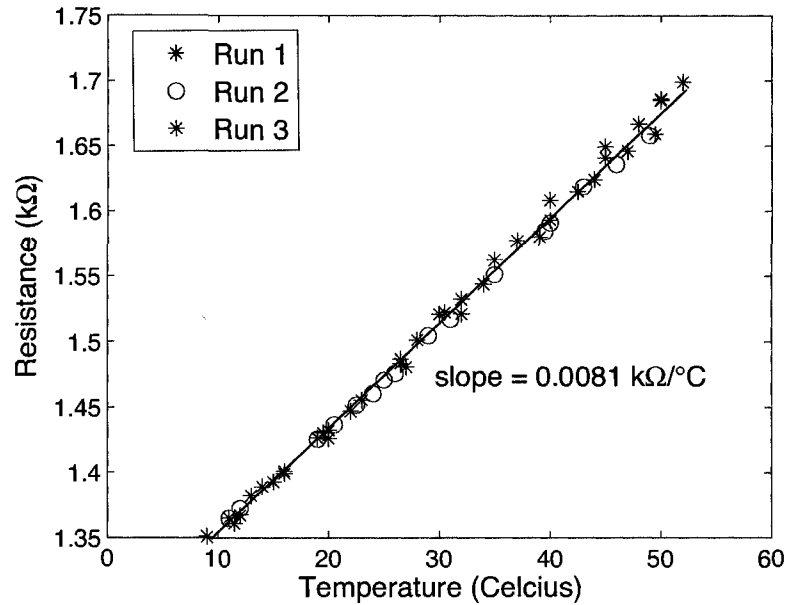


Figure 5.11: Plot of the change in piezoresistance with respect to the change in temperature for three different runs. Temperature coefficient of sensitivity was found to be $0.0081 \text{ k}\Omega \text{ }^{\circ}\text{C}^{-1}$.

shows the change in resistance with respect to change in temperature for three different runs. The temperature coefficient of sensitivity (TCS) was found to be $0.0081 \text{ k}\Omega \text{ }^{\circ}\text{C}^{-1}$, which translated to about $30 \text{ Pa } ^{\circ}\text{C}^{-1}$. Therefore, temperature compensating signal conditioning must be used for underwater measurements.

5.3 Noise

The noise measurements were done using Stanford Research Systems SR570 current preamplifier to extract the noise spectra of the piezoresistors. A current was fed into the SR570, which converted this current to a voltage. An HP89441A vector signal analyzer was used to find the power spectral density per decade. Figure 5.12 shows the diagram of the setup. During the experiment, the sensor was enclosed in an aluminum foil-covered box to avoid noise contributions due to electromagnetic

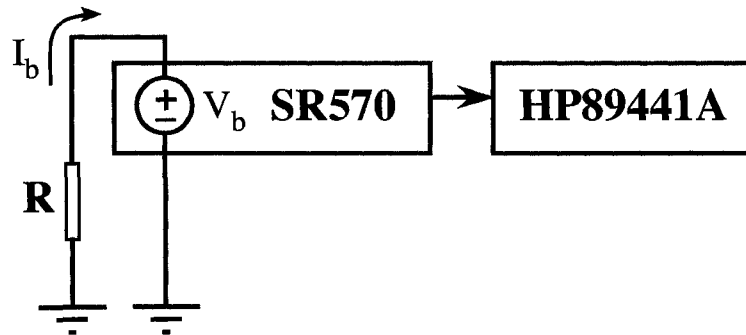


Figure 5.12: Schematic diagram of the noise measurement setup. A current (I_b) was fed through the piezoresistor (R) and into a current preamplifier (SR570), which converted this current to a voltage (V_b). An HP89441A vector signal analyzer was used to find the power spectral density per decade. Figure is courtesy of Paul Lim.

interference. Figure 5.13 shows almost an order of magnitude improvement on the $1/f$ noise level of the sidewall-implanted piezoresistors before and after hydrogen anneal. This result supported reports that surface roughness effect played a major role in the $1/f$ noise level in ion-implanted piezoresistors [315].

5.4 Note and Acknowledgement

The content of this chapter is part of

- “Design, Fabrication, and Characterization of Piezoresistive MEMS Shear Stress Sensors,” presented at the ASME International Mechanical Engineering Congress and Exposition in Orlando, FL in 2005 and included in the conference proceedings [307].
- “Design and characterization of microfabricated piezoresistive floating element-based shear stress sensors,” published in *Sensors and Actuators A* [308].

I would like to thank: Sung-Jin Park for the assistance during the in-plane sensitivity experiment and the LabVIEW code used to gather sensitivity data and Vikram Mukundan for the assistance during the out-of-plane sensitivity experiment.

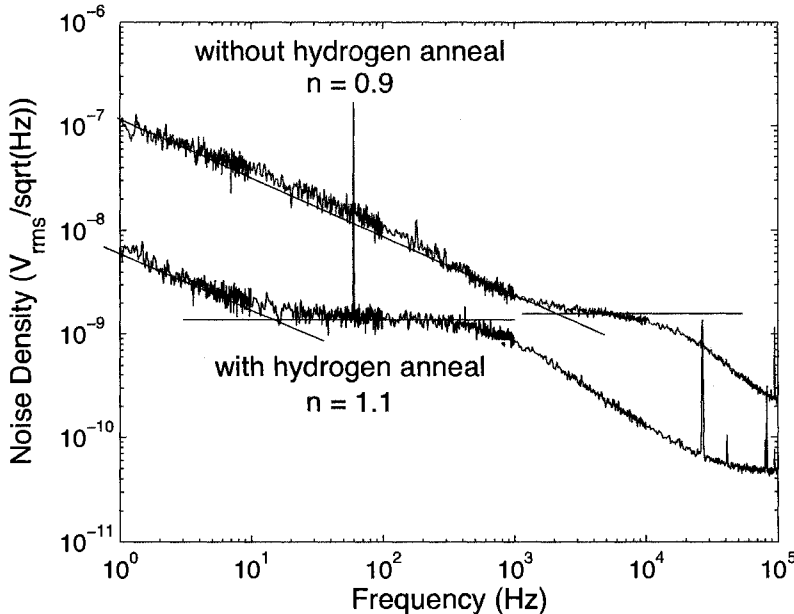


Figure 5.13: Noise characteristics of the piezoresistors with and without hydrogen anneal. The exponents of $1/f^n$ were $n = 1.1$ and $n = 0.9$ for piezoresistors with and without hydrogen anneal, respectively. The noise measurements were done using Stanford Research Systems SR570 current preamplifier. Roll-off above 10^4 Hz is due to low-pass filtering in the low-noise mode operation of SR570.

Chapter 6

Sensor Passivation and Underwater Testing

This chapter starts with a review of common passivation schemes used in MEMS devices and continues with results of reliability tests on different passivation layers. Next, the results from two underwater experiments using ion-implanted sensors are presented. These experiments highlight the response to solid-body rotation using a cylindrical tank and steady, laminar, uniform flow using gravity-driven flume. This chapter concludes with a micro-scale Particle Image Velocimetry (μ PIV) experiment to test the effect of gap size on fluid flow.

6.1 Passivation Schemes

6.1.1 Review

A major difficulty in underwater testing of a MEMS shear stress sensor, or any electronic device, is choosing an appropriate underwater passivation scheme. All electronic components, such as metal traces, bond pads, and piezoresistors need to be protected from their aqueous environment. The passivation layer needs to be corrosion resistant and must provide sufficient isolation from electrolytes. Ideally, the layer is free of residual stress to prevent changes in the mechanical properties of the

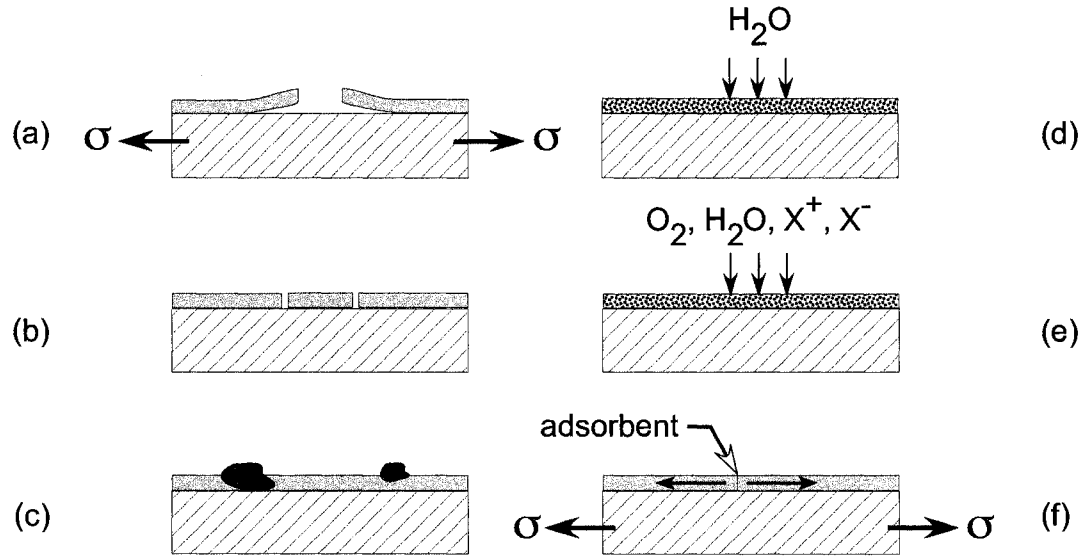


Figure 6.1: Several examples of failure mechanisms: (a) Cracks due to tensile stress with delamination of the passivation film (b) pinholes (c) particle inclusion (d) absorption or swelling (e) ion diffusion (f) adsorption induced stress. Source: Schmitt et al. [316]; ©1999 Elsevier Science Ltd.; reproduced with permission.

microstructure, pinhole-free, and if the device is used for in vivo measurements, biocompatible. Schmitt et al. [316] reviewed common failure modes of passivation layers in microsystems (Figure 6.1). According to the authors, passivation layer failures can be caused by:

1. Mechanical stress and film defects. This includes stress, pinholes, and particle inclusion in the film.
2. Chemical, physicochemical, and electrochemical reactions. This includes absorption, adsorption, corrosion, and diffusion of electrolytes.
3. Combination of the two above; for example, adsorption-induced stress corrosion cracking.

The authors studied the long-term stability of passivation layers on sensor chips in a sodium chloride environment at 25°C for corrosion resistance. Most of the organic

passivation layers (photoresist and polyimide), monolayer of inorganic films (nitride and oxide), and duplex layers of oxide-nitride lasted about a day. However, plasma treating or annealing of the passivation layers prolonged their life to hundreds of hours. The best results without physically modifying the surface of the substrate were obtained with the triplex layer of oxide-nitride-oxide (ONO).

Parylene™, the trademark for a variety of *polyxylylene* polymers, is also considered as a passivation layer for the second underwater test in this project, i.e. the gravity-driven water flume. Various isomers of parylene are available today. Parylene C (*poly-para-xylylene*) is used in this project. The chemical structure of Parylene C is shown in Figure 6.2. Parylene has been widely used as a passivation layer for electronic components and has been used in MEMS devices as a passivation layer [117] and as a structural layer [317, 318]. Some advantages of parylene include [319, 320]:

1. Deposition at room temperature. Parylene exists in a solid form as *di-para-xylylene*, a dimer. The first step is to vaporize the dimer at 150°C and 1.0 torr. The vapor is passed to another chamber where the dimer is *pyrolyzed* at 680°C and 0.5 torr into a *para-xylylene*, a monomer. Finally, the monomer is deposited at 25°C and 0.1 torr and transformed into *poly(para-xylylene)*, a polymer.
2. Surface Conformality. The gaseous nature of parylene deposition allows it to penetrate and coat surfaces that are unreachable by liquid coatings.
3. Relatively stress-free. The deposition occurs at room temperature, minimizing thermal stress. The nature of the polymer also introduces very minimal intrinsic mechanical stress as well.
4. Transparent. The resulting film does not absorb visible light.
5. Superior electrical insulation and low dielectric constant, hence often used in fast signal processing applications.
6. High yield strength. Often used in military applications.
7. Biocompatible. Often used in biomedical applications.

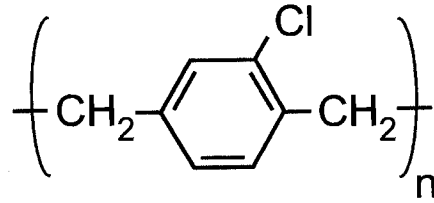


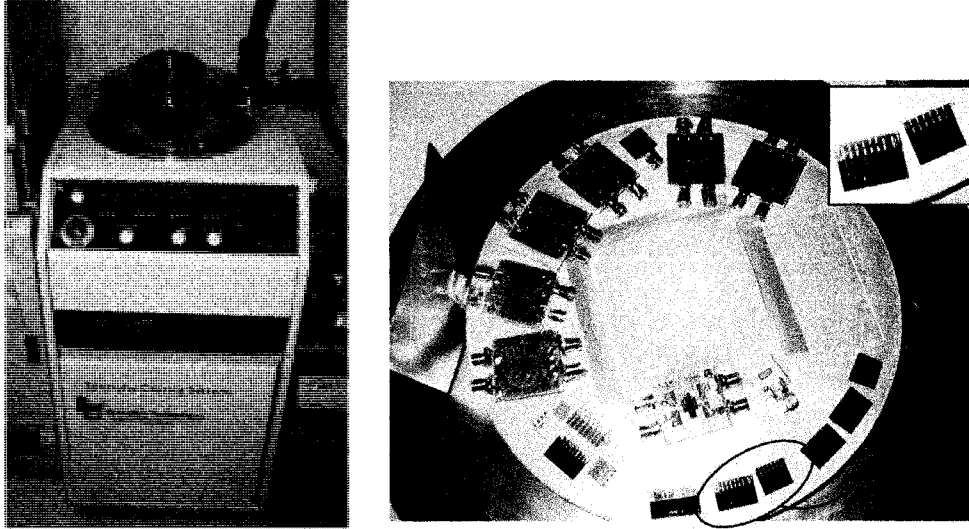
Figure 6.2: Parylene C molecule.

8. Good particle retention.
9. Solvent, acid, and base resistant.
10. Excellent moisture barrier.

6.1.2 Reliability Testing

We decided to use ONO triplex passivation for the first underwater experiment due to the availability of the required processing equipment. Triplex layers of ONO, with thicknesses of 1350 Å, 7150 Å, and 1300 Å were coated using a PECVD process (Section 1.2.2). The ONO triplex layer was annealed at a 400°C nitrogen ambient for 10 minutes at the end of the fabrication process. Some chips were also coated with 1.5 μm of parylene C using Parylene Deposition System, model #2010 from Specialty Coating Systems (Figure 6.3(a)). The bond pads were covered with a tape made of polyimide before the deposition to avoid deposition of parylene directly on top of the pads. After the deposition, this tape was carefully removed to uncover the pads and to allow access for wirebonding (Figure 6.3(b)). The thickness of the deposited film was measured with a micrometer.

Both the ONO triplex and Parylene C were tested as underwater passivation schemes. A gold-coated, copper surface mount board (“surfboard”) and a sensor chip were both mounted on a microscope slide and wirebonded. Subsequently the sensing region was submerged. A simple voltage divider circuit with a bias voltage of 10 V was constructed, with one fixed resistor (1 kΩ) and one piezoresistor (~ 1.7 kΩ). Measurements were done using a GPIB-controlled HP34401A Digital Multi Meter



(a) PDS2010 machine. (b) The top view of the deposition chamber of PDS 2010.

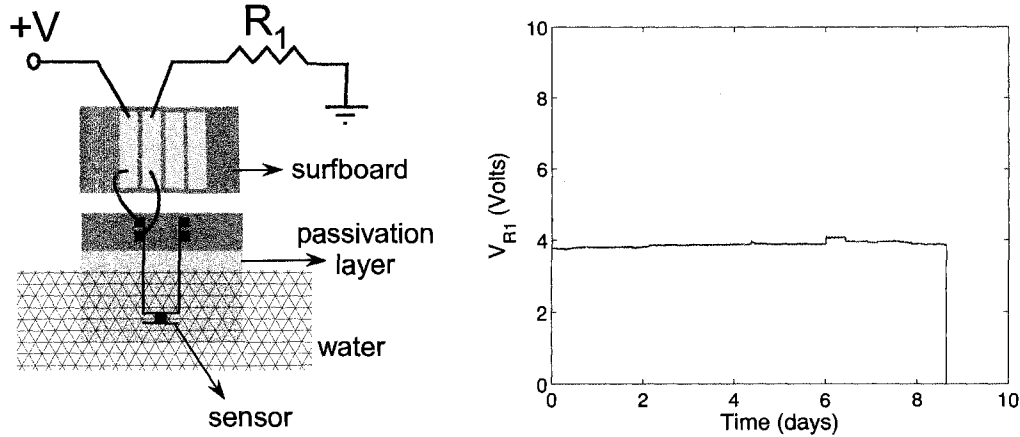
Figure 6.3: Parylene Deposition System 2010 (PDS2010), manufactured by Specialty Coating Systems. Before deposition, the bond pads were covered by kapton tape to prevent parylene deposition on the bond pads. The kapton tape was then peeled off after the deposition and before wirebonding to open access to the bond pads.

(DMM). A schematic of the experiment is shown in Figure 6.4(a). Parylene C (1.5 μm) was shown to be reliable as a passivation layer against aluminum electrolysis for at least 8 days (Figure 6.4(b)). The drift of the piezoresistor during the 8-day period was less than 2%, which corresponds to $|\frac{\Delta R}{R}|$ of 0.0331. The failure was due to corrosion of the wirebonds above the waterline, implying that its life could be longer than 8 days. ONO-passivated sensors immersed underwater in the same circuit configuration survived for at least 36 hours.

6.2 Rotating Table

6.2.1 Theory and Setup

The first test on our shear stress sensors used a transparent cylindrical tank fixed on a rotating table (Figure 6.5). The diameter and height of the tank were 1 and



(a) The schematic diagram for passivation schemes reliability test. (b) Lifetime testing of the Parylene C-coated sensor.

Figure 6.4: The schematic diagram for passivation reliability tests. Two different chips with different passivation materials (ONO triplex layer and parylene C) were tested underwater. Each of the chip-surfboard set was mounted on a microscope slide. The results showed that Parylene C (1.5 μm) was reliable as a passivation layer against aluminum electrolysis for at least 8 days.

0.5 meters, respectively. The tank sat on top of a table, which was rotated by an electric motor. A rectangular aluminum arm, 25 cm (L) \times 5 cm (W) \times 0.1 cm (T), was submerged inside the cylindrical tank and oriented so that the length of the arm is parallel to the radial direction (Figure 6.6). This arm acted as a flat plate with respect to the direction of the flow (U_θ), where the width of the arm is equal to the length of the flat plate.

A shear stress sensor chip was mounted on the aluminum arm at a distance of 15 cm from the center of the cylinder. This problem was modeled as fluid flow over a flat plate (Section 1.2.1) as shown in Figure 6.7. The fluid velocity inside the cylinder was measured using Acoustic Doppler Velocimetry (ADV), which operated by the principle of Doppler shift to measure the fluid velocity in three dimensions. ADV has commonly been used to measure fluid velocity [321, 322]. By measuring the fluid velocity at several points above the sensor, the flow profile could be determined and shear stress could be inferred from the velocity gradient at the wall (aluminum arm).

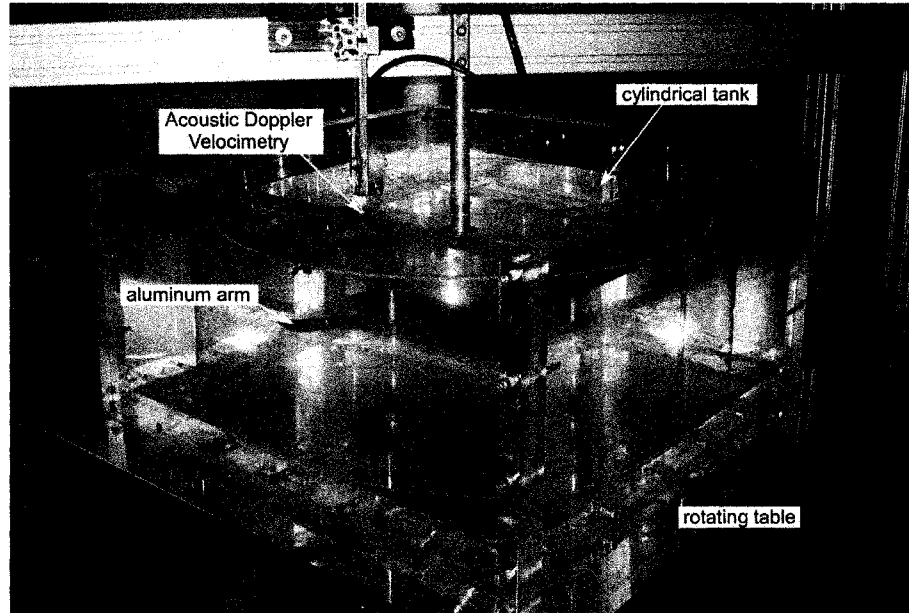


Figure 6.5: Cylindrical tank affixed onto a rotating table.

At the same time, voltage output from the Wheatstone bridge was measured, thereby computing or verifying the sensor sensitivity. The magnitude of the shear stress could be varied by changing the rotational speed of the table, which changed the velocity of the fluid particles inside the cylinder.

6.2.2 Results

Measurements were taken at a horizontal distance of 6, 12, and 18 cm away from the center of the cylinder and at a vertical distance of 5, 10, 15, and 20 cm away from the sensor. Typical measurement results of fluid velocity are shown in Figure 6.8. Fluid velocity fluctuations and uncertainties exceeded the resolution needed to accurately compute a velocity profile and wall shear stress due to unrealized solid-body rotation during the experiment. The flow was found to be unsteady (fluctuating) in all three components and the radial component was non-zero. Based on this experiment, we decided that calibrating and characterizing the sensors in a rotating cylindrical tank was not a reliable technique due to large uncertainties in the measurements.

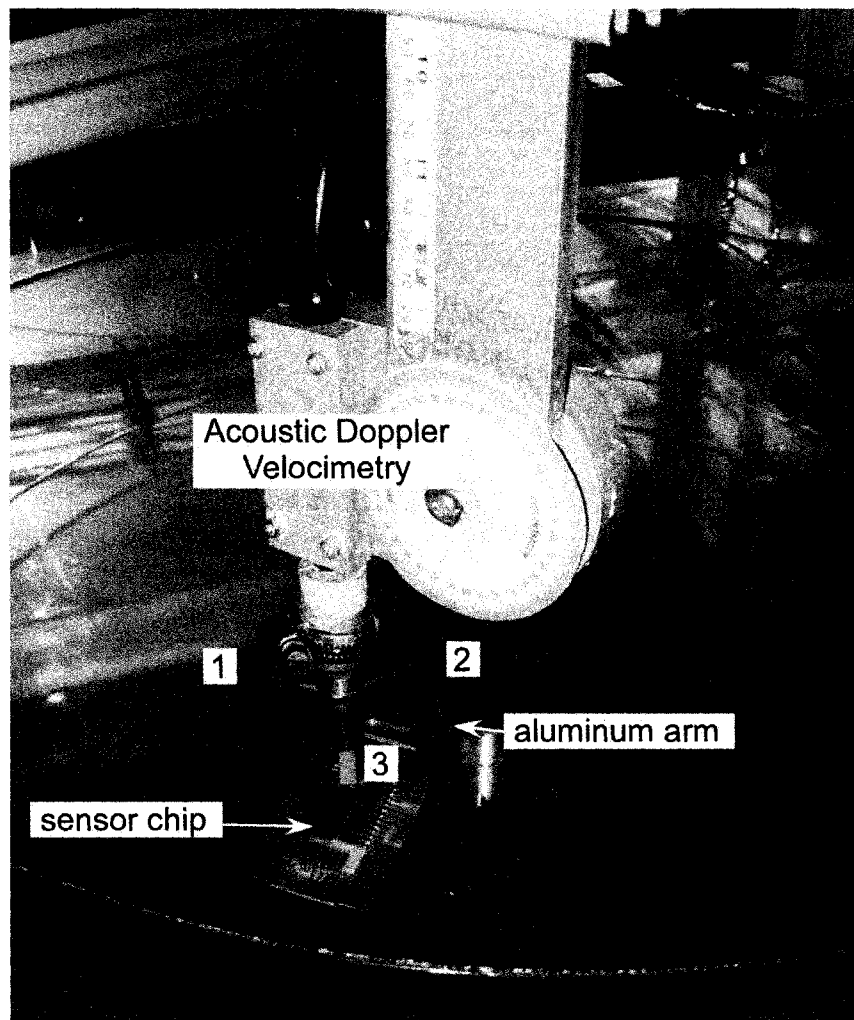


Figure 6.6: Acoustic Doppler Velocimetry (ADV) apparatus with three receivers for the reflected acoustic waves and aluminum arm. A groove, with the same thickness as the sensor and the microscope slide, was machine cut on the top surface of the aluminum arm so that the sensor was flush with the surface of the arm.

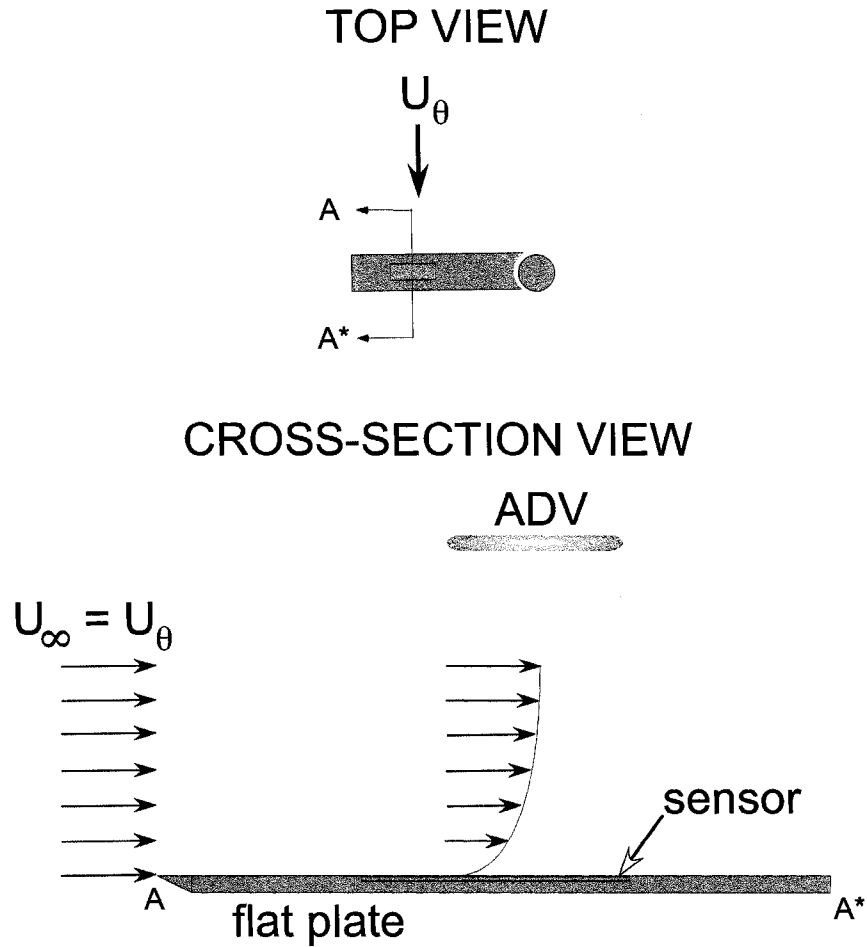
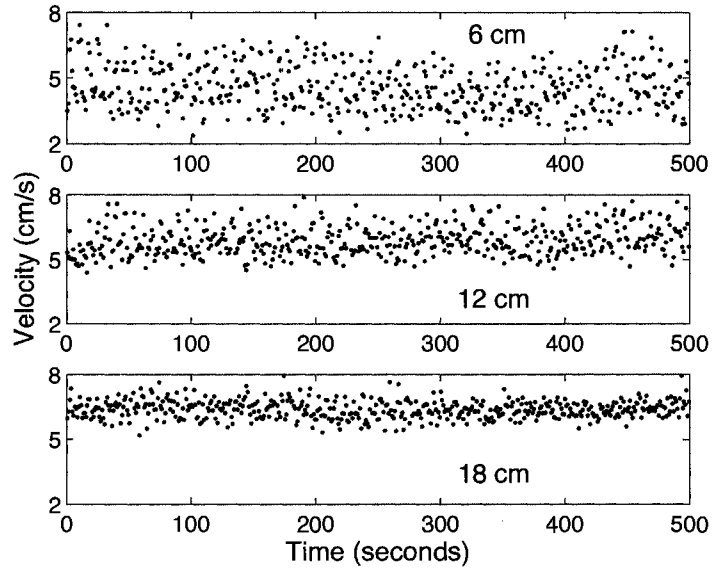
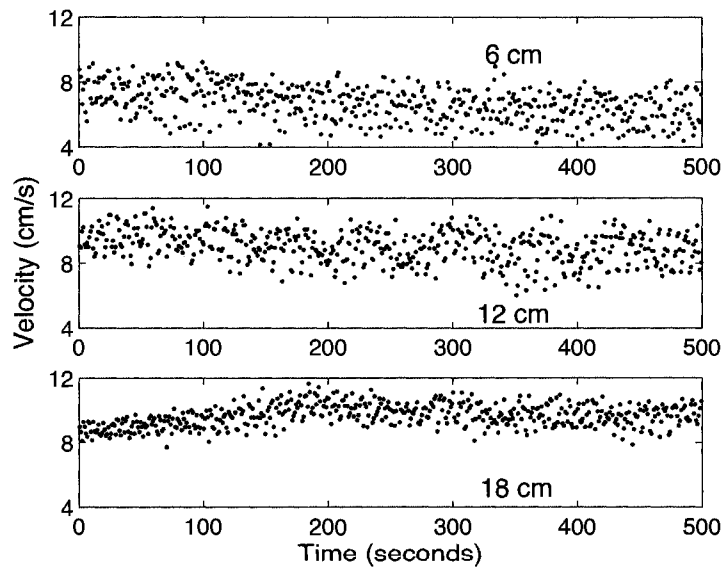


Figure 6.7: Fluid flow and the velocity boundary layer over the aluminum arm, which was modeled as a flat plate. The fluid velocity was measured using Acoustic Doppler Velocimetry (ADV). The device sent out a beam of acoustic waves, at a fixed frequency, from a transmitter probe. These acoustic waves were reflected by the moving fluid particles. The reflections were captured by the receiving probes, which calculated the velocity of the fluid particles in three dimensions. The flow profile could be determined by measuring the fluid velocity at several points above the sensor and shear stress could be inferred from the velocity gradient at the wall.



(a) At a radial distance of 10 cm from the center of the tank and a vertical distance of 6, 12, and 18 cm on top of the aluminum arm.



(b) At a radial distance of 15 cm from the center of the tank and a vertical distance of (top) 6, 12, and 18 cm on top of the aluminum arm.

Figure 6.8: Velocity of fluid particles at several locations in the rotating table.

6.3 Gravity Driven Water Flume

The water flow in the cylindrical tank on a rotating table did not achieve solid-body rotation, as verified by ADV. This may have been due to the presence of the aluminum arm. We then used a gravity-driven water flume to test our shear stress sensors underwater. It consisted of a rectangular water flume. The flow was driven by gravity and facilitated by tilting the flume at a certain angle. We packaged our sensor using polymer flip-chip flexible interconnect technology to isolate the electronics from water.

6.3.1 Packaging: Flip-Chip Flexible Interconnects

A complete fabrication process of the polymer flip-chip flexible interconnects is shown in Figure 6.9, modified slightly from Li et al. [323]. Please refer to Table A.2 for detailed fabrication process steps. The process started with DuPont HN125 kapton film (thickness of 125 μm) taped onto a silicon wafer using a standard kapton tape. This wafer acted only as a backing layer for the subsequent processing steps. A chromium-gold bilayer with thicknesses of 35 and 350 nm, respectively, was evaporated onto the kapton film. Next, chromium-gold traces were patterned by wet etch using Transene gold etchant (42% potassium iodide, 3% iodide, 55% water) and CR-14 chromium etchant (30% ammonium nitrate, 10% acetic acid, and 60% water). The width of the metal traces was 100 μm . The size of the square bond pads contacting the pogo pins and those contacting the aluminum pads on the sensor chip were 2 mm and 500 μm , respectively. Next, 15- μm thick photoresist (SPR220-7) was then spun on and patterned to allow access for the subsequent deposition of conductive polymer on top of the chromium-gold bond pads. Next, a conductive polymer (Epo-Tek-K/5022-115BE) was deposited, squeegeed, and cured in a convection oven at 110°C for 15 minutes. Finally, the photoresist was removed using a conventional resist stripping process and the kapton film was peeled off of the backing wafer. Figure 6.10(a) shows a layout of the metal traces with respect to the sensor chip and the bond pads, while Figure 6.10(b) shows the resulting polymer flip-chip flexible interconnects. Some of the conductive polymer were partly removed during photoresist strip and cleaning

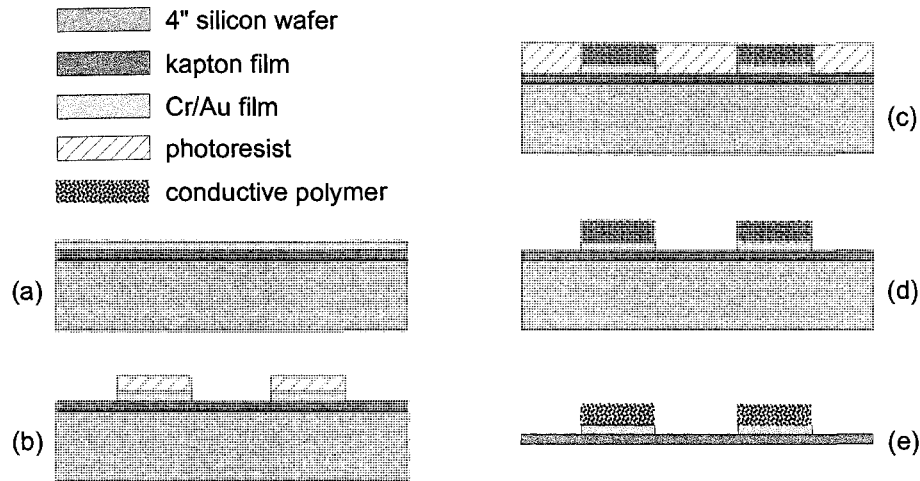
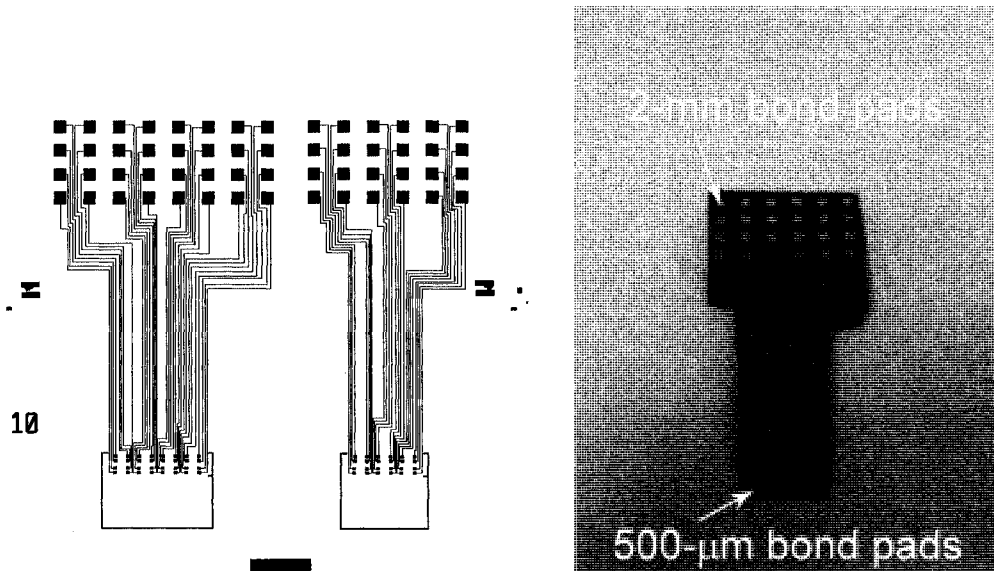


Figure 6.9: Fabrication process steps of the flip-chip flexible interconnects. (a) Kapton film was taped down onto a silicon wafer. Chromium and gold with thicknesses of 35 and 350 nm, respectively, were evaporated on top of the kapton film. (b) The chromium and gold layers were patterned using gold and chromium wet etchants. (c) The resist from the previous step was stripped and another new layer of resist with a thickness of $15\mu\text{m}$ was spun and patterned to allow access to the bond pads. Conductive polymer was then deposited, squeegeed, and cured in a convection oven. (d) The photoresist was removed using a wet etch process. (e) Kapton film was peeled off of the backing silicon wafer.

process at the end. Figure 6.11 shows microscope images of some bond pads with deposited conductive polymer. About 70% of the bond pads had some amounts of conductive polymer at the end of the fabrication process.

The resulting flexible interconnect was flipped, aligned, and contacted onto the bond pads on the sensor chip and thermally bonded at 180°C (about 30°C above the thermoplastic conductive polymer melting temperature), while light pressure was applied. The temperature was held at 180°C for three minutes before it was cooled down. The base resistance of the sidewall-implanted piezoresistor was $0.85\text{ k}\Omega$ and the added resistance from the interconnects was $\sim 0.05\text{ k}\Omega$. A shear sensor chip integrated with flexible interconnects was then affixed onto a microscope slide using epoxy. The microscope slide was then tight-fitted into a groove on a nylon structure (Figure 6.12). This groove ensured that the surface of the sensor chip was flush with the surface



(a) L-Edit™ layout of the bond pads and metal traces on the flexible interconnect. (b) The resulting polymer flip-chip flexible interconnects.

Figure 6.10: Polymer flip-chip flexible interconnects.

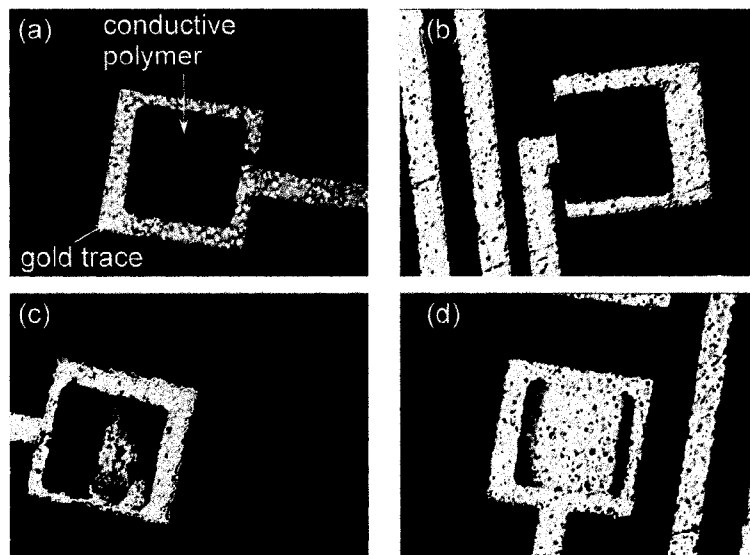


Figure 6.11: Conductive polymer on top of the bond pads at the end of the fabrication process. (a) Good adhesion and good alignment (b) good adhesion with a slight misalignment (c) partly removed (d) completely removed, bad adhesion.

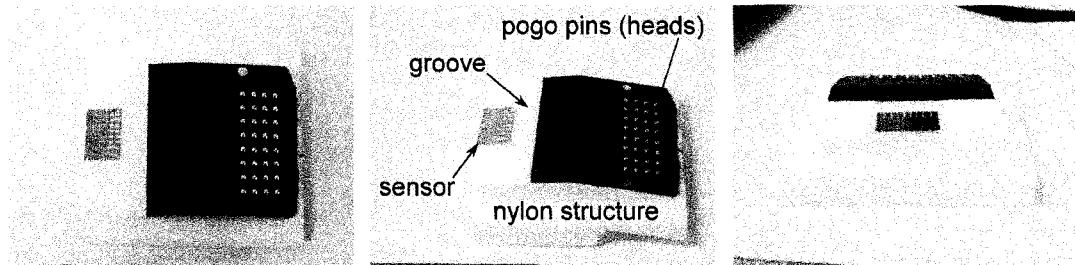


Figure 6.12: The nylon structure and a sensor chip.

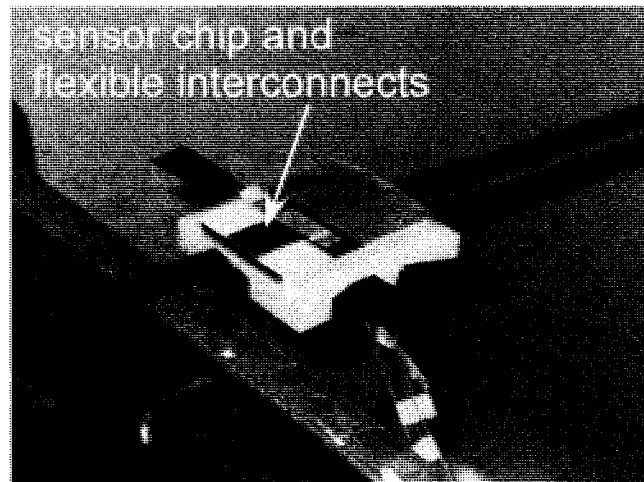


Figure 6.13: Sensor packaging for gravity-driven water flume experiment.

of the nylon structure. The large bond pads on the flexible interconnects were then contacted with the pogo pins and finally an aluminum fixture was used to isolate the pogo pins from water. The electrical contact between the small bond pads on the flexible interconnect and the bond pads on the sensor chip was isolated from water by cured *polydimethylsiloxane* (PDMS), a silicon-based organic polymer. A complete packaged sensor is shown in Figure 6.13. During the underwater experiment, the nylon fixture flush mounted the sensor in a water channel and isolated the electronics.

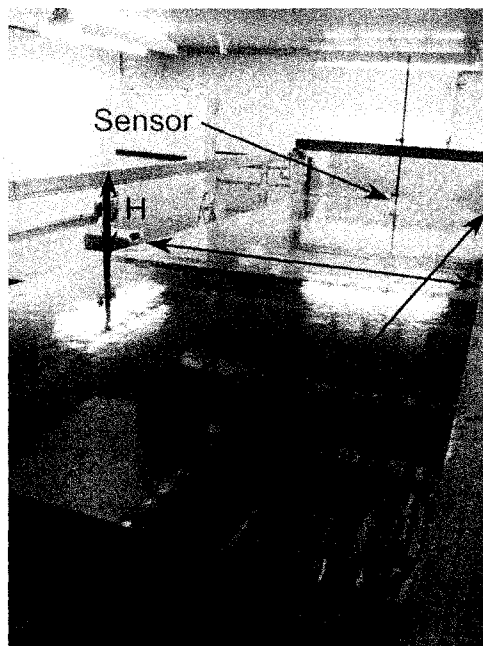
6.3.2 Experiment and Results

A gravity-driven water flume was used to test the performance of the sensors underwater (Figure 6.14). An acrylic extension was built and installed at the end of the flume (Figure 6.15). A rectangular hole was drilled on the acrylic extension to fit the nylon structure so that the surface of the packaged sensor was flush with the surface of the water flume. The tilt angle of the flume was fixed at $\theta = 0.0025$ rad. Water was circulated by two variable speed pumps. Upstream, the first pump filled up the weir with water (Figure 6.16). When it overflowed, the water started flowing downstream due to gravity. A gate (Figure 6.17) controlled the amount of water flowing downstream, and thus controlled the thickness of the water film. Downstream, water flowed into a sink (Figure 6.16) and got recirculated by the second pump. The flow was assumed to be fully developed, steady, and uniform at any cross section of the water channel.

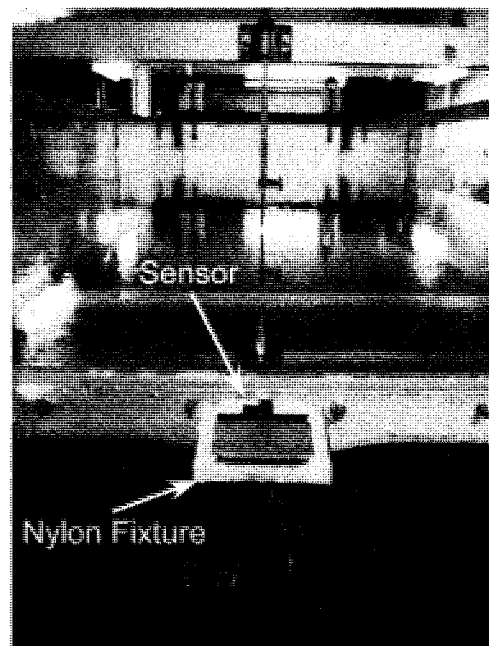
Theoretical bottom wall shear stress, τ_{wall} , was calculated using

$$\tau_{wall} = S_f \rho g R_H(Q) \quad (6.1)$$

where S_f was the air-water interface slope, ρ was water density, g was gravity, R_H was the water channel hydraulic radius, and Q was the flow rate. R_H was defined as the ratio of the cross sectional area (A_c) to the corresponding wetted perimeter (P_w). In this experiment, cross sectional area was constant, therefore $R_H = \frac{A_c}{P_w} = \frac{Wh}{W+2h}$, where h was the height of the water film, a function of Q . The output from sidewall-implanted piezoresistors was captured at 1.1 Hz for 180 seconds. The data samples were time-averaged, excluding the first 60 seconds to allow for settling. The temperature of the water near the bottom wall of the channel was measured using a piezoresistor on an unreleased sensor (~ 0.5 cm apart) that was exposed to the same fluid flow and temperature. Being unreleased, this piezoresistor was insensitive to strain. A typical output plot of the released and unreleased piezoresistors subjected to the same flow is shown in Figure 6.18. Resistance measurements were captured using an HP34401A DMM. A typical performance of the shear stress sensor is shown in Figure 6.19.



(a) Upstream view of the flume.



(b) Downstream view of the flume.

Figure 6.14: The gravity-driven water flume with the dimensions of $L = 14$ ft. , $W = 4$ ft. , and $H = 1$ ft.

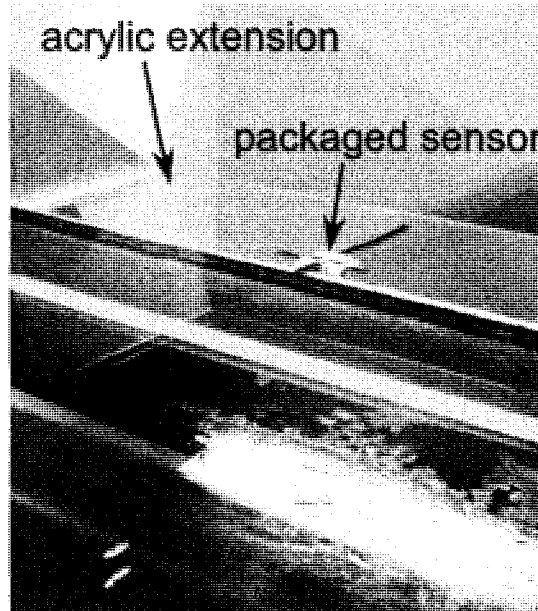


Figure 6.15: An acrylic extension, with the dimensions of $L_a = 1$ ft. and $W_a = 4$ ft., was installed at the end of the water flume. A rectangular hole was drilled to fit the nylon structure such that the surface of the packaged sensor was flush with the surface of the water flume. The sensor was located ~ 0.1 ft. from the leading edge of the acrylic extension.

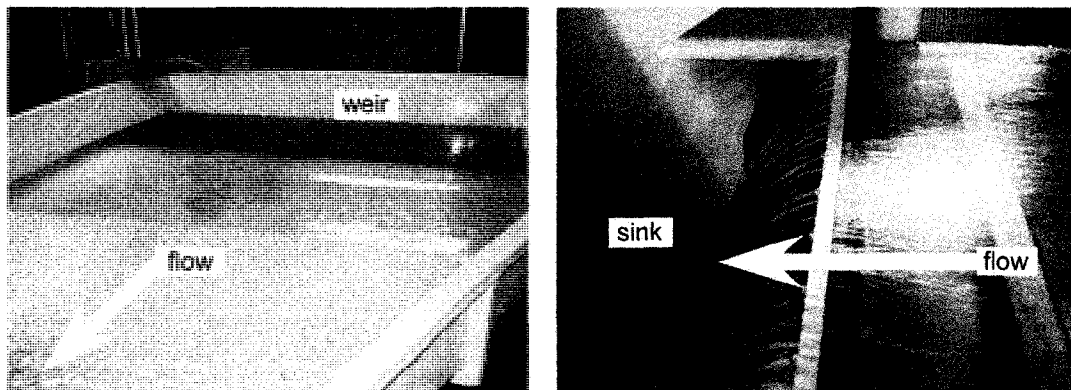
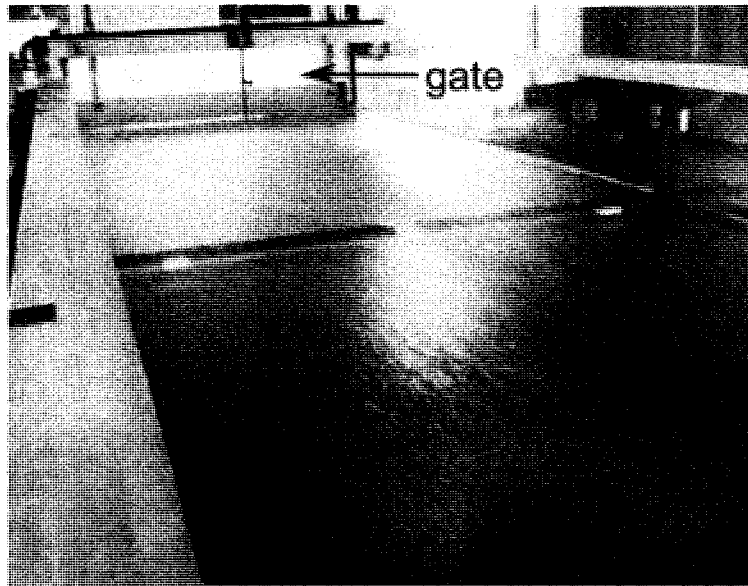
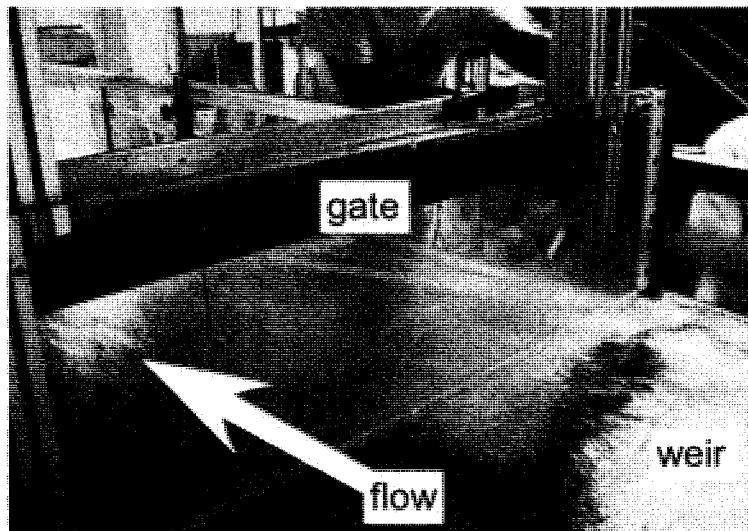


Figure 6.16: Upstream, the first pump fills up the weir (left). Downstream, the water flows into the sink and gets recirculated by the second pump (right).



(a) Downstream view of the gate.



(b) Upstream view of the gate.

Figure 6.17: The opening of the gate could be adjusted to control the amount of water flowing underneath it and the thickness of the water film, h .

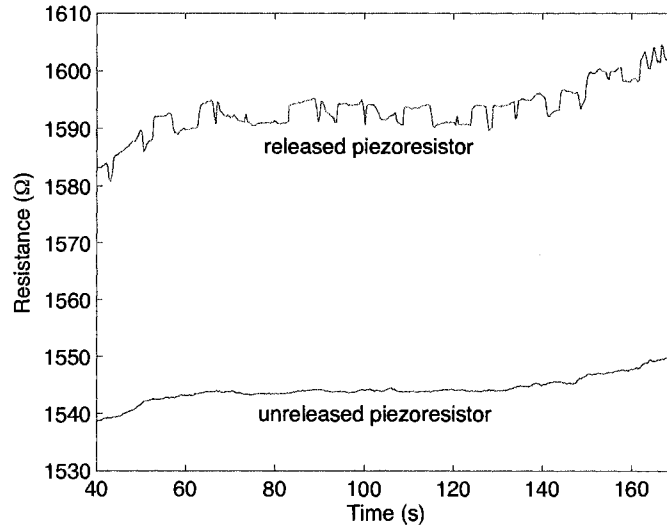


Figure 6.18: A typical DMM output of the piezoresistors on a released and an unreleased sensors subjected to the same flow. The piezoresistor on the released sensor is sensitive to both temperature change and shear stress, while the piezoresistor on the unreleased sensors is only sensitive to temperature change.

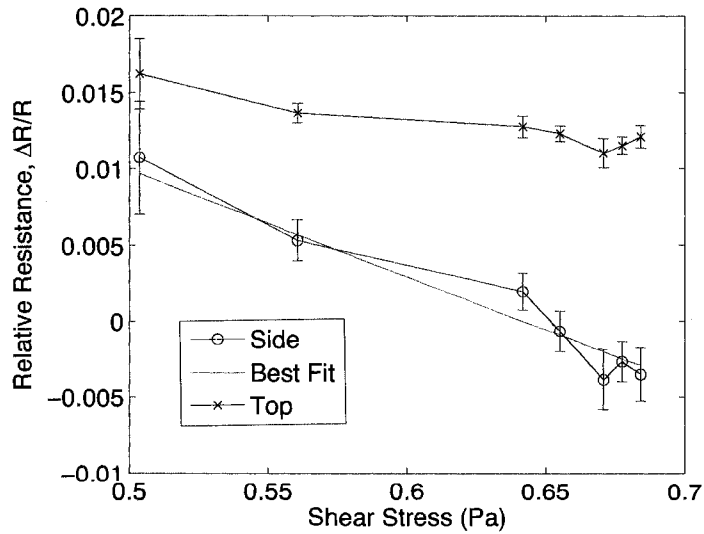


Figure 6.19: Output from both top-implanted and sidewall-implanted piezoresistors subjected to the same flow.

The scatter in the experimental results was due to uncertainties in the measurements. Uncertainty in the slope of the water flume measurements was ± 0.0001 radians, which corresponded to about ± 0.02 Pa of shear stress. Uncertainty in the measurements of the height of the water film (± 300 μm) and the local variation of the temperature at the sensor surface due to convection, which affects the local density of water, were considered negligible in the calculation of theoretical shear stress. The uncertainty bars were the standard deviation of the averaged value of the normalized change in resistance for a given flow rate (shear stress). The normalized change in resistance values observed were still much larger than those predicted by beam mechanics and gravity-driven flow theory (Figure 6.20). This difference was due to unaccounted variations in the air-water interface slope (S_f) above the sensor (local S_f) and fluid-structure interactions. At smaller gate openings, thus smaller flow rates and thinner water films, the assumptions of uniform, steady, fully-developed flow held. An example of this flow is shown in Figure 6.17(a). However, at larger gate openings and larger flow rates, the flow became unsteady and nonuniform. The assumptions of steady, uniform, and fully developed flow did not hold and (6.1) could not be used to compute bottom wall shear stress. Additionally, the flow became three-dimensional as waves, originating from the gate, were reflected by the water flume sidewalls and interfered with each other, as shown in Figure 6.21. As the flow rate increased, the flow became highly unsteady, nonuniform, and most importantly, wavy (Figure 6.22(a)). As a result, determining the actual air-water interface slope, θ_a , during data acquisition was difficult. At higher flow rates, not only the water flume started to vibrate due to enhanced vibration of the pumps, the flow in the weir also became highly unsteady, creating and transferring more vibration to the flume. Moreover, the flow near the free overfall region accelerated with strong curvature in the air-water interface, a non-hydrostatic pressure distribution, and a reduction in water film thickness (Figure 6.22(b)) [324]. This region started from a point, which was about $3 - 4\times$ the water film thickness, measured from the free overfall [324]. The sensor was located ~ 25 cm upstream of the free overfall; therefore, a water film thickness of ~ 6.25 cm or larger would place the sensor within this accelerating flow region. This problem added another complication in determining the actual air-water

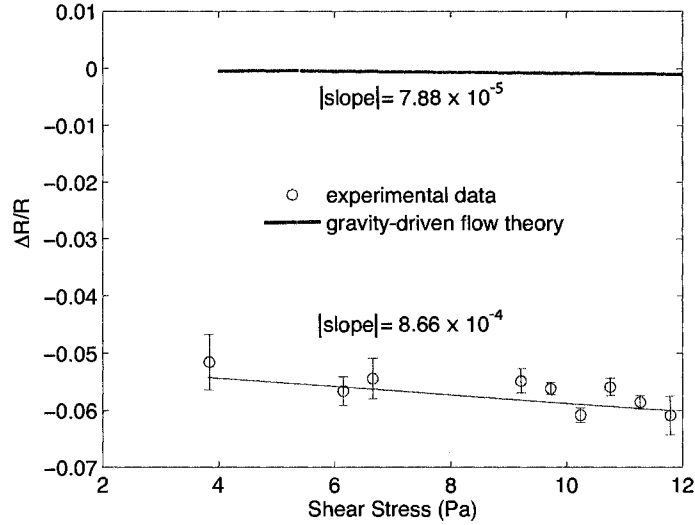


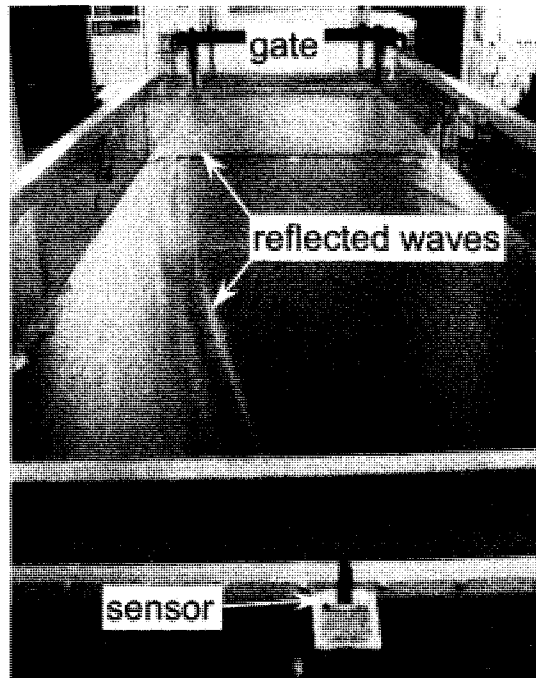
Figure 6.20: Comparison of the normalized change in resistance from experiment and theoretical prediction (beam mechanics and gravity-driven flow). The experimental sensitivity was still an order of magnitude larger than an open-channel gravity-driven-flow theoretical prediction. Large errors are attributed to unsteady and non-uniform flow, uncertainty in local air-water interface slope (local S_f), and unaccounted fluid-structure interactions.

interface slope. According to (6.1), a water film thickness of 6.25 cm corresponded to a shear stress of 1.4 Pa. This suggested that measurement results were obtained when the sensor was within the accelerating flow region, where the air-water interface slope was non-uniform and pressure distribution was non-hydrostatic.

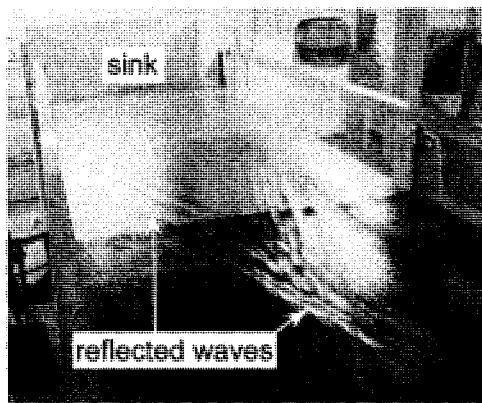
These flow conditions created uncertainties in the experimental results and violated the theoretical bottom wall shear stress predicted by (6.1) (Figure 6.20).

6.4 Micro Particle Image Velocimetry (μ PIV)

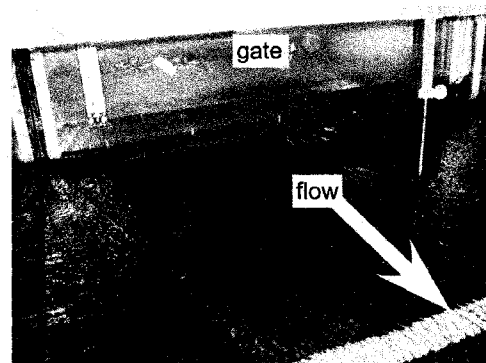
The effect of gap size (between the sensor structure and the substrate) on hydrodynamic flows of interest was studied using a μ PIV system. The result from the experiment was then compared to the result from computer simulations. The result



(a) Wave reflection.

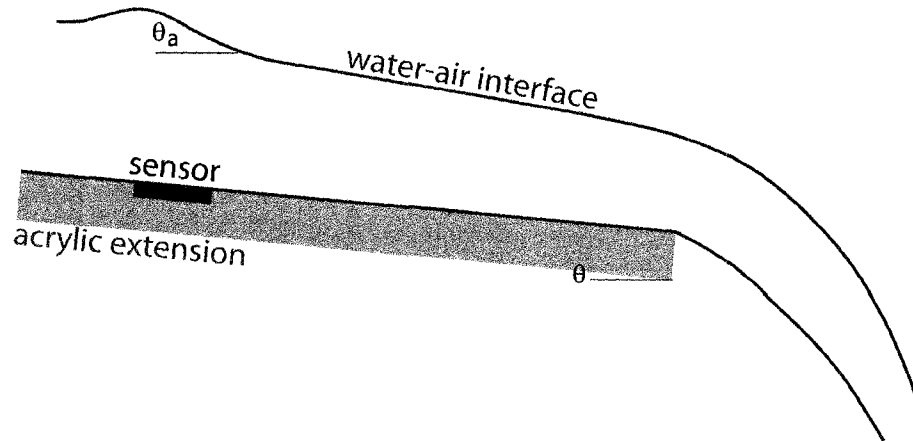


(b) Wave interference.

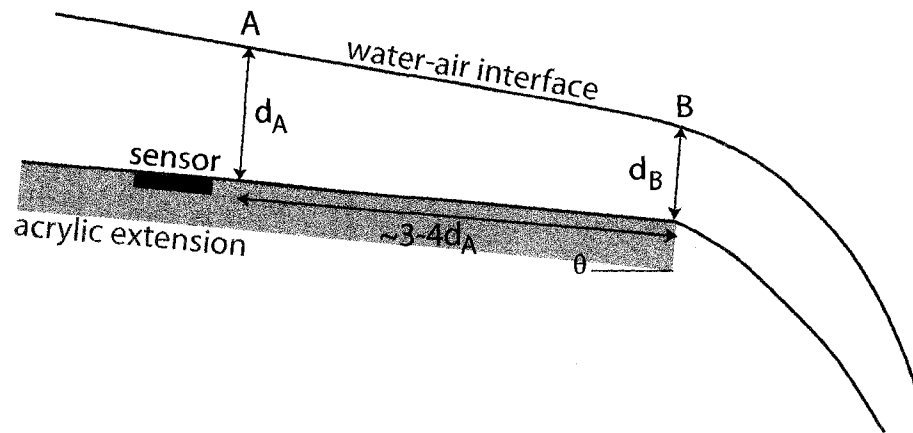


(c) Imperfect gate opening.

Figure 6.21: As the flow rate increases, the flow becomes more unsteady, nonuniform, wavy, and three-dimensional. Some of the waves get reflected by the flume sidewall (a) and interfere with each other (b). These disturbances are felt by the sensor and create uncertainties in the experiment results. In addition, this flow condition invalidates the calculation of bottom wall shear stress, as predicted by (6.1). These waves originate from the imperfect gate opening at the corner (c) and vibration of the water flume to the pumps at higher flow rate.



(a) The actual air-water interface slope above the sensor, θ_a , was different than the slope of the water channel with respect to ground, θ , due to waves. These waves originated from the gate opening, got reflected by the flume sidewalls, and propagated above the sensor.



(b) The accelerating flow region near the free overfall started from A, which was about $3 - 4 \times$ the water film thickness, d_A . From A to B, water film thickness reduced nonlinearly and $d_B = 0.715d_A$ [324].

Figure 6.22: The difference in the experimental results and theoretical predictions were due to unexpected flow behavior, i.e. unsteady, non-uniform, and most importantly wavy. These flow conditions created difficulties in determining the actual air-water interface slope, θ_a , measurements.

from this study can be used as a guidance for future underwater shear stress sensors fabrication process and design.

Particle Image Velocimetry (PIV) is a well-established technique for measuring velocity fields in macroscopic fluid systems. Particles are injected into the flow. The positions of the particles in a region of interest are recorded at two known times using an optical system. It consists of a high-speed digital camera, a high power laser to illuminate the particles, and an optical arrangement to convert the laser output to a light sheet. From these images, the velocity of the particles can be estimated statistically by correlating particle image pairs. Finally, flow streamlines can be inferred. PIV has been applied in a wide range of flow problems, from flow over a vehicle body to the effect of prosthetic heart valves in a cardiovascular system. For a comprehensive review of PIV, please refer to other sources [325,326]. The first successful μ PIV experiment was done using 300 nm diameter polystyrene particles [327]. Further, sub-micron partial resolution has also been achieved [328].

A sensor chip was placed on a sidewall of a molded PDMS mini-channel with dimension of 2 mm \times 2 mm (Figure 6.23). The chip was placed at the fully-developed flow region (Section 1.2.1) inside the channel to ensure uniform velocity profile on top of the sensor. A Leica DM IRB inverted microscope and CCD Leica DFC350 FX were used to visualize the plane perpendicular to the center of the sensors plate element. A schematic diagram of the experimental setup is shown in Figure 6.24. Fluorescent beads (0.7 μ m, Duke Scientific Inc.) were diluted to 0.01% concentration (by volume) and dispensed into the channel at a constant rate by a syringe pump (Harvard Apparatus HA11WD). Images of the particles were recorded at 15 frames sec^{-1} for 6 seconds and an ensemble averaging algorithm was used to calculate the velocity vectors using interrogation (analysis) regions of 50 \times 50 pixels with 50% overlap. The experiment was done under steady and fully-developed flow (constant pressure). No significant disturbance to the flow profile near the sensors due to the gap was observed. The results were in agreement with a 2-D COMSOL Multiphysics simulation (Figure 6.25), which showed that streamlines existed in the gap, however their velocity magnitudes were approximately 0.1% that of the average velocity over the sensors.

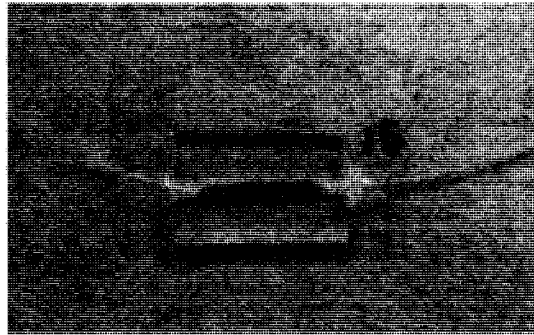


Figure 6.23: A molded PDMS mini channel with dimension of 2 mm × 2 mm.

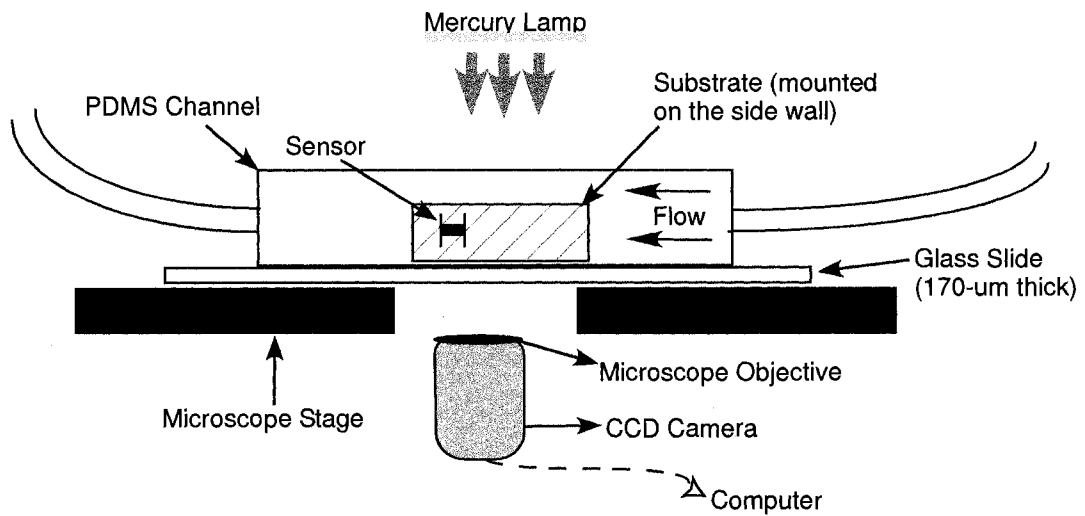
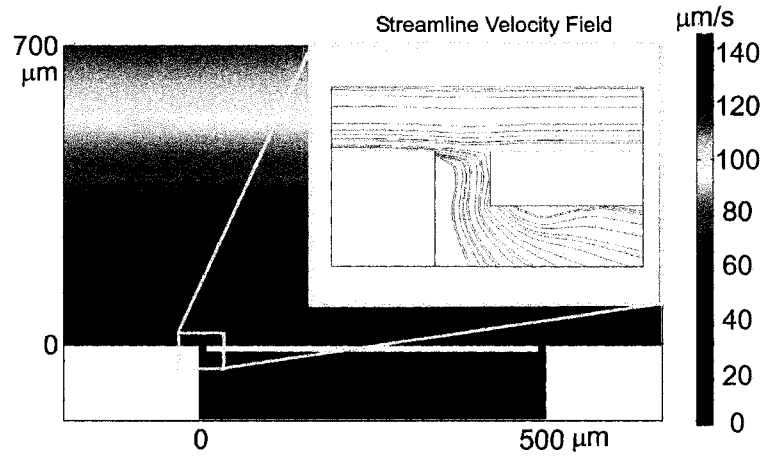
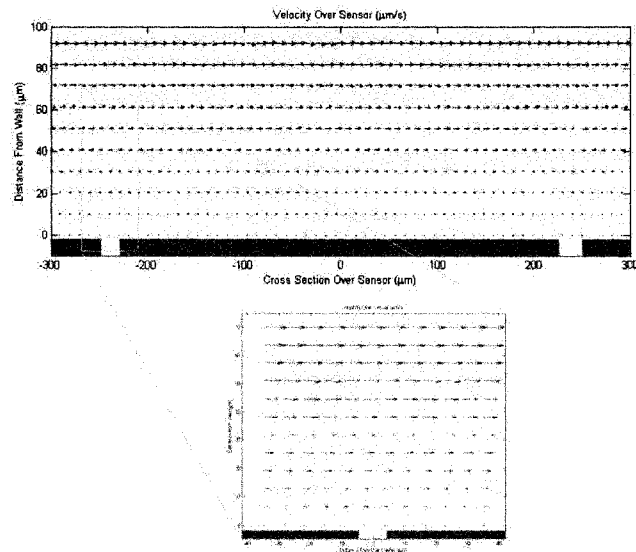


Figure 6.24: A schematic of the experimental setup. The test was run for sensors with 5, 10, 15, and 20- μm gaps. Typical flow velocity $\sim 1 \text{ mm sec}^{-1}$.



(a) COMSOL simulation results.



(b) μ PIV experimental results.

Figure 6.25: The results for 10- μ m gap size COMSOL simulation (a) and its corresponding μ PIV experimental results (b).

6.5 Note and Acknowledgement

Some of the content in this chapter was presented in “Piezoresistive MEMS Underwater Shear Stress Sensors,” *19th IEEE International Conference on Micro Electro Mechanical Systems*, Istanbul, Turkey, 2006, and included in the conference proceedings [329]. I would like to thank: Ratul Narain for the μ PIV flow velocity data and the COMSOL flow simulations, Jeffrey Li for the assistance during the gravity-driven flow experiment and the Matlab code used to gather shear stress data, Caitlin Quance for the assistance during the rotating-table experiment, Ambert Ho for the assistance during the gravity-driven flow experiment, Vikram Mukundan for discussion on shear stress data analysis, and Prof. Ellis Meng of University of Southern California for the assistance in parylene deposition.

Chapter 7

Sidewall Epitaxial Piezoresistors

This chapter presents an alternative method to forming piezoresistors on the sidewall of microstructures by using doped selective epitaxial deposition technique. The fabrication process and the characterization results of piezoresistive microfabricated cantilevers and a floating-element shear stress sensor using this selective epitaxial deposition technique are presented.

7.1 Motivation

As discussed in Chapter 1, in-plane force and shear stress measurements are important in many engineering and science applications, e.g. biomedical and environmental sciences. Several piezoresistive MEMS devices have been designed to measure in-plane forces or shear stress, e.g. planar accelerometers [256, 257], multi-axis AFM [181, 330], stress sensors [331–338], and force sensors for biomechanical measurements [339–341].

Piezoresistive in-plane force sensing has previously relied on CMOS-compatible doping technique (normal implantation or diffusion) to form piezoresistors on the surface of the substrate [331–341] or the oblique-angle ion-implantation technique to form sidewall piezoresistors [181, 256, 257, 330], a technique described in Chapter 4.2. However, similar to the normal implantation process, oblique-angle implantation technique requires an anneal step to activate the dopants and anneal the crystal damage due to high-energy implantation process, resulting in non-uniform doping

profile and deeper junction depth (Figure 3.7). This reduces sensitivity as most of the dopants are not located at the maximum stress concentration, which is the surface of the bending structure. An alternative method to form piezoresistors without the need of post-doping anneal step is to deposit doped epitaxial layer on the surface of interest. An advantage of introducing dopants using epitaxial deposition technique is that the resulting layer (the piezoresistors) can be made very thin (\sim nm), thus increasing the sensitivity of the piezoresistors (Figure 3.7). Piezoresistors formed on top of the substrate surface using doped epitaxial layer have been demonstrated in cantilevers for out-of-plane force sensing [263,264]. Deposition of a very thin piezoresistive layer is required when the dimension of the structure is a constraint. For example, cantilevers fabricated in Harley and Kenny [263] and Liang et al. [264] are on the order of 1000 Å or thinner with junction depths of \sim 300Å. Doped epitaxial deposition is a practical method for such thin piezoresistive cantilevers, especially given the difficulties of implanting shallow junction depths (less than 50 nm), activating dopant atoms, and restoring lattice quality.

In the next sections, we present a novel fabrication technique to form piezoresistors on the sidewall of cantilever force sensors for in-plane sensing applications. The resulting piezoresistors on both sidewalls of the cantilevers form a half-bridge configuration with a conducting metal line contacting between two sidewall piezoresistors (Figure 7.1). We hope to increase the sensitivity of our sensors by using thin doped epitaxial layers to form piezoresistors on the sidewall of our cantilevers. We achieved this by using a recipe to selectively deposit doped single-crystal silicon epitaxial layer on the sidewalls of cantilevered structures. Selective deposition of epitaxial silicon, i.e. the silicon deposits only on exposed regions of silicon, but not on other dielectric films such as silicon oxide or silicon nitride, can be achieved by tailoring the deposition conditions [88,259–262,265,342–344]. Silicon oxide is used as a mask and dichlorosilane (DCS) is used as a source gas in a reduced pressure environment [342]. DCS, together with hydrogen chloride, improve selectivity. Joyce and Baldrey [259] demonstrated one of the earliest selective deposition of silicon epitaxial layers using oxide-masking techniques. A selective deposition technique without the use of hydrogen chloride has also been demonstrated [265,343,344].

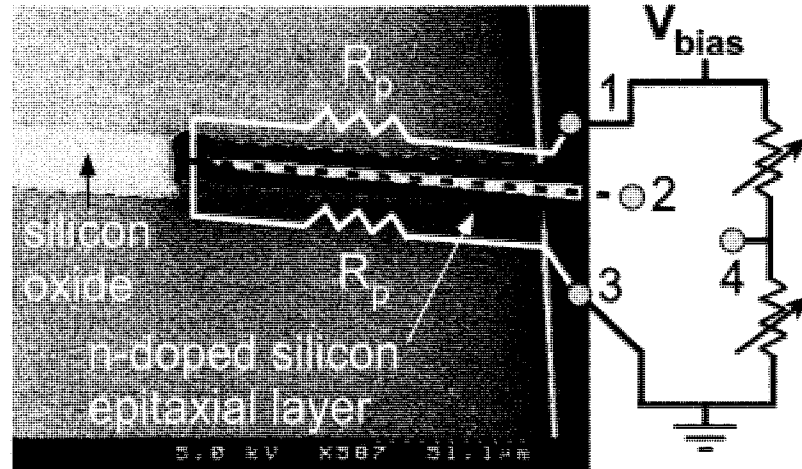


Figure 7.1: Scanning Electron Microscopy (SEM) image of sidewall epitaxial piezoresistors on an unreleased cantilever using selective deposition process. The two piezoresistors on the sidewalls form a half-bridge configuration if a metal line is placed along line 2. The dimensions of the piezoresistors on this cantilever are $500 \mu\text{m}$ (L) \times $20 \mu\text{m}$ (W) \times $2 \mu\text{m}$ (T).

7.2 Fabrication Method

7.2.1 Process Flow

The fabrication process (Figure 7.2) started with 4 in. p-type (boron-doped with device layer resistivity of $3.3 \Omega\text{cm}$) double-polished (100) SOI wafers. The piezoresistors were n-type (phosphorous-doped) to achieve the highest longitudinal piezoresistive coefficient, π_l , in the [110] direction (Figure 3.8(b)) [178], hence the choice of p-type wafers. The wafers were cleaned using “piranha” solution (90% sulfuric acid and 10% hydrogen peroxide). Alignment marks were then patterned onto the wafers using an isotropic silicon plasma etch. The geometry of the cantilevers was defined by etching the device layer ($10\text{-}20 \mu\text{m}$) using DRIE. Next, the wafers were wet oxidized at 1100°C for 36 minutes, resulting in $\sim 3700 \text{ \AA}$ thermal oxide). Oxide masked the subsequent selectively doped epitaxial deposition. The resulting oxide was patterned and etched using BOE (34% ammonium fluoride, 7% hydrogen fluoride, 59% water) to expose silicon (the cantilevers sidewalls) where the piezoresistors would be formed.

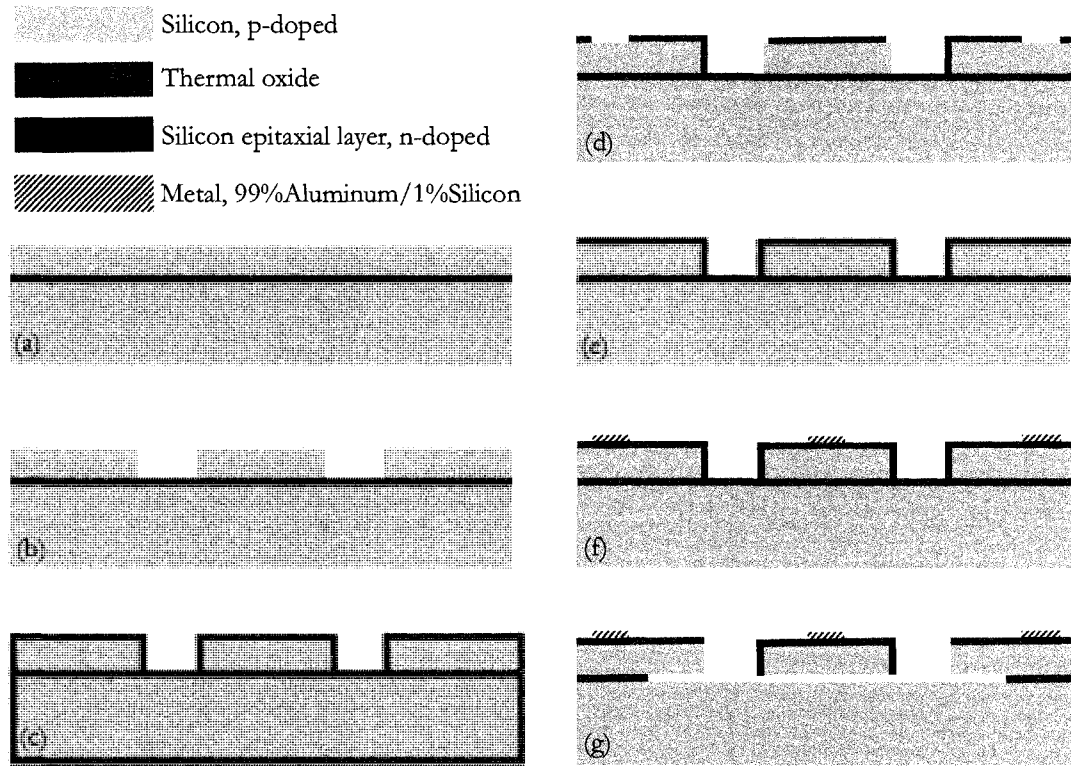


Figure 7.2: Fabrication process flow. (a) 4 in. (100) p-doped (boron) SOI wafer with device layer resistivity of $3.3 \Omega \text{ cm}$. (b) Silicon etch using DRIE process. (c) Wet oxidation at 1100°C for 36 minutes, resulting in $\sim 3700 \text{ \AA}$ thermal oxide. (d) Oxide etch using BOE. (e) Selective n-type epitaxial layer deposition at 980°C and 30 Torr for 8 minutes, resulting in roughly $\sim 2 \mu\text{m}$ of epitaxial layer with resistivity of $\sim 0.005 \Omega \text{ cm}$. (f) Metal sputtering and patterning (replaced here by Focused Ion Beam (FIB) platinum). (g) Release using BOE and Critical Point Drying (CPD).

Next, a phosphorous-doped (concentration $\sim 1 \times 10^{19} \text{ cm}^{-3}$) silicon epitaxial layer was selectively deposited on exposed silicon at 980°C , 30 Torr for 8 minutes, resulting in a doped single-crystal silicon layer with average thickness of $\sim 2 \mu\text{m}$. The typical resistivity of the epitaxial layer was $\sim 0.005 \Omega \text{ cm}$. Metal (99% aluminum and 1% silicon) was then sputtered ($1 \mu\text{m}$) and patterned using aluminum etch (72% phosphoric acid, 3% acetic acid, 3% nitric acid, and 12% water) to form electrical interconnects. While the metal was still protected by the photoresist used in the previous step, the wafers were diced and each die was then released by etching the buried oxide layer using BOE for 150 minutes. The photoresist was then removed from each die using a combination of acetone, methanol, and isopropanol. Finally, each die was dried using Critical Point Drying (CPD). Table A.3 shows the process runsheet.

7.2.2 Challenges and Problems

Following the fabrication process flow described in the previous section, two problems arose:

1. Epitaxial layer was also deposited at the edge of the top surface of the cantilever, thus reducing the area for metal deposition significantly.
2. The central aluminum interconnect on top of the cantilever, which divided the two sidewall piezoresistors in the Wheatstone bridge, was completely etched away during the aluminum etching step.

These problems occurred because of poor step coverage and significant non-uniformity in the photoresist over the topography.

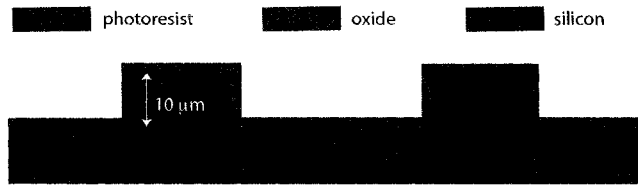
An ideal photoresist was expected to cover the topography with uniform thickness (perfect step coverage) (Figure 7.3(a)). However, the actual uniformity of the photoresist over the topography varied significantly (Figure 7.3(b)). The photoresist covering the wall of the topography was thicker than that in other regions. This part of the photoresist was exposed by the UV light and expected to be completely removed so that the silicon oxide layer underneath could be completely etched away in the subsequent steps (Figure 7.3(c)). Therefore, the exposure time was adjusted

accordingly (20 seconds). However, due to the diffuse nature of light and reflection of light on the surface, this excess exposure time caused a significant exposure of the thinner photoresist on the top surface of the topography. This resulted in exposed silicon oxide layer on the sidewalls, as well as part of the top surface of the topography (near the edge). The exposed silicon oxide layer was then etched away in the subsequent step, exposing the silicon surface. Finally, the epitaxial layer was deposited on the exposed silicon (both the sidewalls and more than $\frac{2}{3}$ of the top surface), which resulted in insufficient room for the aluminum interconnect on the top surface (Figure 7.4). At the edge of the wafer, the photoresist non-uniformity was more significant due to a higher centripetal force during photoresist spinning than that in the center of the wafer (Figure 7.3(d)). The same problem also occurred during aluminum patterning. To get preliminary performance data, this problem was overcome by depositing a platinum interconnect (0.25 μm thick) using Focused Ion Beam (FIB) along one of the sidewall piezoresistors. Figure 7.5 shows SEM image of the released cantilever with FIB platinum.

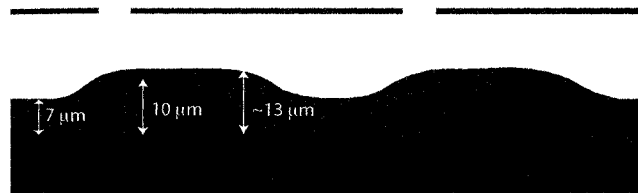
Without the excess exposure, the thicker photoresist covering the walls was not completely exposed and developed away, leaving the bottom part of the walls still covered with resist. This leftover photoresist protected the oxide layer during the oxide etch step and the epitaxial layer did not deposit on the bottom part of the walls (Figure 7.6).

7.3 Characterization

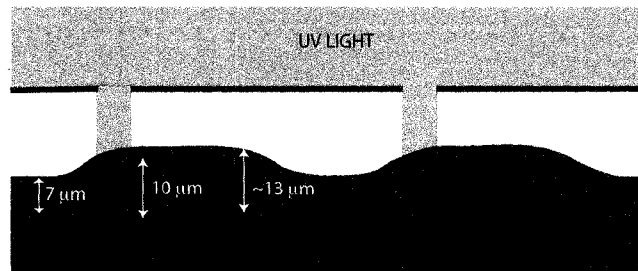
This section discusses the characterization of the sidewall epitaxial piezoresistors. The characterization includes the process deposition rate, the piezoresistor I-V curve and noise, and the resonant frequency and sensitivity of the cantilevers and the shear stress sensor.



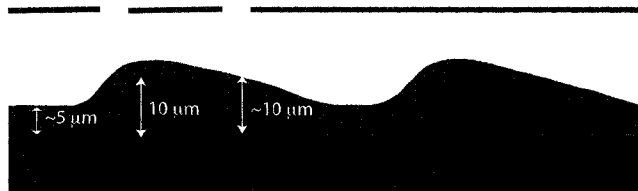
(a) An ideal step coverage



(b) In reality, the photoresist thickness varied across topography.



(c) An extra exposure time was needed to ensure the photoresist covering the walls was completely exposed and developed away. This resulted in excessive exposure of thinner photoresist on the top surface of the topography, loss of photoresist protection on these areas during the oxide etch step, and finally, deposition of epitaxial layer on the exposed silicon.



(d) At the edge of the wafer, the photoresist non-uniformity was more significant due to a higher centripetal force during photoresist spinning than that in the center of the wafer.

Figure 7.3: Problems encountered during the patterning of aluminum due because of poor step coverage and significant non-uniformity in the photoresist over topography.

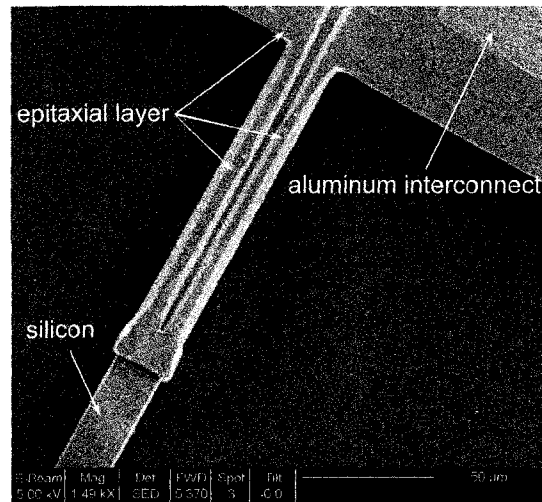


Figure 7.4: SEM image of the cantilever with sidewall epitaxial layers. Photoresist non-uniformity problem left insufficient space for the aluminum interconnect on the top surface of the cantilever.

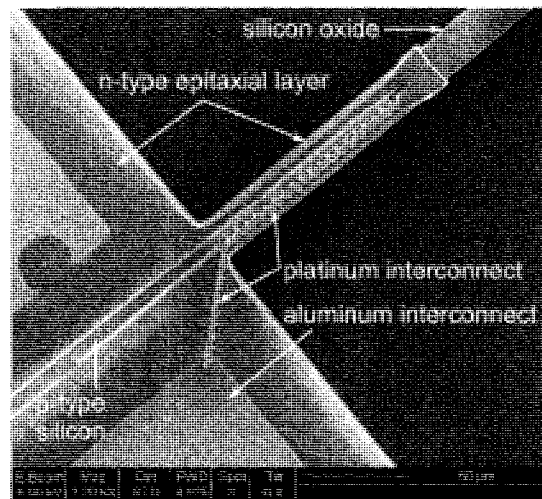


Figure 7.5: SEM image of the cantilever with sidewall epitaxial layers and FIB platinum (shown by the dashed line) deposited on the top of one of the piezoresistors.

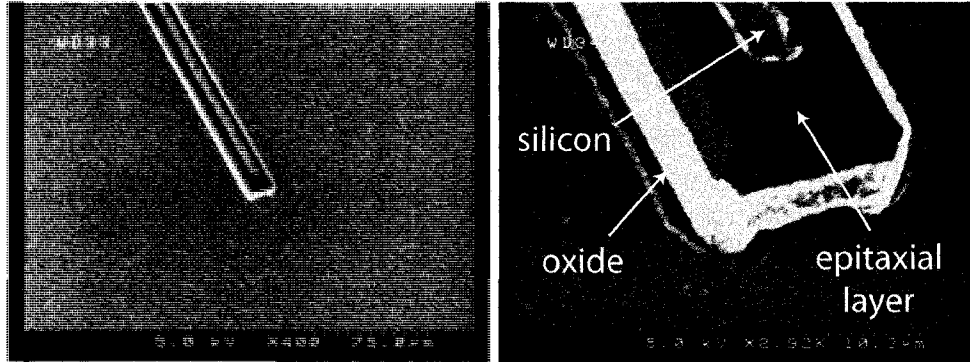


Figure 7.6: SEM images of the tip of a cantilever which did not have the protective oxide completely removed before epitaxial layer deposition. The epitaxial layer deposited on the exposed silicon surface, but did not deposit on the oxide layer due to the selective deposition recipe used in the process.

7.3.1 Deposition Rate

Test structures were included to study trench width effects on the deposition rate of epitaxial silicon layer. These data are useful for applications where the width of the trenches is limited by either space or hard stop requirements, such as in shear stress sensors and accelerometers [256, 257]. The thickness of the epitaxial layer deposited on the sidewall of trenches with varying width (5-500 μm) was measured in the SEM. It was found that as the trench width increases, the deposition rate decreases (Figure 7.7). This may be caused by temperature non-uniformity of exposed silicon surfaces during the deposition process. The silicon surface temperature in the smaller gaps is likely higher than that of the larger ones, thus enhancing the deposition rate [88]. Zhang et al. [265] reported that the deposition rate is independent of the trench (or window) size from 2.5 to 20 μm .

7.3.2 I-V Curve and Noise Characteristics

The electrical characteristics of a piezoresistor is shown in Figure 7.8. The relatively higher noise level might be due to the imperfect contact between platinum, aluminum,

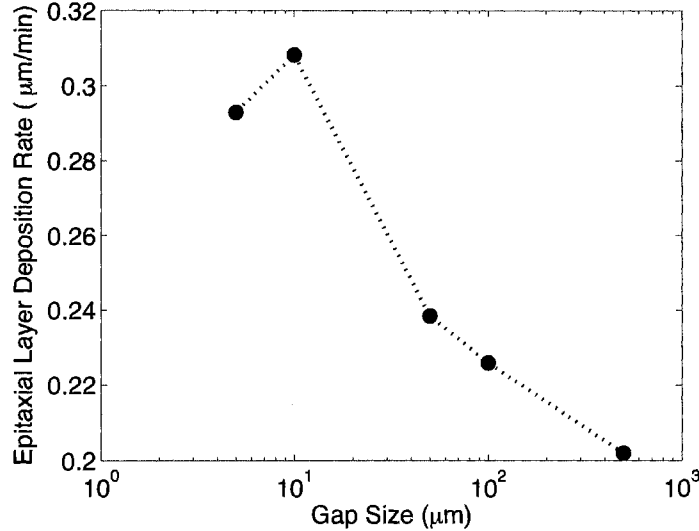


Figure 7.7: Deposition rate as a function of gap size. The deposition was done at 980°C and 30 Torr for 8 minutes.

and the silicon epitaxial layer, especially since the exponent of $1/f^n$ was $n = 1.6$, suggesting constriction resistance and noise $\propto V_{bias}$ [291]. Table 7.1 shows some voltage noise spectral densities of several ion-implanted and epitaxial layer piezoresistors at 10 Hz. The I-V characteristic of the piezoresistor was measured using Agilent 4156B. Resistance was calculated to be ~ 0.6 k Ω with good linearity from -5 to 5 Volts (inset of Figure 7.8).

7.3.3 Sensitivity

The sensitivities of the cantilevers were characterized using the previously reported Laser Doppler Vibrometer (LDV) technique [309, 310] (Section 5.1).

Three cantilevers with different ratios of piezoresistor to cantilever length ($\frac{L_p}{L_c}$) were tested. The cantilevers and a gold-plated surface mount board were epoxied onto a microscope slide. The microscope slide was then mounted on a 90° bracket and on a Jodon piezoelectric shaker (Figure 7.9). The laser head was positioned on top of the bracket setup and the laser was directed at the sidewall tip of the cantilever.

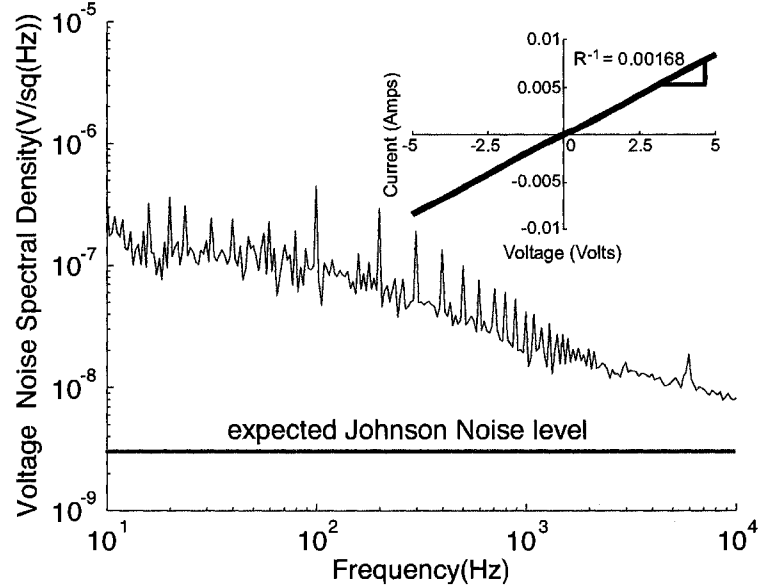


Figure 7.8: Noise spectrum of a 0.6 k Ω sidewall epitaxial piezoresistor with platinum measured using HP3562A Dynamic Signal Analyzer and a bias voltage of 0.1 V. The higher noise level might be due to the imperfect contact between the conductors and uncontrolled electromagnetic noise sources during the experiment. The corresponding I-V curve, measured using Agilent 4156B, showed Ohmic behavior ($r^2 = 0.9997$) and resistance of ~ 0.6 k Ω .

Table 7.1: Voltage noise spectral densities of several ion-implanted and epitaxial layer piezoresistors at 10 Hz.

Authors	Piezoresistor Type	Noise Spectral Density at 10 Hz. [nV/ $\sqrt{\text{Hz}}$]
Pruitt et al. [310]	Normal Implant	30
Chui et al. [303]	Sidewall Implant	130
Harley and Kenny [263]	Normal Epi Layer	160
Yu et al. [296]	Normal Implant	170
Partridge [315]	Sidewall Implant (unencapsulated)	320
Partridge [315]	Sidewall Implant (encapsulated)	40
Park et al. [257]	Sidewall Implant (unencapsulated)	200
Park et al. [257]	Sidewall Implant (encapsulated)	50
This work	Sidewall Epi Layer	200

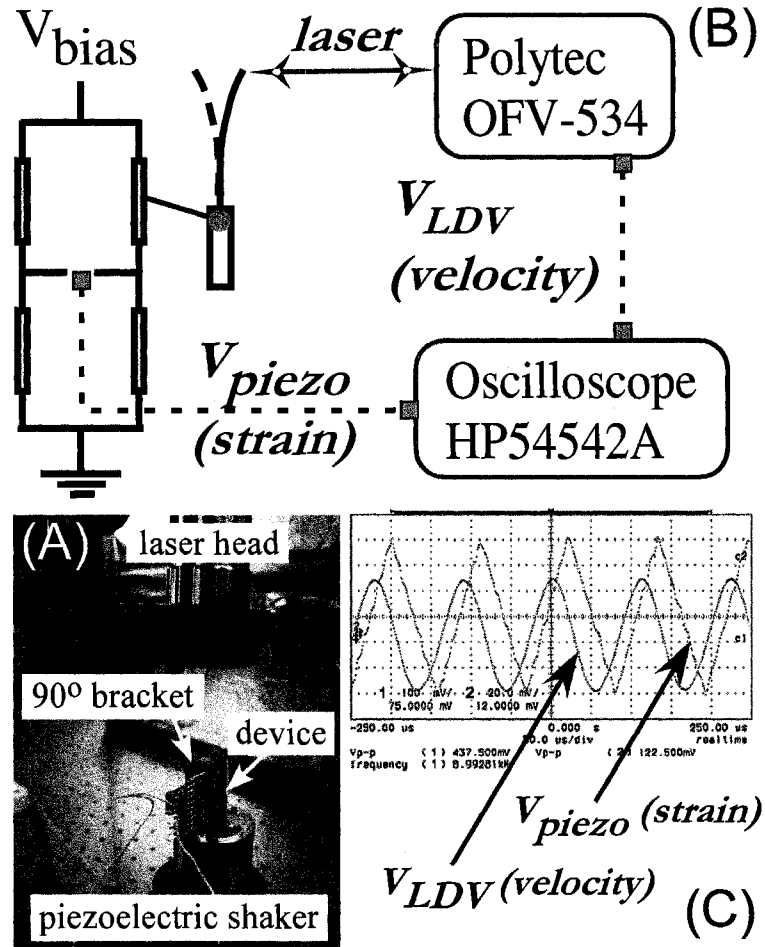


Figure 7.9: (A) The cantilever was mounted on a 90° bracket on a Jodan piezoelectric shaker. (B) Experimental setup for the sensitivity measurement. (C) Response from the vibrometer (Polytec OFV-534 Compact Sensor Head) and the Wheatstone bridge (with 1000× gain from AD622 amplifier) are captured with a HP89441A Vector Signal Analyzer and HP54542A oscilloscope. Two sinusoidal signals with a phase difference of 90° were expected. The triangle signal from the piezoresistor might be caused by a modified dynamic behavior of the cantilever due to the non-uniform cross-sectional area along the length of the cantilever, as shown in Figure 7.1.

Initially, the shaker was driven with white noise signal using a HP89441A Vector Signal Analyzer and the output from the vibrometer (Polytec OFV-534 Compact Sensor Head) is sent back to the signal analyzer to determine the resonant frequency, which was found to be ~ 8.92 kHz. The setting of the LDV controller was set to 10 mm/s/V. Then, the shaker was driven with a sinusoidal signal at the resonant frequency and the response from the vibrometer and the Wheatstone bridge (with $1000\times$ gain from AD622 amplifier) were captured with a HP54542A oscilloscope. The LDV measured the velocity of the tip of the cantilever, which was converted into displacement by integrating the signal. The tip displacement was then converted into input force by multiplication with the experimental spring constant. The Wheatstone bridge measured the strain at the root of the cantilever. Note that in this experiment, the Wheatstone bridge was in $1/4$ -bridge configuration since only one piezoresistor was used as a sensing element (the second one was cancelled out by the presence of the platinum line on top of it). The sensitivity was then inferred by dividing output of the Wheatstone bridge by the input force.

The bending stress at any point P on the cantilever, σ_P , when a point force is applied to the tip of a cantilever can be computed using

$$\sigma_P = \frac{Fly}{I} \quad (7.1)$$

where F is the point force applied at the tip, l is the distance from the tip of the cantilever to point P, y is the distance from the neutral axis of the cantilever to point P, and I is the area moment of inertia of the cantilever. In this chapter, the cantilever is subjected to in-plane bending, therefore $I = \frac{TW^3}{12}$, where T and W are the thickness and width of the cantilever, respectively. The stress must be averaged to take into account different stress levels experienced by infinitesimal elements of the piezoresistor across its length and thickness. In calculating the average stress, σ_{avg} , stresses experienced by all differential elements in the piezoresistor must be integrated

along its length and depth, and averaged, as shown by

$$\sigma_{avg} = \frac{\frac{F}{I} \int_{\frac{1}{2}T-t_j}^{\frac{1}{2}T} y \int_{L_c-L_p}^{L_c} l dl dy}{\left(\int_{\frac{1}{2}T-t_j}^{\frac{1}{2}T} dy \right) \left(\int_{L_c-L_p}^{L_c} dl \right)} \quad (7.2a)$$

$$\begin{aligned} &= \frac{F}{I} \frac{1}{2} (2L_c - L_p) \frac{1}{2} \left(2 \left(\frac{1}{2}T \right) - t_j \right) \\ &= \frac{F}{4I} (2L_c - L_p) (T - t_j) \\ &= \frac{3F}{TW^3} (2L_c - L_p) (T - t_j) \end{aligned} \quad (7.2b)$$

where t_j is the junction depth or the thickness of the piezoresistor, L_c is the length of the cantilever, and L_p is the length of the piezoresistor. The experimental longitudinal piezoresistive coefficients, $\pi_{l,exp}$, are computed using

$$\pi_{l,exp} = \frac{\frac{\Delta R}{R}}{\sigma_{avg}} \quad (7.3a)$$

$$= \frac{\frac{4V_{out}}{V_b}}{\sigma_{avg}} \quad (7.3b)$$

where $\frac{\Delta R}{R}$ is the relative change in the resistance of the piezoresistor due to average applied stress, σ_{avg} . V_{out} and V_b are the output and bias voltage of the $1/4$ -Wheatstone bridge. Substituting (7.2b) into (7.3b) yields

$$\pi_{l,exp} = \frac{\frac{4V_{out}}{V_b}}{\frac{3F}{TW^3} (2L_c - L_p) (T - t_j)}. \quad (7.4)$$

Finally, the experimental piezoresistive coefficient as a function of dopant concentration at room temperature, $P(N)$, can be calculated by dividing (7.3b) by the maximum piezoresistive coefficient, $\pi_{l,max}$, predicted by Kanda (Figure 3.8(b)) [178]. Since the piezoresistor is oriented in the $[100]$ direction, $\pi_{l,max}$ is $102 \times 10^{-11} \text{ Pa}^{-1}$. Figure 7.10 shows the values of experimental $P(N)$ from this work and other researchers [264, 345], as well as the theoretical prediction by Kanda [178]. Scattered

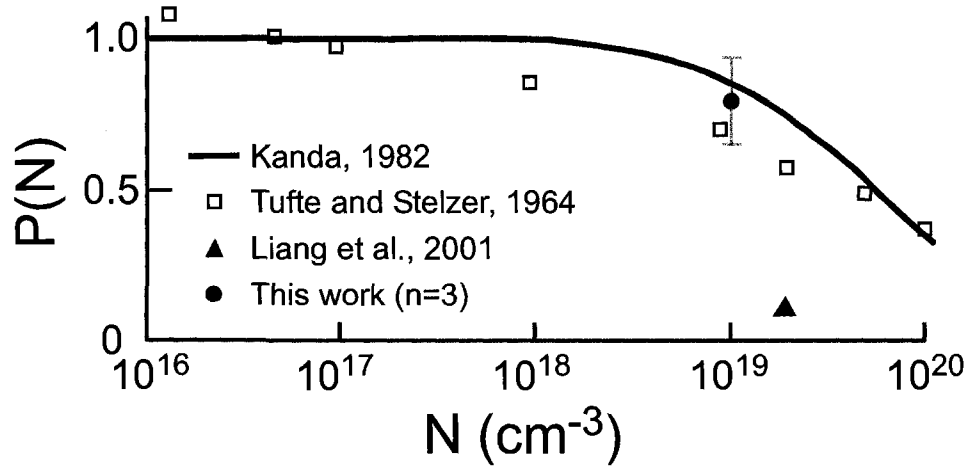


Figure 7.10: The values of experimental $P(N)$ from this work and other researchers [264, 345], as well as the theoretical prediction by Kanda [178].

data from this work could be due to uncertainties in the dimensions of the cantilevers (mainly W and T) and the piezoresistors (mainly t_j).

7.4 Improved Fabrication Method

The fabrication method described in Section 7.2.1 presented some challenges and problems (Section 7.2.2). This section describes a possible process variation to overcome those problems and presents some suggestions for a more reliable and manufacturable fabrication method.

The fabrication process (Figure 7.11) starts with a p-doped SOI wafer. An n-type dopant, e.g. phosphorous, is implanted to form a conductive line. This conductive line would later become the divider between the two sidewall piezoresistors, therefore eliminating the need for metal patterning on the top surface of the cantilevers. Next, a nitride film (~ 3000 Å) is deposited on the wafer surface. This nitride layer would later remain and cover the top surface of the cantilevers during the sidewall oxide etch process. A sufficiently thick layer of LTO (~ 1 μm) can also be used instead of a nitride layer. The thick LTO layer would not fully remain and cover the top surface

of the cantilevers after the sidewall oxide etch process since it would also be etched away (at a faster rate). However, it would still protect most part of the top surface of the cantilevers. The next step is to etch the nitride layer and the silicon underneath to form the geometry of the cantilevers using a DRIE process. Then, a thin layer of oxide ($\sim 1000 \text{ \AA}$) is thermally grown. This step anneals the ion-implanted conductive line and grows a thin layer of oxide on the sidewalls of the cantilevers. Anneal in a nitrogen ambient can be done if further anneal for the conductive line is needed. The next step is to pattern and etch the sidewall oxide using a wet etch process to expose the silicon where the doped epitaxial layer would be deposited. The nitride layer is then etched to allow a via between the conductive line and the epitaxial layer and/or metal, followed by selective epitaxial layer deposition on exposed silicon surfaces and metal sputtering (e.g. aluminum) or evaporation (e.g. gold). Finally, the cantilever release can be done by etching away the buried oxide layer using a wet etch process as described in Section 7.2.1 or by etching silicon from the backside of the wafer using a DRIE process, followed by etching the buried oxide layer using a wet etch process, as described in Section 4.2.

7.5 Note and Acknowledgement

Some of the content of this chapter was presented in “Sidewall Epitaxial Piezoresistor Process for In-Plane Sensing Applications,” *21st IEEE International Conference on Micro Electro Mechanical Systems*, Tucson, Arizona, 2008, and included in the conference proceedings [346]. I would like to thank: Nahid Harjee for depositing FIB platinum, Vikram Mukundan for releasing the cantilevers using CPD, Tracy Fung for the noise data, and Gary Yama of Bosch RTC for the selective epitaxial deposition recipe.

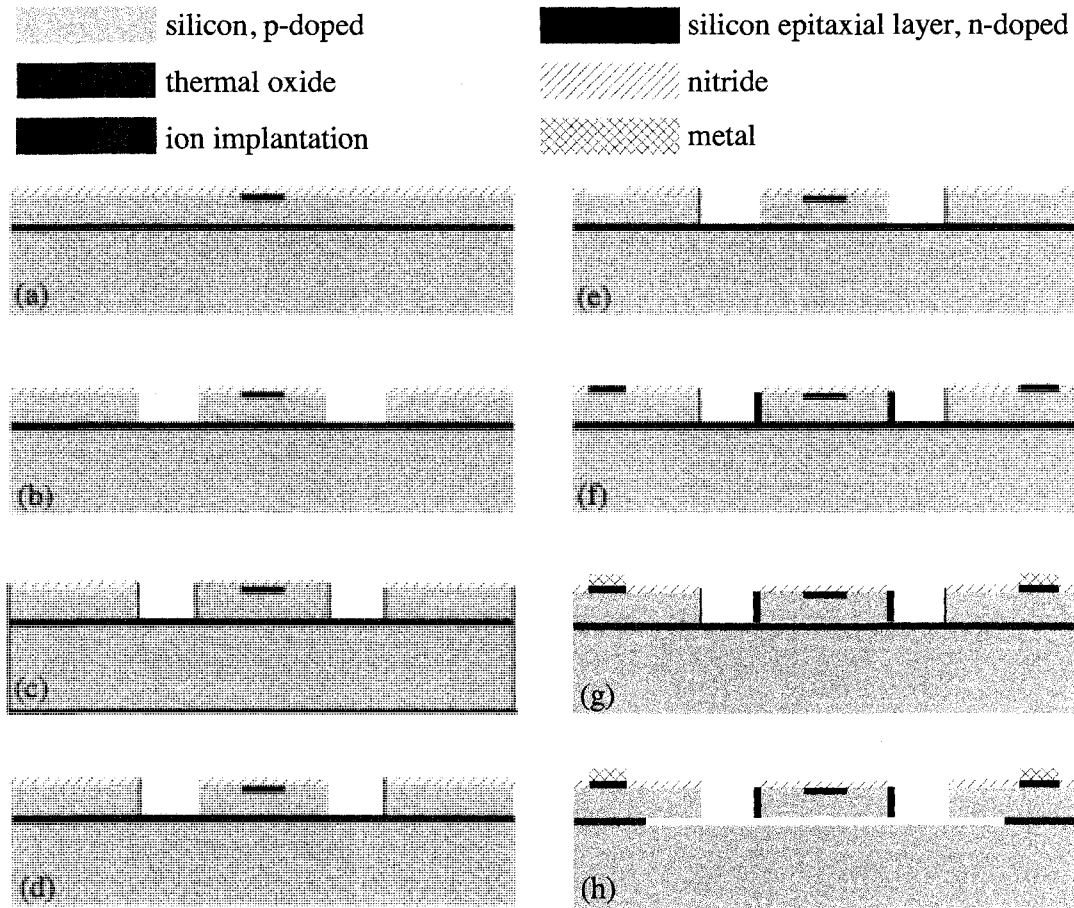


Figure 7.11: An alternative fabrication method to improve the reliability and repeatability of the sidewall epitaxial piezoresistors process: (a) A conducting line is formed using ion implantation and a nitride layer is deposited on the wafer surface. (b) The geometry of the cantilever is defined by etching the nitride and silicon layers using a DRIE process. (c) A thin layer of oxide is thermally grown on the sidewalls. (d) The sidewall oxide is patterned and etched using a wet etch process. (e) The nitride layer is etched to form a via between the conducting line and epitaxial layer and/or metal. (f) Doped epitaxial layer is selectively deposited. (g) Metal is sputtered (for aluminum) or evaporated (for gold). (h) The cantilevers are released.

Chapter 8

Conclusion and Future Work

8.1 Conclusion

This dissertation presented the design, fabrication, characterization, and testing results of microfabricated floating-element shear stress sensors for underwater applications. Direct measurements of shear stress in coral reef environments and cardiovascular systems were the motivation of this project.

The sensors used an oblique-angle ion-implantation technique to form piezoresistors on the sidewall of two tethers and the normal ion-implantation technique to form piezoresistors on the top surface of the other two tethers. Using this configuration, the sensors were sensitive to both in-plane and out-of-plane forces with minimum crosstalk. In the fabrication process, hydrogen anneal was used to smooth the roughness of the sidewalls by reflowing silicon atoms before the sidewall implant step. This anneal step reduced the noise of the resulting piezoresistors.

The in-plane sensitivity of the sensors was characterized using a calibrated microfabricated piezoresistive cantilever. The cantilever was used to apply a known force to the sensor, while output from the sensors was recorded. The cantilever and the out-of-plane sensitivity of the sensor were calibrated using the Laser Doppler Velocimetry technique.

Triplex layers of oxide-nitride-oxide and Parylene C were used to protect the piezoresistors and metal lines from the aqueous environment in solid-body rotation

and gravity driven flow experiments, respectively. In addition to Parylene C, polymer-based flexible flip-chip interconnects were fabricated and used in the gravity-driven flow testing. Micro Particle Image Velocimetry (μ PIV) experiments were used to characterize the effect of gap size on flow disturbance.

Finally, a promising fabrication technique to form piezoresistors on the sidewalls of microstructures by depositing single-crystal silicon epitaxial layer using selective deposition recipe was demonstrated. Piezoresistors were formed on the sidewalls of microfabricated cantilevers for in-plane force sensing. Preliminary results on their sensitivities and electrical characteristics were presented.

8.2 Future Work

The sensors presented in this dissertation still need further research and development before they can be employed in coral reef environments or cardiovascular systems and used as reliable shear stress measurement tools.

The most important and critical aspect is a reliable passivation scheme. Parylene C was demonstrated to be a reliable passivation scheme in this work. Deposition at room temperature and biocompatibility were some of its advantages. However, Parylene C still needs to be tested in saline water before parylene-passivated sensors can be employed in coral reef environments or cardiovascular systems. A novel “superlow biofouling material” could be used as an alternative passivation or coating layer for marine and biomedical applications [347, 348].

Each sensor can measure forces in two directions, i.e. y and z components (Figure 4.1). Two of these sensors can be placed next to each other and oriented 90° with respect to each other to obtain the third force component, x (Figure 4.1), allowing 3-D map of force measurements. These pairs of sensors can be arrayed on a single chip to allow larger force map on a surface. However, spatial resolution will be lost due to interconnects and bond pads from the arrayed sensors. To overcome this, electrical through-wafer interconnects (ETWI) can be used to run interconnects (metal or polysilicon) from one side of a substrate to the other [349, 350]. Bond pads can be placed on the back side of the substrate and connected to the piezoresistors on

the front side of the substrate by ETWI. Since underwater shear stress sensors must be exposed to their liquid environment while the interconnects can not, ETWI also allows a simpler packaging scheme by not having the bond pads, wirebonding, and external wires on the surface exposed to the liquid.

Polymers, such as SU-8, can be used as an alternative material to silicon. SU-8 allows the design and fabrication of flexible shear stress sensors skin, similar to those fabricated by Jiang et al. [112] with microfabricated hot-wire anemometry. However, SU-8 is also prone to swelling when submerged underwater, thus modifying the mechanical characteristics of the floating element. Piezoresistive SU-8/nanoparticles composites have been successfully demonstrated in the past [351]. Integrating piezoresistors with polymers is still an active area of research [351, 352].

Finally, sidewall epitaxial piezoresistors described in Chapter 7 can be integrated with future piezoresistive shear stress sensors. However, this promising technique still needs further research and development. More reliable and repeatable fabrication steps are required, e.g. during photoresist coating, metal sputtering, and sensor release. Spray coating results in a more uniform film and can be used during the lithography steps. The metal line dividing the cantilever sidewall piezoresistors can be replaced by an ion-implanted conductive line. Cantilever release can be done using the DRIE process instead of a wet etch process to avoid device stiction and breaking. Characterization results presented in this dissertation are preliminary and for proof of concept. Cantilevers with different dopant concentrations and dimensions are needed to fully characterize the sidewall piezoresistor performance. These cantilevers must be fabricated using a more repeatable and manufacturable process flow (without FIB metal) as suggested in Section 7.4. Sensitivity characterization can be improved by using a higher-magnification lens to produce a better-focused laser spot and a smoother sinusoidal signal. Noise characterization needs to be repeated in a more controlled setting to minimize external noise sources, e.g. in an improved enclosure and on a vibration-free optical table. The deposition rate (as a function of gap size) data presented in this dissertation were obtained from a set of trenches at the center of the wafer. The sidewall epitaxial layer thickness from other parts of the wafer must also be measured to determine the deposition uniformity and fully characterize

the effect of gap size on the deposition rate. Once completely characterized, these sidewall-epitaxial-piezoresistor cantilevers (or shear stress sensors) can be passivated with Parylene C and their noise and sensitivity can be characterized in liquid. Fluid-structure interactions between the sensors and their surrounding liquid must also be studied to accurately predict the sensor resonant frequency and dynamic behavior. Mini channel and μ PIV can be used to characterize and test in-plane sensitivity of the sensors. The rotating table and the gravity-driven water flume described in Section 6 were prone to mechanical vibrations from the motor or pumps. Consequently, theoretical flow profiles were difficult to achieve.

Appendix A

Process Run Sheets

This section lists the fabrication process run sheets used in this work to fabricate shear stress sensors, polymer flip-chip flexible interconnects, and selective sidewall epitaxial piezoresistors. All the fabrication processes were done at the Stanford Nanofabrication Facility (SNF). All the tools/equipment used in this work were available at SNF, unless otherwise noted (e.g. Ginzton Lab). Note that exposure time in the lithography steps may vary.

Table A.1: Shear stress sensor fabrication process run sheet.

Step	Process	Target	Setting 1	Setting 2	Tool
0	Scribe Wafers	-	-	-	diamond-tip scriber
1	Clean Wafers	-	piranha	20 min., 120°C	wbnonmetal
2	Lithography Mask 1 Alignment Marks	1 μm SPR3612	hard contact	exposure: 1 sec. gap: 40 μm wait: 5 sec. CI1	YES Oven svgcoat (9,2,1) karlsuss/EV svgdev (3,1) 110°C oven (30 min.)
3	Silicon Etch	4000 Å	nitride etch recipe	1.5 min.	drytek2
4	Resist Strip	-	piranha	-	wbnonmetal
5	Diffusion Clean	-	standard clean	-	wbdiffusion
6	Oxide Growth	250 Å	WET850	13 min.	tylan1-4
7	Lithography Mask 2 Piezo Implant	1.6 μm SPR3612	hard contact	exposure: 1.3 sec. gap: 40 μm wait: 5 sec. CI1	YES oven svgcoat (9,2,2) karlsuss/EV svgdev (4,2) 110°C oven (30 min.)
8	Ion Implantation	0.3 μm	boron	$1 \times 10^{15} \text{ cm}^{-2}$ 50 keV, 7°	implanter350
9	Resist Strip	-	oxygen plasma piranha	-	matrix wbnonmetal

Continued on Next Page...

Table A.1 – Continued

Step	Process	Target	Setting 1	Setting 2	Tool
10	Lithography Mask 3 Conductive Region Implant	1.6 μm SPR3612	hard contact	exposure: 1.3 sec. gap: 40 μm wait: 5 sec. CI1	YES oven svgcoat (9,2,2) karlsuss/EV svgdev (4,2) 110°C oven (30 min.) implanter350
11	Ion Implantation	0.3 μm	boron	$1 \times 10^{16} \text{ cm}^{-2}$ 50 keV, 7°	
12	Resist Strip	-	oxygen plasma piranha	-	matrix wbnonmetal
13	Oxide Etch	250 Å	6:1 BOE	-	wbnonmetal
14	Diffusion Clean	-	standard clean	-	wbdiffusion
15	RTA	-	1050°C	75 sec.	ag4108
16	Diffusion Clean	-	standard clean	-	wbdiffusion
17	LTO	1.1 μm	LTO400	70 min.	tylanbpsg
18	Lithography Mask 4 Frontside Etch	1.6 μm SPR3612	hard contact	exposure: 1.3 sec. gap: 40 μm wait: 5 sec. CI1	YES oven svgcoat (9,2,2) karlsuss/EV svgdev (4,2) 110°C oven (30 min.) UV expose (15 min.) amtetcher
19	LTO Etch	1.1 μm	program 4	35 min.	

Continued on Next Page...

Table A.1 – Continued

Step	Process	Target	Setting 1	Setting 2	Tool
20	Polymer removal	-	process 1	60 sec.	drytek2
21	Silicon Etch	7-20 μm	ANB SHAL	4-5 min.	STSetch
22	Resist and Polymer Strip	-	oxygen plasma piranha	-	matrix wbnonmetal
23	LTO Etch	0.2 μm	20:1 BOE	2-3 min.	wbnonmetal
24	Diffusion Clean	-	without HF dip	-	wbdiffusion
25	Hydrogen Anneal	-	1000°C	10 Torr, 5 min.	epi1
26	Lithography Mask 5 Sidewall Implant	1.6 μm SPR3612	hard contact	exposure: 9.9 sec. gap: 40 μm wait: 5 sec. CI1	YES oven svgcoat (9,2,2) karlsuss/EV svgdev (4,2) 110°C oven (45 min.)
27	Ion Implantation	$4 \times 10^{15} \text{ cm}^{-2}$	boron	40 keV, 20°	implanter350
28	Resist Strip	-	oxygen plasma piranha	-	matrix wbnonmetal
29	LTO Etch	8000-10,000 Å	6:1 BOE	12 min.	wbnonmetal
30	Diffusion Clean	-	standard clean	-	wbdiffusion
31	RTA	-	1050°C	75 sec.	ag4108
32	Oxide Growth	2100 Å	WET1000A	30 min., 5 min.	tylan1-4
33	Lithography Mask 6 Via Etch	1 μm SPR3612	hard contact	exposure: 1 sec. gap: 40 μm wait: 5 sec. CI1	YES oven svgcoat (9,2,1) karlsuss/EV svgdev (3,1)

Continued on Next Page...

Table A.1 – Continued

Step	Process	Target	Setting 1	Setting 2	Tool
34	Oxide Etch	2100 Å	6:1 BOE	600 sec.	wbsonmetal
35	Resist Strip	-	piranha	-	wbsonmetal
36	Diffusion Clean	-	standard clean	50:1 HF (2×)	wbdiffusion
37	Sputtering	1 µm	99%Al/1%Si	600 sec.	gryphon
38	Lithography	1.6 µm SPR3612	hard contact	exposure: 1 sec.	YES oven
	Mask 7			gap: 40 µm	svgcoat (9,2,2)
	Metal Etch			wait: 5 sec.	karlsuss/EV
				CI1	svgdev (4,2)
39	Aluminum Etch	1 µm	aluminum etch	4 min.	wbsonmetal
	<i>Aluminum must be completely gone in the trenches. Etch more if needed.</i>				
40	Resist Strip	-	piranha	-	wbsonmetal
41	Silicon Etch	60 Å	contact clean	30 sec.	drytek2
	<i>Steps 42-49 are needed only for oxide/nitride/oxide triplex layer passivation.</i>				
	<i>The equipment "stspecvd" need to be decontaminated before use to make it a semi-clean equipment.</i>				
42	Oxide Deposition	1300 Å	std.lfox	5.5 min.	stspecvd
43	Nitride Deposition	5400 Å	aabnit540	120 min.	stspecvd
44	Oxide Deposition	1300 Å	std.lfox	5.5 min.	stspecvd
45	Lithography	1.6 µm SPR3612	hard contact	exposure: 1.3 sec.	YES oven
	Mask 8			gap: 40 µm	svgcoat (9,2,2)
	Open Bond Pads			wait: 5 sec.	karlsuss/EV
				CI1	svgdev (4,2)
46	Oxide Etch	1300 Å	oxide etch	1.5 min.	wbsonmetal
47	Nitride Etch	5400 Å	nitride etch	2.5 min.	drytek2

Continued on Next Page...

Table A.1 – Continued

Step	Process	Target	Setting 1	Setting 2	Tool
48	Oxide Etch	1300 Å	oxide etch	1.5 min.	wbmetal
49	Resist Strip	-	piranha	-	wbnonmetal
50	Frontside Protection	10 µm SPR220-7	-	-	YES oven svgcoat (9,6,3) 90°Coven (30 min.)
51	Lithography Mask 9 Backside Etch	10 µm SPR220-7	hard contact	exposure: 14 sec. gap: 40 µm wait: 5 sec. CI1	YES oven svgcoat (9,6,9) karlsuss/EV svgdev (6,N/A) 110°C oven (45 min.) UV expose (15 min.)
<i>No resist bake at the svgcoat. Multi exposure is recommended, e.g. 4 × 3.5 sec. instead of 1 × 14 sec.</i>					
<i>After coating, wait at least 2 hr. before exposure.</i>					
52	Silicon Etch	300-500 µm	deep	80-120 min.	stsetch
53	Oxide Etch	~ 0.5µm (BOX)	6:1 BOE	~ 6 min.	wbmetal
54	Resist and Polymer Strip	-	oxygen plasma piranha	-	drytek2 wbmetal
55	Diffusion Clean	-	standard clean	-	wbmetal
56	FGA	-	400°C	2 hr.	tylanfga

Table A.2: Polymer flip-chip flexible interconnects fabrication process run sheet.

Step	Process	Target	Setting 1	Setting 2	Tool
<i>Kapton film (DuPont HN125) with a thickness of 125 μm is cut into a 4 in.-wafer shape and then taped onto the top surface of a 4 in.-silicon wafer using standard kapton tape. Make sure that the kapton film and the backing wafer are in perfect contact to minimize air pockets between them.</i>					
1	Chromium Deposition	35 nm	evaporation	-	Ginzton Lab
2	Gold Deposition	350 nm	evaporation	-	Ginzton Lab
3	Lithography Mask 1 Metal Etch	1.6 μm SPR3612	hard contact	exposure: 1.3 sec. gap: 40 μm wait: 5 sec. CI1	YES Oven svgcoat (9,2,1) karlsuss/EV svgdev (4,2) 110°C oven (30 min.) wbgeneral
4	Gold Etch	350 nm	Transene Gold Etchant	-	wbgeneral
5	Chromium Etch	35 nm	CR-14 Chromium Etchant	-	wbgeneral
6	Resist Strip	-	acetone methanol isopropanol	-	wbsolvent
7	Lithography Mask 2 Open Bond Pads	15 μm SPR220-7	hard contact	exposure: 15-20 sec. gap: 40 μm wait: 5 sec. CI1	YES Oven svgcoat (9,6,9) karlsuss/EV svgdev (6,N/A) 110°C oven (30 min.)

Continued on Next Page...

Table A.2 – Continued

Step	Process	Target	Setting 1	Setting 2	Tool
8	Conductive Polymer	15 μm Epo-Tek-K/5022-115BE	squeegee	-	-
9	Polymer Curing	-	-	-	110°C oven (15 min.)
10	Resist Strip	-	acetone methanol isopropanol	-	wbsolvent

*The kapton film is released from its backing wafer by peeling off the kapton tape.
The kapton film is then cut into individual pieces of polymer flexible interconnects.*

Table A.3: Selective sidewall epitaxial piezoresistor process run sheet.

Step	Process	Target	Setting 1	Setting 2	Tool
0	Scribe Wafers	-	-	-	diamond-tip scribe
1	Clean Wafers	-	piranha	20 min., 120°C	wbnonmetal
2	Lithography Mask 1 Silicon Etch	1.6 μm SPR3612	hard contact	exposure: 1.5 sec. gap: 40 μm wait: 5 sec. CI1	YES Oven svgcoat (9,2,2) karlsuss/EV svgdev (4,2) 110°C oven (30 min.) UV-light bake
3	Silicon Etch	10-20 μm	SMOOSHALL	3-6 min.	stsetch
4	Resist and Polymer Strip	-	oxygen plasma piranha	recipe 013	gasonic wbnonmetal
5	Diffusion Clean	-	standard clean	-	wbdiffusion
6	Oxide Growth	3800 \AA	WET1050	36 min.	tylan1-2
7	Lithography Mask 2 Oxide Etch	7-10 μm SPR220-7	hard contact	exposure: 10-15 sec. gap: 40 μm wait: 5 sec. CI1	YES Oven svgcoat (9,6,9) karlsuss/EV svgdev (6,N/A) 110°C oven (30 min.)
8	Oxide Etch	3800 \AA	6:1 BOE	4.5 min.	wbnonmetal
9	Resist Strip	-	piranha	-	wbnonmetal
10	Diffusion Clean	-	standard clean	-	wbdiffusion
11	Epitaxial Deposition	2 μm	Table B.1	8 min.	epi

Continued on Next Page...

Table A.3 – Continued

Step	Process	Target	Setting 1	Setting 2	Tool
12	Diffusion Clean	-	standard clean	-	wbdiffusion
13	Sputtering	2 μm	99%Al/1%Si	2 \times 600 sec.	gryphon
14	Lithography	7-10 μm SPR220-7	hard contact	exposure: 10-15 sec.	YES oven
	Mask 3			gap: 40 μm	svgcoat (9,6,9)
	Metal			wait: 5 sec.	karlsuss/EV
	Patterning			CI1	svgdev (6,N/A)
					110°C oven (30 min.)
15	Aluminum Etch	2 μm	aluminum etch	8 min.	wbmetal
16	Resist Strip	-	piranha	-	wbmetal
17	Silicon Etch	60 \AA	contact clean	30 sec.	drytek2
18	Diffusion Clean	-	standard clean	-	wbmetal
19	FGA	-	400°C	2 hr.	tylanfga
	<i>The next lithography step is to protect aluminum during the release (oxide etch).</i>				
20	Lithography	1.6 μm SPR3612	hard contact	exposure: 1.5 sec.	YES oven
	Mask 1			gap: 40 μm	svgcoat (9,2,2)
	Silicon Etch			wait: 5 sec.	karlsuss/EV
				CI1	svgdev (4,2)
					110°C oven (30 min.)
21	Wafer Sawing	-	-	-	wafersaw
	<i>The chips must be kept wet from step#22 to step #24 by submerging them in a beaker of water during the transition between steps.</i>				
22	Oxide Etch	0.5 μm (BOX)	6:1 BOE	2 hr.	wbgeneral

Continued on Next Page...

Table A.3 – Continued

Step	Process	Target	Setting 1	Setting 2	Tool
23	Resist Strip	-	acetone methanol isopropanol	-	wbsolvent
24	Critical Point Drying	-	-	2 hrs.	cpd

Appendix B

Selective Epitaxial Deposition Recipe

This section lists the recipe used in the selective epitaxial piezoresistor fabrication process.

Table B.1: Selective doped epitaxial deposition recipe. The deposition time can be varied according to the desired epi layer thickness (step #16), while the deposition temperature and pressure are 980°C and 30 Torr, respectively.

	START	HEAT1	HEAT2	ETCH1	ETCH2	ETCH3	COOL	HOMESUS
step #	1	2	3	4	5	6	7	8
time (sec.)	0.1	200	40	120	120	60	200	15
token	-	-	-	-	-	-	-	-
center (°C)	800	1170R	1170	1170	1170	1170	800R	800
dep/vent	vent	vent	vent	vent	vent	vent	vent	vent
N ₂ H ₂	20H	10HR	10H	10H	80HR	80H	80H	10HR
rotation	0	25RU	25U	25U	25U	25D	25D	0
HCl Hi	0V	0V	20E	20E	20E	20E	20E	0V
HCl	0V	0V	500E	500E	500E	500E	500E	0V
DCS	0	0	0	0	0	0	0	0
SiH ₄	0	0	0	0	0	0	0	0
N-Src	0	0	0	0	0	0	0	0
N-Inj	0	0	0	0	0	0	0	0
N-Dil	0	0	0	0	0	0	0	0
front	0	0	0	0	0	0	0	0
side	0	0	0	0	0	0	0	0
rear	0	0	0	20R	20	20	0R	0
pressure	ATM	ATM	ATM	ATM	ATM	ATM	ATM	ATM
vent match	0	0	0	0	0	0	0	0

Continued on Next Page...

Table B.1 - Continued

	LOAD	ROTATE	TEMP UP	BAKE	TEMP DN	STAB	TEMP CK
step #	9	10	11	12	13	14	15
time (sec.)	0.1	20	200	180	90	60	0.1
token	load	-	-	-	-	-	-
center (°C)	700	800R	1130R	1130	980R	980	980S
dep/vent	vent	vent	vent	vent	vent	vent	vent
N ₂ H ₂	10H	20HR	20H	20H	40HR	40H	40H
rotation	0	35RD	*same	*same	*same	*same	*same
HCl Hi	0V	0V	0V	0V	0V	0V	0V
HCl	0V	0V	0V	0V	500VR	500V	500V
DCS	0	0	0	0	400R	400	400
SiH ₄	0	0	0	0	0	0	0
N-Src	0	0	0	180	180	180	180
N-Inj	0	0	0	60	60	60	60
N-Dil	0	0	0	0	0	0	0
front	0	0	20	20	0	0	20
side	0	0	50	50	0	0	50
rear	0	0	10	10	0	0	10
pressure	ATM	ATM	30	30	30	30	30
vent match	0	0	1	1	1	1	1

Continued on Next Page...

Table B.1 – Continued

	DEP	POSTPRG	RAMPDN	HOMESUS	UNLOAD	REHEAT	END
step #	16	17	18	19	20	21	22
time (sec.)	480	10	85	15	0.1	30	1
token	-	-	backfill	-	unload	-	end
center (°C)	980	980	800R	800	700	800R	800
dep/vent	deposit	vent	vent	vent	vent	vent	vent
N ₂ H ₂	40H	40H	40H	10HR	10H	20H	20H
rotation	*same	*same	10RD	0	0	0	0
HCl Hi	0V	0V	0V	0V	0V	0V	0V
HCl	500E	0V	0V	0V	0V	0V	0V
DCS	400	0	0	0	0	0	0
SiH ₄	0	0	0	0	0	0	0
N-Src	180	0	0	0	0	0	0
N-Inj	60	0	0	0	0	0	0
N-Dil	0	0	0	0	0	0	0
front	20	0	0	0	0	0	0
side	50	0	0	0	0	0	0
rear	10	0	0	0	0	0	0
pressure	30	30	ATM	ATM	ATM	ATM	ATM
vent match	1	1	0	0	0	0	0

Appendix C

TSUPREM-4 Codes

```
# This code is used to simulate the dopant profiles from  
# "top piezoresistor" and "conducting region" implants.
```

```
# NOTE: There are some indented lines in this code.  
# In the actual TSUPREM-4 code, they are written on the same line  
# as the proceeding line. Here, they are written in two separate  
# lines due to the margin rules of this dissertation document.
```

```
option device=X  
option device=ps plot.out=shearsensor.plot
```

```
# x width is only 1 micron with 3 data points, look at middle  
line x loc=0.0 spacing=0.5 tag=left  
line x loc=1.0 spacing=0.5 tag=right
```

```
# depth of analysis is 12 microns, spacing interpolates  
# from top to bottom  
line y loc=0.0 spacing=0.01 tag=top  
line y loc=12.0 spacing=0.10 tag=bottom
```

```
region silicon xlo=left xhi=right ylo=top yhi=bottom
bound exposed xlo=left xhi=right ylo=top yhi=top
initialize <100> impurity=phosphorus i.resistivity=5.00

# Oxide grown before the implant.
method vertical pd.full ^pair.rec grid.oxi=1.0
diffusion time=10 temperature=800 inert
diffusion time=10 temperature=850 dry02
diffusion time=13 temperature=850 wet02
diffusion time=10 temperature=850 dry02
diffusion time=10 temperature=850 t.final=800 inert

# List the layers
select
print.1d layers x.v=0.0

# Top piezoresistor implant is done at 1E15 cm-2, 50 keV, 7 deg tilt
# Conducting region implant is done at 1E16 cm-2, 50 keV, 7 deg tilt
implant boron dose=1.0E15 energy=50 tilt=7 damage

# Plot the dopant profiles after implant
select z=log10(abs(doping)) title="Doping Profile, Before Anneal"
plot.1d x.val=0.25 y.min=14 y.max=21 x.min=-0.2 x.max=12.0 symbol=2
select z=log10(boron)
plot.1d x.val=0.25 y.min=14 y.max=21 x.min=-0.2 x.max=12.0
    ^axes ^clear
select z=log10(phosphorus)
plot.1d x.val=0.25 y.min=14 y.max=21 x.min=-0.2 x.max=12.0
    ^axes ^clear

electrical resist
```

```
# List the layers
select
print.1d layers x.v=0.0

#List the metallurgical junctions
select z=doping
print.1d spot=0

# Remove the implant oxide and RTA in dry O2
etch oxide all
method vertical pd.full ^pair.rec grid.oxi=1.0
diffusion time= 0.042 temperature=400 t.rate= +6000.00 inert
diffusion time= 1.25 temperature=1050 inert
diffusion time= 0.042 temperature= 1050 t.rate= -6000.00 inert

# Plot the dopant profiles after RTA anneal
select z=log10(abs(doping)) title="Doping Profile, After RTA"
plot.1d x.val=0.25 y.min=12 y.max=21 x.min=-0.2 x.max=12.0 symbol=3
  ^axes ^clear
select z=log10(boron)
plot.1d x.val=0.25 y.min=12 y.max=21 x.min=-0.2 x.max=12.0
  ^axes^clear
select z=log10(phosporous)
plot.1d x.val=0.25 y.min=12 y.max=21 x.min=-0.2 x.max=12.0
  ^axes^clear

electrical resist

# List the layers
select
```

```
print.1d layers x.v=0.0

# List the metallurgical junctions
select z=doping
print.1d spot=0

# LTO Deposition
deposition oxide THICKNES=1 temperat=400

# The steps below are needed if LTO densification is needed.
# densification wet950
# method vertical pd.full pair.rec grid.oxi=1.0
# diffusion time= 30 temperature= 950 inert
# diffusion time= 5 temperature= 950 dryO2
# diffusion time= 20 temperature= 950 wetO2
# diffusion time= 5 temperature= 950 dryO2
# diffusion time= 30 temperature= 850 t.final=750 inert

# Plot the dopant profiles after LTO densification
# select z=log10(abs(doping)) title="Doping Profile After
  LTO Densification"
# plot.1d x.val=0.25 y.min=12 y.max=21 x.min=-0.2 x.max=12.0 symbol=4
  ^axes ^clear
# select z=log10(boron)
# plot.1d x.val=0.25 y.min=12 y.max=21 x.min=-0.2 x.max=12.0
  ^axes ^clear
# select z=log10(phosporous)
# plot.1d x.val=0.25 y.min=12 y.max=21 x.min=-0.2 x.max=12.0
  ^axes ^clear

electrical resist
```

```
# List the layers
select
print.1d layers x.v=0.0

# List the metallurgical junctions
select z=doping
print.1d spot=0

# The steps below are needed if protective oxide for
# sidewall implant is needed.
# Protective oxide for side wall - RTO
# method vertical pd.full ^pair.rec grid.oxi=1.0
# diffusion time= 0.083 temperature=400 t.rate= +6000.00 wetO2
# diffusion time= 1.5 temperature=1050 wetO2
# diffusion time= 0.083 temperature= 1050 t.rate= -6000.00 wetO2

# Plot the dopant profiles after Side Wall Protective Oxide
# select z=log10(abs(doping)) title="Doping Profile, After Side Wall
  Protective Oxide"
# plot.1d x.val=0.25 y.min=12 y.max=21 x.min=-0.2 x.max=12.0 symbol=5
  ^axes ^clear
# select z=log10(boron)
# plot.1d x.val=0.25 y.min=12 y.max=21 x.min=-0.2 x.max=12.0
  ^axes ^clear
# select z=log10(phosphorous)
# plot.1d x.val=0.25 y.min=12 y.max=21 x.min=-0.2 x.max=12.0
  ^axes ^clear

electrical resist
```

```
# List the layers
select
print.1d layers x.v=0.0

# List the metallurgical junctions
select z=doping
print.1d spot=0

# Hydrogen Anneal
method vertical pd.full ^pair.rec grid.oxi=1.0
diffusion time= 0.083 temperature=400 t.rate= +6000.00 inert
diffusion time= 5.0 temperature=1000 F.H2=100
diffusion time= 0.083 temperature= 1050 t.rate= -6000.00 inert

electrical resist

# List the layers
select
print.1d layers x.v=0.0

# List the metallurgical junctions
select z=doping
print.1d spot=0

# Etch all oxide and RTA Anneal for Side Piezo
etch oxide all
method vertical pd.full ^pair.rec grid.oxi=1.0
diffusion time= 0.083 temperature=400 t.rate= +6000.00 inert
diffusion time= 1.25 temperature=1050 inert
diffusion time= 0.083 temperature= 1050 t.rate= -6000.00 inert
```



```
# Plot the dopant profiles after anneal
select z=log10(abs(doping)) title="Doping Profile After 2nd
      RTA Anneal"
plot.1d x.val=0.25 y.min=12 y.max=21 x.min=-0.2 x.max=12.0 symbol=3
      ^axes ^clear
select z=log10(boron)
plot.1d x.val=0.25 y.min=12 y.max=21 x.min=-0.2 x.max=12.0
      ^axes ^clear
select z=log10(antimony)
plot.1d x.val=0.25 y.min=12 y.max=21 x.min=-0.2 x.max=12.0
      ^axes ^clear

# List the layers
select
print.1d layers x.v=0.0

# List the metallurgical junctions
select z=doping
print.1d spot=0

electrical resist

#Grow final passivation oxide
method vertical pd.full ^pair.rec grid.oxi=1.0
diffusion time= 35 temperature= 800 t.rate= +5.71 inert
diffusion time= 10 temperature= 1000 dryO2
diffusion time= 30 temperature= 1000 wetO2
diffusion time= 10 temperature= 1000 dryO2
diffusion time= 5 temperature= 1000 inert
diffusion time= 30 temperature= 1000 t.rate= -8.33 inert
```

```
#Plot the dopant profiles after oxidation
select z=log10(abs(doping)) title="Doping Profile
      After Passivation Oxide Growth"
plot.1d x.val=0.25 y.min=12 y.max=21 x.min=-0.2 x.max=12.0 symbol=4
      ^axes ^clear
select z=log10(boron)
plot.1d x.val=0.25 y.min=12 y.max=21 x.min=-0.2 x.max=12.0
      ^axes ^clear
select z=log10(antimony)
plot.1d x.val=0.25 y.min=12 y.max=21 x.min=-0.2 x.max=12.0
      ^axes ^clear

#List the layers
select
print.1d layers x.v=0.0

# List the metallurgical junctions
select z=doping
print.1d spot=0

electrical resist

# End of Code

=====

# This code is used to simulate the dopant profiles from
# "sidewall piezoresistor" implant.

# In this code, indented lines should be written
# on the same line as the preceding line.
```

```
option device=X
option device=ps plot.out=shearsensor.plot

# x width is only 1 micron with 3 data points, look at middle
line x loc=0.0 spacing=0.5 tag=left
line x loc=1.0 spacing=0.5 tag=right

# depth of analysis is 12 microns, spacing interpolates
# from top to bottom
line y loc=0.0 spacing=0.01 tag=top
line y loc=12.0 spacing=0.10 tag=bottom

region silicon xlo=left xhi=right ylo=top yhi=bottom
bound exposed xlo=left xhi=right ylo=top yhi=top
initialize <100> impurity=phosphorus i.resistivity=5.00

# The steps below are needed if protective oxide for
# sidewall implant is needed.
# Protective oxide for side wall - RTO
# method vertical pd.full ^pair.rec grid.oxi=1.0
# diffusion time= 0.083 temperature=400 t.rate= +6000.00 wetO2
# diffusion time= 1.5 temperature=1050 wetO2
# diffusion time= 0.083 temperature= 1050 t.rate= -6000.00 wetO2

# Sidewall implant is done at 4E15 cm-2, 40 keV, 20 deg tilt
# with respect to the wafer surface normal axis, which corresponds to
# 70 deg tilt with respect to the sidewall normal axis.
implant boron dose=4.0E15 energy=40 tilt=70 damage

# Plot the dopant profiles after sidewall implant
```

```
select z=log10(abs(doping)) title="Doping Profile
  After Sidewall Implant"
plot.1d x.val=0.25 y.min=14 y.max=21 x.min=-0.2 x.max=12.0 symbol=2
select z=log10(boron)
plot.1d x.val=0.25 y.min=14 y.max=21 x.min=-0.2 x.max=12.0
  ^axes ^clear
select z=log10(phosphorus)
plot.1d x.val=0.25 y.min=14 y.max=21 x.min=-0.2 x.max=12.0
  ^axes ^clear

electrical resist

# List the layers
select
print.1d layers x.v=0.0

#List the metallurgical junctions
select z=doping
print.1d spot=0

# Etch all oxide and RTA Anneal for Side Piezo
etch oxide all
method vertical pd.full ^pair.rec grid.oxi=1.0
diffusion time= 0.083 temperature=400 t.rate= +6000.00 inert
diffusion time= 1.25 temperature=1050 inert
diffusion time= 0.083 temperature= 1050 t.rate= -6000.00 inert

# Plot the dopant profiles after anneal
select z=log10(abs(doping)) title="Doping Profile
  After RTA Anneal
plot.1d x.val=0.25 y.min=12 y.max=21 x.min=-0.2 x.max=12.0 symbol=3
```

```
^axes ^clear
select z=log10(boron)
plot.1d x.val=0.25 y.min=12 y.max=21 x.min=-0.2 x.max=12.0
^axes ^clear
select z=log10(antimony)
plot.1d x.val=0.25 y.min=12 y.max=21 x.min=-0.2 x.max=12.0
^axes ^clear

# List the layers
select
print.1d layers x.v=0.0

# List the metallurgical junctions
select z=doping
print.1d spot=0

electrical resist

#Grow final passivation oxide
method vertical pd.full ^pair.rec grid.oxi=1.0
diffusion time= 35 temperature= 800 t.rate= +5.71 inert
diffusion time= 10 temperature= 1000 dryO2
diffusion time= 30 temperature= 1000 wetO2
diffusion time= 10 temperature= 1000 dryO2
diffusion time= 5 temperature= 1000 inert
diffusion time= 30 temperature= 1000 t.rate= -8.33 inert

#Plot the dopant profiles after oxidation
select z=log10(abs(doping)) title="Doping Profile
After Passivation Oxide Growth"
plot.1d x.val=0.25 y.min=12 y.max=21 x.min=-0.2 x.max=12.0 symbol=4
```

```
      ^axes ^clear
select z=log10(boron)
plot.1d x.val=0.25 y.min=12 y.max=21 x.min=-0.2 x.max=12.0
      ^axes ^clear
select z=log10(antimony)
plot.1d x.val=0.25 y.min=12 y.max=21 x.min=-0.2 x.max=12.0
      ^axes ^clear

#List the layers
select
print.1d layers x.v=0.0

# List the metallurgical junctions
select z=doping
print.1d spot=0

electrical resist

# End of Code
```

Appendix D

Chemical Symbols

Please turn to the next page.

Table D.1: The chemical symbols corresponding to the chemical names used in this work. Note that in this dissertation, *silicon oxide* and *silicon nitride* are commonly shortened to just *oxide* and *nitride*, respectively.

Chemical Names	Chemical Symbols or Formulas
acetic acid	CH ₃ COOH
acetone	CH ₃ COCH ₃
argon	Ar
arsenic	As
arsine	AsH ₃
aluminum	Al
ammonium fluoride	NH ₄ F
ammonium nitrate	NH ₄ NO ₃
boron	B
chrome	Cr
diamond	C
diborane	B ₂ H ₆
dichlorosilane (DCS)	SiH ₂ Cl ₂
germanium	Ge
hydrogen	H ₂
hydrogen chloride	HCl
hydrogen fluoride	HF
hydrogen peroxide	H ₂ O ₂
iodide	I
isopropyl alcohol (isopropanol)	C ₃ H ₈ O
methanol	CH ₃ OH
nitric acid	HNO ₃
nitrogen	N ₂

Continued on Next Page...

Table D.1 – Continued

Chemical Names	Chemical Symbols or Formulas
parylene	Figure 6.2
phosphine	PH_3
phosphoric acid	H_3PO_4
phosphorous	Ph
potassium iodide	KI
silane	SiH_4
silicon	Si
silicon carbide	SiC
silicon chloride	SiCl_4
silicon oxide	SiO_2
silicon nitride	Si_3N_4
sodium chloride	NaCl
sulfuric acid	H_2SO_4
trichlorosilane	SiHCl_3
water	H_2O

Bibliography

- [1] R. H. Haynes and A. C. Burton, "Role of the non-newtonian behavior of blood in hemodynamics," *Am J Physiol*, vol. 197, no. 5, pp. 943–950, 1959.
- [2] B. M. Johnston, P. R. Johnston, S. Corney, and D. Kilpatrick, "Non-newtonian blood flow in human right coronary arteries: steady state simulations," *Journal of Biomechanics*, vol. 37, no. 5, pp. 709–720, 2004.
- [3] S. C. Cowin, S. Weinbaum, and Y. Zeng, "A case for bone canaliculi as the anatomical site of strain generated potentials," *Journal of Biomechanics*, vol. 28, no. 11, pp. 1281–1297, 1995.
- [4] J. L. Williams, J. P. Iannotti, A. Ham, J. Bleuit, and J. H. Chen, "Effects of fluid shear stress on bone cells," *Biorheology*, vol. 31, no. 2, pp. 163–70, 1994.
- [5] D. B. Burr, A. G. Robling, and C. H. Turner, "Effects of biomechanical stress on bones in animals," *Bone*, vol. 30, no. 5, pp. 781–786, 2002.
- [6] M. M. LaBarbera, "Principles of design of fluid transport systems in zoology," *Science*, vol. 249, no. 4972, pp. 992–1000, 1990.
- [7] B. B. L. Langille and F. F. O'Donnell, "Reductions in arterial diameter produced by chronic decreases in blood flow are endothelium-dependent," *Science*, vol. 231, no. 4736, pp. 405–7, 1986, 0036-8075.
- [8] G. G. H. Gibbons and V. V. J. Dzau, "The emerging concept of vascular remodeling," *The New England journal of medicine*, vol. 330, no. 20, pp. 1431–8, 1994.

- [9] R. D. Rudic, E. G. Shesely, N. Maeda, O. Smithies, S. S. Segal, and W. C. Sessa, "Direct evidence for the importance of endothelium-derived nitric oxide in vascular remodeling," *Journal of Clinical Investigation*, vol. 101, no. 4, pp. 731–736, 1998.
- [10] V. A. Korshunov and B. C. Berk, "Strain-dependent vascular remodeling: The "glagov phenomenon" is genetically determined," *Circulation*, vol. 110, no. 2, pp. 220–226, 2004.
- [11] V. A. Korshunov, S. M. Schwartz, and B. C. Berk, "Vascular remodeling: Hemodynamic and biochemical mechanisms underlying glagov's phenomenon," *Arterioscler Thromb Vasc Biol*, vol. 27, no. 8, pp. 1722–1728, 2007.
- [12] C. G. Caro, J. M. Fitz-Gerald, and R. C. Schroter, "Atheroma and arterial wall shear: Observation, correlation, and proposal of a shear dependent mass transfer mechanism for atherogenesis," *Proceedings of the Royal Society of London B*, vol. 177, pp. 109–159, 1971.
- [13] C. K. Zarins, D. P. Giddens, B. K. Bharadvaj, V. S. Sottiurai, R. F. Mabon, and S. Glagov, "Carotid bifurcation atherosclerosis. quantitative correlation of plaque localization with flow velocity profiles and wall shear stress," *Circ Res*, vol. 53, no. 4, pp. 502–514, 1983.
- [14] C. C. W. Kerber, S. S. T. Hecht, K. K. Knox, R. R. B. Buxton, and H. H. S. Meltzer, "Flow dynamics in a fatal aneurysm of the basilar artery," *AJNR, American journal of neuroradiology*, vol. 17, no. 8, pp. 1417–21, 1996.
- [15] A. M. Malek, S. L. Alper, and S. Izumo, "Hemodynamic shear stress and its role in atherosclerosis," *JAMA: The Journal of the American Medical Association*, vol. 282, no. 21, pp. 2035–2042, 1999.
- [16] O. Traub and B. C. Berk, "Laminar shear stress : Mechanisms by which endothelial cells transduce an atheroprotective force," *Arterioscler Thromb Vasc Biol*, vol. 18, no. 5, pp. 677–685, 1998.

- [17] A. M. Shaaban and A. J. Duerinckx, "Wall shear stress and early atherosclerosis: A review," *Am. J. Roentgenol.*, vol. 174, no. 6, pp. 1657–1665, 2000.
- [18] C. A. Taylor, T. J. R. Hughes, and C. K. Zarins, "Finite element modeling of three-dimensional pulsatile flow in the abdominal aorta: Relevance to atherosclerosis," *Annals of Biomedical Engineering*, vol. 26, no. 6, pp. 975–987, 1998.
- [19] C. A. Taylor, T. J. R. Hughes, and C. K. Zarins, "Finite element modeling of blood flow in arteries," *Computer Methods in Applied Mechanics and Engineering*, vol. 158, no. 1-2, pp. 155–196, 1998.
- [20] C. R. Hill, J. C. Bamber, and G. Haar, *Physical Principles of Medical Ultrasonics*. John Wiley and Sons, 2004.
- [21] J. S. Milner, J. A. Moore, B. K. Rutt, and D. A. Steinman, "Hemodynamics of human carotid artery bifurcations: Computational studies with models reconstructed from magnetic resonance imaging of normal subjects," *Journal of Vascular Surgery*, vol. 28, no. 1, pp. 143–156, 1998.
- [22] V. L. Morgan, J. Graham, Thomas P., R. J. Roselli, and C. H. Lorenz, "Alterations in pulmonary artery flow patterns and shear stress determined with three-dimensional phase-contrast magnetic resonance imaging in fontan patients," *J Thorac Cardiovasc Surg*, vol. 116, no. 2, pp. 294–304, 1998.
- [23] J. A. Moore, D. A. Steinman, D. W. Holdsworth, and C. R. Ethier, "Accuracy of computational hemodynamics in complex arterial geometries reconstructed from magnetic resonance imaging," *Annals of Biomedical Engineering*, vol. 27, no. 1, pp. 32–41, 1999.
- [24] H. A. Silber, D. A. Bluemke, P. Ouyang, Y. P. Du, W. S. Post, and J. A. C. Lima, "The relationship between vascular wall shear stress and flow-mediated dilation: endothelial function assessed by phase-contrast magnetic resonance angiography," *J Am Coll Cardiol*, vol. 38, no. 7, pp. 1859–1865, 2001.

- [25] C. A. Taylor, C. P. Cheng, L. A. Espinosa, B. T. Tang, D. Parker, and R. J. Herfkens, "In vivo quantification of blood flow and wall shear stress in the human abdominal aorta during lower limb exercise," *Annals of Biomedical Engineering*, vol. 30, no. 3, pp. 402–408, 2002.
- [26] I. Owan, D. B. Burr, C. H. Turner, J. Qiu, Y. Tu, J. E. Onyia, and R. L. Duncan, "Mechanotransduction in bone: osteoblasts are more responsive to fluid forces than mechanical strain," *American Journal of Physiology - Cell Physiology*, vol. 42, no. 3, pp. C810–C815, 1997.
- [27] R. Smalt, F. T. Mitchell, R. L. Howard, and T. J. Chambers, "Induction of no and prostaglandin e2 in osteoblasts by wall-shear stress but not mechanical strain," *Am J Physiol Endocrinol Metab*, vol. 273, no. 4, pp. E751–758, 1997.
- [28] C. C. R. Jacobs, C. C. E. Yellowley, B. B. R. Davis, Z. Z. Zhou, J. J. M. Cimbala, and H. H. J. Donahue, "Differential effect of steady versus oscillating flow on bone cells," *Journal of Biomechanics*, vol. 31, no. 11, pp. 969–76, 1998, 0021-9290.
- [29] J. You, G. C. Reilly, X. Zhen, C. E. Yellowley, Q. Chen, H. J. Donahue, and C. R. Jacobs, "Osteopontin gene regulation by oscillatory fluid flow via intracellular calcium mobilization and activation of mitogen-activated protein kinase in mc3t3-e1 osteoblasts," *J. Biol. Chem.*, vol. 276, no. 16, pp. 13 365–13 371, 2001.
- [30] T. L. H. Donahue, T. R. Haut, C. E. Yellowley, H. J. Donahue, and C. R. Jacobs, "Mechanosensitivity of bone cells to oscillating fluid flow induced shear stress may be modulated by chemotransport," *Journal of Biomechanics*, vol. 36, no. 9, pp. 1363–71, 2003.
- [31] S. G. Monismith, "Hydrodynamics of coral reefs," *Annual Review of Fluid Mechanics*, vol. 39, no. 1, pp. 37–55, 2007.

- [32] M. A. Reidenbach, S. G. Monismith, J. R. Koseff, G. Yahel, and A. Genin, "Boundary layer turbulence and flow structure over a fringing coral reef," *Limnology and Oceanography*, vol. 51, no. 5, pp. 1956–1968, 2006.
- [33] A. Genin, G. Yahel, M. A. Reidenbach, S. B. Monismith, and J. R. Koseff, "Intense benthic grazing on phytoplankton in coral reefs revealed using the control volume approach," *Oceanography*, vol. 15, pp. 90–96, 2002.
- [34] M. E. Baird and M. J. Atkinson, "Measurement and prediction of mass transfer to experimental coral reef communities," *Limnology and Oceanography*, vol. 42, no. 8, pp. 1685–1693, 1997.
- [35] D. R. Bellwood, T. P. Hughes, C. Folke, and M. Nystrom, "Confronting the coral reef crisis," *Nature*, vol. 429, no. 6994, pp. 827–833, 2004.
- [36] P. L. Wiberg, "A theoretical investigation of boundary layer flow and bottom shear stress for smooth, transitional, and rough flow under waves," *Journal of Geophysical Research*, vol. 100, no. c11, p. 22667, 1995.
- [37] R. G. Dean and R. A. Dalrymple, *Water Wave Mechanics for Engineers and Scientists*. World Scientific, 1991.
- [38] W. D. Grant and O. S. Madsen, "Combined wave and current interaction with a rough bottom," *Journal of Geophysical Research*, vol. 84, no. C4, pp. 1797–1808, 1979.
- [39] M. R. Raupach and A. S. Thom, "Turbulence in and above plant canopies," *Annual Review of Fluid Mechanics*, vol. 13, no. 1, pp. 97–129, 1981.
- [40] J. Finnigan, "Turbulence in plant canopies," *Annual review of fluid mechanics*, vol. 32, no. 1, p. 519, 2000.
- [41] M. A. Reidenbach, J. R. Koseff, and S. G. Monismith, "Laboratory experiments of fine-scale mixing and mass transport within a coral canopy," *Physics of Fluids*, vol. 19, no. 7, pp. 075 107–11, 2007.

- [42] M. A. Reidenbach, "The effects of waves and morphology on mass transfer within branched reef corals," *Limnology and oceanography*, vol. 51, no. 2, p. 1134, 2006.
- [43] R. J. Lowe, J. R. Koseff, and S. G. Monismith, "Oscillatory flow through submerged canopies: 1. velocity structure," *Journal of geophysical research*, vol. 110, no. c10, p. C10016, 2005.
- [44] R. J. Lowe, J. R. Koseff, S. G. Monismith, and J. L. Falter, "Oscillatory flow through submerged canopies: 2. canopy mass transfer," *Journal of geophysical research*, vol. 110, no. c10, p. C10017, 2005.
- [45] J. C. Andrews and G. L. Pickard, "The physical oceanography of coral reef systems," in *Ecosystems of the World: Coral Reefs*, Z. Dubinsky, Ed. Amsterdam: Elsevier, 1990, pp. 11–45.
- [46] G. K. Batchelor, *An Introduction to Fluid Dynamics*, 2000th ed. Cambridge University Press, 2000.
- [47] B. R. Munson, D. F. Young, and T. H. Okiishi, *Fundamentals of Fluid Mechanics*. John Wiley and Sons, 1994.
- [48] I. M. Cohen and P. K. Kundu, *Fluid Mechanics*, 3rd ed. Academic Press, 2004.
- [49] F. M. White, *Viscous Fluid Flow*, 3rd ed. McGraw-Hill Science/Engineering/Math, 2005.
- [50] R. W. Fox and A. T. McDonald, *Introduction to Fluid Mechanics*, 2005th ed. Wiley, 2005.
- [51] E. Bonaccorso, M. Kappl, and H.-J. Butt, "Hydrodynamic force measurements: Boundary slip of water on hydrophilic surfaces and electrokinetic effects," *Physical Review Letters*, vol. 88, no. 7, p. 076103, 2002.
- [52] R. M. Sorensen, *Basic Wave Mechanics: For Coastal and Ocean Engineers*. Wiley-Interscience, 1993.

- [53] T. Beer, *Environmental oceanography: an introduction to the behaviour of coastal waters*. Pergamon Press, 1983.
- [54] S. R. Massel, *Ocean surface waves*. World Scientific, 1996.
- [55] S. C. Jain, *Open-channel Flow*. John Wiley and Sons, 2000.
- [56] H. Chanson, *The Hydraulics of Open Channel Flow*. Butterworth-Heinemann, 2004.
- [57] J. B. Angell, "Micromachined silicon transducers for measuring force, pressure, and motion," in *4th European Solid-State Circuits Conference*, Amsterdam, 1978.
- [58] A. R. Atwell, R. S. Okojie, K. T. Kornegay, S. L. Roberson, and A. Beliveau, "Simulation, fabrication, and testing of bulk micromachined 6h-sic high-g piezoresistive accelerometers," *Sensors and Actuators A*, vol. 104, pp. 11–18, 2003.
- [59] M. Mehregany, C. Zorman, N. Rajan, and C.-H. Wu, "Silicon carbide mems for harsh environments," *Proceedings of the IEEE*, vol. 86, no. 8, pp. 1594–1609, 1998.
- [60] C.-H. Wu, C. Zorman, and M. Mehregany, "Fabrication and testing of bulk micromachined silicon carbide piezoresistive pressure sensors for high temperature applications," *Sensors Journal, IEEE*, vol. 6, no. 2, pp. 316–324, 2006.
- [61] R. Ziermann, J. von Berg, W. Reichert, E. Obermeier, M. Eickhoff, and G. Krotz, "A high temperature pressure sensor with β -sic piezoresistors on soi substrates," in *Solid State Sensors and Actuators, 1997. TRANSDUCERS '97 Chicago., 1997 International Conference on*, vol. 2, 1997, pp. 1411–1414 vol.2.

- [62] M. Werner, P. Gluche, M. Adamschik, E. Kohn, and H.-J. Fecht, "Review on diamond based piezoresistive sensors," in *Industrial Electronics, 1998. Proceedings. ISIE '98. IEEE International Symposium on*, vol. 1, 1998, pp. 147–152 vol.1.
- [63] M. Werner, G. Krtz, H. Mller, M. Eickhoff, P. Gluche, M. Adamschik, C. Johnston, and P. R. Chalker, "High-temperature sensors based on sic and diamond technology," *Sensors Update*, vol. 5, no. 1, pp. 141–190, 1999.
- [64] M. Werner and W. Fahrner, "Review on materials, microsensors, systems and devices for high-temperature and harsh-environment applications," *Industrial Electronics, IEEE Transactions on*, vol. 48, no. 2, pp. 249–257, 2001.
- [65] J. K. Luo, Y. Q. Fu, H. R. Le, J. A. Williams, S. M. Spearing, and W. I. Milne, "Diamond and diamond-like carbon mems," *Journal of Micromechanics and Microengineering*, vol. 17, pp. S147–S163, 2007.
- [66] M. Rabarot, J. Bablet, M. Ruty, M. Kipp, I. Chartier, and C. Dubarry, "Thick su-8 photolithography for biomems," in *Micromachining and Microfabrication Process Technology VIII*, vol. 4979. San Jose, CA, USA: SPIE, 2003, pp. 382–393.
- [67] R. Melamud, A. Davenport, G. Hill, I. Chan, F. Declercq, P. Hartwell, and B. Pruitt, "Development of an su-8 fabry-perot blood pressure sensor," in *The 18th IEEE International Conference on Micro Electro Mechanical Systems*, Miami, Florida, USA, 2005, pp. 810–813.
- [68] N. Klejwa, N. Harjee, R. Kwon, S. M. Coulthard, and B. L. Pruitt, "Transparent su-8 three-axis micro strain gauge force sensing pillar arrays for biological applications," in *Solid-State Sensors, Actuators and Microsystems Conference, 2007. TRANSDUCERS 2007. International*, Lyon, France, 2007, pp. 2259–2262.
- [69] H. Qing, E. Meng, T. Yu-Chong, C. M. Rutherglen, J. Erickson, and J. Pine, "Parylene neuro-cages for live neural networks study," in *TRANSDUCERS*,

Solid-State Sensors, Actuators and Microsystems, 12th International Conference on, 2003, E. Meng, Ed., vol. 2, 2003, pp. 995–998.

- [70] E. Meng, P. J. Chen, D. Rodger, Y. C. Tai, and M. Humayun, “Implantable parylene mems for glaucoma therapy,” in *Microtechnology in Medicine and Biology, 2005. 3rd IEEE/EMBS Special Topic Conference on*, P. J. Chen, Ed., 2005, pp. 116–119.
- [71] J. D. Gelorme, R. J. Cox, and S. A. R. Gutierrez, “Photoresist composition and printed circuit boards and packages made therewith,” Nov 21, 1989 1989.
- [72] H. Lorenz, M. Despont, N. Fahrni, N. LaBianca, P. Renaud, and P. Vettiger, “Su-8: a low-cost negative resist for mems,” *Journal of Micromechanics and Microengineering*, vol. 7, no. 3, pp. 121–124, 1997.
- [73] R. J. Grow, Q. Wang, J. Cao, D. Wang, and H. Dai, “Piezoresistance of carbon nanotubes on deformable thin-film membranes,” *Applied Physics Letters*, vol. 86, no. 9, pp. 093 104–3, 2005.
- [74] C. K. M. Fung, M. Q. H. Zhang, Z. Dong, and W. J. Li, “Fabrication of cnt-based mems piezoresistive pressure sensors using dep nanoassembly,” in *Nanotechnology, 2005. 5th IEEE Conference on*, M. Q. H. Zhang, Ed., 2005, pp. 199–202 vol. 1.
- [75] T. Toriyama, Y. Tanimoto, and S. Sugiyama, “Characteristics of silicon nano wire as piezoresistor for nano electro mechanical systems,” in *Micro Electro Mechanical Systems, 2001. MEMS 2001. The 14th IEEE International Conference on*, 2001, pp. 305–308.
- [76] D. V. Dao, T. Toriyama, and S. Sugiyama, “Noise and frequency analyses of a miniaturized 3-dof accelerometer utilizing silicon nanowire piezoresistors,” in *IEEE Sensors*, Vienna, Austria, 2004, pp. 1464–1467 vol.3.
- [77] M.-W. Shao, Y.-Y. Shan, N.-B. Wong, and S.-T. Lee, “Silicon nanowire sensors for bioanalytical applications: Glucose and hydrogen peroxide detection,” *Advanced Functional Materials*, vol. 15, no. 9, pp. 1478–1482, 2005.

- [78] G. T. A. Kovacs, *Micromachined Transducers Sourcebook*, 1st ed. McGraw-Hill Science/Engineering/Math, 1998.
- [79] S. D. Senturia, *Microsystem Design*, 1st ed. Kluwer Academic Publishers, 2001.
- [80] M. J. Madou, *Fundamentals of Microfabrication*, 2nd ed. CRC Press, 2002.
- [81] M. Gad-el Hak, *The MEMS Handbook*, 2nd ed. CRC Press, 2005.
- [82] C. Liu, *Foundations of MEMS*. Prentice Hall, 2005.
- [83] K. D. Wise, "A multielectrode microprobe for biopotential recording," Ph.D., Stanford University, 1969.
- [84] Samaun, "An integrated circuit piezoresistive pressure sensor for biomedical instrumentation," Ph.D., Stanford University, 1971.
- [85] L. M. Roylance, "A miniature integrated circuit accelerometer for biomedical applications," Ph.D., Stanford University, 1978.
- [86] L. Roylance and J. Angell, "Batch-fabricated silicon accelerometer," *IEEE Transactions on Electron Devices*, vol. 26, no. 12, pp. 1911–1917, 1979.
- [87] "Mems market to reach \$12.5 billion in 2010," Electronics.ca Research Network, 1/23/2006.
- [88] J. D. Plummer, M. D. Deal, and P. B. Griffin, *Silicon VLSI Technology Fundamentals, Practice, and Modeling*. New Jersey: Prentice Hall, Inc, 2000.
- [89] M. R. Head and I. Rechenberg, "The preston tube as a means of measuring skin friction," *Journal of Fluids Mechanics Digital Archive*, vol. 14, pp. 1–17, 1962.
- [90] F. H. Clauser, "Turbulent boundary layers in adverse pressure gradients," *Journal of the Aeronautical Sciences*, vol. 21, pp. 91–108, 1954.

- [91] K. G. Winter, "An outline of the techniques available for the measurement of skin friction in turbulent boundary layers," *Progress in Aerospace Sciences*, vol. 18, pp. 1–57, 1977.
- [92] H. H. Fernholz, "New developments and applications of skin-friction measuring techniques," *Measurement science & technology*, vol. 7, no. 10, p. 1396, 1996.
- [93] J. Haritonidis, "The measurement of wall shear stress," in *Advances in Fluid Mechanics Measurements*. Springer-Verlag, 1989, pp. 229–261.
- [94] R. Goldstein, *Fluid Mechanics Measurements*, 1st ed. CRC, 1996.
- [95] J. W. Naughton and M. Sheplak, "Modern developments in shear-stress measurement," *Progress in Aerospace Sciences*, vol. 38, no. 6-7, pp. 515–570, 2002.
- [96] C. Liu, J.-B. Huang, Z. Zhu, F. Jiang, S. Tung, Y.-C. Tai, and C.-M. Ho, "A micromachined flow shear-stress sensor based on thermal transfer principles," *Microelectromechanical Systems, Journal of*, vol. 8, no. 1, pp. 90–99, 1999.
- [97] C. G. Lomas, "Fundamentals of hot wire anemometry," *The Journal of the Acoustical Society of America*, vol. 87, no. 3, p. 1379, 1990.
- [98] H. H. Bruun, *Hot-Wire Anemometry: Principles and Signal Analysis*. Oxford University Press, 1995.
- [99] H. H. Bruun, "Hot-film anemometry in liquid flows," *Measurement science & technology*, vol. 7, no. 10, p. 1301, 1996.
- [100] J. D. Vagt and H. H. Fernholz, "Use of surface fences to measure wall shear stress in three-dimensional boundary layers," *Aeronautical Quarterly*, vol. 24, pp. 87–91, 1973.
- [101] J. M. Allen, "Improved sensing element for skin-friction balance measurements," *AIAA*, vol. 18, no. 11, pp. 1342–1345, 1980.
- [102] J. M. Allen, "Experimental study of error sources in skin-friction balance measurements," *Fluids Engineering*, vol. 99, pp. 197–204, 1977.

- [103] M. Acharya, "Development of a floating element for the measurement of surface shear stress," *AIAA journal*, vol. 23, no. 1, p. 410, 1985.
- [104] M. Acharya, J. Bornstein, and M. P. Escudier, "Turbulent boundary layers on rough surfaces," *Experiments in fluids*, vol. 4, no. 1, pp. 33–47, 1986.
- [105] M. Sheplak, L. Cattafesta, T. Nishida, and C. B. McGinley, "Mems shear stress sensors: Promise and progress," in *24th AIAA Aerodynamic Measurement Technology and Ground Testing Conference*, Portland, Oregon, 2004, pp. AIAA 2004–2606.
- [106] B. W. v. Oudheusden and J. H. Huijsing, "Integrated flow friction sensor," *Sensors and Actuators B: Chemical*, vol. 15, no. 2, pp. 135–144, 1988.
- [107] J.-B. Huang, C. Liu, F.-K. Jiang, S. Tung, Y.-C. Tai, and C.-M. Ho, "Fluidic shear-stress measurement using surface-micromachined sensors," in *TENCON '95. 1995 IEEE Region 10 International Conference on Microelectronics and VLSI*, 1995, pp. 16–19.
- [108] J.-B. Huang, C.-M. Ho, S. Tung, C. Liu, and Y.-C. Tai, "Micro thermal shear stress sensor with and without cavity underneath," in *Instrumentation and Measurement Technology Conference, 1995. IMTC/95. Proceedings. 'Integrating Intelligent Instrumentation and Control'.*, IEEE, 1995, p. 171.
- [109] J.-B. Huang, S. Tung, C.-M. Ho, C. Liu, and Y.-C. Tai, "Improved micro thermal shear-stress sensor," *Instrumentation and Measurement, IEEE Transactions on*, vol. 45, no. 2, pp. 570–574, 1996.
- [110] F. Jiang, Y.-C. Tai, J.-B. Huang, and C.-M. Ho, "Polysilicon structures for shear stress sensors," in *IEEE Region 10 International Conference on Microelectronics and VLSI*, 1995, pp. 12–15.
- [111] F. Jiang, Y.-C. Tai, B. Gupta, R. Goodman, S. Tung, J.-B. Huang, and C.-M. Ho, "A surface-micromachined shear stress imager," in *The Ninth Annual*

- International Workshop on Micro Electro Mechanical Systems*, 1996, pp. 110–115.
- [112] F. Jiang, Y.-C. Tai, K. Walsh, T. Tsao, G.-B. Lee, and C.-M. Ho, “A flexible mems technology and its first application to shear stress sensor skin,” in *Tenth Annual International Workshop on Micro Electro Mechanical Systems*, 1997, pp. 465–470.
- [113] F. Jiang, Y. Xu, T. Weng, Z. Han, Y.-C. Tai, A. Huang, C.-M. Ho, and S. Newbern, “Flexible shear stress sensor skin for aerodynamics applications,” in *The Thirteenth Annual International Conference on Micro Electro Mechanical Systems*, Miyazaki, Japan, 2000, pp. 364–369.
- [114] Y. Xu, F. Jiang, Q. Lin, J. Clendenen, S. Tung, and Y.-C. Tai, “Underwater shear-stress sensor,” in *The Fifteenth IEEE International Conference on Micro Electro Mechanical Systems*, Las Vegas, USA, 2002, pp. 340–343.
- [115] Y. Xu and Y.-C. Tai, “Selective deposition of parylene c for underwater shear-stress sensors,” in *12th International Conference on Solid-State Sensors, Actuators and Microsystems, TRANSDUCERS 2003.*, vol. 2, 2003, pp. 1307–1310 vol.2.
- [116] Y. Xu, Y.-C. Tai, A. Huang, and C.-M. Ho, “Ic-integrated flexible shear-stress sensor skin,” *Microelectromechanical Systems, Journal of*, vol. 12, no. 5, pp. 740–747, 2003.
- [117] Y. Xu, J. Clendenen, S. Tung, F. Jiang, and Y.-C. Tai, “Underwater flexible shear-stress sensor skins,” in *17th IEEE International Conference on Micro Electro Mechanical Systems*, Maastricht, The Netherlands, 2004, pp. 833–836.
- [118] K. S. Breuer, “Active control of wall pressure fluctuations in a turbulent boundary layer,” in *ASME Symposium of Flow Noise Modeling, Measurement, and Control*, vol. 168, 1993, pp. 39–48.

- [119] R. Rathnasingham and K. S. Breuer, "Active control of turbulent boundary layers," *Journal of fluid mechanics*, vol. 495, p. 209, 2003.
- [120] M. A. Schmidt, "Microsensors for the measurement of shear forces in turbulent boundary layers," Ph.D. dissertation, Massachusetts Institute of Technology, 1988.
- [121] M. Schmidt, R. Howe, S. Senturia, and J. Haritonidis, "Design and calibration of a microfabricated floating-element shear-stress sensor," *Electron Devices, IEEE Transactions on*, vol. 35, no. 6, pp. 750–757, 1988.
- [122] T. Pan, D. Hyman, M. Mehregany, E. Reshotko, and S. Garverick, "Microfabricated shear stress sensors, part 1: Design and fabrication," *AIAA journal*, vol. 37, no. 1, p. 66, 1999.
- [123] D. Hyman, "Microfabricated shear stress sensors, part 2: Testing and calibration," *AIAA journal*, vol. 37, no. 1, p. 73, 1999.
- [124] A. V. Desai and M. A. Haque, "Design and fabrication of a direction sensitive mems shear stress sensor with high spatial and temporal resolution," *Journal of Micromechanics and Microengineering*, vol. 14, no. 12, pp. 1718–1725, 2004.
- [125] J. Zhe, V. Modi, and J. Farmer, K. R., "A microfabricated wall shear-stress sensor with capacitive sensing," *Microelectromechanical Systems, Journal of*, vol. 14, no. 1, pp. 167–175, 2005, 1057-7157.
- [126] K.-Y. Ng, J. Shajii, and M. Schmidt, "A liquid shear-stress sensor fabricated using wafer bonding technology," in *International Conference on Solid-State Sensors and Actuators, 1991. TRANSDUCERS '91.*, 1991, pp. 931–934.
- [127] J. Shajii, K.-Y. Ng, and M. Schmidt, "A microfabricated floating-element shear stress sensor using wafer-bonding technology," *Microelectromechanical Systems, Journal of*, vol. 1, no. 2, pp. 89–94, 1992.
- [128] H. D. Goldberg, K. S. Breuer, and M. A. Schmidt, "A silicon wafer-bonding technology for microfabricated shear-stress sensors with backside contacts," in

Solid-State Sensor and Actuator Workshop, Hilton Head Island, South Carolina, USA, 1994, pp. 111–115.

- [129] M. Schober, E. Obermeier, S. Pirskawetz, and H. H. Fernholz, “A mems skin-friction sensor for time resolved measurements in separated flows,” *Experiments in fluids*, vol. 36, no. 4, pp. 593–599, 2004.
- [130] Y. Li, M. Papila, T. Nishida, L. Cattafesta, and M. Sheplak, “Modeling and optimization of a side-implanted piezoresistive shear stress sensor,” in *SPIE 13th International Symposium on Smart Structures and Materials*, San Diego, California, 2006, pp. #6174–7.
- [131] Y. Li, T. Nishida, D. P. Arnold, and M. Sheplak, “Microfabrication of a wall shear stress sensor using side-implanted piezoresistive tethers,” in *SPIE 14th Annual International Symposium on Smart Structures and Materials*, San Diego, CA, 2007, pp. #6529–13.
- [132] Y. Li, V. Chandrasekharan, B. Bertolucci, T. Nishida, L. Cattafesta, and M. Sheplak, “A mems shear stress sensor for turbulence measurements,” in *AIAA-2008-269, 46th AIAA Aerospace Sciences Meeting and Exhibit*, Reno, Nevada, 2008.
- [133] Y. Li, V. Chandrasekharan, B. Bertolucci, T. Nishida, L. Cattafesta, D. Arnold, and M. Sheplak, “A laterally-implanted piezoresistive skin-friction sensor,” in *Solid-State Sensors, Actuators, and Microsystems Workshop*, Hilton Head, SC, 2008, pp. 304–307.
- [134] A. Padmanabhan, H. D. Goldberg, K. S. Breuer, and M. A. Schmidt, “A silicon micromachined floating-element shear-stress sensor with optical position sensing by photodiodes,” in *Solid-State Sensors and Actuators, 1995 and Eurosensors IX. Transducers '95. The 8th International Conference on*, vol. 2, 1995, pp. 436–439.

- [135] A. Padmanabhan, H. Goldberg, K. Breuer, and M. Schmidt, "A wafer-bonded floating-element shear stress microsensors with optical position sensing by photodiodes," *Microelectromechanical Systems, Journal of*, vol. 5, no. 4, pp. 307–315, 1996.
- [136] F.-G. Tseng and C.-J. Lin, "Polymer mems-based fabry-perot shear stress sensor," *Sensors Journal, IEEE*, vol. 3, no. 6, pp. 812–817, 2003.
- [137] S. Horowitz, T. Chen, V. Chandrasekaran, K. Tedjojuwono, T. Nishida, L. Cattafesta, and M. Sheplak, "A micromachined geometric moiré interferometric floating-element shear stress sensor," in *42nd AIAA Aerospace Sciences Meeting and Exhibit*, Reno, Nevada, 2004, pp. AIAA 2004–1042.
- [138] S. Horowitz, T.-A. Chen, V. Chandrasekaran, K. Tedjojuwono, L. Cattafesta, T. Nishida, and M. Sheplak, "A wafer-bonded, floating element shear-stress sensor using a geometric moire optical transduction technique," in *Solid-State Sensors, Actuators and Microsystems Workshop*, Hilton Head Island, South Carolina, USA, 2004, pp. 13–18.
- [139] W. Thomson, "On the electro-dynamic qualities of metals:—effects of magnetization on the electric conductivity of nickel and of iron," *Proceedings of the Royal Society of London*, vol. 8, pp. 546–550, 1856, 0370-1662.
- [140] H. Tomlinson, "On the increase in resistance to the passage of an electric current produced on wires by stretching," *Proceedings of the Royal Society of London (1854-1905)*, vol. 25, no. 1, pp. 451–453, 1876.
- [141] H. Tomlinson, "The influence of stress and strain on the action of physical forces," *Philosophical transactions of the Royal Society of London*, vol. 174, pp. 1–172, 1883.
- [142] P. W. Bridgman, "Some properties of single metal crystals," *PNAS*, vol. 10, no. 10, pp. 411–415, 1924.

- [143] P. W. Bridgman, "General survey of the effects of pressure on the properties of matter," *Proceedings of the Physical Society*, vol. 41, no. 1, p. 341, 1928, 0370-1328.
- [144] P. W. Bridgman, "The effect of homogeneous mechanical stress on the electrical resistance of crystals," *Physical review*, vol. 42, no. 6, p. 858, 1932, 0031-899X.
- [145] H. Rolnick, "Tension coefficient of resistance of metals," *Physical Review*, vol. 36, no. 3, p. 506, 1930.
- [146] M. Allen, "The effect of tension on the electrical resistance of single bismuth crystals," *Physical review*, vol. 42, no. 6, p. 848, 1932.
- [147] M. Allen, "The effect of tension on the electrical resistance of single antimony crystals," *Physical review*, vol. 43, no. 7, p. 569, 1933.
- [148] M. Allen, "The tension coefficients of resistance of the hexagonal crystals zinc and cadmium," *Physical review*, vol. 49, no. 3, p. 248, 1936.
- [149] M. Allen, "The effect of tension on the electrical resistance of single tetragonal tin crystals," *Physical review*, vol. 52, no. 12, p. 1246, 1937.
- [150] J. W. Cookson, "Theory of the piezo-resistive effect," *Physical Review*, vol. 47, no. 2, p. 194, 1935.
- [151] F. Pockels, *Elektrizitat und Magnetismus I (Handbuch der Physik vol 4)*, 1905.
- [152] M. Trainer, "Kelvin and piezoelectricity," *European Journal of Physics*, vol. 24, no. 5, p. 535, 2003, 0143-0807.
- [153] J. Curie and P. Curie, "Developpement, par pression, de l'electricite polaire dans les cristaux hemiedres a faces inclinees," *C. R. Acad. Sci.*, vol. 91, pp. 294-295, 1880.
- [154] W. Voight, *Lehrbuch der Kristallphysik*, Leipzig, 1910.

- [155] W. Thomson, "Elements of a mathematical theory of elasticity," *Philosophical Transactions of the Royal Society of London*, vol. 146, p. 481, 1856, 0261-0523.
- [156] W. Thomson, "Note by lord kelvin on electric molecules for the explanation of the piezoelectric and pyro-electric properties of crystals," *Philosophical Magazine*, vol. 36, p. 1, 1893.
- [157] W. Thomson, "On the theory of pyro-electricity and piezo-electricity of crystals," *Philosophical Magazine*, vol. 36, pp. 453–9, 1893.
- [158] W. Thomson, "On the piezo-electric property of quartz," *Philosophical Magazine*, vol. 36, no. 331-42, 1893.
- [159] D. Clark and G. Dätwyler, "Stress-strain relationships under tension impact loading," in *Symposium on Impact Testing*, Atlantic City, 1938.
- [160] P. K. Stein, "1936 - a banner year for strain gages and experimental stress analysis - an historical perspective," *Experimental Techniques*, vol. 30, no. 1, pp. 23–41, 2006.
- [161] E. E. Simmons, "Method and apparatus for making strain gauges," Feb 23, 1940 1940.
- [162] E. E. Simmons, "Strain gauge," Jul 23, 1941 1941.
- [163] A. C. Ruge, "Strain gage," June 6, 1944 1944.
- [164] J. Bardeen and W. Shockley, "Deformation potentials and mobilities in non-polar crystals," *Physical review*, vol. 80, no. 1, p. 72, 1950, 0031-899X.
- [165] C. S. Smith, "Piezoresistance effect in germanium and silicon," *Physical Review*, vol. 94, no. 1, p. 42, 1954.
- [166] W. P. Mason and R. N. Thurston, "Use of piezoresistive materials in the measurement of displacement, force, and torque," *The Journal of the Acoustical Society of America*, vol. 29, no. 10, p. 1096, 1957.

- [167] J. C. Sanchez and W. V. Wright, "Recent developments in flexible silicon strain gages," in *Semiconductor and conventional strain gages*, M. Dean, Ed. New York: Academic Press, 1962, pp. 307–345.
- [168] H. A. Nielsen, *From Locomotives to Strain Gages*. New York, NY: Vantage Press, 1985.
- [169] J. A. Hoerni, "Planar silicon diodes and transistors," in *Electron Devices Meeting, 1960 International*, vol. 6, 1960, p. 50.
- [170] O. Paul, J. Gaspar, and P. Ruther, "Advanced silicon microstructures, sensors, and systems," *IEEE Transactions on Electrical and Electronic Engineering*, vol. 2, no. 3, p. 199, 2007.
- [171] K. D. Wise, "Integrated sensors, mems, and microsystems: Reflections on a fantastic voyage," *Sensors and Actuators A: Physical*, vol. 136, no. 1, pp. 39–50, 2007.
- [172] W. G. Pfann and R. N. Thurston, "Semiconducting stress transducers utilizing the transverse and shear piezoresistance effects," *Journal of Applied Physics*, vol. 32, no. 10, pp. 2008–2019, 1961.
- [173] O. N. Tuftte, P. W. Chapman, and D. Long, "Silicon diffused-element piezoresistive diaphragms," *Journal of Applied Physics*, vol. 33, no. 11, pp. 3322–3327, 1962.
- [174] K. E. Petersen, "Silicon as a mechanical material," *Proceedings of the IEEE*, vol. 70, no. 5, pp. 420–457, 1982.
- [175] I. S. Sokolnikoff, *Mathematical Theory of Elasticity*. Malabar, FL: R.E. Krieger Pub. Co., 1983.
- [176] W. A. Brantley, "Calculated elastic constants for stress problems associated with semiconductor devices," *Journal of Applied Physics*, vol. 44, no. 1, pp. 534–535, 1973.

- [177] D. R. Franca and A. Blouin, "All-optical measurement of in-plane and out-of-plane young's modulus and poisson's ratio in silicon wafers by means of vibration modes," *Measurement Science and Technology*, vol. 15, pp. 859–868, 2004.
- [178] Y. Kanda, "A graphical representation of the piezoresistance coefficients in silicon," *IEEE Transactions on Electron Devices*, vol. 29, no. 1, pp. 64–70, 1982.
- [179] O. N. Tufte and E. L. Stelzer, "Piezoresistive properties of silicon diffused layers," *Applied Physics*, vol. 34, no. 2, pp. 313–318, 1963.
- [180] W. D. Cussins, "Effects produced by the ionic bombardment of germanium," *Proceedings of the Physical Society. Section B*, vol. 68, no. 4, p. 213, 1955.
- [181] B. W. Chui, T. W. Kenny, H. J. Mamin, B. D. Terris, and D. Rugar, "Independent detection of vertical and lateral forces with a sidewall-implanted dual-axis piezoresistive cantilever," *Applied Physics Letters*, vol. 72, no. 11, pp. 1388–1390, 1998.
- [182] M. Tortonese, R. C. Barrett, and C. F. Quate, "Atomic resolution with an atomic force microscope using piezoresistive detection," *Applied Physics Letters*, vol. 62, no. 8, pp. 834–836, 1993.
- [183] J. Harley and T. Kenny, "1/f noise considerations for the design and process optimization of piezoresistive cantilevers," *Microelectromechanical Systems, Journal of*, vol. 9, no. 2, pp. 226–235, 2000.
- [184] K. Matsuda, K. Suzuki, K. Yamamura, and Y. Kanda, "Nonlinear piezoresistance effects in silicon," *Journal of Applied Physics*, vol. 73, no. 4, pp. 1838–1847, 1993.
- [185] R. J. Wilfinger, P. H. Bardell, and D. S. Chhabra, "The resonistor: A frequency selective device utilizing the mechanical resonance of a silicon substrate," *IBM Journal of Research and Development*, vol. 12, no. 1, pp. 113–118, 1968.

- [186] T. N. Jackson, M. A. Tischler, and K. D. Wise, "An electrochemical p-n junction etch-stop for the formation of silicon microstructures," *Electron Device Letters, IEEE*, vol. 2, no. 2, pp. 44–45, 1981, 0741-3106.
- [187] K. Petersen, P. Barth, J. Poydock, J. Brown, J. J. Mallon, and J. Bryzek, "Silicon fusion bonding for pressure sensors," in *Solid-State Sensor and Actuator Workshop, 1988. Technical Digest., IEEE*, P. Barth, Ed., 1988, pp. 144–147.
- [188] J. Bardeen and W. H. Brattain, "The transistor, a semi-conductor triode," *Physical Review*, vol. 74, no. 2, p. 230, 1948.
- [189] W. F. Brinkman, "The transistor: 50 glorious years and where we are going," in *Solid-State Circuits Conference, 1997. Digest of Technical Papers. 43rd ISSCC., 1997 IEEE International*, 1997, pp. 22–26, 425.
- [190] D. I. Pomerantz, "Anodic bonding," 1968.
- [191] R. Noyce, "Semiconductor device-and-lead structure," 1961.
- [192] W. F. Brinkman, D. E. Haggan, and W. W. Troutman, "A history of the invention of the transistor and where it will lead us," *Solid-State Circuits, IEEE Journal of*, vol. 32, no. 12, pp. 1858–1865, 1997.
- [193] R. M. Finne and D. L. Klein, "A water-amine-complexing agent system for etching silicon," *Journal of The Electrochemical Society*, vol. 114, no. 9, pp. 965–970, 1967.
- [194] C. S. Fuller, "Diffusion of donor and acceptor elements into germanium," *Physical Review*, vol. 86, no. 1, p. 136, 1952.
- [195] S. M. Hu, "Formation of stacking faults and enhanced diffusion in the oxidation of silicon," *Journal of Applied Physics*, vol. 45, no. 4, pp. 1567–1573, 1974.
- [196] E. B. Karlsson, "The nobel prize in physics," in *The Nobel Prize: The First 100 Years*, A. W. Levinovitz and N. Ringertz, Eds. World Scientific, 2001, p. 235.

- [197] J. S. C. Kilby, "Turning potential into realities: The invention of the integrated circuit (nobel lecture)," *ChemPhysChem*, vol. 2, no. 8-9, pp. 482–489, 2001.
- [198] F. Laermer and A. Schilp, "Method of anisotropically etching silicon," Mar 26, 1996 1996.
- [199] J. B. Lasky, "Wafer bonding for silicon-on-insulator technologies," *Applied Physics Letters*, vol. 48, no. 1, pp. 78–80, 1986.
- [200] J. F. Marshall, "Method for electrolytically etching semiconductor material," Oct 18, 1977 1977.
- [201] J. F. Marshall, "Fabrication of semiconductor devices utilizing ion implantation," 1977.
- [202] M. Shimbo, K. Furukawa, K. Fukuda, and K. Tanzawa, "Silicon-to-silicon direct bonding method," *Journal of Applied Physics*, vol. 60, no. 8, pp. 2987–2989, 1986.
- [203] C. Kittel, *Introduction to Solid State Physics*, 8th ed. New York: John Wiley and Sons, 2005.
- [204] J. F. Nye, *Physical Properties of Crystals: Their Representation by Tensors and Matrices*. Oxford University Press, 1985.
- [205] R. F. Pierret, *Semiconductor Device Fundamentals*, 2nd ed. Addison Wesley, 1996.
- [206] G. Neudeck and R. F. Pierret, *Semiconductor Fundamentals Volume Modular (Modular series on solid state devices)*. Addison-wesley, 1982.
- [207] Y. Sun, S. E. Thompson, and T. Nishida, "Physics of strain effects in semiconductors and metal-oxide-semiconductor field-effect transistors," *Journal of Applied Physics*, vol. 101, no. 10, pp. 104503–22, 2007.
- [208] G. E. Kimball, "The electronic structure of diamond," *The Journal of Chemical Physics*, vol. 3, no. 9, pp. 560–564, 1935.

- [209] J. F. Mullaney, "Optical properties and electronic structure of solid silicon," *Physical Review*, vol. 66, no. 11-12, p. 326, 1944.
- [210] C. Herring, "Transport properties of a many valley semiconductor," *Bell Syst. Tech. J.*, vol. 34, pp. 237–290, 1955.
- [211] C. Herring, "Transport and deformation-potential theory for many-valley semiconductors with anisotropic scattering," *Physical review*, vol. 101, no. 3, p. 944, 1956.
- [212] D. Long, "Stress dependence of the piezoresistance effect," *Journal of Applied Physics*, vol. 32, no. 10, pp. 2050–2051, 1961.
- [213] C. Herring, "Theory of the thermoelectric power of semiconductors," *Physical review*, vol. 96, no. 5, p. 1163, 1954.
- [214] R. Keyes, *The effects of elastic deformation on the electrical conductivity of semiconductors*. New York: Academic Press, 1960, vol. 11.
- [215] M. Becker and H. Y. Fan, "Optical properties of semiconductors. iii. infra-red transmission of silicon," *Physical Review*, vol. 76, no. 10, p. 1531, 1949.
- [216] H. Y. Fan, "Temperature dependence of the energy gap in monatomic semiconductors," *Physical Review*, vol. 78, no. 6, p. 808, 1950.
- [217] B. Abeles, "Theory of the galvanomagnetic effects in germanium," *Physical review*, vol. 95, no. 1, p. 31, 1954.
- [218] M. Shibuya, "Magnetoresistance effect in cubic semiconductors with spheroidal energy surfaces," *Physical review*, vol. 95, no. 6, p. 1385, 1954.
- [219] S. Meiboom, "Theory of the galvanomagnetic effects in n-germanium," *Physical review*, vol. 93, no. 5, p. 1121, 1954.
- [220] R. W. Keyes, "Explaining strain [in silicon]," *Circuits and Devices Magazine, IEEE*, vol. 18, no. 5, pp. 36–39, 2002.

- [221] M.-S. Lin, "A better understanding of the channel mobility of si mosfets based on the physics of quantized subbands," *Electron Devices, IEEE Transactions on*, vol. 35, no. 12, pp. 2406–2411, 1988.
- [222] Y. Ohmura, "Role of the valence band density of states in the piezoresistance of p-type semiconductors si and ge," *Journal of the Physical Society of Japan*, vol. 62, no. 10, p. 3615, 1993.
- [223] K. Matsuda, "Strain-dependent hole masses and piezoresistive properties of silicon," in *Computational Electronics, 2004. IWCE-10 2004. Abstracts. 10th International Workshop on*, 2004, pp. 173–174.
- [224] M. V. Fischetti, Z. Ren, P. M. Solomon, M. Yang, and K. Rim, "Six-band [bold k [center-dot] p] calculation of the hole mobility in silicon inversion layers: Dependence on surface orientation, strain, and silicon thickness," *Journal of Applied Physics*, vol. 94, no. 2, pp. 1079–1095, 2003.
- [225] R. Oberhuber, G. Zandler, and P. Vogl, "Subband structure and mobility of two-dimensional holes in strained si/sige mosfet's," *Physical Review B*, vol. 58, no. 15, p. 9941, 1998.
- [226] T. Toriyama and S. Sugiyama, "Analysis of piezoresistance in p-type silicon for mechanical sensors," *Microelectromechanical Systems, Journal of*, vol. 11, no. 5, pp. 598–604, 2002.
- [227] G. L. Bir and G. E. Pikus, *Symmetry and strain-induced effects in Semiconductors*. New York: John Wiley and Sons, 1974.
- [228] W. H. Kleiner and L. M. Roth, "Deformation potential in germanium from optical absorption lines for exciton formation," *Physical Review Letters*, vol. 2, no. 8, p. 334, 1959.
- [229] G. E. Pikus and G. L. Bir, "Cyclotron and paramagnetic resonance in strained crystals," *Physical Review Letters*, vol. 6, no. 3, p. 103, 1961.

- [230] J. C. Hensel and G. Feher, "Valence band parameters in silicon from cyclotron resonances in crystals subjected to uniaxial stress," *Physical Review Letters*, vol. 5, no. 7, p. 307, 1960.
- [231] H. Hasegawa, "Theory of cyclotron resonance in strained silicon crystals," *Physical Review*, vol. 129, no. 3, p. 1029, 1963.
- [232] J. C. Hensel and G. Feher, "Cyclotron resonance experiments in uniaxially stressed silicon: Valence band inverse mass parameters and deformation potentials," *Physical Review*, vol. 129, no. 3, p. 1041, 1963.
- [233] J. C. Hensel, H. Hasegawa, and M. Nakayama, "Cyclotron resonance in uniaxially stressed silicon. ii. nature of the covalent bond," *Physical Review*, vol. 138, no. 1A, p. A225, 1965.
- [234] J. C. Hensel and K. Suzuki, "Quantum resonances in the valence bands of germanium. ii. cyclotron resonances in uniaxially stressed crystals," *Physical Review B*, vol. 9, no. 10, p. 4219, 1974.
- [235] L. Smith, V. Moroz, G. Eneman, P. Verheyen, F. Nouri, L. Washington, M. Jurczak, O. Penzin, D. Pramanik, and K. De Meyer, "Exploring the limits of stress-enhanced hole mobility," *Electron Device Letters, IEEE*, vol. 26, no. 9, pp. 652–654, 2005.
- [236] S. E. Thompson, S. Suthram, Y. Sun, G. Sun, S. Parthasarathy, M. Chu, and T. Nishida, "Future of strained si/semiconductors in nanoscale mosfets," in *Electron Devices Meeting, 2006. IEDM '06. International*, 2006, pp. 1–4.
- [237] S. Suthram, J. C. Ziegert, T. Nishida, and S. E. Thompson, "Piezoresistance coefficients of (100) silicon nmosfets measured at low and high channel stress," *Electron Device Letters, IEEE*, vol. 28, no. 1, pp. 58–61, 2007.
- [238] S.-J. Park, A. J. Rastegar, J. R. Mallon, A. A. Barlian, T. H. Fung, and B. L. Pruitt, "Ion implanted piezoresistive cantilever design and performance," in *Solid-State Sensors and Actuators Workshop*, Hilton Head Island, S.C., 2008.

- [239] I. Synopsis, 2004.
- [240] J. C. Wolfe and W. Zagozdzon-Wosik, "Method and apparatus for doping silicon wafers using a solid dopant source and rapid thermal processing," 1995.
- [241] B. H. Justice and R. F. Aycock, "Spin-on dopant method," Dec 12, 1983 1983.
- [242] P. P. Steve, M. C. Mark, and M. W. Kevin, "P+ structural layers for microelectromechanical systems using spin-on dopants," *Sensor Letters*, vol. 2, pp. 211–216, 2004.
- [243] Z. T. Zhu, E. Menard, K. Hurley, R. G. Nuzzo, and J. A. Rogers, "Spin on dopants for high-performance single-crystal silicon transistors on flexible plastic substrates," *Applied Physics Letters*, vol. 86, no. 13, pp. 133507–3, 2005.
- [244] R. S. Ohl, "Properties of ionic bombarded crystals," *Bell Syst. Tech. J.*, vol. 31, no. 104, 1952.
- [245] W. Shockley, "Forming semiconductive devices by ionic bombardment," October 28, 1954 1954.
- [246] J. A. Davies, J. Denhartog, L. Eriksson, and J. W. Mayer, "Ion implantation of silicon: I. atom location and lattice disorder by means of 1.0-mev helium ion scattering," *Can. J. Phys./Rev. Can. Phys.*, vol. 45, no. 12, pp. 4053–4071, 1967.
- [247] J. W. Mayer, O. J. Marsh, G. A. Shifrin, and R. Baron, "Ion implantation of silicon: II. electrical evaluation using hall-effect measurements," *Can. J. Phys./Rev. Can. Phys.*, vol. 45, no. 12, pp. 4073–4089, 1967.
- [248] J. F. Gibbons, "Ion implantation in semiconductors; part I: Range distribution theory and experiments," *Proceedings of the IEEE*, vol. 56, no. 3, pp. 295–319, 1968.
- [249] L. N. Large, "Ion implantation: A new method of doping semiconductors," *Contemporary Physics*, vol. 10, no. 5, pp. 505 – 531, 1969.

- [250] T. E. Seidel and A. U. MacRae, "Some properties of ion implanted boron in silicon," *Trans. Met. Soc. AIME*, 245: 491-8(Mar. 1969).; *From Conference on Preparation and Properties of Electronic Materials: Optical and Nuclear Radiation, Chicago, Ill. See CONF-680838.*, 1969, system Entry Date: 06/03/2001 Source: NSA-23-042455; DTIE (Division of Technical Information Extension) Language: English.
- [251] J. F. Gibbons, "Ion implantation in semiconductors; part ii: Damage production and annealing," *Proceedings of the IEEE*, vol. 60, no. 9, pp. 1062–1096, 1972.
- [252] J. W. Mayer, "Ion implantation in semiconductors," in *Electron Devices Meeting, 1973 International*, vol. 19, 1973, pp. 3–5.
- [253] J. A. Davies, "Early ion implantation history (or "how i met jim mayer and hogsted phim!")," *Materials Chemistry and Physics*, vol. 46, no. 2-3, pp. 111–117, 1996.
- [254] C. B. Yarling, "History of industrial and commercial ion implantation 1906–1978," in *The 46th international symposium of the american vacuum society*, vol. 18. Seattle, Washington (USA): AVS, 2000, pp. 1746–1750.
- [255] B. W. Chui, T. W. Kenny, H. J. Mamin, B. D. Terris, and D. Rugar, "Independent detection of vertical and lateral forces with a sidewall-implanted dual-axis piezoresistive cantilever," *Applied Physics Letters*, vol. 72, no. 11, pp. 1388–1390, 1998.
- [256] A. Partridge, J. K. Reynolds, B. W. Chui, E. M. Chow, A. M. Fitzgerald, L. Zhang, N. I. Maluf, and T. W. Kenny, "A high-performance planar piezoresistive accelerometer," *Microelectromechanical Systems, Journal of*, vol. 9, no. 1, pp. 58–66, 2000.
- [257] W.-T. Park, A. Partridge, R. N. Candler, V. Ayanoor-Vitikkate, G. Yama, M. Lutz, and T. W. Kenny, "Encapsulated submillimeter piezoresistive accelerometers," *Microelectromechanical Systems, Journal of*, vol. 15, no. 3, pp. 507–514, 2006.

- [258] J. F. Gibbons, "Ion implantation in semiconductors; part i: Range distribution theory and experiments," *Proceedings of the IEEE*, vol. 56, no. 3, pp. 295–319, 1968.
- [259] B. D. Joyce and J. A. Baldrey, "Selective epitaxial deposition of silicon," *Nature*, vol. 195, pp. 485–486, 1962.
- [260] M. Lutz and A. Partridge, "Gap tuning for surface micromachined structures in an epitaxial reactor," July 7, 2004 2004.
- [261] M. Bartek, P. T. J. Gennissen, P. J. French, P. M. Sarro, and R. F. Wolfenbittel, "Study of selective and non-selective deposition of single- and polycrystalline silicon layers in an epitaxial reactor," in *International Conference on Solid State Sensors and Actuators 1997. TRANSDUCERS 1997*, vol. 2, Chicago, 1997, pp. 1403–1406.
- [262] B. Kim, R. Melamud, M. A. Hopcroft, S. A. Chandorkar, G. Bahl, M. Messina, R. N. Chandler, G. Yama, and T. Kenny, "Si-sio₂ composite mems resonators in cmos compatible wafer-scale thin-film encapsulation," in *IEEE International Frequency Control Symposium, 2007 Joint with the 21st European Frequency and Time Forum*, Geneva, Switzerland, 2007, pp. 1214–1219.
- [263] J. A. Harley and T. W. Kenny, "High-sensitivity piezoresistive cantilevers under 1000 Å thick," *Applied Physics Letters*, vol. 75, no. 2, pp. 289–291, 1999.
- [264] Y. A. Liang, S.-W. Ueng, and T. W. Kenny, "Performance characterization of ultra-thin n-type piezoresistive cantilevers," in *The 11th International Conference on Solid-State Sensors and Actuators*, Munich, Germany, 2001, pp. 998–1001.
- [265] W. Zhang, N. S. Lloyd, K. Osman, J. M. Bonar, J. S. Hamel, and D. M. Bagnall, "Selective epitaxial growth using dichlorosilane and silane by low pressure chemical vapor deposition," *Microelectronic Engineering*, vol. 73-74, pp. 514–518, 2004.

- [266] A. D. Kurtz and C. Gravel, "Semiconductor transducers using transverse and shear piezoresistance," in *22nd Annual ISA Conference*, ser. Proceedings of the 22nd Annual ISA Conference, Chicago, IL, 1967.
- [267] W. P. Mason, J. J. Forst, and L. M. Tornillo, "Recent developments in semiconductor strain transducers," in *15th Annual Conference of The Instrument Society of America*, New York, NY, 1962, pp. 110–120.
- [268] D. R. Kerr and A. G. Milnes, "Piezoresistance of diffused layers in cubic semiconductors," *Applied Physics*, vol. 34, no. 4, pp. 727–731, 1963.
- [269] J. Richter, O. Hansen, A. Nylandsted Larsen, J. Lundsgaard Hansen, G. F. Eriksen, and E. V. Thomsen, "Piezoresistance of silicon and strained si0.9ge0.1," *Sensors and Actuators A: Physical*, vol. 123-124, pp. 388–396, 2005.
- [270] J. Richter, A. Hyldgard, K. Birkelund, M. B. Arnoldus, O. Hansen, and E. V. Thomsen, "Determination of packaging induced 3d stress utilizing a piezocoefficient mapping device," in *Micro Electro Mechanical Systems, 2007. MEMS. IEEE 20th International Conference on*, A. Hyldgard, Ed., 2007, pp. 69–72.
- [271] J. Richter, A. Hyldgard, K. Birkelund, O. Hansen, and E. V. Thomsen, "Real-time 3d stress measurement in curing epoxy packaging," in *Solid-State Sensors, Actuators and Microsystems Conference, 2007. TRANSDUCERS 2007. International*, A. Hyldgard, Ed., 2007, pp. 2083–2086.
- [272] E. Lund and T. Finstad, "Measurement of the temperature dependency of the piezoresistance coefficients in p-type silicon," *Advances in Electronic Packaging - ASME*, vol. 26-1, pp. 215–218, 1999.
- [273] E. Lund and T. G. Finstad, "Design and construction of a four-point bending based set-up for measurement of piezoresistance in semiconductors," *Review of Scientific Instruments*, vol. 75, no. 11, pp. 4960–4966, 2004.
- [274] F. J. Morin, T. H. Geballe, and C. Herring, "Temperature dependence of the piezoresistance of high-purity silicon and germanium," *Physical Review*, vol. 105, no. 2, p. 525, 1957.

- [275] A. D. Kurtz, "Adjusting crystal characteristics to minimize temperature dependency," in *Instrument Society of America, Winter Meeting*, St. Louis, Missouri, 1961.
- [276] C. H. Cho, R. C. Jaeger, and J. C. Suhling, "Experimental characterization of the temperature dependence of the piezoresistive coefficients of silicon," in *Thermal and Thermomechanical Phenomena in Electronics Systems, 2006. IThERM '06. The Tenth Intersociety Conference on*, R. C. Jaeger, Ed., 2006, pp. 928–935.
- [277] K. Matsuda, Y. Kanda, K. Yamamura, and K. Suzuki, "Nonlinearity of piezoresistance effect in p- and n-type silicon," *Sensors and Actuators A: Physical*, vol. 21, no. 1-3, pp. 45–48, 1990.
- [278] J. M. Chen and N. C. MacDonald, "Measuring the nonlinearity of silicon piezoresistance by tensile loading of a submicron diameter fiber using a microinstrument," *Review of Scientific Instruments*, vol. 75, no. 1, pp. 276–278, 2004.
- [279] T. Manku and A. Nathan, "Valence energy-band structure for strained group-iv semiconductors," *Journal of Applied Physics*, vol. 73, no. 3, pp. 1205–1213, 1993.
- [280] F. N. Hooge, " $1/f$ noise is no surface effect," *Physics Letters A*, vol. 29, no. 3, pp. 139–140, 1969.
- [281] F. N. Hooge, "Discussion of recent experiments on $1/f$ noise," *Physica A*, vol. 60, no. 1, p. 130, 1972.
- [282] T. G. M. Kleinpenning, " $1/f$ noise in thermo emf of intrinsic and extrinsic semiconductors," *Physica A*, vol. 77, no. 1, p. 78, 1974.
- [283] R. F. Voss and J. Clarke, "Flicker ($1/f$) noise: Equilibrium temperature and resistance fluctuations," *Physical Review B*, vol. 13, no. 2, p. 556, 1976.

- [284] F. N. Hooge and L. K. J. Vandamme, "Lattice scattering causes $1/f$ noise," *Physics Letters A*, vol. 66, no. 4, pp. 315–316, 1978.
- [285] F. N. Hooge, T. G. M. Kleinpenning, and L. K. J. Vandamme, "Experimental studies on $1/f$ noise," *Reports on Progress in Physics*, vol. 44, no. 5, pp. 479–532, 1981.
- [286] P. Dutta and P. M. Horn, "Low-frequency fluctuations in solids: $1/f$ noise," *Reviews of Modern Physics*, vol. 53, no. 3, p. 497, 1981.
- [287] D. M. Fleetwood and N. Giordano, "Resistivity dependence of $1/f$ noise in metal films," *Physical Review B*, vol. 27, no. 2, p. 667, 1983.
- [288] A. van der Ziel, "Unified presentation of $1/f$ noise in electron devices: fundamental $1/f$ noise sources," *Proceedings of the IEEE*, vol. 76, no. 3, pp. 233–258, 1988.
- [289] L. K. J. Vandamme, "Bulk and surface $1/f$ noise," *Electron Devices, IEEE Transactions on*, vol. 36, no. 5, pp. 987–992, 1989, 0018-9383.
- [290] F. N. Hooge, " $1/f$ noise sources," *Electron Devices, IEEE Transactions on*, vol. 41, no. 11, pp. 1926–1935, 1994, 0018-9383.
- [291] L. K. J. Vandamme and G. Trefan, " $1/f$ noise in homogeneous and inhomogeneous media," *Circuits, Devices and Systems, IEE Proceedings-*, vol. 149, no. 1, pp. 3–12, 2002.
- [292] L. K. J. Vandamme, "Noise as a diagnostic tool for quality and reliability of electronic devices," *Electron Devices, IEEE Transactions on*, vol. 41, no. 11, pp. 2176–2187, 1994.
- [293] M. B. Weissman, " $1/f$ noise and other slow, nonexponential kinetics in condensed matter," *Reviews of Modern Physics*, vol. 60, no. 2, pp. 537–571, 1988.
- [294] O. Hansen and A. Boisen, "Noise in piezoresistive atomic force microscopy," *Nanotechnology*, vol. 10, no. 1, pp. 51–60, 1999.

- [295] S. Bhardwaj, M. Sheplak, and T. Nishida, "S/n optimization and noise considerations for piezoresistive microphones," in *16th International Conference on Noise in Physical Systems and 1/f Fluctuations*, G. Bosman, Ed., Gainesville, Florida, USA, 2001.
- [296] X. Yu, J. Thaysen, O. Hansen, and A. Boisen, "Optimization of sensitivity and noise in piezoresistive cantilevers," *Journal of Applied Physics*, vol. 92, no. 10, pp. 6296–6301, 2002.
- [297] A. L. McWhorter, "1/f noise and related surface effects in germanium," Research Laboratory of Electronics and Lincoln Laboratory, Massachusetts Institute of Technology, Technical Report, May 20 1955.
- [298] A. L. McWhorter, *Semiconductor Surface Physics*. Philadelphia, PA: University of Pennsylvania Press, 1957.
- [299] J. R. Mallon, A. J. Rastegar, A. A. Barlian, M. T. Meyer, T. H. Fung, and B. L. Pruitt, "Low 1/f noise, full bridge, microcantilever with longitudinal and transverse piezoresistors," *Applied Physics Letters*, vol. 92, no. 3, p. 033508, 2008.
- [300] T. G. M. Kleinpenning and A. H. d. Kuijper, "Relation between variance and sample duration of 1/f noise signals," *Journal of Applied Physics*, vol. 63, no. 1, pp. 43–45, 1988.
- [301] B. Neri, C. Ciofi, and V. Dattilo, "Noise and fluctuations in submicrometric alsi interconnect lines," *Electron Devices, IEEE Transactions on*, vol. 44, no. 9, pp. 1454–1459, 1997.
- [302] E. P. Vandamme and L. K. J. Vandamme, "Current crowding and its effect on 1/f noise and third harmonic distortion - a case study for quality assessment of resistors," *Microelectronics Reliability*, vol. 40, no. 11, pp. 1847–1853, 2000.

- [303] B. W. Chui, T. D. Stowe, T. W. Kenny, H. J. Mamin, B. D. Terris, and D. Rugar, "Low-stiffness silicon cantilevers for thermal writing and piezoresistive readback with the atomic force microscope," *Applied Physics Letters*, vol. 69, no. 18, pp. 2767–2769, 1996.
- [304] L. K. J. Vandamme and S. Oosterhoff, "Annealing of ion-implanted resistors reduces the $1/f$ noise," *Journal of Applied Physics*, vol. 59, no. 9, pp. 3169–3174, 1986.
- [305] R. Dieme, G. Bosman, T. Nishida, and M. Sheplak, "Sources of excess noise in silicon piezoresistive microphones," *The Journal of the Acoustical Society of America*, vol. 119, no. 5, pp. 2710–2720, 2006.
- [306] M. C. M. Lee and M. C. Wu, "Thermal annealing in hydrogen for 3-d profile transformation on silicon-on-insulator and sidewall roughness reduction," *Microelectromechanical Systems, Journal of*, vol. 15, no. 2, pp. 338–343, 2006.
- [307] A. A. Barlian, S.-J. Park, V. Mukundan, and B. L. Pruitt, "Design, fabrication, and characterization of piezoresistive mems shear stress sensors," in *ASME International Mechanical Engineering Congress and Exposition*, Orlando, Florida, USA, 2005, pp. IMECE2005–81 849.
- [308] A. A. Barlian, S.-J. Park, V. Mukundan, and B. L. Pruitt, "Design and characterization of microfabricated piezoresistive floating element-based shear stress sensors," *Sensors and Actuators A: Physical*, vol. 134, no. 1, pp. 77–87, 2007.
- [309] B. L. Pruitt and T. W. Kenny, "Piezoresistive cantilevers and measurement system for low force electrical contact measurements," *Sensors and Actuators A: Physical*, vol. 104, no. 1, pp. 68–77, 2003.
- [310] B. Pruitt, W.-T. Park, and T. Kenny, "Measurement system for low force and small displacement contacts," *Microelectromechanical Systems, Journal of*, vol. 13, no. 2, pp. 220–229, 2004.

- [311] J. J. Wortman and R. A. Evans, "Young's modulus, shear modulus, and poisson's ratio in silicon and germanium," *Applied Physics*, vol. 36, no. 1, pp. 153–156, 1965.
- [312] J. C. Greenwood, "Silicon in mechanical sensors," *Journal of Physics E: Scientific Instruments*, vol. 21, pp. 1114–1128, 1988.
- [313] B. Bhushan and X. Li, "Micromechanical and tribological characterization of doped single-crystal silicon and polysilicon films for microelectromechanical systems devices," *Materials Research*, vol. 12, no. 1, pp. 54–63, 1997.
- [314] J. P. Holman, *Experimental Methods for Engineers*, 6th ed. New York: McGraw-Hill, Inc, 1994.
- [315] A. Partridge, "Lateral piezoresistive accelerometer with epipoly encapsulation," Ph.D., Stanford University, 2003.
- [316] G. Schmitt, J.-W. Schultze, F. Fabbendder, G. Bub, H. Luth, and M. J. Schoning, "Passivation and corrosion of microelectrode arrays," *Electrochimica Acta*, vol. 44, pp. 3865–3883, 1999.
- [317] Z. Fan, J. Engel, J. Chen, and C. Liu, "Parylene surface-micromachined membranes for sensor applications," *Microelectromechanical Systems, Journal of*, vol. 13, no. 3, pp. 484–490, 2004.
- [318] K. Rakesh, W. Zhuo, K. Waqas, L. Yuefa, and X. Yong, "Parylene cantilevers integrated with polycrystalline silicon piezoresistors for surface stress sensing," *Applied Physics Letters*, vol. 91, no. 8, p. 083505, 2007.
- [319] "<http://www.parylene.com>, para tech coating, inc., aliso viejo, ca."
- [320] "<http://www.scscoatings.com/>, specialty coating systems, indianapolis, in."
- [321] G. Voulgaris, "Evaluation of the acoustic doppler velocimeter (adv) for turbulence measurements*," *Journal of atmospheric and oceanic technology*, vol. 15, no. 1, p. 272, 1998.

- [322] S. N. Lane, P. M. Biron, K. F. Bradbrook, J. B. Butler, J. H. Chandler, M. D. Crowell, S. J. McLelland, K. S. Richards, and A. G. Roy, "Three-dimensional measurement of river channel flow processes using acoustic doppler velocimetry," *Earth Surface Processes and Landforms*, vol. 23, no. 13, pp. 1247–1267, 1998.
- [323] C. Li, F. Sauter, R. Azizkhan, C. Ahn, and I. Papautsky, "Polymer flip-chip bonding of pressure sensors on flexible kapton film for neonatal catheters," in *Micro Electro Mechanical Systems, 2004. 17th IEEE International Conference on. (MEMS)*, Maastricht, The Netherlands, 2004, pp. 749–752.
- [324] F. M. Henderson, *Open Channel Flow*. University of Michigan: Macmillan, 1970.
- [325] R. J. Adrian, "Particle-imaging techniques for experimental fluid mechanics," *Annual Review of Fluid Mechanics*, vol. 23, no. 1, p. 261, 1991.
- [326] R. J. Adrian, "Twenty years of particle image velocimetry," *Experiments in fluids*, vol. 39, no. 2, p. 159, 2005.
- [327] J. G. Santiago, "A particle image velocimetry system for microfluidics," *Experiments in fluids*, vol. 25, no. 4, p. 316, 1998.
- [328] C. D. Meinhart, "Piv measurements of a microchannel flow," *Experiments in fluids*, vol. 27, no. 5, p. 414, 1999.
- [329] A. A. Barlian, R. Narain, J. T. Li, C. E. Quance, A. C. Ho, V. Mukundan, and B. L. Pruitt, "Piezoresistive mems underwater shear stress sensors," in *19th IEEE International Conference on Micro Electro Mechanical Systems*, Istanbul, Turkey, 2006, pp. 626–629.
- [330] B. Chui, H. Mamin, B. Terris, D. Rugar, and T. Kenny, "Sidewall-implanted dual-axis piezoresistive cantilever for afm data storage readback and tracking," in *The Eleventh Annual International Workshop on Micro Electro Mechanical Systems*, Heidelberg, Germany, 1998, pp. 12–17.

- [331] L. Wang and D. J. Beebe, "Shear sensitive silicon piezoresistive tactile sensor prototype," in *Micromachined Devices and Components IV*, vol. 3514. Santa Clara, CA, USA: SPIE, 1998, pp. 359–367.
- [332] B. J. Kane, M. R. Cutkosky, and G. T. A. Kovacs, "A traction stress sensor array for use in high-resolution robotic tactile imaging," *Microelectromechanical Systems, Journal of*, vol. 9, no. 4, pp. 425–434, 2000, 1057-7157.
- [333] R. C. Jaeger, J. C. Suhling, R. Ramani, A. T. Bradley, and J. Xu, "Cmos stress sensors on (100) silicon," *Solid-State Circuits, IEEE Journal of*, vol. 35, no. 1, pp. 85–95, 2000.
- [334] J. C. Suhling, "Silicon piezoresistive stress sensors and their application in electronic packaging," *IEEE sensors journal*, vol. 1, no. 1, p. 14, 2001.
- [335] J. Bartholomeyczik, S. Brugger, P. Ruther, and O. Paul, "Multidimensional cmos in-plane stress sensor," *Sensors Journal, IEEE*, vol. 5, no. 5, pp. 872–882, 2005.
- [336] M. Doelle, C. Peters, P. Ruther, and O. Paul, "Piezo-fet stress-sensor arrays for wire-bonding characterization," *Microelectromechanical Systems, Journal of*, vol. 15, no. 1, pp. 120–130, 2006.
- [337] J. Richter, A. Hyldgard, K. Birkelund, M. B. Arnoldus, O. Hansen, and E. V. Thomsen, "Determination of packaging induced 3d stress utilizing a piezocoefficient mapping device," in *Micro Electro Mechanical Systems, 2007. MEMS. IEEE 20th International Conference on*, A. Hyldgard, Ed., 2007, pp. 69–72.
- [338] P. Gieschke, J. Richter, J. Joos, P. Ruther, and O. Paul, "Four-degree-of-freedom solid state mems joystick," in *Micro Electro Mechanical Systems, 2008. MEMS 2008. IEEE 21st International Conference on*, J. Richter, Ed., 2008, pp. 86–89.
- [339] M. C. Hsieh, Y. K. Fang, M.-S. Ju, G.-S. Chen, J.-J. Ho, C. H. Yang, P. M. Wu, G. S. Wu, and T. Y.-F. Chen, "A contact-type piezoresistive micro-shear stress

- sensor for above-knee prosthesis application,” *Journal of microelectromechanical systems*, vol. 10, no. 1, p. 121, 2001, 1057-7157.
- [340] L. Beccai, S. Roccella, A. Arena, F. Valvo, P. Valdastri, A. Menciassi, M. C. Carrozza, and P. Dario, “Design and fabrication of a hybrid silicon three-axial force sensor for biomechanical applications,” *Sensors and Actuators A: Physical*, vol. 120, no. 2, pp. 370–382, 2005.
- [341] M. S. Bartsch, W. Federle, R. J. Full, and T. W. Kenny, “A multiaxis force sensor for the study of insect biomechanics,” *Microelectromechanical Systems, Journal of*, vol. 16, no. 3, pp. 709–718, 2007.
- [342] J. L. Regolini, D. Bensahel, E. Scheid, and J. Mercier, “Selective epitaxial silicon growth in the 650–1100 [degree]c range in a reduced pressure chemical vapor deposition reactor using dichlorosilane,” *Applied Physics Letters*, vol. 54, no. 7, pp. 658–659, 1989.
- [343] N. Afshar-Hanai, J. M. Bonar, A. G. R. Evans, G. J. Parker, C. M. K. Starbuck, and H. A. Kemhadjian, “Thick selective epitaxial growth of silicon at 960c using silane only,” *Microelectronic Engineering*, vol. 18, no. 3, pp. 237–246, 1992.
- [344] J. M. Bonar and G. J. Parker, “Selective low pressure chemical vapor deposition epitaxy using silane only for advanced device applications,” *Materials Science and Technology*, vol. 11, no. 1, pp. 31–35, 1995.
- [345] O. N. Tufte and E. L. Stelzer, “Piezoresistive properties of heavily doped n-type silicon,” *Physical Review*, vol. 133, no. 6A, p. A1705, 1964.
- [346] A. A. Barlian, N. Harjee, V. Mukundan, T. H. Fung, S.-J. Park, and B. L. Pruitt, “Sidewall epitaxial piezoresistor process for in-plane sensing applications,” in *21st IEEE International Conference on Micro Electro Mechanical Systems*, Tucson, Arizona, 2008, pp. 331–334.
- [347] Z. Zhang, S. Chen, Y. Chang, and S. Jiang, “Surface grafted sulfobetaine polymers via atom transfer radical polymerization as superlow fouling coatings,” *The Journal of Physical Chemistry B*, vol. 110, no. 22, pp. 10 799–10 804, 2006.

- [348] Z. Zhang, T. Chao, S. Chen, and S. Jiang, "Superlow fouling sulfobetaine and carboxybetaine polymers on glass slides," *Langmuir*, vol. 22, no. 24, pp. 10 072–10 077, 2006.
- [349] E. M. Chow, "Electrical through-wafer interconnects and microfabricated cantilever arrays using through-wafer silicon etching," Ph.D., Stanford University, 2001.
- [350] E. M. Chow, V. Chandrasekaran, A. Partridge, T. Nishida, M. Sheplak, C. F. Quate, and T. W. Kenny, "Process compatible polysilicon-based electrical through-wafer interconnects in silicon substrates," *Journal of Microelectromechanical Systems*, vol. 11, no. 6, pp. 631–640, 2002.
- [351] L. Gammelgaard, J. Richter, M. Lillemose, E. V. Thomsen, and A. Boisen, "Piezoresistive su-8/nano particle composites," in *International Workshop on Nanomechanical Sensors*, Copenhagen, Denmark, 2006, pp. 54–55.
- [352] H. C. Chiamori, J. W. Brown, E. V. Adhiprakasha, E. T. Hantsoo, J. B. Straalsund, N. A. Melosh, and B. L. Pruitt, "Suspension of nanoparticles in su-8: Processing and characterization of nanocomposite polymers," *Microelectronics Journal*, vol. 39, no. 2, pp. 228–236, 2008.